PROCESSING, MORPHOLOGY AND PROPERTIES OF GRAPHENE REINFORCED POLYMER NANOCOMPOSITES

A DISSERTATION
SUBMITTED TO THE FACULTY OF THE GRADUATE SCHOOL
OF THE UNIVERSITY OF MINNESOTA
BY

HYUNWOO KIM

IN PARTIAL FULFILLMENT OF THE REQUIREMENTS
FOR THE DEGREE OF
DOCTOR OF PHILOSOPHY

CHRISTOPHER W. MACOSKO, ADVISOR

SEPTEMBER 2009

Acknowledgements

I am truly grateful to numerous people who have helped and encouraged me for my doctoral study at the University of Minnesota. First, I owe my deep gratitude to my advisor Professor Chris Macosko for all his guidance and support on my study here. He has always been a great example of passionate and inspiring researcher to me. I would like to thank Professor Michael Tsapatsis, Professor Andreas Stein and Professor Satish Kumar for reviewing my thesis work and becoming thesis defense committee member. I was very fortunate to work with Professor Andreas Stein especially for the first two years of my Ph.D. I learned a lot of synthetic chemistry side of the polymer nanocomposite research from him and his students. Professor Tsapatsis also helped my research by kindly letting me use the gas permeation set-up and the BET apparatus in his laboratory.

This thesis would not be possible without financial supports from the NIST Advanced Technology Research Program with IMATION Corp., Industrial Partnership for Research in Interfacial and Material Engineering at University of Minnesota with General Motors and Abu Dhabi-Minnesota Institute for Research Excellence program. I appreciate Professor Robert Prud'homme at Princeton University, John Lettow and John Crain from Vorbeck Materials for their providing thermally exfoliated graphite oxide.

I am indebted to many colleagues that I have met during my stay at the University of Minnesota. Dr. David Giles has helped me with rheometry and other polymer characterization techniques. Former student Michael Dolgovskij first guided me to polymer extrusion and related peripherals. Former post doctor Miura Yutaka was a great synthetic chemistry teacher. I also thank Fan Li, Kwanho Chang and Sangwoo Lee for their training me on transmission electron microscopy. Many staff in the University of Minnesota Characterization Facility have made their expertise and support available to me.

It was a great pleasure for me to spend last five years with wonderful friends in this department. Spending time with former and current group members Carlos Lopez-Barron, Zhengxi Zhu, Ling Zhang, Jie Song, Dawud Tan, Harikrishnan G., Suqin Tan,

Michael Castro and Patrick Lee made my lab life very enjoyable. I found working with four hard-working undergraduate students (Michael Beaulieu, Dominick Bindl, Albina Khusainova and Adam Reimnitz) very valuable experience. I also enjoyed sharing my office (also known as “the polymer exile”) with other polymer group members. Other students and post doctors especially those from Korea made my after-work life more joyful and showed great friendship to me. I should not forget delivering my appreciation to helpful administrative staff in the department of chemical engineering and materials science.

Finally, my deepest gratitude goes to my family and friends in Korea. My parents have been supporting me so patiently even though they still don’t understand why their son had to study “plastics” for five years in the United States. I wish her best luck to my sister Kyu-rhee for her future career. All my good friends have been so nicely motivating me over the phone. Still, my girl friend, Ji-yeon was my greatest reason to live and work hard.

Dedication

To my loved family and friends.

Abstract

A unique combination of excellent electrical, thermal and mechanical properties has made graphene a multi-functional reinforcement for polymers. The goal of this research has been three-fold: exfoliation of graphite for higher surface area, development of effective strategies for processing and characterization of graphene based polymer composites and understanding their processing, structure and property relationships.

Exfoliated carbon sheets can be obtained from graphite oxide (GO). Functionalized graphene sheets (FGS) are formed by rapid pyrolysis of GO. Despite size reduction and distortion in the flat graphene structure by thermal treatments, FGS have high electrical conductivity and can be melt-processed into polymers. GO can be chemically modified with isocyanate, which improves dispersability in organic solvents and polymers. Although not as thermally stable and electrical conductive as FGS, isocyanate treated GO (iGO) has a larger diameter and is advantageous for retaining high toughness of the composites.

FGS and iGO were incorporated into a range of model polymers. Solvent aided blending led to better dispersion of FGS in thermoplastic polyurethane than melt processing. Via solvent mixing, polyurethane became electrically conductive at even less than 0.5 wt% of FGS. With 3 wt% iGO, tensile modulus was increased up to 10 times and N_2 permeation was reduced by 90%, implying high aspect ratio of exfoliated sheets. Morphology of melt compounded graphite and FGS in poly(ethylene-2,6-naphthalate) was characterized with electron microscopy, X-ray scattering, melt rheology and solid property measurements. Unlike graphite, dispersion of FGS quantified from different routes spreads over a wide range due to structural irregularity and simplified model assumptions. Melt viscoelasticity and electrical properties of polycarbonate were significantly modified by graphite orientation. Flow-induced orientation reduced property gains by graphene dispersion, while quiescent-state annealing restored rigidity and electrical conductivity of the composites. Using melt-state rheological and dielectric measurements, micro-structural evolution of FGS in polystyrene was monitored through annealing. Temporal property changes were analogous to the aging response of colloidal

glasses and also influenced by matrix chain relaxation dynamics. Graphene-based polymer nanocomposites can be a new versatile soft material with numerous advantages. For maximized benefits, composite morphology must be tailored appropriately with understanding of its structure-property relationships.

Table of Contents

List of Tables

List of Figures

List of Abbreviations

a	Power law exponent correlating shear modulus and angular frequency of oscillatory deformation
a_T	Frequency shift factor
A	Area of parallel electrodes for dielectric measurements
A, A_i	Functions of Eshelby's tensor in Mori and Tanaka's model
A_f	Aspect ratio
C	Sample capacitance
C_0	Vacuum capacitance
C_r	Characteristic ratio for polymer chains
d	Interlayer spacing, diameter of disk-like particles or distance between parallel electrodes for dielectric measurements
d_f	Fractal dimension
D	Dielectric dissipation factor
D_r	Rotary diffusivity of Brownian disks
E	Young's modulus
E'	Tensile storage modulus
E''	Tensile loss modulus
E_{11}	Transverse tensile modulus
E_m, E_{matrix}	Young's modulus of matrix
$E_{reinforcement}$	Tensile modulus of Reinforcement
G_i	Shear modulus
G'	Storage shear modulus
G'_0	Linear viscoelastic storage shear modulus
G''	Loss Shear modulus
h	Thickness of disk-like particles
ΔH	Area of differential scanning calorimetric exotherm
I	Azimuthal X-ray scattering intensity distribution

I_j	Functions of β_i, K_i and G_i in Chow's model
J_j	Functions of β_i, K_i and G_i in Chow's model
k	Boltzmann constant, $1.3806503 \times 10^{-23}$ m^2 kg s^{-2} K^{-1}
K_i	Bulk modulus
l	Length of polymer's repeating groups
M_n	Number average molecular weight
M_w	Weight average molecular weight
M_v	Viscosity average molecular weight
P	Gas permeability
P_0	Permeability of unfilled polymers
P_{He}	Helium permeability
P_{N2}	Nitrogen permeability
q	Scattering vector
r	Radius of disk-like particles
t	Time
T	Temperature
T_0	Reference temperature for time-temperature superposition
$T_{g,\,soft}$	Glass transition temperature of polyurethane soft segment
T_{mix}	Melt compounding temperature
x	Backbone fractal dimension
$\alpha_\perp$	Coefficient of thermal expansion in thickness direction
$\alpha_{//}$	Coefficient of thermal expansion in plane direction
α_{11}	Transverse coefficient of thermal expansion
β	Power law exponent between shear modulus and annealing time
β_i	Volumetric thermal expansion coefficient
δ	Phase angle between E' and E''
Δ	Full width at half maximum of azimuthal X-ray scattering distribution

ε^*	Complex dielectric permittivity
ε'	Real part of complex dielectric permittivity
ε''	Imaginary part of complex dielectric permittivity
ε_0	Vacuum permittivity, 8.854×10^{-12} F/m
ϕ	Volume fraction of inclusions, or azimuthal X-ray scattering angle
ϕ_0	Center of azimuthal X-ray scattering distribution
ϕ_{per}	Threshold volume fraction for percolation
ϕ_{sphere}	Percolation threshold of interpenetrating, randomly packed spheres
γ	Shear strain
γ_{crit}	Critical strain
η	Viscosity
η^*	Complex viscosity
η_0	Zero shear viscosity
λ_N	Longest relaxation time of polymer chains
ν	Exponent for power law scaling between modulus and ϕ-ϕ_{perc}, or AC frequency
ν_m	Poisson's ratio of matrix
θ	X-ray scattering angle
ρ	Density
σ^*	Complex electrical conductivity
σ'	Real part of complex electrical conductivity
σ''	Imaginary part of complex electrical conductivity
$\sigma_{ultimate}$	Ultimate strength of polymers
τ_ξ	Average time for charge carriers to travel a percolated cluster of a correlation length ξ
ω	Frequency of oscillatory shear deformation

ω_c	Cross-over frequency between power-law regime and DC plateau in electrical conductivity versus AC frequency
ω_d	Angular AC frequency
ξ	Correlation length for percolated particle cluster
ζ	Critical exponents associated with percolating particle cluster size

AC	Alternating current
AcPh-iGO	Acetylphenyl isocyanate-treated graphite oxide
AFM	Atomic force microscopy
ATR	Attenuated total reflection
BDO	1,4-buthanediol
BET	Brunauer, Emmett and Teller
CNT	Carbon nanotubes
CTE	Coefficient of thermal expansion
DC	Direct current
DMA	Dynamic mechanical analysis
DMF	*N*,*N*-dimethylformamide
DSC	Differential scanning calorimetry
EMI	Electro-magnetic interference
FGS	Functionalized Graphene Sheets
FTIR	Fourier-transform infrared spectroscopy
FWHM	Full width at half maximum
GO	Graphite oxide
iGO	Isocyanate-treated graphite oxide
IR	Infrared
LAOS	Large-amplitude oscillatory shear deformation
MA	Maleic anhydride

MDI	Methylene Diphenyl diisocyanate
MWCNT	Multi-walled carbon-nanotubes
PC	Polycarbonate
PDI	Polydispersity index
PE	Polyethylene
PEN	Poly(ethylene-2,6-naphthalate)
Ph-iGO	Phenyl isocyanate-treated graphite oxide
PS	Polystyrene
RSA II	Rheometrics Solids Analyzer II
SEC	Size exclusion chromatography
TEM	Transmission electron microscopy
THF	Tetrahydrofuran
TPU	Thermoplastic polyurethane
TTS	Time-temperature superposition
WAXD	Wide-angle X-ray diffraction
WLF	Williams-Landel-Ferry
XPS	X-ray photoelectron spectroscopy
XRD	X-ray diffraction

Chapter 1. Introduction: Polymer/Graphene Layered Nanocomposite

1.1. Polymer/Graphene Layered Nanocomposites

Plastics have many outstanding properties: light weight, toughness, good elongation, easy processing and low cost. However, comparing with ceramics and metals, low stiffness, strength, flammability and high permeability to gases and solvents can be their weaknesses. In some applications, higher thermal and electrical conductivity could be advantageous. Reinforcement with nano meter sized fillers can overcome many of these drawbacks if they are well dispersed in the matrix polymer. Most property enhancements can be achieved at significantly smaller loadings than conventional micron sized glass or carbon fibers and resulting "nanocomposites" are much lighter in weight.

Since they were pioneered by researchers at Toyota Motors in the late 1980's,[1,2] organically modified layered silicates[3] have been a main subject of interest for the reinforcing nano-material. Metal cations on negatively charged silicate surface[4] can be exchanged with organic modifiers such as alkylammonium surfactants, which increases the miscibility with polymers (Figure 1-1 (a)).[5] Partial or complete dispersion of these layers in the matrix polymer leads to the "intercalated" or "exfoliated" nanocomposites, as depicted in Figure 1-1 (b).[3] Their key benefits are improved mechanical properties,[6,7] dimensional stability,[8,9] gas barrier,[10] and flame resistance[11] of host polymers. Carbon nanotubes (CNT) also attracted huge interest with their unique combination of excellent mechanical, electrical and thermal properties.[12] Since Ajayan *et al.* first successfully embedded an array of multi-wall CNT into epoxy,[13] CNT have been used for producing polymer fibers with enhanced toughness,[14] and composites that are electrically[15] or thermally[16] conductive at extremely small levels of incorporation.

Graphite is a 2-dimensional carbon material which is naturally abundant. In graphite, sp^2 hybridized carbons are covalently bonded in hexagonal manner forming individual sheets called "graphene" and these sheets are bound together by van der Waals

forces. Graphite has been used in many industrial applications such as lubricants[17] and high temperature gaskets.[18] Especially, one-carbon-atom thick graphene can be a very promising reinforcement, providing combined benefits of both layered silicates and CNT. Unlike layered silicates, it has exceptional electrical and thermal transport properties.[19,20] Unlike CNT, these 2-dimensional carbon layers can reduce gas permeability of host membranes,[21,22] and can be derived from naturally occurring graphite at a fraction of cost. Moreover, its in-plane mechanical properties are similar to those of CNT (Young's modulus E = 1 TPa, ultimate strength $\sigma_{ultimate}$ = 140 GPa).[23,24] The potentially high aspect ratio of single graphene sheets indicates that graphene can greatly improve mechanical and gas barrier properties at small incorporation if it is well exfoliated in a polymer matrix as illustrated in Figure 1-1 (b).[22,25]

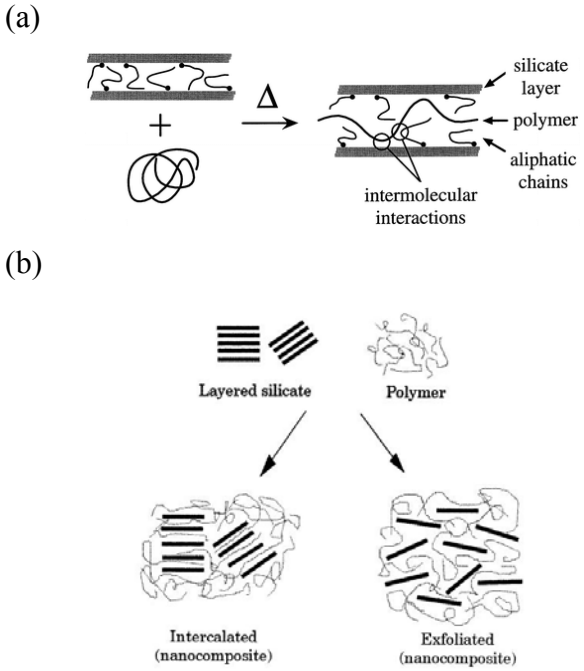

Figure 1-1. (a) Scheme describing interaction between a polymer chain and organically modified layered silicates. Adapted from reference 5. (b) Different stages of composites arising from dispersion of layered silicates in polymers: intercalated and exfoliated state. Images adapted and reproduced from reference 3.

Nonetheless, to date the exfoliation of graphite to graphene and its incorporation into polymers have been rarely reported. Low solubility, strong interaction and small spacing between stacked graphene planes make it nearly impossible to achieve a fully separated state of graphene by pure mechanical mixing with solvents/polymers. Many have attempted to exfoliate graphite sheets using intercalation with alkali metals[26] or exposing them to strong acidic conditions.[27-31] Expansion of layer spacing takes place via heat treatment,[26,28,30] or alternatively exposure to microwave radiation followed by mechanical grinding.[32,33] These expanded graphite platelets can be incorporated into polymers via solvent mixing,[29,34] in-situ polymerization,[30,31] or coating onto polymer particles followed by melt processing.[33] Expanded graphite yielded relatively better dispersion than un-intercalated graphite. Still, complete exfoliation to the level of single atomic sheets was not attained using these approaches. The thickness of resulting layers is typically 10 ~ 100 nm which is much greater than single graphene sheet thickness (0.34 nm).[35]

While deriving graphene from graphite was regarded nearly impossible for decades, recently developed strategies[36] have paved a way for polymer nanocomposites reinforced with graphene. Novoselov and Geim[19] first demonstrated free-standing single layer carbons from repeated mechanical cleavages of graphite with Scotch tapes. Isolation of graphene was also achieved via liquid-phase exfoliation.[37,38] Even bottom-up approaches such as chemical vapor deposition[39] and epitaxial graphitization[40] have been also reported. However, difficulties in large-scale production limit their practical applications. Moreover, obtained high-purity graphene layers tend to stack into graphite again or scroll into tubes[41] in order to minimize surface energy.

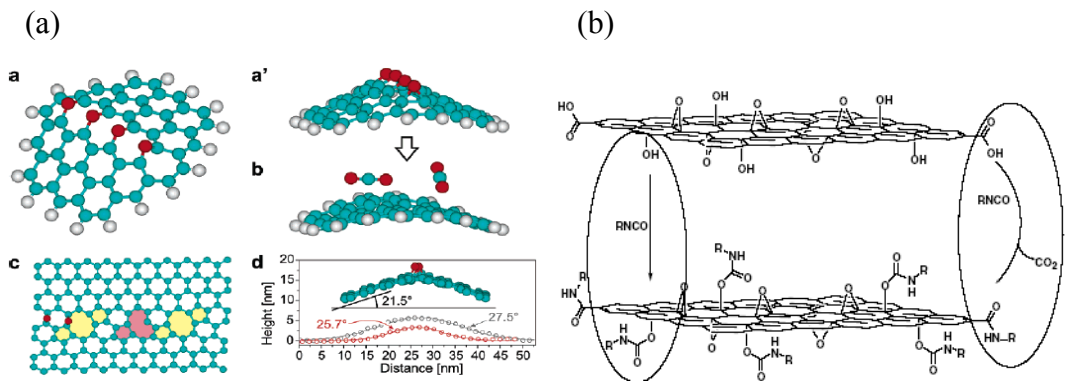

Figure 1-2. Schematics for (a) thermal exfoliation and (b) chemical modification of GO. (a) **a**, **a'**. Depicting a line of oxygen atoms on GO. **b**. CO_2 released during thermal reduction **c**, will leave atomistic vacancies in the carbon grids. **d**. Oxygen incorporation bends GO, which remains bent even after losing oxygens. Images adapted from reference 42. (b) Isocyanate can react with surface hydroxyl and carboxylic acid groups on GO forming carbamate and amide bonds. Image adapted from reference 45.

Recently discovered approaches starting from graphite oxide (GO) may be more feasible since they allow mass production of exfoliated carbon sheets. As shown in Figure 1-2, covalently-bonded oxygen groups on the GO surface serve as potential sites for gas-producing thermal decomposition[42,43] or chemical functionalization.[44,45] CO_2 produced by rapidly heating (~ 2000 °C/min) GO up to 1050 °C pressurizes and mechanically splits apart GO stacks bound by van der Waals forces.[43] An enormous surface area (700-1500 m^2/g), polar surface oxygens and high electrical conductivity[42] of the resulting material (functionalized graphene sheets, FGS) lead to composites with superior mechanical, electrical and thermal properties.[21,46] Structural deformation by oxidation and pyrolysis prevents re-stacking of layers, but reduces the ability of FGS to stiffen especially glassy polymers.[21,47] Stankovich and coworkers[44,45] showed that isocyanate-treated GO (iGO) readily forms a stable suspension in polar aprotic organic solvents, in contrast to the starting GO, enabling fabrication of completely exfoliated graphite/polymer nanocomposites via solvent blending. Electrical conduction of graphite

can be restored by *in-situ* chemical reduction of GO,[48] exhibiting electrical percolation at as low as 0.1 vol%.[44]

1.2. Overview of Thesis

This thesis addresses processing, morphology and properties of polymer nanocomposites reinforced FGS and iGO. These two exfoliated carbons derived from GO were selected as the reinforcement since even grams of materials can be produced in one batch. First, synthesis routes to GO, FGS and iGO are illustrated in Chapter 2. Physical and chemical characterization of these carbon sheets were conducted using atomic force microscopy, X-ray diffraction, liquid-phase solubility tests, vibrational spectroscopy and surface analysis techniques. Detailed characterization procedures and results are summarized therein.

In Chapter 3, processing, structure and properties of graphene/thermoplastic polyurethane (TPU) nanocomposites are presented. FGS and iGO were dispersed into TPU via three different composite manufacturing techniques: melt compounding, solvent mixing and *in-situ* polymerization. Morphology of dispersed graphene and properties from different blending routes are compared.

Chapter 4 focuses on quantification of graphene dispersion using various characterization techniques. FGS and un-exfoliated graphite are dispersed into poly(ethylene-2,6-naphthalate) with melt intercalation. Real and reciprocal space morphological information of dispersed particles are obtained with electron microscopy, and small and wide angle X-ray scattering. Melt rheology and electrical conductivity measurements are also employed to evaluate threshold concentration for rigidity and connectivity percolation. From tensile stiffness, thermal expansion and hydrogen permeation of the composites, quantified measures for graphene dispersion are extracted.

In Chapter 5, effects of post-processing on graphite orientation, and solid or melt state properties are discussed. After incorporation of graphite and FGS into polycarbonate (PC), orientation of graphitic layers was controlled via injection, compression molding and prolonged thermal annealing. Dispersion and orientation of graphite were

characterized with electron microscopy and X-ray scattering. Their influences on electrical conductivity and melt viscoelasticity of PC composites are examined.

In Chapter 6, melt-state rheological and dielectric measurements are introduced to probe micro-structural evolution of FGS clusters in polystyrene melts after large deformation. It is demonstrated that application of shear reduces melt elasticity and electrical conductivity of the composites, which can be recovered via quiescent annealing. Effects of annealing conditions such as temperature, particle concentration, and matrix molecular weight on the aging response are addressed.

Finally, Chapter 7 summarizes all key results of this polymer/graphene nanocomposite study and provides suggestions for future research directions. Processing-morphology-property relationships of polymers reinforced with graphene are revisited.

1.3. References

(1) Usuki, A.; Kojima, Y.; Kawasumi, M.; Okada, A.; Fukushima, Y.; Kurauchi, T.; Kamigaito, O. *J. Mater. Res.* **1993**, *8*, 1179-84.

(2) Usuki, A.; Kawasumi, M.; Kojima, Y.; Okada, A.; Kurauchi, T.; Kamigaito, O. *J. Mater. Res.* **1993**, *8*, 1174-8.

(3) Alexandre, M.; Dubois, P. *Mater. Sci. Eng., R* **2000**, *R28*, 1-63.

(4) van Olphen, H. *Clay Colloid Chemistry*; 2nd ed.; John Wiley & Sons: New York, 1977.

(5) Vaia, R. A.; Giannelis, E. P. *Macromolecules* **1997**, *30*, 7990-7999.

(6) Kojima, Y.; Usuki, A.; Kawasumi, M.; Okada, A.; Fukushima, Y.; Kurauchi, T.; Kamigaito, O. *J. Mater. Res.* **1993**, *8*, 1185-9.

(7) Cho, J. W.; Paul, D. R. *Polymer* **2000**, *42*, 1083-1094.

(8) Yano, K.; Usuki, A.; Okada, A.; Kurauchi, T.; Kamigaito, O. *J. Polym. Sci., Part A: Polym. Chem.* **1993**, *31*, 2493-8.

(9) Yoon, P. J.; Fornes, T. D.; Paul, D. R. *Polymer* **2002**, *43*, 6727-6741.

(10) Messersmith, P. B.; Giannelis, E. P. *J. Polym. Sci., Part A: Polym. Chem.* **1995**, *33*, 1047-57.

(11) Gilman, J. W.; Jackson, C. L.; Morgan, A. B.; Harris, R., Jr.; Manias, E.; Giannelis, E. P.; Wuthenow, M.; Hilton, D.; Phillips, S. H. *Chem. Mater.* **2000**, *12*, 1866-1873.

(12) Moniruzzaman, M.; Winey, K. I. *Macromolecules* **2006**, *39*, 5194-5205.

(13) Ajayan, P. M.; Stephan, O.; Colliex, C.; Trauth, D. *Science* **1994**, *265*, 1212-1214.

(14) Behabtu, N.; Green, M. J.; Pasquali, M. *Nanotoday* **2008**, *3*, 24-34.
(15) Bryning, M. B.; Islam, M. F.; Kikkawa, J. M.; Yodh, A. G. *Adv. Mater.* **2005**, *17*, 1186-1191.
(16) Choi, E. S.; Brooks, J. S.; Eaton, D. L.; Al-Haik, M. S.; Hussaini, M. Y.; Garmestani, H.; Li, D.; Dahmen, K. J. *J. Appl. Phys.* **2003**, *94*, 6034-6039.
(17) Tamashuasky, A. V. In *National Lubricating Grease Institute 72nd Annual Meeting* San Antonio, TX, 2005.
(18) Chung, D. D. L. *J. Mater. Sci.* **1987**, *22*, 4190-4198.
(19) Novoselov, K. S.; Geim, A. K.; Morozov, S. V.; Jiang, D.; Zhang, Y.; Dubonos, S. V.; Grigorieva, I. V.; Firsov, A. A. *Science* **2004**, *306*, 666-669.
(20) Smith, A. W.; Rasor, N. S. *Phys. Rev.* **1956**, *104*, 885-91.
(21) Kim, H.; Macosko, C. W. *Macromolecules* **2008**, *41*, 3317-3327.
(22) Kalaitzidou, K.; Fukushima, H.; Drzal, L. T. *Carbon* **2007**, *45*, 1446-1452.
(23) Kelly, B. T. *Physics of Graphite*; 1st ed.; Applied Science: London, 1981.
(24) Lee, C.; Wei, X.; Kysar, J. W.; Hone, J. *Science* **2008**, *321*, 385-388.
(25) Kalaitzidou, K.; Fukushima, H.; Drzal, L. T. *Composites: Part A* **2007**, *38*, 1675-1682.
(26) Viculis, L. M.; Mack, J. J.; Mayer, O. M.; Hahn, H. T.; Kaner, R. B. *J. Mater. Chem.* **2005**, *15*, 974-978.
(27) Carr, K. E. *Carbon* **1970**, *8*, 155-66.
(28) Chen, G.; Wu, D.; Weng, W.; Wu, C. *Carbon* **2003**, *41*, 619-621.
(29) Zheng, W.; Wong, S.-C.; Sue, H.-J. *Polymer* **2002**, *43*, 6767-6773.
(30) Zou, J.-F.; Yu, Z.-Z.; Pan, Y.-X.; Fang, X.-P.; Ou, Y.-C. *J. Polym. Sci., Part B: Polym. Phys.* **2002**, *40*, 954-963.
(31) Pan, Y.-X.; Yu, Z.-Z.; Ou, Y.-C.; Hu, G.-H. *J. Polym. Sci., Part B: Polym. Phys.* **2000**, *38*, 1626-1633.
(32) Fukushima, H. PhD Thesis, Michigan State University, 2003.
(33) Kalaitzidou, K.; Fukushima, H.; Drzal, L. T. *Compos. Sci. Technol.* **2007**, *67*, 2045-2051.
(34) Shen, J.-W.; Chen, X.-M.; Huang, W.-Y. *J. Appl. Polym. Sci.* **2003**, *88*, 1864-1869.
(35) Al-Jishi, R.; Dresselhaus, G. *Phys. Rev. B* **1982**, *26*, 4514-22.
(36) Jacoby, M. *Chem. Eng. News* **2009**, *87*, 14-20.
(37) Hernandez, Y.; Nicolosi, V.; Lotya, M.; Blighe, F. M.; Sun, Z.; De, S.; McGovern, I. T.; Holland, B.; Byrne, M.; Gun'Ko, Y. K.; Boland, J. J.; Niraj, P.; Duesberg, G.; Krishnamurthy, S.; Goodhue, R.; Hutchison, J.; Scardaci, V.; Ferrari, A. C.; Coleman, J. N. *Nat. Nanotechnol.* **2008**, *3*, 563-568.
(38) Lotya, M.; Hernandez, Y.; King, P. J.; Smith, R. J.; Nicolosi, V.; Karlsson, L. S.; Blighe, F. M.; De, S.; Wang, Z.; McGovern, I. T.; Duesberg, G. S.; Coleman, J. N. *J. Am. Chem. Soc.* **2009**, *131*, 3611-3620.
(39) Kim, K. S.; Zhao, Y.; Jang, H.; Lee, S. Y.; Kim, J. M.; Kim, K. S.; Ahn, J.-H.; Kim, P.; Choi, J.-Y.; Hong, B. H. *Nature* **2009**, *457*, 706-710.

(40) Emtsev, K. V.; Bostwick, A.; Horn, K.; Jobst, J.; Kellogg, G. L.; Ley, L.; McChesney, J. L.; Ohta, T.; Reshanov, S. A.; Roehrl, J.; Rotenberg, E.; Schmid, A. K.; Waldmann, D.; Weber, H. B.; Seyller, T. *Nat. Mater.* **2009**, *8*, 203-207.

(41) Viculis, L. M.; Mack, J. J.; Kaner, R. B. *Science* **2003**, *299*, 1361.

(42) Schniepp, H. C.; Li, J.-L.; McAllister, M. J.; Sai, H.; Herrera-Alonso, M.; Adamson, D. H.; Prud'homme, R. K.; Car, R.; Saville, D. A.; Aksay, I. A. *J. Phys. Chem. B* **2006**, *110*, 8535-8539.

(43) McAllister, M. J.; Li, J.-L.; Adamson, D. H.; Schniepp, H. C.; Abdala, A. A.; Liu, J.; Herrera-Alonso, M.; Milius, D. L.; Car, R.; Prud'homme, R. K.; Aksay, I. A. *Chem. Mater.* **2007**, *19*, 4396-4404.

(44) Stankovich, S.; Dikin, D. A.; Dommett, G. H. B.; Kohlhaas, K. M.; Zimney, E. J.; Stach, E. A.; Piner, R. D.; Nguyen, S. T.; Ruoff, R. S. *Nature* **2006**, *442*, 282-286.

(45) Stankovich, S.; Piner, R. D.; Nguyen, S. T.; Ruoff, R. S. *Carbon* **2006**, *44*, 3342-3347.

(46) Ramanathan, T.; Abdala, A. A.; Stankovich, S.; Dikin, D. A.; Herrera-Alonso, M.; Piner, R. D.; Adamson, D. H.; Schniepp, H. C.; Chen, X.; Ruoff, R. S.; Nguyen, S. T.; Aksay, I. A.; Prud'Homme, R. K.; Brinson, L. C. *Nat. Nanotechnol.* **2008**, *3*, 327-331.

(47) Kim, H.; Macosko, C. W. *Polymer* **2009**, *50*, 3797-3809.

(48) Stankovich, S.; Dikin, D. A.; Piner, R. D.; Kohlhaas, K. A.; Kleinhammes, A.; Jia, Y.; Wu, Y.; Nguyen, S. T.; Ruoff, R. S. *Carbon* **2007**, *45*, 1558-1565.

Chapter 2. Exfoliation of Graphite

2.1. Introduction

Rapid pyrolysis[1,2] and surface modification[3,4] of graphite oxide (GO) are two most efficient routes to exfoliation of graphite, which yield relatively large quantity of single carbon sheets. Resulting materials, functionalized graphene sheets (FGS) and isocyanate-treated graphite oxide (iGO), can be dispersed into polymers via conventional solvent or melt processes without significant particle re-aggregation. This chapter covers experimental procedures for synthesis and characterization of exfoliated graphitic nano-particles. Also, major observations from particle characterization using atomic force microscopy (AFM), X-ray diffraction (XRD), solubility tests, surface analysis and vibrational spectroscopy are reported. Results presented in this chapter and Chapter 3 were reproduced from a manuscript currently in preparation for publication.

2.2. Experimental

2.2.1. Particle Synthesis

FGS and iGO all start from a common starting material, graphite oxide (GO). While there are a number of procedures reported for GO synthesis,[5-7] they all involve oxidation in concentrated acidic medium using strong oxidizing agents such as potassium permanganate, chlorate or bichromate. Among them, Hummers and Offeman's[8] method was used since reaction can complete in relatively short time (~ 1 hr). GO was produced from high purity graphite powders (SP-1 graphite, Bay Carbon, average particle diameter: 30 μm). 5 g of SP-1 graphite in a 250 mL round-bottom flask was stirred in a mixture of concentrated sulfuric acid (95-98%, 80 mL) and sodium nitrate (2.5 g, Sigma-Aldrich) in an ice bath. After slowly adding 20 g of potassium permanganate (Sigma-Aldrich), the suspension was removed from the ice bath. The reaction flask was kept open to allow evolution of gas from the mixture. When the temperature exceeded 40 °C, the mixture was cooled again in the ice maintaining temperature at ~ 35 °C. The

temperature began to decrease in 1 hr and vigorous effervescence ceased. Then GO paste was gradually diluted in de-ionized water (6 L) with stirring. Diluted solution was treated with 30% hydrogen peroxide in order to reduce permanganate ions[9] to soluble $MnSO_4$ and filtered with a fritted glass filter. The filter cake was occasionally rinsed with 10% hydrochloric acid to reduce sulfate ions and circumvent swelling of the product.[9] Complete removal of sulfates was confirmed from no precipitation reaction with barium chloride. The product was repeatedly washed with de-ionized water for more than 2 weeks until pH of filtrate from washing becomes ~ 6. GO was dried in a vacuum oven at 45 °C before use.

After drying GO for 1 week, graphite oxide (2 g) was treated with 80 mmol of phenyl isocyanate (Ph-iGO) or acetylphenyl isocyanate (AcPh-iGO) for iGO synthesis[4] in anhydrous *N,N*-dimethylformamide (DMF, 200 mL) under N_2 for 48 hrs. All reagents were obtained from Sigma Aldrich and used as received. After reaction, iGO was precipitated by adding into methylene chloride (1 L) and washed several times on a fritted glass filter.

FGS was provided by Prof. Robert Prud'homme at Princeton University (0.5 g) and Vorbeck Materials (5 g).[10] Synthesis of FGS is described in Schniepp *et al.*[1] GO was prepared from graphite with a nominal size of 45 μm. Oxidation was performed for 96 hrs at room temperature following Staudenmaier's method[7] using potassium chlorate in mixed sulfuric and nitric acid. For thermal exfoliation, a quartz tube containing dry GO powders purged with argon was inserted for 30 s into a furnace pre-heated at 1050 °C. The surface area of as-received FGS estimated by Brunauer, Emmett and Teller (BET)[11] N_2 adsorption (Autosorb-1, Quantachrome) is ~ 800 m^2/g.

2.2.2. Particle Characterization

Dimensions of exfoliated GO and FGS were estimated with AFM (Proximal Nanoprobe Scanning Probe Nanoscope, Digital Instruments). Suspensions of GO in de-ionized water and FGS in tetrahydrofuran (THF) were prepared at 10 μg/ml by mild stirring for ~ 3 weeks (GO) and ~ 2 days (FGS). Sonication was avoided since it may

cause a size reduction of particles. Particles were deposited onto a mica substrate (grade V1, Ted Pella) by coating a droplet of the suspension with a glass pipet. Contact-mode imaging of GO and FGS on mica was conducted with V-shape gold coated silicon nitride cantilevers (spring constant, k = 0.12 N/m, tip radius, r = 20 nm, Veeco Probes) under ambient conditions.

X-ray photoelectron (XPS) and Raman spectroscopy can provide information on physical and chemical states of graphitic materials.[1,12-14] XPS of graphitic particles were collected with a Surface Science model SSX-100 (graphite) and a Physical Electronic model 555 spectrometer (GO, Ph-iGO and FGS) with MgK_α radiation. After degassing in an introduction chamber (~ 1 hr), samples were placed into a hemispherical analyzer where the pressure is maintained below 1.5×10^{-7} torr. An accelerating voltage of 12 kV at 250 W power was used for data acquisition. For a single survey scan, 3 sweeps were averaged with a pass energy of 200 eV. After identifying reflections corresponding to binding energies of C_{1s} and O_{1s}, higher resolution spectra were recorded with pass energy of 25 eV. Atomic concentration estimation and peak fitting were conducted with Auger Scan Version 3.1 program. Raman spectra were obtained using a Witec Alpha300R confocal Raman microscope connected with a class III Argon laser source (Omnichrome, CA) with wavelength of 514.5 nm. For each spectrum, the signal integrated over 20 sec was recorded.

Fourier-transform infrared (FTIR) spectra of graphite powders were obtained over the wavenumber range of 650-4000 cm^{-1} with Nicolet Magna-IR 750 at a resolution of 2 cm^{-1}. Graphite, FGS, GO and iGO were coated on KBr disks from solutions in THF (0.5 mg/mL) and FTIR was performed in a transmission mode with dry N_2 purge after completely removing THF in vacuo at 50 °C. Spectra averaged over 32-64 scans were base-line subtracted using a linear base-line extrapolated from where no appreciable absorption is detected.

XRD of graphite and its derivatives was performed with a combined small and wide angle instrument (SAXSESS, Anton Paar) with CuK_α radiation. Dry powders were placed between Kapton tapes. XRD was operated at a generator voltage of 40 kV and

current of 50 mA. Acquired spectra were background subtracted with a diffraction pattern of Kapton tapes.

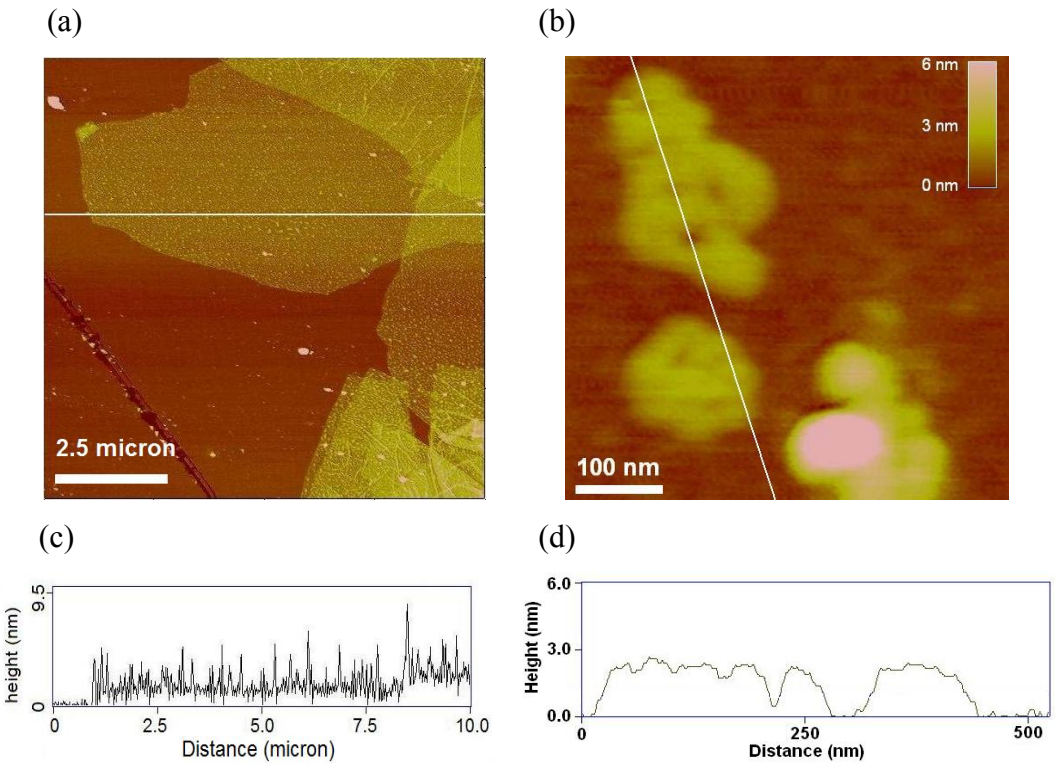

Figure 2-1. Contact mode AFM scan of (a) GO and (b) FGS on mica. Height profiles of (c) GO and (d) FGS along the straight white lines.

2.3. Results and Discussion

2.3.1. AFM of particles

Representative contact-mode height profiles of GO and FGS lying on mica are compared in Figure 2-1 (a) and (b). Typical lateral size of GO determined from AFM is ~ 10 μm, which is substantially greater than the diameter of FGS, 50-400 nm. Considering the diameter of the starting graphite material (45 μm) for FGS,[1] significant size reduction during oxidation[15] and pyrolysis is evident. Figure 2-1 (c) and (d) are height scans of GO and FGS sheets along the straight lines drawn in Figure 2-1 (a) and (b). Height differences of GO plates are in multiples of 1 nm, which agrees with the average

thickness of isolated GO sheets from AFM found in literature.[4,16,17] Single-layer thickness indicates that oxidized graphite can be fully exfoliated in water owing to increased hydrophilicity.[18] The difference of ~ 0.3 nm from inter-lamellar spacing of dry GO determined by XRD[19] ~ 0.7 nm may originate from the surface water absorption. It was also demonstrated by spin-coating experiments that dot-like structures on the GO surface can be displaced by the centrifugal forces. These mobile entities on the surface might be inorganic salts, not removed by repeated washing or deposited from atmosphere after specimen preparation. For FGS, thickness varies even within a single platelet due to the wrinkled and buckled nature[1] of FGS (Figure 2-1 (d)). The minimum thickness of 1.8 nm falls in the thickness range of fully exfoliated FGS layer on highly oriented pyrolytic graphite found by Schinepp *et al.*[1] The specific surface area A can be related to the density (2.28 g/cm^3)[20] and the thickness h of the disks assuming the area of the disk perimeter is negligible. $h \approx 2 / A \cdot$ (density). The measured BET surface area of FGS ~ 800 m^2 gives h ~ 1.1 nm, which is close to the AFM estimate.

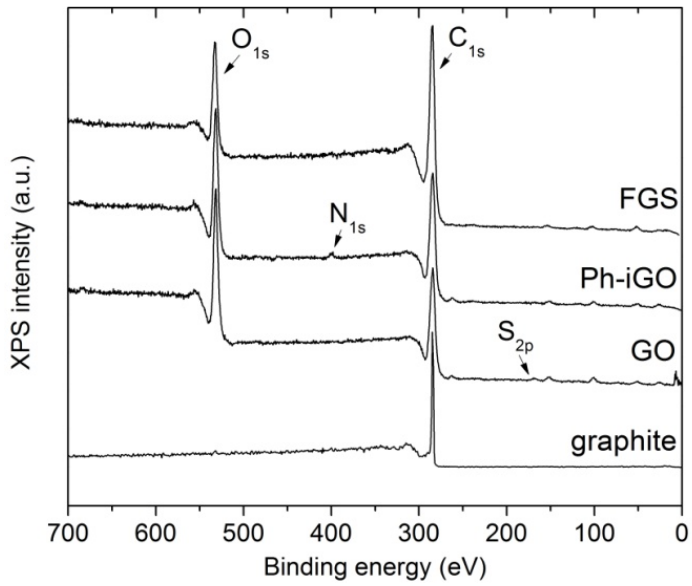

Figure 2-2. XPS survey scans of graphite, GO, Ph-iGO and FGS. Spectra were vertically shifted for clarity.

Table 2-1. Atomic Concentrations of Graphitic Derivatives from XPS

Element	C	O	N	S
Graphite	~ 100	0	-	-
GO	69	30	-	1
Ph-iGO	72	27	1	-
FGS	82	18	-	-

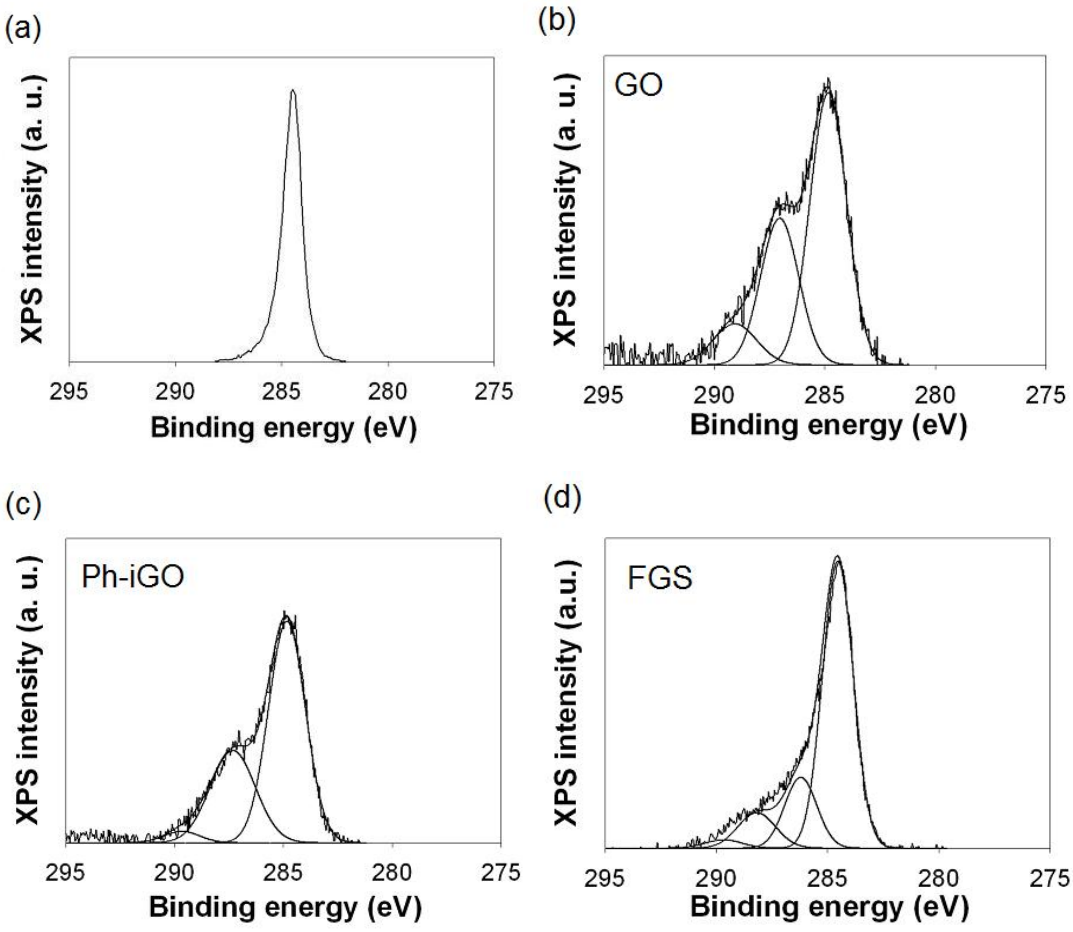

Figure 2-3. High resolution C_{1s} XPS spectrum of (a) graphite, (b) GO, (c) Ph-iGO and (d) FGS. Curves inside are deconvoluted curve fits of the spectrum.

2.3.2. XPS

Survey XPS scans of graphite, GO, Ph-iGO and FGS in the range of 0-700 eV are provided in Figure 2-2. Notable reflections at binding energy of ~ 169, 285, 402 and 533 eV correspond to S_{2p}, C_{1s}, N_{1s} and O_{1s} level, respectively.[21] From the peak intensities, atomic concentrations in each graphitic derivative were estimated (Table 2-1). A small amount of Si detected at ~ 153 eV (Si_{2s}) and 101 eV (Si_{2p}) was not included. Oxidation increased oxygen concentration in graphite up to 30%. Considering significantly higher oxygen contents in starting GO reported by Schniepp *et al.* (27 mol%)[1] than in FGS (18 mol%, Table 2-1), significant oxygen loss during rapid pyrolysis is evident. Note XPS only measures composition near the sample surface, which can be different from the bulk composition due to moisture absorption. The actual concentration of C to O in similar FGS estimated by elemental analysis[1] is as high as 10:1. Besides carbon and oxygen, sulfur was detected from GO and nitrogen from iGO. The trace of sulfur in GO may be from sulfate ions physically trapped in closed pores or covalently esterified with surface hydroxyl.[9] Nitrogen is due to carbamate or amide groups in iGO, which also substantiates surface functionalization with isocyanate.

C_{1s} XPS spectra of particles obtained in high resolution are presented in Figure 2-3. C_{1s} spectrum of graphite is nearly symmetric centered at 284.5 eV (Figure 2-3 (a)). Slight intensity redistribution toward higher binding energy may be originating from atmospheric oxidation.[19] The spectrum becomes more anisotropic after oxidation, which can be deconvoluted into several small peaks (Figure 2-3 (b) and (c)). It is suggestive of formation of carbon-oxygen bonds such as C-O, C=O and O-C=O with higher binding energy.[12,16,19] Thermal reduction[1] of GO is also inferred from the less pronounced intensity shoulder for FGS (Figure 2-3 (d)).

2.3.3. Raman Spectroscopy

Raman spectroscopy is used for analyzing hybridization state in carbons[14,22,23] (Figure 2-4). Confocal Raman spectra of graphite, GO and FGS are essentially identical to ones found in literature.[12,14] Two reflections at 1550-1650 cm^{-1} and 1350 cm^{-1} are

common for all three materials, despite different relative intensity, peak location and width. G band at 1550-1650 cm^{-1} stems from vibration of sp^2-hybridized graphitic domains.[22] It is strongest in the spectrum of un-treated graphite implying its graphitic domains are mainly intact. In contrast, both FGS and GO exhibit relatively weak G band with peak broadening. A shift of G band for GO to slightly higher wavenumber can be attributed to isolation of carbon double bonds after oxidation.[14] Oxidation diminished the G band intensity but also intensified the D band centered at 1350 cm^{-1}. Although originating from the vibration of sp^2-carbons in breathing modes, the D band response requires sp^3-hybridized carbons for its activation.[14,24] Therefore it reflects presence of defect-like amorphous domains.[23] Incorporation of oxygen to the surface necessitates flat graphitic carbons to be displaced into out-of-plane geometry inducing sheet deformation.[1,15] The slightly enhanced G to D ratio of FGS may be accounted for by partial restoration of graphitic domains through "self-healing" during thermal reduction.[13,14] A small Raman response at 1350 cm^{-1} of pristine graphite, which was also observed by others,[14,24-26] implies a small fraction of disordered carbons presumably near the platelet edges, and is related to the average crystallite size.[23]

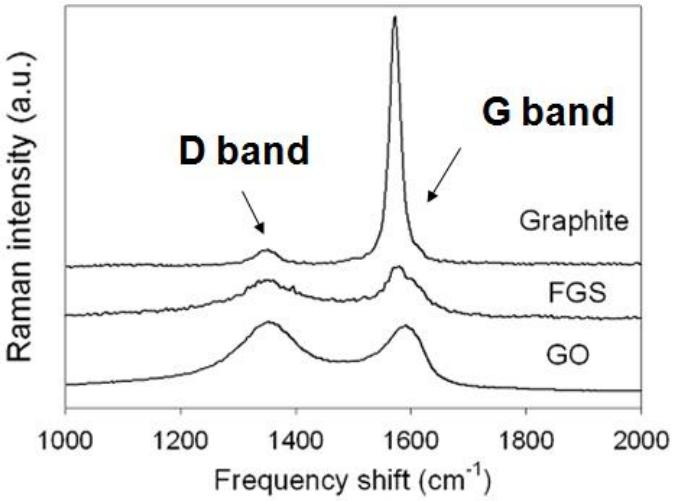

Figure 2-4. Raman spectra of graphite, FGS and GO. Spectra were shifted vertically for clarity.

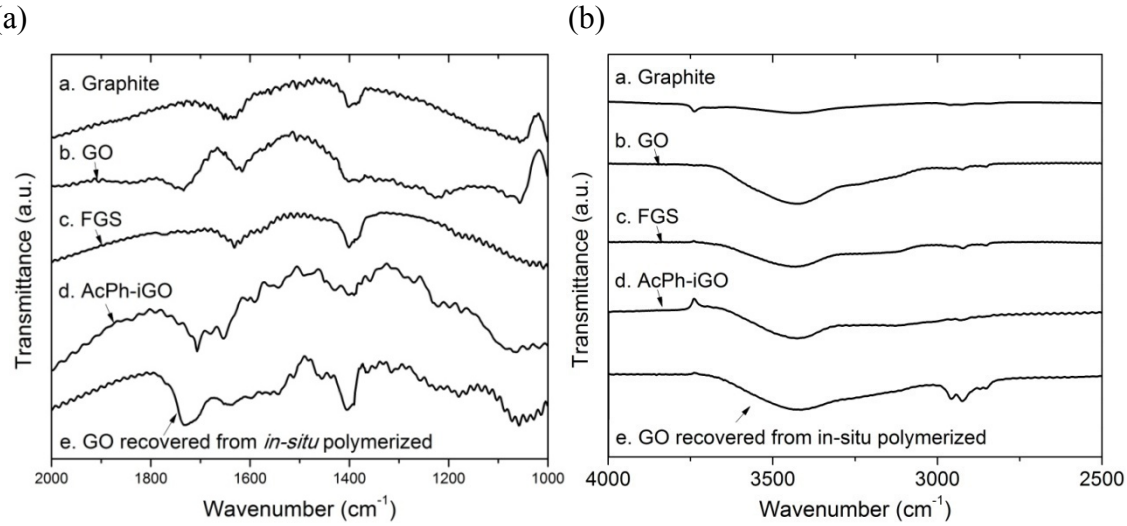

Figure 2-5. FTIR spectrum of a. graphite, b. GO, c. FGS, d. AcPh-iGO and e. GO recovered from *in-situ* polymerized thermoplastic polyurethane composites at (a) 1000-2000 and (b) 2500-4000 cm^{-1}. Spectra were shifted vertically for clarity.

2.3.4. FTIR

IR transmittance of each graphitic material in the range of 1000-2000 cm^{-1} is shown in Figure 2-5 (a). Chemical and structural changes of graphite upon oxidation, rapid pyrolysis and isocyanate functionalization could be detected from FTIR. Noticeable absorptions of GO are located at 1730 (carbonyl or carboxyl C=O stretching), 1620 (C-O-C or adsorbed H_2O deformation vibration), 1410 (O-H deformation vibration), 1370 (C-OH deformation vibration), 1230 (C-OH stretching) and 1050 cm^{-1} (skeletal C-O or C-C stretching).[9,16,19,27] After graphite oxidation, a broad band at 3000-3700 cm^{-1} also appears in the IR spectrum (Figure 2-5 (b)), which signifies stretching vibration of surface hydroxyls (~ 3400) and water absorption (~ 3200 cm^{-1}).[4,16,27]

FGS shows similar IR spectrum to graphite: intensity of features associated with C=O and C-O stretching at 1000-2000 cm^{-1} is substantially attenuated suggesting loss of oxygen groups through thermal treatments. However, the hydroxyl and H_2O stretching band at 3000-3700 cm^{-1} is still observed, which indicates some functionalities are still present. Note pristine graphite and FGS are not completely IR inactive in the range of

1000-2000 cm^{-1}. An absorption band near 1620 cm^{-1} may be from skeletal vibrations of un-oxidized aromatic domains as well as vibrations of the cyclic ether groups (C-O-C) or water molecules.[4,27] One located at ~ 1400 cm^{-1} may reflect C-OH groups in amorphous defects or particle edges, or an experimental artifact stemming from subtraction of background signal (atmospheric CO_2 and H_2O).

After treating GO with acetylphenyl isocyanate, absorption bands were shifted to 1700, 1650 (C=O stretching in carbamate esters and amide groups, respectively) and 1540 cm^{-1} (vibration of CNH groups) which all are related to carbamate and amide formation.[4] We prepared composites based on thermoplastic polyurethane (TPU) via *in-situ* polymerization with GO as described in Chapter 3. Although only appearing as shoulders to the stronger reflections, GO recovered from the *in-situ* polymerized TPU using THF extraction also has analogous IR features which is indicative of grafting of TPU chains on GO via urethane or amide linkages. Possible complication by physi-sorption of TPU on GO surface should be excluded since the supernatant portion after the centrifugation of THF containing Soxhlet-extracted GO did not display any absorptions related to TPU confirming complete removal of free TPU chains with repeated washing. Besides these reflections, strong C-H stretching absorptions at 2850 ~ 3000 cm^{-1} (Figure 2-5 (b)) also corroborate the existence of alkyl chains on the GO surface.

2.3.5. XRD

Intercalation by functional groups leads to increased average inter-gallery spacing of layered materials. A sharp reflection at $2\theta = 26.4°$ in the X-ray scattering pattern of pristine graphite (Figure 2-6 (a)) originates from the inter-layer (002) spacing (d = 0.34 nm). XRD indicates that GO has an expanded spacing, d = 0.70 nm ($2\theta = 12.7°$) due to the intercalation by oxygen containing groups and moisture.[9,16,19] As well as a shift to lower angle, peak becomes broader due to disorder introduced from variation in spacing. Upon treating GO with phenyl isocyanate, layer spacing increases further to d = 0.95 nm (2θ = 9.3°) since GO is separated by bulkier isocyanate moieties. In the scattering intensity profile of FGS, characteristic peaks reflecting structural periodicity are absent,

which signifies complete exfoliation or at least spacing > 2 nm. Inter-gallery spacing of AcPh-iGO (d = 1.23 nm, 2θ = 7.2°) is greater than that of Ph-iGO (Figure 2-6 (b)), probably due to the larger molecule size of acetylphenyl isocyanate. Higher surface coverage of acetylphenyl isocyanate may also contribute to the larger distance since it has higher reactivity with the GO hydoxyls.[4] This increased layer distance after thermal and chemical treatments can be advantageous for dispersion since intercalative diffusion of polymer chains can take place more readily.

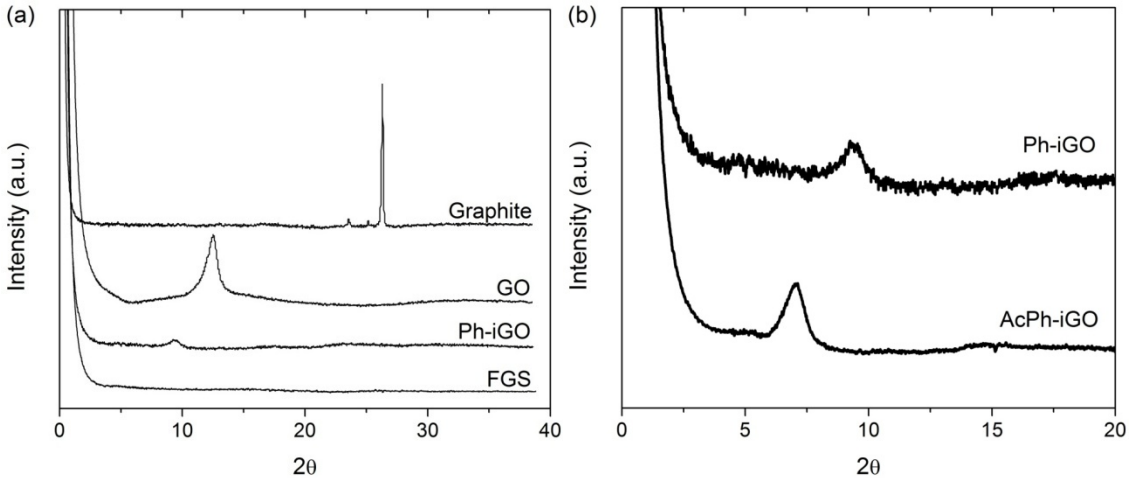

Figure 2-6. XRD intensity profiles of (a) graphite, GO, Ph-iGO, FGS, (b) Ph-iGO and AcPh-iGO. Profiles were vertically shifted for clarity.

2.3.6. Solubility Tests

Stankovich *et al.*[4] demonstrated that surface properties of GO and organically modified GO can be examined by testing suspension stability in common solvents. GO and Ph-iGO dispersions in de-ionized water and THF (1 mg/ml) were prepared with ultrasonication for 1 hr. Figure 2-7 (a) and (b) show GO and iGO suspensions 4 hrs after ultrasonication. GO forms a stable suspension in aqueous media since polar surface oxygen groups can have hydrogen bonding interaction with suspending medium.[18] Even 4 hrs after mixing, darkness of GO suspension implies good dispersability in water while large precipitation was observed in THF. GO treated with isocyanate can be suspended

well even in a relatively non-polar, aprotic medium such as THF. For Ph-iGO, THF turned out to be a better solvent than water, which signifies inversion in surface properties. GO formed fairly good dispersions in DMF (left sample in Figure 2-7 (c)).

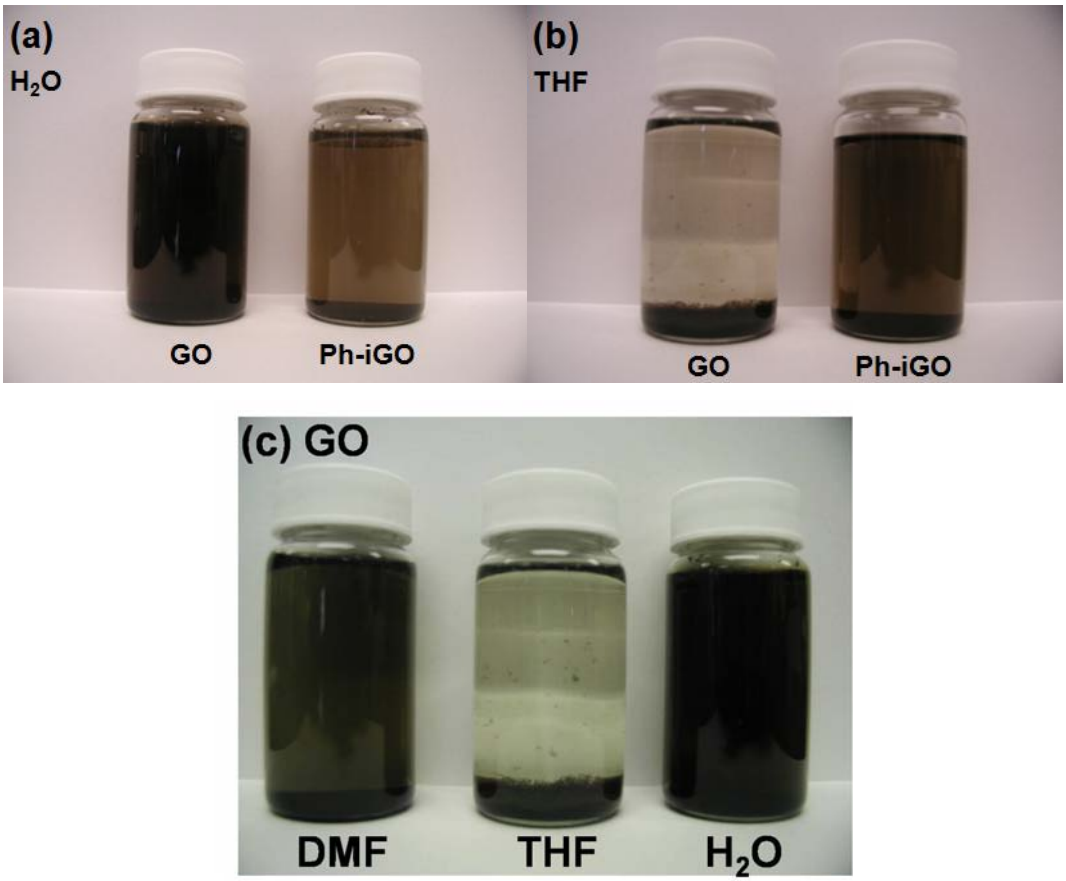

Figure 2-7. (a) De-ionized water and (b) THF containing GO and Ph-iGO, and (c) DMF, THF and water containing GO at 1 mg/mL 4 hrs after sonication for 1 hr.

2.4. Summary

Graphitic reinforcements that can potentially be exfoliated inside polymers were prepared from thermal treatments and isocyanate functionalization of GO. Average size of GO is as high as 10 μm while its thickness dimension measured after liquid-phase exfoliation is only ~ 1 nm as demonstrated by AFM. Thermal exfoliation resulted in considerable size reduction of GO. XPS revealed significant covalent incorporation of

oxygen in GO. Less oxygen content in FGS implies thermal reduction of GO during pyrolysis treatments. After oxidation, a substantial portion of crystalline carbons was transformed into the amorphous state, which distorts the flat graphene structure. Chemical intercalation of oxygen and isocyanate progressively increased inter-gallery spacing of graphite. FGS does not display any characteristic reflections in its XRD implying highly disordered state. Chemically modified GO could be dispersed in organic solvents. This inversion in surface properties will enable fabrication of polymer/GO composites via solvent-based processes as described in the next chapter.

2.5. References

(1) Schniepp, H. C.; Li, J.-L.; McAllister, M. J.; Sai, H.; Herrera-Alonso, M.; Adamson, D. H.; Prud'homme, R. K.; Car, R.; Saville, D. A.; Aksay, I. A. *J. Phys. Chem. B* **2006**, *110*, 8535-8539.

(2) McAllister, M. J.; Li, J.-L.; Adamson, D. H.; Schniepp, H. C.; Abdala, A. A.; Liu, J.; Herrera-Alonso, M.; Milius, D. L.; Car, R.; Prud'homme, R. K.; Aksay, I. A. *Chem. Mater.* **2007**, *19*, 4396-4404.

(3) Stankovich, S.; Dikin, D. A.; Dommett, G. H. B.; Kohlhaas, K. M.; Zimney, E. J.; Stach, E. A.; Piner, R. D.; Nguyen, S. T.; Ruoff, R. S. *Nature* **2006**, *442*, 282-286.

(4) Stankovich, S.; Piner, R. D.; Nguyen, S. T.; Ruoff, R. S. *Carbon* **2006**, *44*, 3342-3347.

(5) Hennig, G. R. *Prog. Inorg. Chem.* **1959**, *1*, 125-205.

(6) Brodie, B. C. *Philos. Trans. R. Soc. London* **1859**, *149*, 249-259.

(7) Staudenmaier, L. *Ber. Dtsch. Chem. Ges.* **1898**, *31*, 1481.

(8) Hummers, W. S., Jr.; Offeman, R. E. *J. Am. Chem. Soc.* **1958**, *80*, 1339.

(9) Titelman, G. I.; Gelman, V.; Bron, S.; Khalfin, R. L.; Cohen, Y.; Bianco-Peled, H. *Carbon* **2005**, *43*, 641-649.

(10) Vorbeck Materials, http://www.vorbeck.com, Accessed July 27, 2009.

(11) Brunauer, S.; Emmett, P. H.; Teller, E. *J. Am. Chem. Soc.* **1938**, *60*, 309-19.

(12) Stankovich, S.; Dikin, D. A.; Piner, R. D.; Kohlhaas, K. A.; Kleinhammes, A.; Jia, Y.; Wu, Y.; Nguyen, S. T.; Ruoff, R. S. *Carbon* **2007**, *45*, 1558-1565.

(13) Yang, D.; Velamakanni, A.; Bozoklu, G.; Park, S.; Stoller, M.; Piner, R. D.; Stankovich, S.; Jung, I.; Field, D. A.; Ventrice, C. A., Jr.; Ruoff, R. S. *Carbon* **2009**, *47*, 145-152.

(14) Kudin, K. N.; Ozbas, B.; Schniepp, H. C.; Prud'homme, R. K.; Aksay, I. A.; Car, R. *Nano Lett.* **2008**, *8*, 36-41.

(15) Li, J.-L.; Kudin, K. N.; McAllister, M. J.; Prud'homme, R. K.; Aksay, I. A.; Car, R. *Phys. Rev. Lett.* **2006**, *96*, 176101/1-176101/4.

(16) Kovtyukhova, N. I.; Ollivier, P. J.; Martin, B. R.; Mallouk, T. E.; Chizhik, S. A.; Buzaneva, E. V.; Gorchinskiy, A. D. *Chem. Mater.* **1999**, *11*, 771-778.

(17) Eda, G.; Fanchini, G.; Chhowalla, M. *Nat. Nanotechnol.* **2008**, *3*, 270-274.

(18) Wen, X.; Garland, C. W.; Hwa, T.; Kardar, M.; Kokufuta, E.; Li, Y.; Orkisz, M.; Tanaka, T. *Nature* **1992**, *355*, 426-8.

(19) Hontoria-Lucas, C.; Lopez-Peinado, A. J.; Lopez-Gonzalez, J. d. D.; Rojas-Cervantes, M. L.; Martin-Aranda, R. M. *Carbon* **1995**, *33*, 1585-92.

(20) Kim, H.; Macosko, C. W. *Macromolecules* **2008**, *41*, 3317-3327.

(21) NIST X-ray Photoelectron Spectroscopy Database, http://srdata.nist.gov/xps/Default.aspx, Accessed August 10, 2009.

(22) Dresselhaus, M. S.; Dresselhaus, G.; Jorio, A.; Souza Filho, A. G.; Saito, R. *Carbon* **2002**, *40*, 2043-2061.

(23) Tuinstra, F.; Koenig, J. L. *J. Chem. Phys.* **1970**, *53*, 1126-30.

(24) Hernandez, Y.; Nicolosi, V.; Lotya, M.; Blighe, F. M.; Sun, Z.; De, S.; McGovern, I. T.; Holland, B.; Byrne, M.; Gun'Ko, Y. K.; Boland, J. J.; Niraj, P.; Duesberg, G.; Krishnamurthy, S.; Goodhue, R.; Hutchison, J.; Scardaci, V.; Ferrari, A. C.; Coleman, J. N. *Nat. Nanotechnol.* **2008**, *3*, 563-568.

(25) Jeong, H.-K.; Lee, Y. P.; Lahaye, R. J. W. E.; Park, M.-H.; An, K. H.; Kim, I. J.; Yang, C.-W.; Park, C. Y.; Ruoff, R. S.; Lee, Y. H. *J. Am. Chem. Soc.* **2008**, *130*, 1362-1366.

(26) Lotya, M.; Hernandez, Y.; King, P. J.; Smith, R. J.; Nicolosi, V.; Karlsson, L. S.; Blighe, F. M.; De, S.; Wang, Z.; McGovern, I. T.; Duesberg, G. S.; Coleman, J. N. *J. Am. Chem. Soc.* **2009**, *131*, 3611-3620.

(27) Szabo, T.; Berkesi, O.; Dekany, I. *Carbon* **2005**, *43*, 3186-3189.

Chapter 3. Thermoplastic Polyurethane/Graphene Nanocomposites: Processing, Morphology and Properties

3.1. Overview

The previous chapter covered synthesis and characterization of thermally exfoliated (functionalized graphene sheets, FGS) and chemically modified (isocyanate treated graphite oxide, iGO) graphite oxide (GO). These intercalated or exfoliated graphene sheets were dispersed into segmented thermoplastic elastomer (thermoplastic polyurethane, TPU) by three different blending methods: melt intercalation, solvent mixing and *in-situ* polymerization. The morphology of dispersed graphene sheets was characterized with electron microscopy and X-ray scattering. Solid properties of TPU composites such as electrical conductivity, tensile modulus and gas permeation were measured, from which dispersion state of graphene can be inferred. Hard-soft domain separation behavior of TPU containing graphene was examined via differential scanning calorimetry (DSC), dynamic mechanical analysis (DMA) and Fourier-transform infrared spectroscopy (FTIR). Part of the work introduced in this chapter as well as Chapter 2 was presented at the Annual Technology Conference for Society of Plastic Engineers[1] on June 2009 and a manuscript for publication is currently in preparation.

3.2. Introduction

TPU is an elastomeric block copolymer consisting of alternating hard and soft blocks which phase separate readily due to their chemical incompatibility. Hard domains usually consisting of diisocyanate and chain extenders act as physical cross-linkers that dissociate at elevated temperature, and as rigid fillers reinforcing soft domains. Due to melt processibility and a wide range of tunable mechanical and physical properties, TPU has been used for a variety of applications such as fibers, coatings, adhesives[2] and bio-mimetic materials.[3] However, despite good extensibility, low stiffness and tensile

strength can be drawbacks in structural applications especially for TPU with low hard segment content. Water vapor and other gas permeability can be another drawback. These weak mechanical and gas barrier properties can be complemented by reinforcing with rigid layered nano-fillers. Graphene can be a multi-functional reinforcement material, making versatile new nanocomposites possible. Potential application areas range from electro-magnetic reflective materials to electrically or thermally-conductive, moisture barrier adhesives, paints and packaging films at even lower than 1 wt% loading.

Melt intercalation, solution mixing and *in-situ* polymerization have been three most common routes to disperse nanoparticles into polymers.[4,5] In melt intercalation, compounding takes place above the glass transition temperature for amorphous polymers or above the melting point for semi-crystalline polymers,[6,7] which is often mechanically aided by extrusion.[8,9] Melt-state compounding is the most economically viable and environmentally friendly approach since it doesn't necessitate solvents. However, surface modification of reinforcements[10] or even use of additional dispersion aids[11] is needed when polymer matrix and additive phases are immiscible, and some polymers are subject to thermal degradation at high temperature.[12]

Solution mixing involves dispersion of nano-fillers and dissolution of matrix polymers in co-solvents, often assisted by ultrasonication. Composites are recovered from the solution via solvent evaporation or coagulation after blending. In order to improve particle dispersion thermodynamically or kinetically, surface modification of nano-fillers,[13] dispersion aide[14] (e.g. surfactants) and ultrasonication are often employed. Nonetheless, slow solvent evaporation can induce particle re-aggregation and scaling-up is restricted by cost and environmental limitations of solvents.

Instead of blending with polymers, composites can be produced from monomers which can be polymerized in the presence of dispersed nano-particles.[15] Since monomers more readily swell the dispersed phase than long-chain polymers and reactive chain tethering on the particle surface is also possible,[16] enhanced particle dispersion is expected from this approach. However, in bulk polymerization, viscosity increase with

polymerization often prevents good mixing[17] and reduced matrix molecular weight by particle addition is also reported.[15,18]

Melt compounding,[10,19] solvent mixing[19-21] and *in-situ* polymerization[15,22-25] have been used for production of nanocomposites based on TPU. Notable property gains from nano-particle incorporation are increased stiffness and toughness without compromising high extensibility,[15,21] enhanced shape memory[20] and gas barrier performances.[25] Finnigan and co-workers[19] reported that even with the same materials, different levels of particle dispersion, hard-soft domain phase separation and thermo-mechanical properties could be observed after melt and solvent blending. Tien and Wei,[15] and Pattanayak and Jana[23,24] demonstrated that using layered silicates with reactive functional groups (-OH) can greatly improve particle dispersion and tensile strength as well as stiffness of the composites due to facilitated particle swelling and increased interfacial strength. Since FGS and GO also have surface hydroxyls which can react with -NCO groups, they may also serve as pseudo chain extenders. Reportedly, surface grafting of GO with long chain alkyl-chlorosilane[26] and amino groups[27] have been successful.

For this study, exfoliated graphite sheets were incorporated into polyester based TPU containing relatively small fraction of hard segment (~ 25 wt%). Compounding with typical un-intercalated graphite and FGS was conducted via melt intercalation. FGS composites were also prepared by solvent blending and *in-situ* polymerization. iGO was processed into TPU only using solvent blending due to thermal decomposition of GO and its derivatives[27-29] at the melt processing temperature window of TPU. Using chain extension reaction of GO, TPU/GO composites were also fabricated via *in-situ* polymerization.

3.3. Experimental

3.3.1. Materials and Processing

TPU resin used for melt and solvent blending was Avalon 70AE (Shore hardness: 70AE, density: 1.21 g/cm^3) provided by Huntsman Polyurethanes.[30] Avalon 70AE is a soft elastomer containing ~ 25 wt% hard segment. Highest hard segment dissociation

temperature is ~ 150 ^{o}C and soft segment glass transition occurs at –43 ^{o}C as determined by DSC. Zero-shear melt viscosity at 180 ^{o}C measured by rotational rheometry (ARES, TA instruments) is ~ 600 Pa·s. For the *in-situ* formulation of Avalon 70AE, its starting materials, ester based-polyol (Daltorez P765, Huntsman Polyurethanes, M_w = 2200), 4,4'-methylene diphenyl diisocyanate (MDI, Rubinate 44, Huntsman Polyurethanes) and 1,4-buthanediol (BDO, Sigma Aldrich) were also obtained. Flake graphite (surface enhanced, grade # 3775) was purchased from Asbury Carbons[31] and is denoted as "graphite" for the rest of this Chapter. FGS provided by Vorbeck Materials[32] was used. GO, Ph-iGO and AcPh-iGO were synthesized from high purity graphite (SP-1, Bay Carbon) as described in Chapter 2. Surface area of as-received graphite and FGS estimated by Brunauer, Emmett and Teller (BET)[33] N_2 adsorption (Autosorb-1, Quantachrome) are 29 and ~ 800 m^2/g, respectively. For the weight to volume fraction conversion, density of graphite (2.28 g/cm^3)[34] was used for all graphite reinforcements.

TPU composites were prepared via melt compounding, solvent blending and *in-situ* polymerization. Cryo-pulverized (Spex 6700 Freezer/Mill) TPU powders were dried with graphite or FGS in vacuum at 50 ^{o}C for 24 hrs before melt processing. They were fed into a recirculating, conical twin-screw extruder (Microcompounder, DACA Instruments) at 180 ^{o}C and blended under dry N_2 for 6 min at the screw speed of 360 RPM. Melt compounded samples were further processed with hot pressing at 180 °C into films or bars for testing. For ~ 0.1 mm thick film-shaped specimen, vacuum dried DACA extrudates placed between Teflon coated aluminum foils were pressed at 140 kPa for 2 min. Bar-shaped composites were produced by pressing extrudates in a mold (2 cm × 1 cm × 1 mm) at 70 kPa for 8 min and then annealing without pressure for 30 min.

FGS and iGO were also blended with TPU in solution state. Varying amounts of graphitic additives were dispersed in *N,N*-dimethylformamide (DMF, 20 mL) and stirred for 2 days (FGS) or 20 days (iGO). Dry TPU powders (~ 2 g) were added to the suspensions to produce 0, 0.5, 1.0 and 3.0 wt% samples and stirred for additional 2 days. FGS/TPU and GO/TPU composites were prepared via *in-situ* polymerization technique. Polymerization and blending were carried out in DMF rather than in bulk-phase since a

rapid viscosity increase with polymerization made mixing difficult. 0, 0.05, 0.1 and 0.3 g of dry FGS or GO was first dispersed in anhydrous DMF (~ 180 mL) and stirred for 1 day (FGS) and 7 days (GO). Polyol and BDO were dehydrated at 60 ^{o}C under vacuum for 24 hrs and MDI was also vacuum dried at 30 ^{o}C for 2 hrs. A mixture of polyol and MDI was stirred at 95 ^{o}C under N_2 for 4 hrs to form a pre-polymer. FGS/DMF or GO/DMF suspension was poured into the pre-polymer at 45 ^{o}C and stirred further for at least 6 hrs (FGS) or 24 hrs (GO). A chain extender, BDO was added to the pre-polymer/FGS or GO/DMF solution and stirring continued for additional 24 ~ 72 hrs. Weight and molar ratios of each component used for TPU and composites synthesis are provided in Table 3-1. Note that MDI is used in 0.2 - 5% excess from ideal molar fraction (50%) to compensate for consumption by trapped moisture and –OH groups in FGS and GO. After polymerization, composites in the solution were recovered by coagulation in methanol with vigorous mixing, filtered and dried under vacuum at 50 ^{o}C for 48 hrs. After drying, products were re-dispersed in DMF. DMF solutions containing solvent blended or *in-situ* polymerized samples were cast on a heated glass plate (~ 55 ^{o}C) for DMF removal, and dried for additional 48 hrs without heating. Drying cast films continued for 48 hrs in a vacuum oven at 50 ^{o}C before characterization.

Table 3-1. Weight and Molar Fractions of Components for TPU and Composites Synthesis

Sample	Weight fraction (%)				Mole fraction (%)		
	Reinforcement	Polyol	MDI	BDO	Polyol	MDI	BDO
TPU	0	73.3	21.9	4.8	19.1	50.2	30.7
FGS/TPU	0.5	73.0	21.8	4.7	19.2	50.5	30.3
	0.9	72.6	21.8	4.7	19.2	50.6	30.3
	2.7	71.1	21.5	4.7	19.0	50.7	30.2
GO/TPU	0.5	72.8	21.9	4.8	19.0	50.1	30.9
	0.9	71.2	23.4	4.5	18.4	53.4	28.2
	2.8	68.6	24.2	4.4	17.7	55.0	27.3

3.3.2. Characterization

Number (M_n) and weight (M_w) average molecular weights of Avalon 70AE and *in-situ* polymerized TPU were determined by size exclusion chromatography (SEC, Waters 717 Plus HPLC Autosampler) at room temperature using tetrahydrofuran (THF) as a mobile phase and polystyrene standards (EasiCal PS-2, Polymer Laboratories). Before running SEC, TPU matrix was separated from *in-situ* polymerized composites with a Soxhlet extraction setup. Using THF boiling at 85 ^oC, TPU extract was collected for 24 hrs from the composites retained in 1.5 mm-thick cellulose thimbles (Advantec, No. 84). TPU in THF was centrifuged (CR 3-22, Jouan) for 10 min at 5000 RPM and only supernatant was used for SEC.

FTIR spectra in attenuated total reflection (ATR) mode of TPU and composites were obtained over the wavenumber range of 650-4000 cm^{-1} with Nicolet Magna-IR 750 at a resolution of 2 cm^{-1}. After vacuum dehydrating at room temperature for 24 hrs, films were pressed against ZnSe crystal and spectra averaged over 40 scans were taken from 2-3 different sample locations. IR transmittance in the range of 1800-1650 cm^{-1} (absorption of carbonyl groups)[35] were base-line subtracted using a linear base-line drawn from 1800 cm^{-1} to 2800 cm^{-1} where no noticeable absorption is detected. Intensity normalization was also carried out by the area over bands occurring at 2800-3000 cm^{-1} (C-H stretching vibrations of aliphatic CH_2 groups) as an internal standard.[36]

DSC measurements of TPU and composite samples were carried out with TA Instruments DSC Q1000. ~ 10 mg of dry samples were loaded into non-hermetic aluminum pans. DSC scans were performed at the rate of 10 ^oC/min from -100 to 250 ^oC. Hard segment dissociation temperature and soft segment glass transition temperature ($T_{g,soft}$) were determined using TA Instruments Universal Analysis 2000 software.

Temperature dependence of mechanical properties of solvent cast and *in-situ* polymerized composites was monitored in a dynamic temperature ramp mode using Rheometrics Solids Analyzer II (RSA II). 3 mm wide and 0.1 mm thick strips were cut from the cast films and dried in vacuo at room temperature. They were mount between

film fixtures of RSA II and temperature was changed from -60 to 150 ^{o}C at the rate of 3 ^{o}C/min. Dynamic tensile storage *E'* and loss moduli *E''* were measured at 1 rad/s. During tests, static pretension on the specimens was kept at about 200% of dynamic forces which were maintained between 0.2 and 1.0 N using auto-tension and auto-strain adjustments. Soft segment glass transition temperature $T_{g,\ soft}$ was estimated from the temperature at maximum tan δ (=*E''*/*E'*).

Real-space morphology of graphene in TPU was visualized with transmission electron microscopy. Composites were cryo-microtomed (Leica Ultracut) with a diamond knife at –90 ^{o}C into 100 nm thick slices and placed on 400-mesh Cu TEM (transmission electron microscopy) grids. Solvent cast films were embedded in epoxy matrix (TRA-BOND 2115, Tra-Con) prior to the microtome. TEM was operated with JEOL 1210 at an accelerating voltage of 120 kV. Wide-angle X-ray diffraction (WAXD) intensity of composites was collected in a transmission mode with a Bruker-AXS microdiffractometer and CuKα radiation (45 kV and 40 mA). X-rays were directed to ~ 3 mm wide film cuts in thickness and transverse direction. Scattering intensity in a weighted sum ($2I_{transverse} + I_{thickness}$) after normalization based on scattering volume is reported.

Electrical conductivity of graphene composites were measured with an 11-point dc surface resistance meter (PRS-801, Prostat). Measurements were repeated on 3-4 different areas of the composite films to ensure sample uniformity and their geometric averages are reported. Both film and bar-shaped specimens from melt blending were used to investigate effects of post-processing on electrical conduction.

Mechanical properties of composites were tested with RSA II and TA Instruments Minimat. 4 mm wide strips were cut from the center of the composite films. Tensile deformation at the rate of 5×10^{-4} /s was applied to the strips with RSA II to evaluate static Young's moduli, *E*. Ultimate mechanical properties (e.g. strain at break, tensile strength and toughness) were measured with Minimat. Similar 4-mm wide films were stretched at a constant rate (0.024 /s) until they fractured.

Gas permeability tests based on a constant volume-variable pressure method[37] were conducted on disk-cut (diameter: 4.2 cm) composite films using a home built apparatus.[38] Helium or N_2 flow was fed to one side of the specimen at 1 atm and the pressure change in the opposite, evacuated side was monitored over time. Volumetric flow rates from the pressure change were converted into permeation constants via normalization with the pressure gradient across the sample, film area and thickness.

For solvent extraction of the composites, solvent blended and *in-situ* polymerized FGS and GO composite films (1 cm × 2 cm × 0.1 mm) were immersed into 18 mL of THF in glass vials. Sample shapes 5 min and 24 hrs after immersion are compared.

3.4. Results and Discussion

After melt- and solvent-state blending, *in-situ* polymerization of graphene and TPU, matrix properties of the composites were characterized with SEC, FTIR, DSC and DMA. Graphene dispersion was examined using TEM and WAXD. Electrical conductivity, mechanical properties and gas permeation of the hybrids were measured and tabulated data can be found in Appendix A.

3.4.1. Matrix Molecular Weights

PS-calibrated M_w, M_n and polydispersity indices (PDI = M_w/M_n) of TPU are summarized in Table 3-2. Average molecular weights of Avalon 70AE are 96,000 (M_w) and 55,000 g/mol (M_n) with PDI of 1.7. After melt extrusion, molecular weight of Avalon 70AE was slightly reduced (M_w = 85,000 g/mol) implying thermal degradation of urethane groups[39] during processing at 180 °C. Molecular weights of TPU polymerized in DMF is slightly smaller than those of Avalon 70AE, but higher than those of the pre-polymer collected before the chain extension reaction (10,000-11,000 (M_w) and 5,000-7,000 g/mol (M_n)). TPU extracted from 0.5 wt% FGS and 2.8 wt% GO/TPU *in-situ* polymerized samples has even lower molecular weight, possibly due to isocyanate consumption by moisture and surface –OH groups of FGS and GO. Note shoulders toward smaller retention time in the SEC traces (Figure 3-1) of TPU recovered from *in-*

situ polymerized 0.9 wt%, 2.7 wt% FGS and 0.5 wt% GO samples, presumably resulting from a fraction of particles extracted along with TPU and suspended in the THF mobile phase even after centrifugation. Their SEC traces were deconvoluted to yield two Gaussian distributions and one located at lower retention time was excluded for calculating M_w and M_n in Table 3-2. However, their nominal molecular weights and PDI are still greater than those of neat TPU implying presence of particles complicating interpretation of the SEC results. FGS diameter ranges from 50 to 400 nm (see Section 2.3.1), which means the radius of gyration of smaller particles can be comparable with that of typical polymer chains[40] if these thin flexible membranes adopt a "crumpled sphere" configuration in solvents.[41] These mismatches in matrix molecular weights from different processing did not affect solid properties of TPU significantly as discussed later.

Table 3-2. Average Molecular Weights of TPU

Molecular weight (kg/mol)	As received	Melt processed	*In-situ* polymerized						
			TPU	wt% of FGS			wt% of GO		
				0.5	0.9	2.7	0.5	0.9	2.8
M_w	96	85	68	57	115	103	155	90	28
M_n	55	59	39	27	45	39	49	53	17
PDI	1.7	1.4	1.7	2.1	2.6	2.6	3.2	1.7	1.7

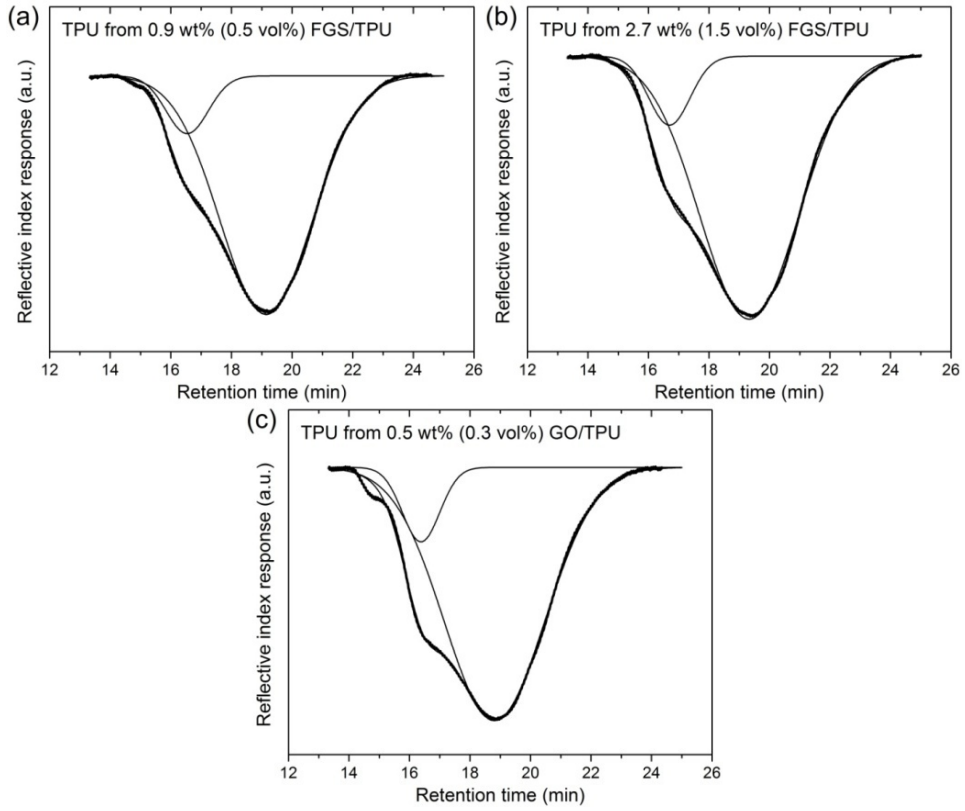

Figure 3-1. SEC traces of TPU extracted from *in-situ* polymerized (a) 0.9 wt%, (b) 2.7 wt% FGS and (c) 0.5 wt% GO/TPU composites. Peak deconvolutions based on the Gaussian distributions are also shown.

3.4.2. FTIR

In the ATR-FTIR spectra of TPU and composites (Figure 3-2), there exist at least two distinguished bands: a main peak centered at 1730 and a relatively small shoulder around 1715 cm^{-1}. They respectively are associated with C=O groups that are "free" (non-hydrogen bonded) and hydrogen bonded with urethane N-H groups.[42] Higher intensity at 1730 cm^{-1} indicates that a majority of C=O groups is not hydrogen bonded regardless of the sample type and processing methods. 3 wt% FGS incorporated via melt blending or solvent mixing doesn't seem to influence hydrogen bonding of the C=O groups of the matrix as the ratio between hydrogen bonded and "free" carbonyl groups is not altered (Figure 3-2 (a) and (b)).

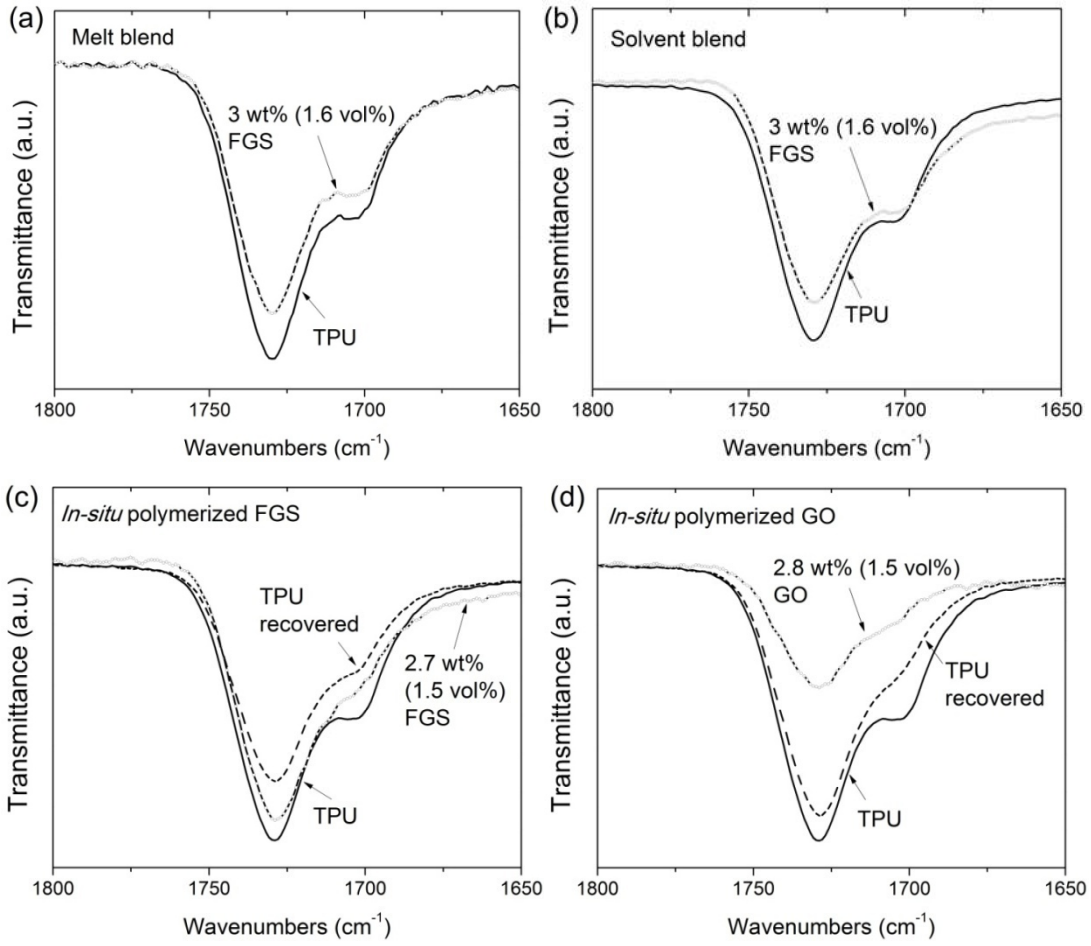

Figure 3-2. ATR FTIR spectrum of (a) melt blended FGS, (b) solvent blended FGS, *in-situ* polymerized (c) FGS and (d) GO/TPU composites. For *in-situ* polymerized samples, FTIR spectrum of TPU recovered from the composites are also shown.

However, reduced hydrogen bonding can be inferred from diminished shoulder intensity at 1715 cm^{-1} for *in-situ* polymerized FGS or GO composite samples (Figure 3-2 (c) and (d)). Sterically hindered inter-chain interaction by the presence of FGS sheets will not be the case since solvent mixed FGS did not affect hydrogen bonding of Avalon 70AE. FTIR of GO and FGS recovered from *in-situ* polymerized composites (Figure 2-5 (a) in Chapter 2) implies TPU chain tethering on the functionalized graphene surface. Mobility of chains bound to rigid particles will be greatly restricted, which hinders formation of inter-chain hydrogen bonding. Interestingly, TPU matrices extracted from

the composites also display some reduction in carbonyl hydrogen bonding indicating hard segment length distribution was modified by particle addition during synthesis. FGS and GO were added after pre-polymer synthesis, but before adding the chain extender, BDO. Since FGS and GO with multiple hydroxyl and carboxylic acid functionalities may react with isocyanate in pre-polymers and un-reacted MDI, chain extension by BDO will be less likely, which is required for the formation of longer hard segment that phase separates and forms hydrogen bonded domains more readily.

3.4.3. DSC

Differential calorimetric properties of TPU and composites are provided in Table 3-3 and Figure 3-3. In the DSC trace of as-received Avalon 70AE (Figure 3-3 (a)), there exists a number of endotherms at 80, 87, 117 and 149 °C, which is indicative of multiple dissociation processes of inter-urethane hydrogen bonding upon heating. Two endotherms at 87 and 117 °C were eliminated after melt and solvent processing implying they are associated with aging. $T_{g,\ soft}$ of as-received, melt blended and solvent mixed TPU is all around -40 °C. Their DSC thermograms are similar to that of polyester based TPU containing 28 wt% hard segment reported by Seymour and Cooper.[43] They assigned these two endotherms (type I and II) to thermal disordering of hydrogen bonded urethane groups in relatively short range order.[44] In contrast, neat TPU polymerized in DMF is distinctive in hard segment melting behavior. Type I and II are located at slightly lower temperature (71 and 144 °C) and two additional endothermic peaks appear at 92 and 203 °C. Melting above 200 °C can be assigned to type III which is considered to originate from disordering of well ordered microcrystalline hard domain composed of longer hard segment.[43] This suggests broad hard segment length distribution in solvent polymerized TPU, which may aid phase segregation between soft and hard domains. TPU was synthesized in DMF in a two-step process: pre-polymer formation followed by chain extension by BDO. MDI was used 0.2% in excess from the ideal stoichiometric ratio for 25 wt% hard segment formulation to circumvent molecular weight reduction. Due to the excess amount of MDI, it is possible relatively large fraction of MDI remained un-

reacted after pre-polymer formation but participated chain extension reaction with BDO, which in turn led to longer hard segment. In fact, the relatively high M_w of the pre-polymer (10-11k) determined from SEC implies near equi-molar ratio (1:1) between MDI and polyol in the pre-polymer and significant amount of un-reacted MDI after reaction. Despite this possible discrepancy in hard segment length distribution, solvent polymerized TPU and Avalon 70AE are not noticeably different in solid properties except lack of strain hardening behavior for solvent polymerized TPU (Figure 3-10).

Soft segment glass transition and hard domain melting of Avalon 70AE are hardly affected by addition of graphite via melt and solvent processing (Figure 3-3 (b) and (c)). One exception is emergence of a new endotherm at ~ 100 °C in case of solvent mixed 3 wt% FGS composites, which is suggestive of formation of a new polymorph composed of short hard segment after aging. Interestingly, in the first heating cycle of GO and iGO composites, a broad exotherm around 210 °C appears, the area of which grows proportionally to filler concentration (Table 3-3). It coincides with the onset temperature (~ 210 °C) for the exothermic thermal decomposition of GO and its intercalation compounds.[27-29]

Thermal behaviors of *in-situ* polymerized composites are distinguished from TPU synthesized without graphene (Figure 3-3 (d) and (e)). In the DSC thermograms of FGS/TPU composites, only two different types of endotherms are located at 70-80 °C (type I) and ~ 100 °C (except 0.9 wt% FGS sample). Unlike neat TPU, endothermic events above 200 °C (type III) were not observed: no detectable inter-urethane association.[43] GO/TPU composites also show only type I endotherms around ~ 80 °C even though detection of thermal responses higher than 150 °C was not possible due to the broad exotherm caused by GO decomposition. Moreover, $T_{g,\ soft}$ of *in-situ* polymerized samples which is higher than that of neat TPU (-38 °C) by 1-4 °C (Table 3-3) also implies increased mixing between TPU soft segment and urethane groups. Pure TPU matrix extracted from the composites display lower $T_{g,\ soft}$ and higher hard segment melting temperature than those of composites, indicating that inter-urethane association is stronger without FGS and GO.

Table 3-3. Calorimetric Properties of TPU Composites

Sample		Soft segment Tg (°C)		Hard domain dissociation (°C)	Exotherm	
		DSC	DMA		Peak (°C)	ΔH (J/g)
Avalon 70AE		-43	-	80, 87, 117, 149	-	-
Melt blend	TPU	-41	-	85, 152	-	-
	20 wt% Graphite	-42	-	84, 150	-	-
	3 wt% FGS	-43	-	86, 148	-	-
Solvent mixed	TPU	-41	-33	83, 154	-	-
	3 wt% FGS	-41	-36	83, 99, 150	-	-
	3 wt% Ph-iGO	-39	-	84, 153	219	22.7
	3 wt% AcPh-iGO	-40	-	81, 148	209	15.5
In-situ polymerized FGS/TPU	TPU	-38	-30	71, 92, 144, 203	-	-
	0.5 wt%	-35	-24	72, 99	-	-
	TPU, 0.5 wt%	-37	-	79, 133	-	-
	0.9 wt%	-35	-	79, 134	-	-
	TPU, 0.9 wt%	-38	-	80, 136	-	-
	2.7 wt%	-34	-26	74, 102	-	-
	TPU, 2.7 wt%	-37	-	82, 124	-	-
In-situ polymerized GO/TPU	0.5 wt%	-37	-23	78, 118	215	1.9
	TPU, 0.5 wt%	-37	-	79, 126	-	-
	0.9 wt%	-38	-	83	208	6.5
	TPU, 0.9 wt%	-39	-	82, 134	-	-
	2.8	-37	-27	89	201	22.4
	TPU, 2.8 wt%	-39	-	77, 130	-	-

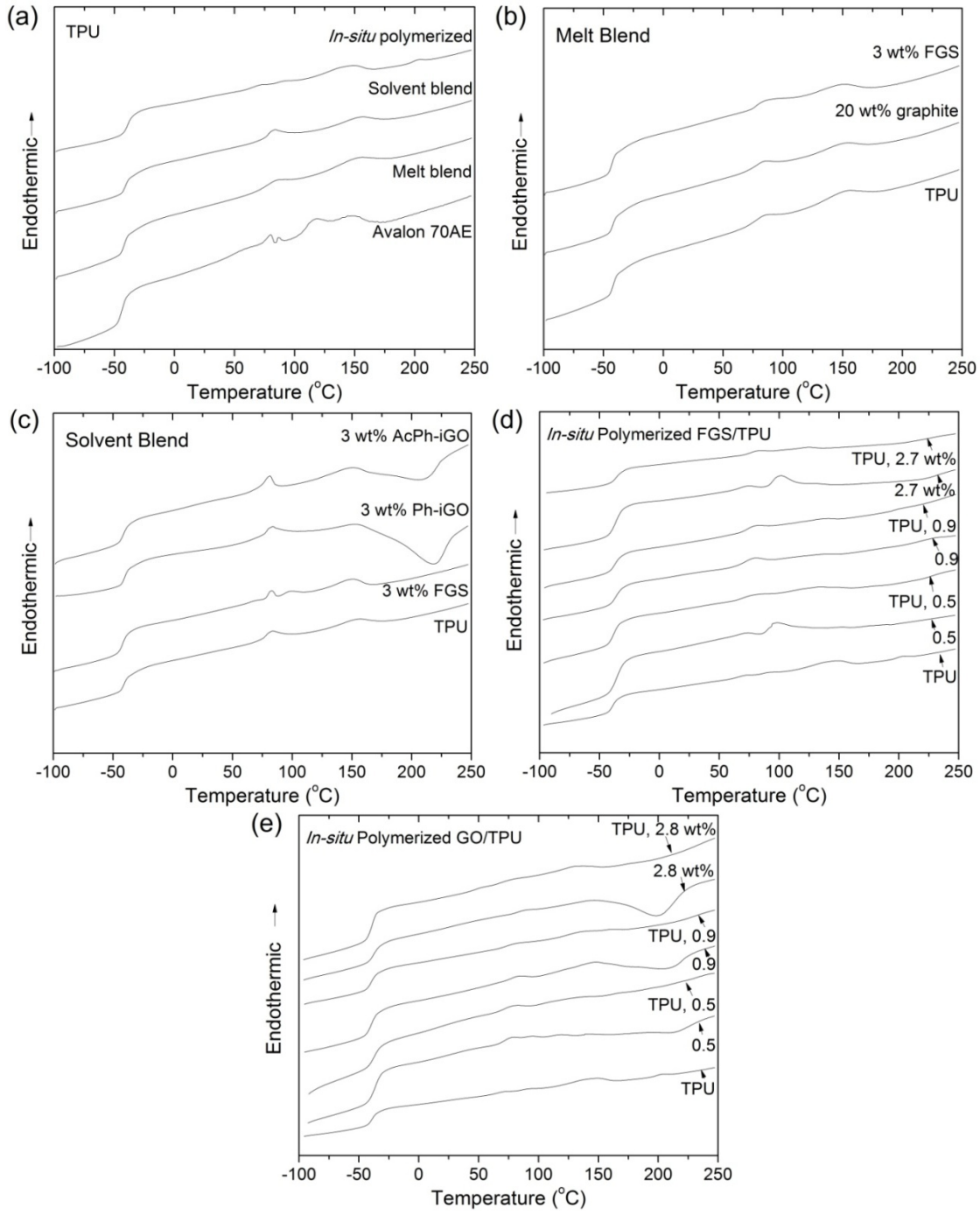

Figure 3-3. DSC thermograms of (a) TPU samples processed in different routes, (b) melt compounded, (c) solvent mixed, *in-situ* polymerized (d) FGS/TPU, (e) GO/TPU composites and TPU extracted from composites.

3.4.4. DMA

E', *E''* and tan δ of solvent blended and *in-situ* polymerized composites as a function of temperature are compared in Figure 3-4. *E'* of all samples decreases drastically and tan δ reaches maximum at -40 ~ -30 °C: softening of TPU at $T_{g,\ soft}$. Dispersion of FGS and GO improves TPU modulus, most significantly in the rubbery plateau region (temperature $T > T_{g,\ soft}$). Less pronounced modulus enhancements below $T_{g,\ soft}$ can be attributed to increased matrix modulus which undercuts modulus contrast between matrix and reinforcement phase. In case of solvent blended samples, there are no considerable changes by FGS addition in $T_{g,\ soft}$, tan δ and relaxation behaviors caused by hard domain dissociation above 100 °C. However, for *in-situ* polymerized samples, FGS or GO dispersion increased $T_{g,\ soft}$ by 3-9 °C (see also Table 3-3). As well as higher $T_{g,\ soft}$, 0.5 wt% FGS or GO composites exhibit higher tan δ than neat TPU reflecting increased polyurethane inter-domain mixing.[44] Less significant increases in rubbery plateau modulus by FGS or GO incorporation may also be attributed to reduction in matrix modulus by the phase-mixing in TPU. However, tan δ peak of composites containing higher fraction of FGS and GO (2.7-2.8 wt%) is smaller than that of TPU due to enhanced rubbery modulus. Interestingly, *E'* of *in-situ* polymerized samples does not decline at 110 ~ 120 °C as precipitously as that of solvent mixed ones. Presence of another *E'* plateau at ~ 150 °C for FGS composites suggests mechanical relaxation is suppressed up to higher temperature. Although there is no strong evidence yet, one possible origin of the extended rubbery plateau is formation of networks that do not thermally dissociate at 100 ~ 150 °C, which FGS with multiple oxygen groups might have participated in.

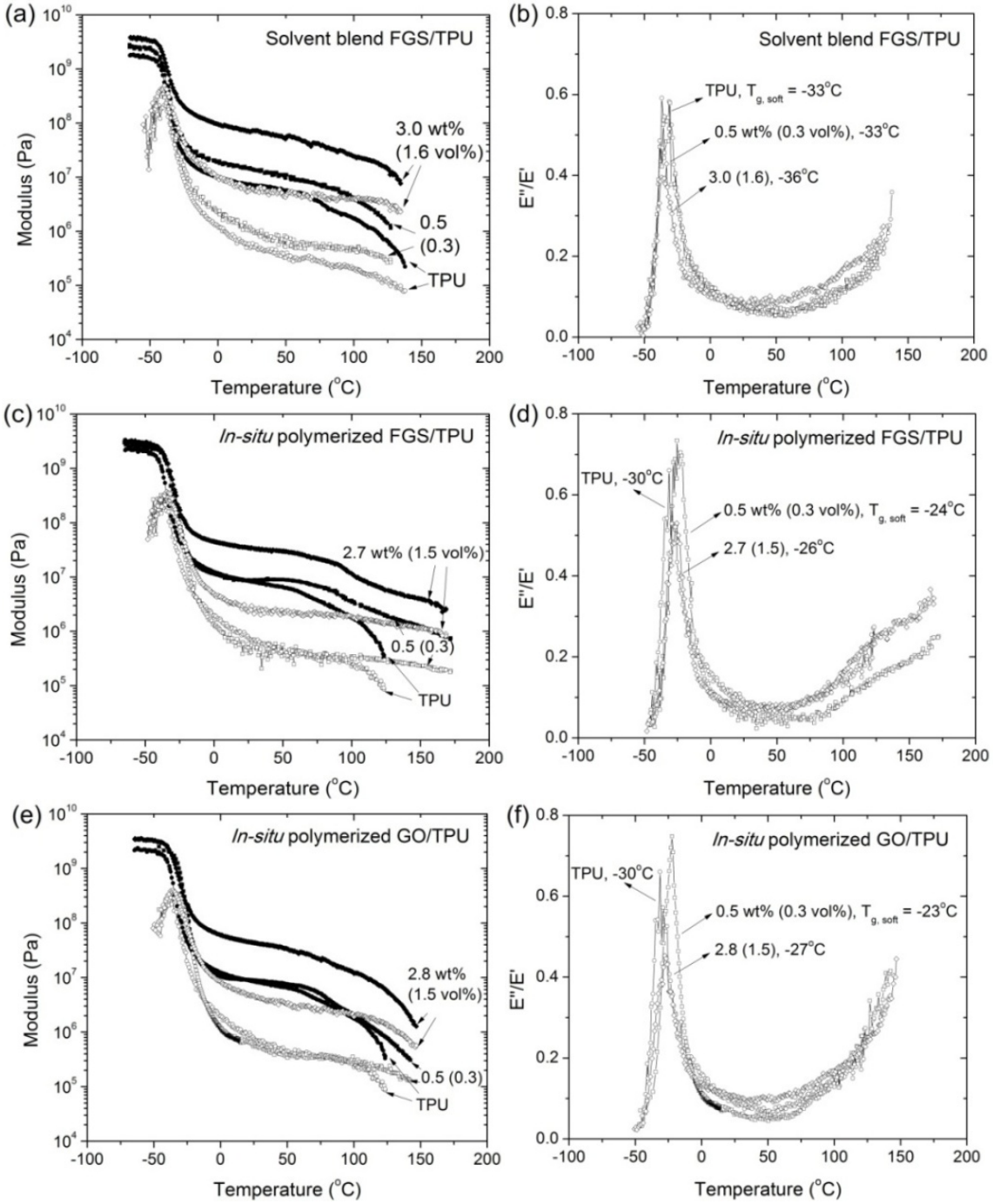

Figure 3-4. Dynamic storage *E'* (closed) and loss modulus *E''* (open symbols), tan δ changes with temperature for (a), (b) solvent blended FGS, *in-situ* polymerized (c), (d) FGS/TPU and (e), (f) GO/TPU composites. TPU soft segment glass transition temperature $T_{g,\,soft}$ determined from maximum tan δ location is also shown.

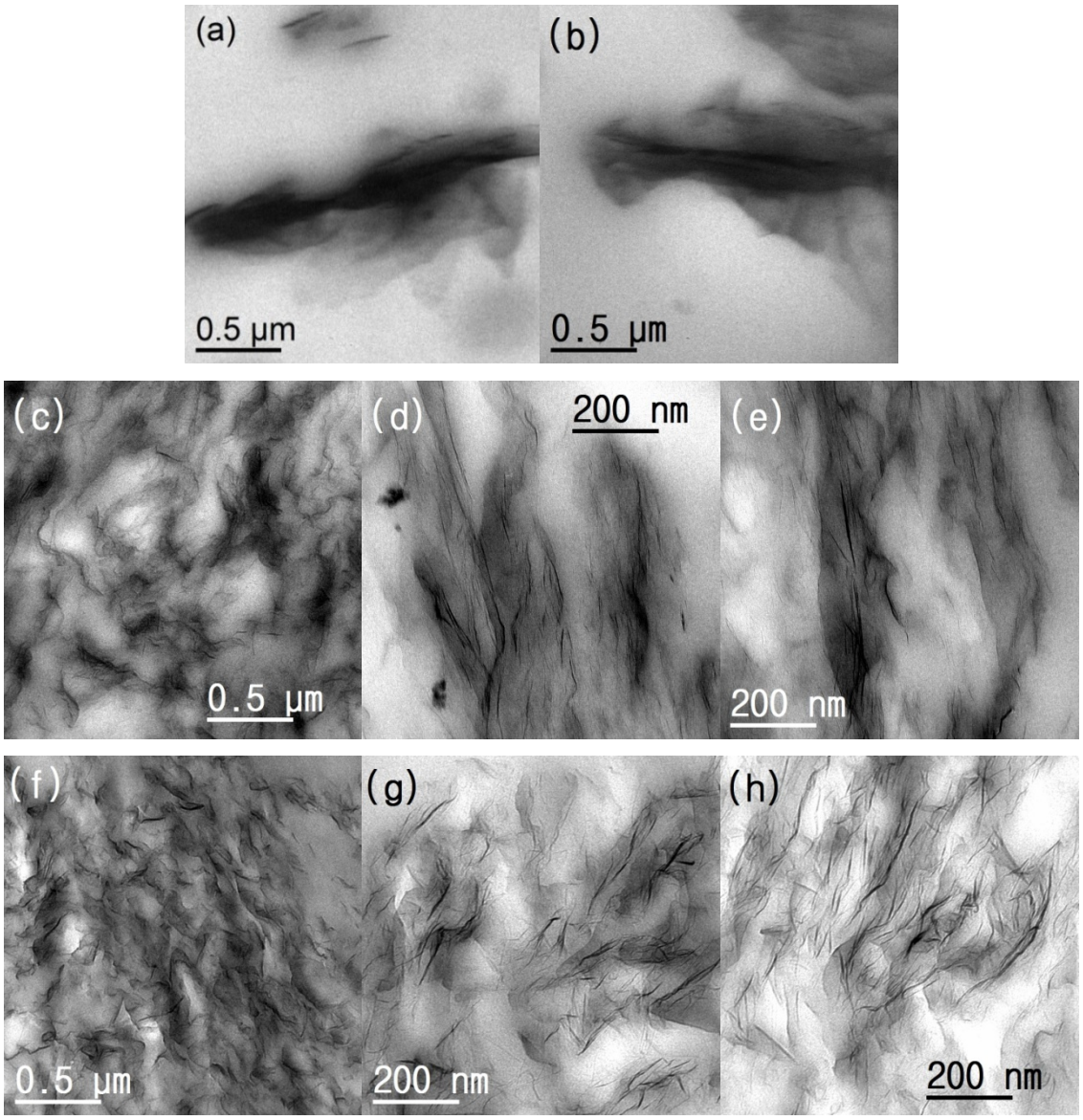

Figure 3-5 (continued to the next page). TEM micrographs of (a), (b) 5 wt% (2.7 vol%) graphite, (c), (d), (e) melt blended, (f), (g), (h) solvent mixed, (i), (j), (k) *in-situ* polymerized ~ 3 wt% (1.6 vol%) FGS, (l) solvent mixed 3 wt% Ph-iGO, (m), (n) AcPh-iGO and (o), (p), (q) *in-situ* polymerized 2.8 wt% (1.5 vol%) GO/TPU composites.

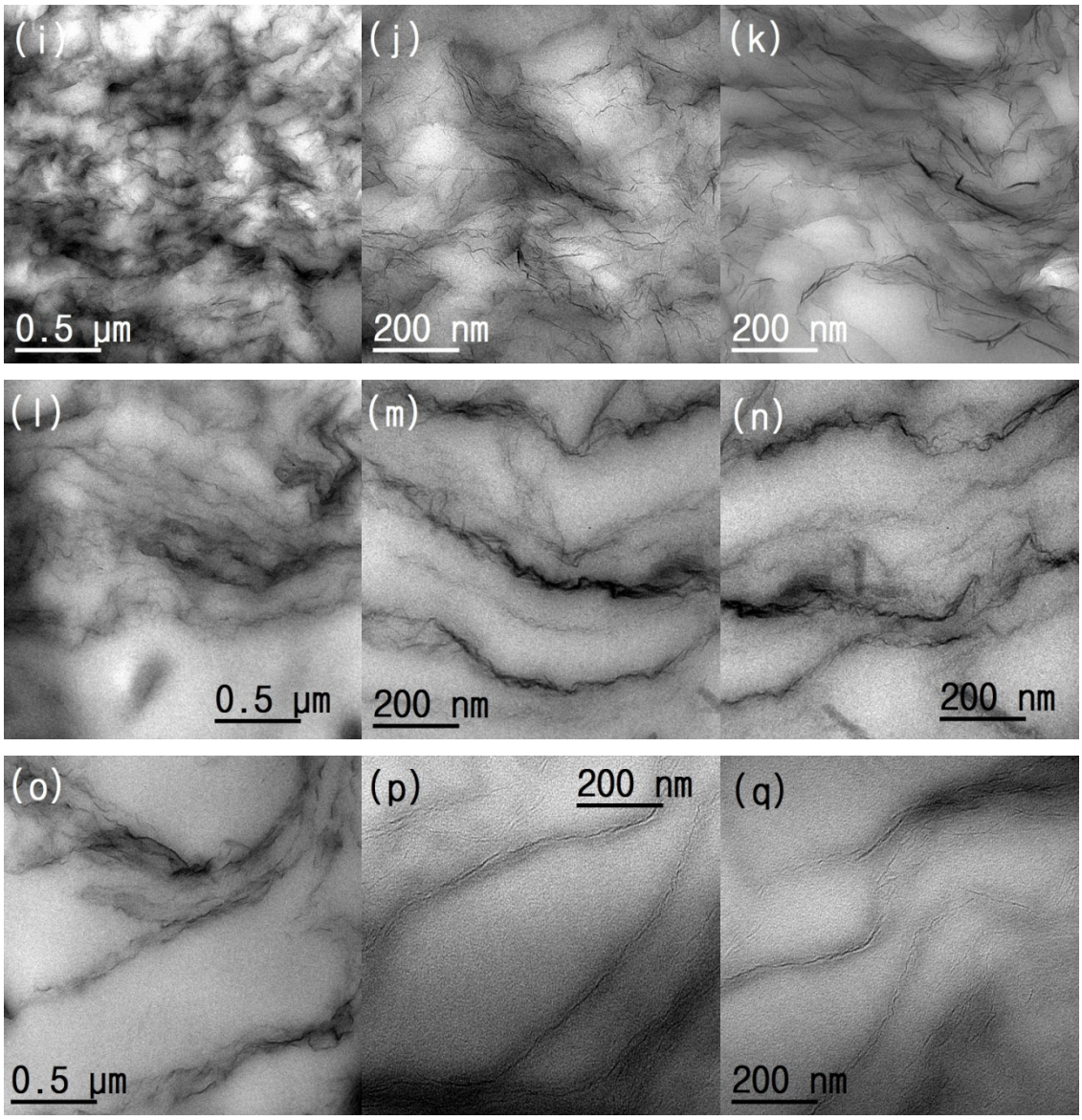

Figure 3-5 (continued from the previous page). TEM of TPU composites.

3.4.5. Morphological Characterization

Real- and reciprocal-space morphological information of TPU composites were obtained using TEM (Figure 3-5) and WAXD (Figure 3-6). Melt blended graphite composites show a thick tactoid-like structure in TEM (Figure 3-5 (a) and (b)) and a sharp reflection at $2\theta = 26.4°$ in WAXD (Figure 3-6 (a)). On the contrary, thin sheets of FGS blended under the same condition are homogenously distributed in Figure 3-5 (c)

even at lower particle concentration. Exfoliated morphology can also be inferred from its WAXD: no scattering in scattering angle > 3.5°. WAXD of solvent blended and *in-situ* polymerized FGS composites also lack reflections by layered nano-particles. TEM imaging also reveals differences in FGS structure dispersed via different compounding routes. Unlike the randomly oriented, curved thin sheets seen in solvent mixed or *in-situ* polymerized samples (Figure 3-5 (g), (h), (j) and (k)), melt compounded FGS appears predominantly as highly oriented with some stacking (Figure 3-5 (d) and (e)). Higher matrix viscosity in melt state, and compressive and extensional mechanical stress associated with the extrusion process may result in these subtle morphological differences, which are not captured with WAXD. Size of FGS visualized in TEM micrographs is tens to hundreds nm, which agrees with the diameter of as-received particles (50 ~ 400 nm) measured with atomic force microscopy (AFM, Figure 2-1).

Surface modification with isocyanate also led to GO sheets that can be well-separated after solvent mixing (Figure 3-5 (l)). Nonetheless, in higher magnification (Figure 3-5 (m) and (n)), layered stacks of a few iGO sheets can be also viewed. This type of morphology can be described as "intercalated" as broad reflections centered at 2θ ~ 4-7° in the WAXD (Figure 3-6 (b)) suggests. Note that GO sheets still remain layered after treating with isocyanate, while rapid pyrolysis of GO completely exfoliates layers (see Figure 2-6 (a)). Medium viscosity (zero shear viscosity, η_0 ~ 1 mPa·s (DMF) versus ~ 600 Pa·s (TPU melt at 180 °C)) implies that particles will experience significantly smaller stress levels in solution than in melt processing. Furthermore, if particle-matrix attraction cannot compete with particle-particle interaction, particles can aggregate rapidly after cessation of stirring for solvent evaporation. Interestingly, GO particles that are *in-situ* polymerized with TPU are more extended and inter-connected (Figure 3-5 (o), (p) and (q)). Functionalization with TPU chains may improve chemical affinity with the matrix, which should stretch out GO sheets.[45] Moreover, reaction of surface –OH groups by TPU terminated at each end with –NCO groups can result in particles bridging,[27] which can pillar graphene sheets and thus increase their persistence length. Note that diameter of chemically functionalized GO appearing TEM images is substantially smaller

than the AFM observation (Figure 2-1, ~ 10 μm) for as-synthesized GO. Particle attrition during prolonged blending may play a role.

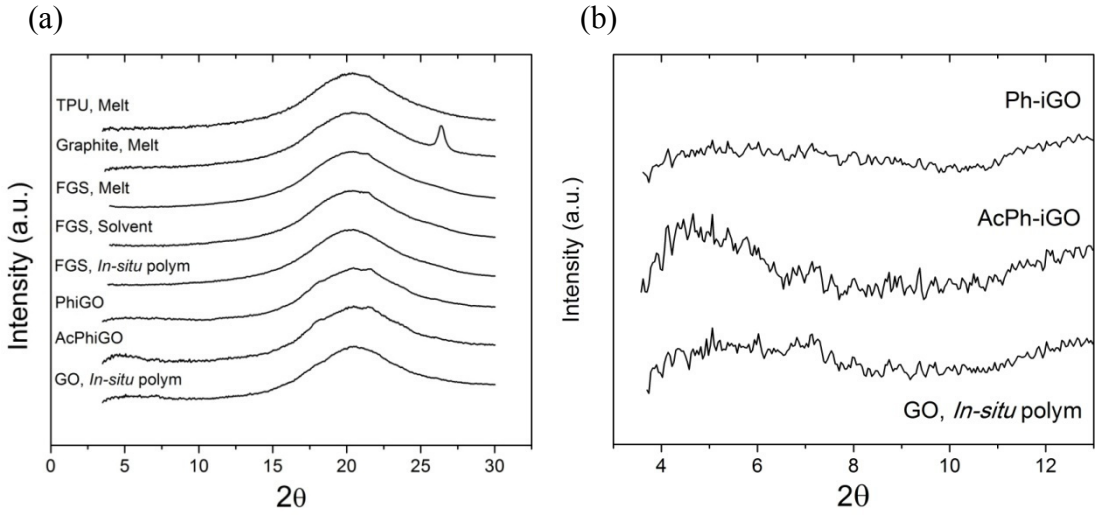

Figure 3-6. (a) WAXD profiles of TPU composites. (b) WAXD patterns in 2θ = 3.5-13° for solvent blended Ph-iGO, AcPh-iGO and *in-situ* polymerized GO composites are reproduced.

3.4.6. Electrical Conductivity

Electrical properties of TPU can be dramatically influenced by graphene addition as summarized in Figure 3-7. Both graphite and FGS effectively reduce the surface resistance, but they differ greatly in the onset concentration for electrical percolation. (> 2.7 vol% for un-treated graphite versus < 0.5 vol% for FGS). Conductivity measurements indicate that the average particle aspect ratio, A_f (ratio of diameter to thickness) of FGS is considerably greater than that of graphite since for randomly oriented disks, the percolation threshold[34] is inversely proportional to A_f. Among FGS composites, conductivity of *in-situ* polymerized and solvent blended samples is higher than melt blended ones at the same filler volume fraction. Resistance decrease takes place at even less than 0.3 vol% of FGS in case of solvent mixed samples while it required > 0.5 vol% for melt intercalation. This trend agrees with the TEM observation which indicated better

dispersion from solvent-based strategies. Although processed with solvents, percolation threshold of *in-situ* polymerized composites is slightly greater, which lies between 0.3 and 0.5 vol%. Covalently grafted TPU chains on FGS surface may hinder direct contacts between platelets, and also reduce effective particle aspect ratios.[46] For melt processed samples, molding composites into the bar shape followed by brief annealing helped improving conductivity further. Annealing may aid particles to disorient and regain contacts between one another. Note that there are no data for GO or iGO in Figure 3-7. They showed no decrease in surface resistance due to loss of electrical conductivity after graphite oxidation.[29] Graphite oxide can be chemically or thermally reduced[47] to restore electrical conductivity. However, chemical reduction must be conducted in a solution state in the presence of the matrix polymer to circumvent rapid re-aggregation of reduced graphite oxide.[48] This was not attempted since electrophilic atoms in polyurethane can react with typical reducing agents such as hydrazine.[49]

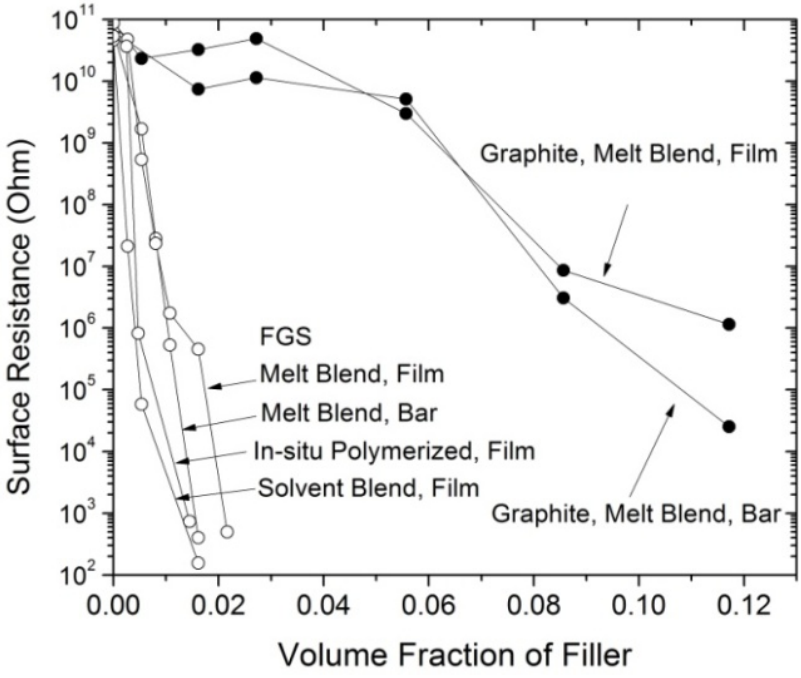

Figure 3-7. Surface resistance of melt blended graphite/TPU composites (closed) and melt blended, solution mixed and *in-situ* polymerized FGS/TPU composite (open symbols).

3.4.7. Mechanical Properties

Reinforcement with graphene sheets also greatly enhances stiffness of polymers as shown in Figure 3-8. 200% increase in tensile modulus of TPU was observed at 12 vol% of graphite while similar or even greater improvements were obtained only by 1.6 vol% (3 wt%) of FGS or iGO. Higher stiffening efficiency of exfoliated graphite can be attributed to higher particle A_f. Effective medium theories such as one by Mori and Tanaka[50] for tensile stiffness of composites filled with rigid ellipsoidal inclusions can be used to quantify the extent of dispersion (e.g. A_f) from modulus measurements.[34,51,52] Tandon and Weng[53] derived an analytical formula from Mori and Tanaka for transverse modulus E_{11} of composites containing mono-dispersed ellipsoids with perfect planar orientation.

$$\frac{E_{11}}{E_m} = \frac{1}{1+\phi(-2\nu_m A_3 + (1-\nu_m)A_4 + (1+\nu_m)A_5 A)/2A} \tag{3.1}$$

where ϕ, E_m and ν_m are concentration of the reinforcing inclusions, Young's modulus and Poisson's ratio of the matrix. A and A_i are functions of ϕ, ν_m and components of Eshelby's tensor[54,55], the detailed formula for which can be found in Tandon and Weng. For modeling of composite modulus, E_{TPU} was assumed to be 6.1 and 6.6 MPa for melt and solvent processed Avalon 70AE, and 7.2 MPa for *in-situ* polymerized TPU as determined experimentally. Both theoretical and experimental estimation[56,57] suggest in-plane modulus of graphene $E_{graphite}$ is about 1060 GPa. Matrix Poisson's ratio ν_{TPU} of 0.48 considering small matrix compressibility for elastomers[58] and graphite Poisson's ratio ν_{TPU} of 0.006 were used.[59] Fitting experimental modulus data with equation (3.1) indicates that solvent dispersed FGS and Ph-iGO are mechanically equivalent to flat rigid disks (E = 1 TPa) with A_f of ~ 600 and ~ 800, while A_f of untreated graphite is only 38. FGS dispersed via solvent blending appears to more effectively stiffen TPU than that via melt processing (A_f = 220). However, modulus increase by FGS incorporated via *in-situ* polymerization is not as pronounced despite what appears to be good dispersion by TEM (compare Figure 3-5 (j) and (k) to (g) and (h)). As the FTIR of composites suggests (Figure 3-2 (c) and (d)), FGS addition during TPU synthesis tends to suppress hydrogen

bonding between proton acceptors (-C=O) and donors (-N-H) in polymerized TPU which physically cross-links chains. Therefore, stiffness gain from reinforcement with graphene can be compromised considerably by reduced matrix mechanical property.

It should be also noted that the aspect ratio, A_f of iGO from modulus modeling (400 ~ 800) is far smaller than highest possible A_f of isolated GO sheets estimated from AFM analysis (~ 10,000, see Figure 2-1 (a)). While particle attrition may play a role, iGO layers are mainly dispersed as highly-curved stacks intercalated by polymer, see Figure 3-5 (l), (m) and (n). Brune and Bicerano[60] argued that these stacks will have significantly diminished modulus and A_f compared with isolated sheets. Also as noted by Schaefer and Justice,[61] quantified graphene dispersion from the modulus modeling rather reflects a local persistence length of the flexible layers due to high flexibility of thin carbon sheets.

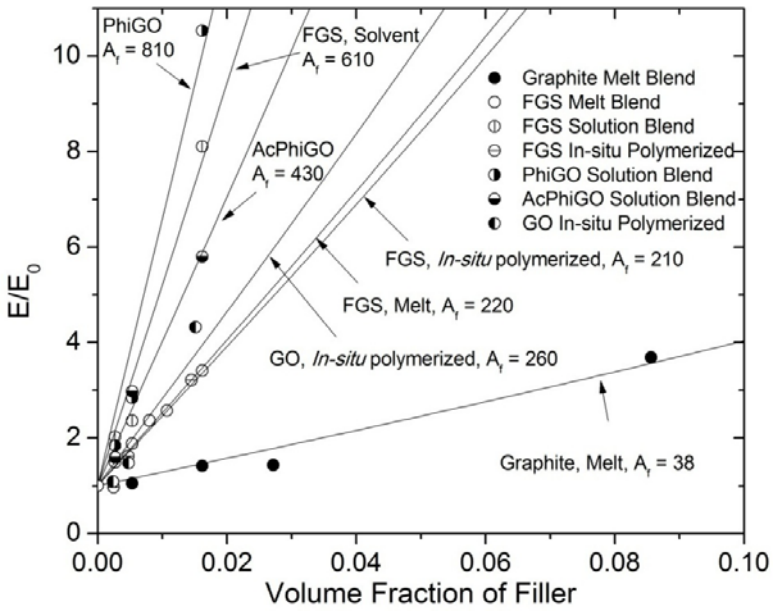

Figure 3-8. Young's moduli E normalized by matrix modulus E_0 of graphite/TPU composites. Straight lines are predictions based on Mori-Tanaka's theory.[50]

As also discussed in Chapter 4 and 5, the same FGS provided a surprisingly low modulus increase for rigid glassy polymers such as poly(ethylene-2,6-naphthalate)[34] and polycarbonate.[52] Mori and Tanaka predicted accordingly low A_f (20 ~ 30). This reduced

reinforcing efficacy can be attributed to defects in the sheet structure formed by oxidation and pyrolysis, which can possibly reduce effective in-plane tensile stiffness of FGS to 72 GPa (see Figure 4-13 (b)).[34] However, A_f of FGS estimated from modulus enhancements for TPU is as high as ~ 600. Modulus modeling of the composites containing 1 vol% of ellipsoidal inclusions (A_f = 200) based on Mori and Tanaka (Figure 3-9) indicates that there will be no additional gain in the composite stiffness when the reinforcement modulus, $E_{reinforcement}$ is greater than 10^4 times of the matrix modulus, E_{matrix}. For elastomeric TPU (E_{matrix} = 6.6 MPa), $E_{reinforcement}/E_{matrix}$ is greater than the threshold even when reinforcement modulus is 72 GPa, implying stiffening performance is not affected by the reduction in $E_{reinforcement}$. However, for rigid polymers such as poly(ethylene-2,6-naphthalate) (E_{matrix} = 2.3 GPa),[34] the decrease in reinforcement modulus diminishes the composite modulus substantially due to relatively small particle/matrix stiffness ratio.

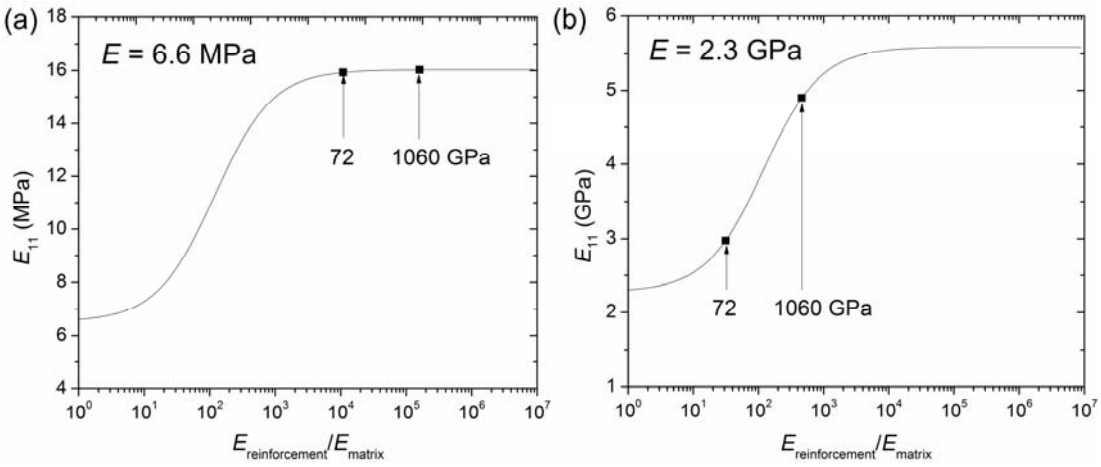

Figure 3-9. Transverse tensile modulus E_{11} predicted by Mori-Tanaka's theory[50] of (a) elastomeric (E = 6.6 MPa) and (b) glassy (E = 2.3 GPa) polymer composites reinforced with 1 vol% A_f = 200 ellipsoids with varying in-plane stiffness.

Ultimate mechanical properties (e.g. strain at break, tensile strength and toughness) were determined by stretching ~ 4 mm wide composite films at a constant rate (0.024 /s) until the fracture using Minimat. Representative stress-strain responses of TPU

composites are shown in Figure 3-10. Melt or Solvent blended graphite and FGS composites display a small increase in toughness (area under stress-strain curves) at small concentration (5 wt% graphite and 0.5 wt% FGS), but subsequent decreases at higher loadings (Table A-2 and Figure 3-10 (a), (b) and (c)). Fracture can initiate more easily from the matrix-filler interfaces due to weaker adhesion. However, in case of Ph-iGO (Figure 3-10 (d)), composite films all broke at higher elongation than neat TPU. Less well dispersed morphology of Ph-iGO may lead to smaller interfacial area and surface modification may strengthen the adhesion. Tensile behaviors of composites *in-situ* polymerized with FGS or GO (Figure 3-10 (f) and (g)) are distinctive compared with solvent blended ones. Unlike neat *in-situ* polymerized TPU, composites polymerized with small incorporation of FGS and GO show strain hardening behaviors around 500% strain in their stress-strain curves resulting significantly enhanced tensile strength. Higher soft-hard domain mixing[44] and surface grafting with TPU could account for this trend. However, higher amount (2.7 ~ 2.8 wt%) of FGS and GO doesn't improve the strength as significantly, possibly owing to excessive decrease in inter-urethane hydrogen bonding or matrix molecular weight reduction.

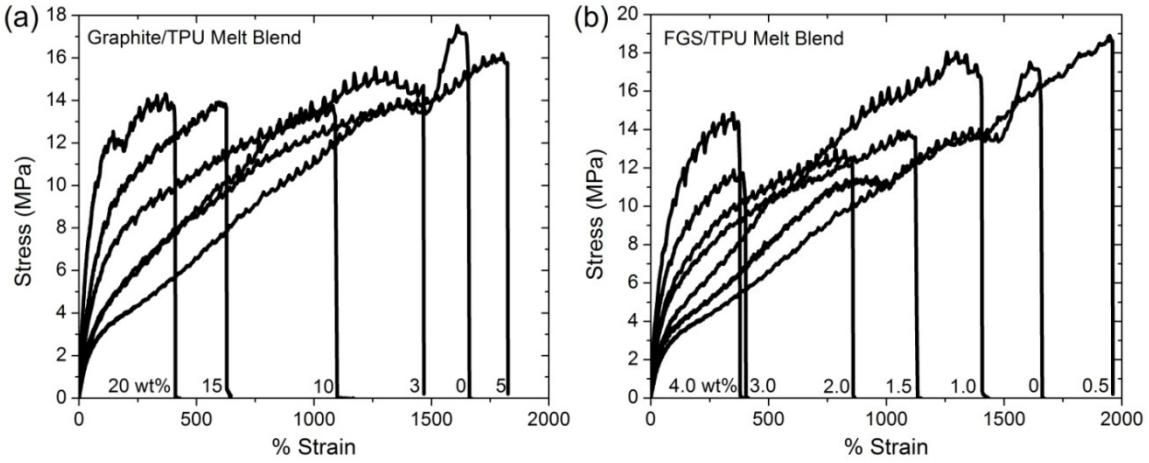

Figure 3-10 (continued to the next page). Stress-strain responses of TPU composites reinforced with melt blended (a) graphite, (b) FGS, solvent blend (c) FGS, (d) Ph-iGO, (e) AcPh-iGO, *in-situ* polymerized (f) FGS and (g) GO.

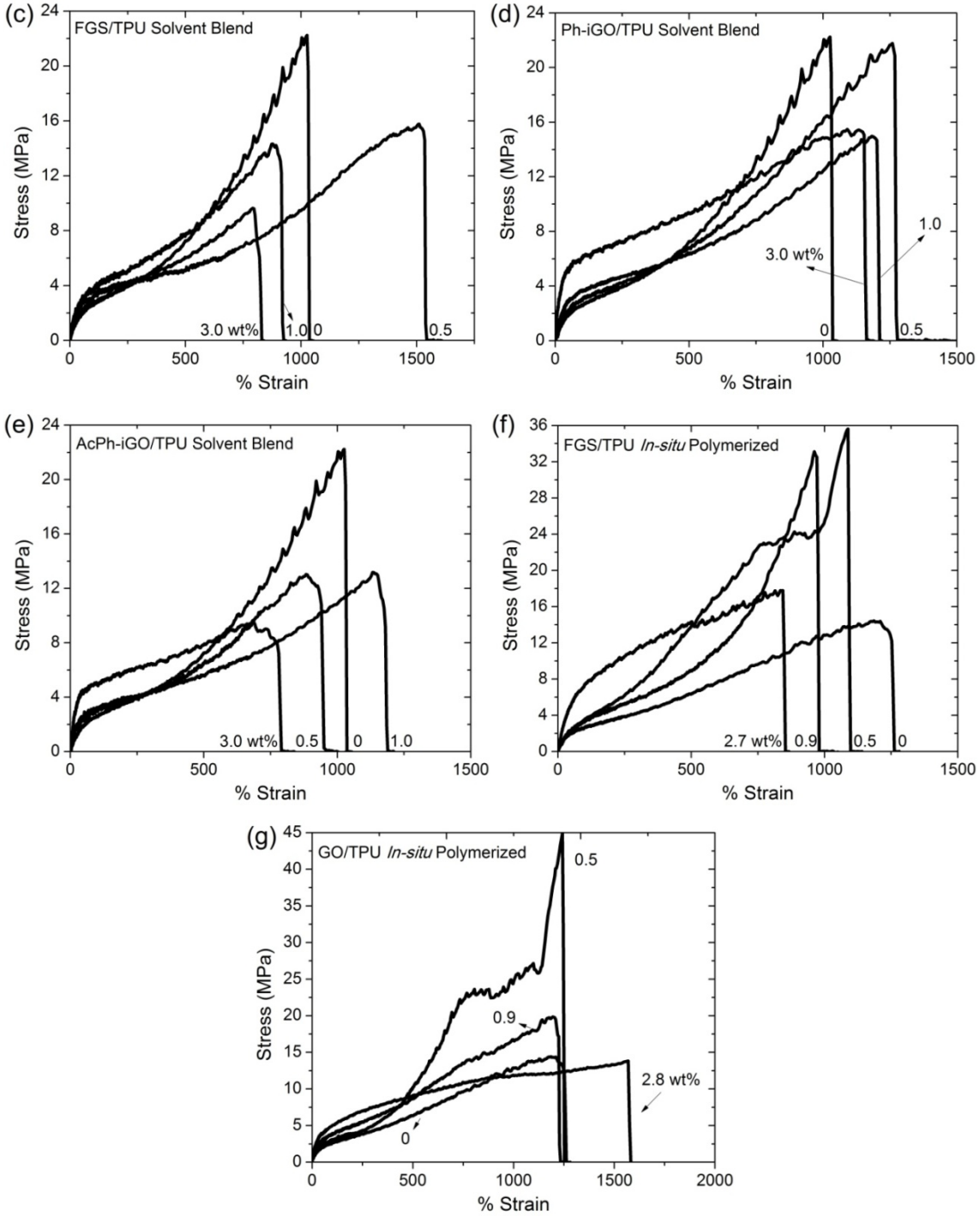

Figure 3-10 (continued from the previous page). Stress-strain responses of TPU composites.

3.4.8. Gas Permeation

Relative He and N_2 permeability of TPU films filled with graphitic platelets at 35 °C is summarized in Figure 3-11. Remarkably reduced N_2 permeation (Figure 3-11 (a)) shows that exfoliated carbon sheets can be used as impermeable barriers in polymeric membranes. Experimentally measured P_{N2} were fitted with a gas permeation model by Lape and coworkers[62] for mono-dispersed parallel flakes in random array. Up to 90% decrease by 1.6 vol% (3 wt%) iGO is comparable to what uni-directionally aligned A_f = 400 ~ 500 flat impermeable flakes potentially result in, corroborating high aspect ratio of exfoliated carbon sheets. Considering layer misalignment in reality that significantly reduces the barrier enhancement,[63] actual particle A_f can be even greater than 400 ~ 500. Note that 3 wt% (1.6 vol%) of Ph-iGO leads to a remarkable 80 to 1 decrease in P_{N2}. Since the barrier performance of 2-dimensional platelets is determined only by particle A_f, not by the micro-mechanics of sheets, iGO with lager diameter can be more advantageous for minimizing gas permeation. Moreover, disk-like particles tend to adopt parallel orientation in nematic transition as the shape anisotropy and particle concentration grow.[64] Reduction in N_2 permeability by *in-situ* polymerized FGS is not as significant. Again, decreased inter-urethane hydrogen bonding caused by FGS addition may increase gas diffusion rate through matrix. Note that decrease in He permeation (Figure 3-11 (b)) is not as significant as that in N_2 permeation as also indicated by small A_f values from modeling. With addition of particles, defects (e.g. free volume) can be introduced preferentially allowing transport of smaller molecules[25] which may rationalize A_f mismatch between N_2 and He permeation modeling.

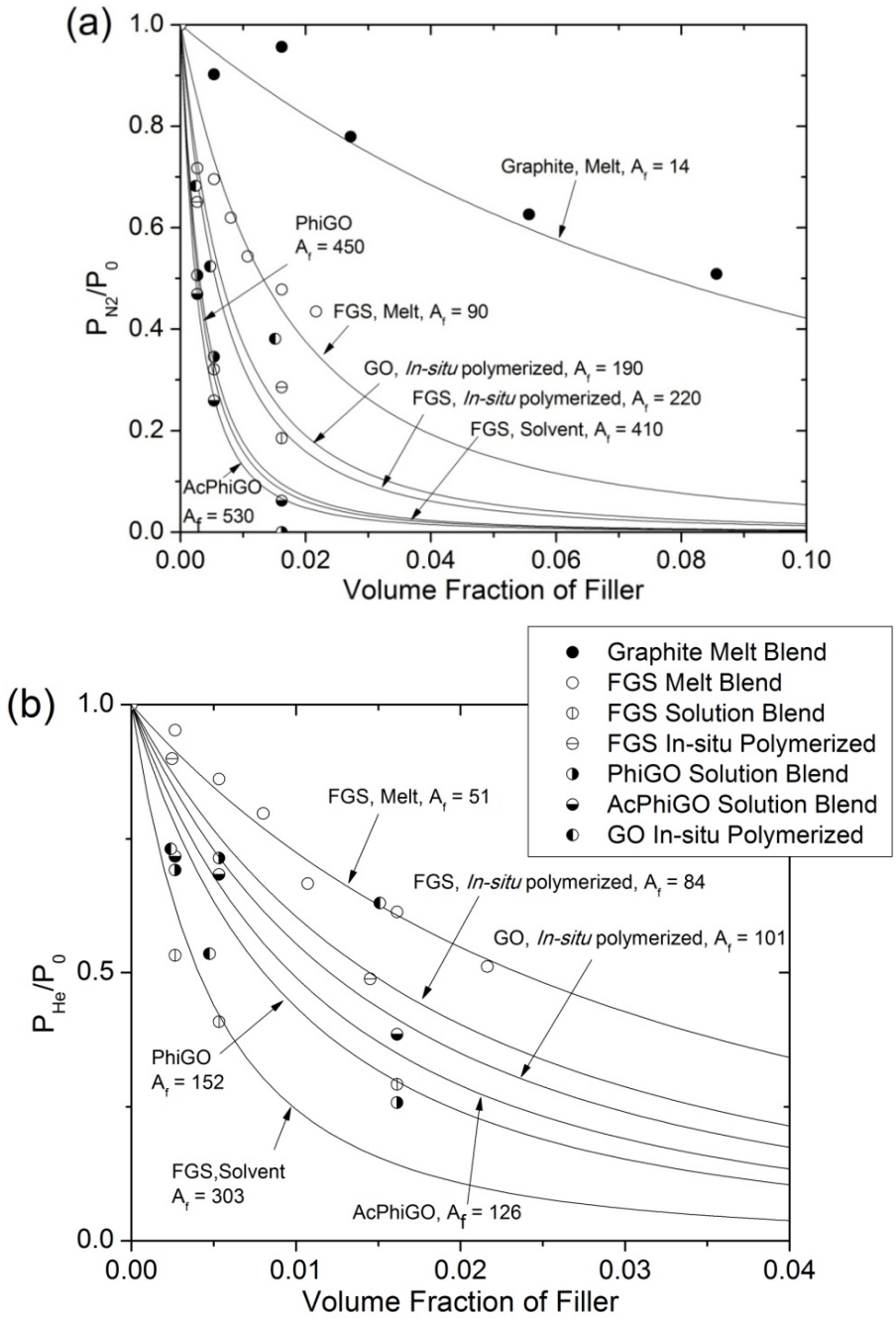

Figure 3-11. (a) N_2 and (b) He permeability of TPU composites normalized by permeability P_0 of neat TPU. Solid curves are predictions based on Lape *et al.*[62]

(a) (b)

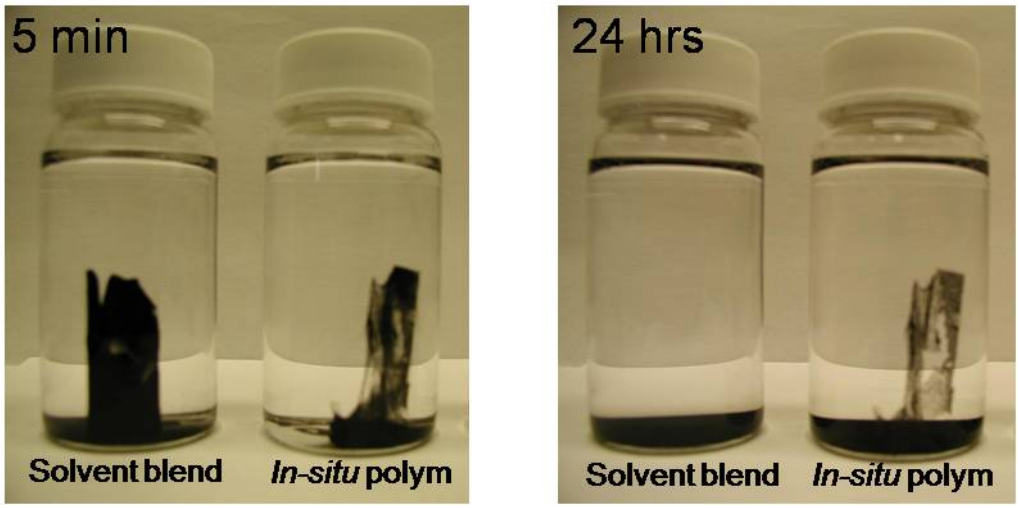

(c)

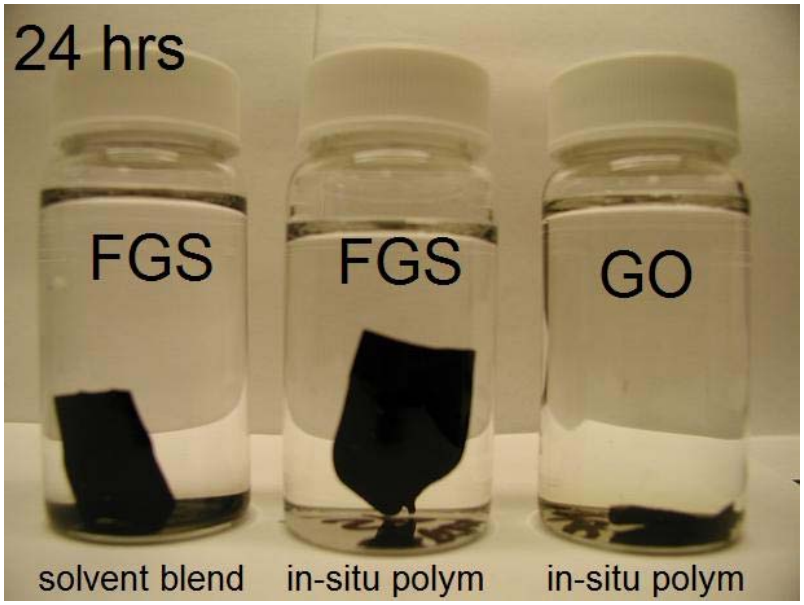

Figure 3-12. Solvent mixed and *in-situ* polymerized composite films containing ~ 0.5 vol% FGS particles soaked for (a) 5 min and (b) 24 hrs in 18 ml THF. (c) Solvent blended and *in-situ* polymerized TPU with ~ 1.5 vol% FGS or GO immersed for 24 hrs in THF.

3.4.9. Solvent Extraction

Despite limited hydrogen bonding in *in-situ* polymerized composites, graphene functionalized with multiple -OH groups may serve as a pseudo chain extender substituting for inter-urethane physical links. Figure 3-12 (a) and (b) shows solvent blended and *in-situ* polymerized ~ 1.0 wt% (0.5 vol%) FGS/TPU films after 5 min and 24 hrs' immersion in THF. A fraction of particulates maintaining the original shape implies only *in-situ* polymerized FGS could not be completely extracted by THF in 24 hrs. This particle network could not be disturbed even by intensive shaking. FGS functionalized with TPU may form a sample spanning internal network that can self-sustain via chemical or physical cross-links mediated by grafted polymer chains. DMA of *in-situ* polymerized hybrids (Figure 3-4 (c)) also substantiates the existence of the network-like structures even at 0.5 wt% of FGS. Film shape of samples with higher fraction (~ 3 wt%) of reinforcements was all preserved even after 24 hrs immersion (Figure 3-12 (c)). However, some particle settlements indicate an extractable fraction in the solvent mixed FGS sample, while *in-situ* polymerized FGS and GO display good resistance against THF extraction.

3.5. Summary

Graphite, GO and exfoliated graphite derived from GO were dispersed into TPU via melt compounding, solvent mixing and *in-situ* polymerization. FGS is compatible with melt compounding, an economically viable composite manufacturing route and as electrically conductive as natural graphite.[28] However, significant size reduction and structural distortion may reduce the reinforcement efficiency for polymers. The large diameter of GO sheets can be preserved using chemical modification, which is beneficial for applications that require high aspect ratio of disk-like particles such as gas barrier membranes. Strong interfacial bonding with matrix polymers enabled by surface functionalization is another advantage. Disadvantages are it cannot be melt processed due to thermal instability and in order to regain electrical conductivity, *in-situ* chemical reduction is necessary. Solvent-based processes were more effective for obtaining well

distributed FGS throughout the matrix than melt processing as suggested by TEM and solid property enhancements. With only 3 wt% of graphene, a 3 to 10 fold increase in tensile modulus and 90% reduction in N_2 permeability were observed. FGS dispersed by *in-situ* polymerization formed strongly cross-linked networks, but also inhibited inter-chain hydrogen bonding in TPU matrix.

3.6. References

(1) Kim, H.; Macosko, C. W. *Ann Tech Conf- Soc Plast Eng* **2009**, 122-125.

(2) Woods, G. *The ICI polyurethanes book*; Wiley: New York, 1990.

(3) Lamda, N. M. K.; Woodhouse, K. A.; Cooper, S. L. *Polyurethanes in biomedical applications*; CRC Press: Boca Raton, FL, 1998.

(4) Alexandre, M.; Dubois, P. *Mater. Sci. Eng., R* **2000**, *R28*, 1-63.

(5) Moniruzzaman, M.; Winey, K. I. *Macromolecules* **2006**, *39*, 5194-5205.

(6) Vaia, R. A.; Jandt, K. D.; Kramer, E. J.; Giannelis, E. P. *Macromolecules* **1995**, *28*, 8080-5.

(7) Vaia, R. A.; Jandt, K. D.; Kramer, E. J.; Giannelis, E. P. *Chem. Mater.* **1996**, *8*, 2628-2635.

(8) Cho, J. W.; Paul, D. R. *Polymer* **2000**, *42*, 1083-1094.

(9) Poetschke, P.; Bhattacharyya, A. R.; Janke, A.; Goering, H. *Compos. Interfaces* **2003**, *10*, 389-404.

(10) Chavarria, F.; Paul, D. R. *Polymer* **2006**, *47*, 7760-7773.

(11) Kawasumi, M.; Hasegawa, N.; Kato, M.; Usuki, A.; Okada, A. *Macromolecules* **1997**, *30*, 6333-6338.

(12) Fornes, T. D.; Yoon, P. J.; Paul, D. R. *Polymer* **2003**, *44*, 7545-7556.

(13) Sun, Y.-P.; Fu, K.; Lin, Y.; Huang, W. *Acc. Chem. Res.* **2002**, *35*, 1096-1104.

(14) Lotya, M.; Hernandez, Y.; King, P. J.; Smith, R. J.; Nicolosi, V.; Karlsson, L. S.; Blighe, F. M.; De, S.; Wang, Z.; McGovern, I. T.; Duesberg, G. S.; Coleman, J. N. *J. Am. Chem. Soc.* **2009**, *131*, 3611-3620.

(15) Tien, Y. I.; Wei, K. H. *Macromolecules* **2001**, *34*, 9045-9052.

(16) Zhu, J.; Kim, J.; Peng, H.; Margrave, J. L.; Khabashesku, V. N.; Barrera, E. V. *Nano Lett.* **2003**, *3*, 1107-1113.

(17) Widya, T.; Macosko, C. *J. Macromol. Sci., Part B: Phys.* **2005**, *44*, 897-908.

(18) Usuki, A.; Kojima, Y.; Kawasumi, M.; Okada, A.; Fukushima, Y.; Kurauchi, T.; Kamigaito, O. *J. Mater. Res.* **1993**, *8*, 1179-84.

(19) Finnigan, B.; Martin, D.; Halley, P.; Truss, R.; Campbell, K. *Polymer* **2004**, *45*, 2249-2260.

(20) Koerner, H.; Price, G.; Pearce, N. A.; Alexander, M.; Vaia, R. A. *Nat. Mater.* **2004**, *3*, 115-120.

(21) Liff, S. M.; Kumar, N.; McKinley, G. H. *Nat. Mater.* **2007**, *6*, 76-83.
(22) Xia, H.; Song, M. *J. Mater. Chem.* **2006**, *16*, 1843-1851.
(23) Pattanayak, A.; Jana, S. C. *Polymer* **2005**, *46*, 3275-3288.
(24) Pattanayak, A.; Jana, S. C. *Polymer* **2005**, *46*, 3394-3406.
(25) Osman, M. A.; Mittal, V.; Morbidelli, M.; Suter, U. W. *Macromolecules* **2003**, *36*, 9851-9858.
(26) Matsuo, Y.; Tabata, T.; Fukunaga, T.; Fukutsuka, T.; Sugie, Y. *Carbon* **2005**, *43*, 2875-2882.
(27) Herrera-Alonso, M.; Abdala, A. A.; McAllister, M. J.; Aksay, I. A.; Prud'homme, R. K. *Langmuir* **2007**, *23*, 10644-10649.
(28) Schniepp, H. C.; Li, J.-L.; McAllister, M. J.; Sai, H.; Herrera-Alonso, M.; Adamson, D. H.; Prud'homme, R. K.; Car, R.; Saville, D. A.; Aksay, I. A. *J. Phys. Chem. B* **2006**, *110*, 8535-8539.
(29) Stankovich, S.; Dikin, D. A.; Piner, R. D.; Kohlhaas, K. A.; Kleinhammes, A.; Jia, Y.; Wu, Y.; Nguyen, S. T.; Ruoff, R. S. *Carbon* **2007**, *45*, 1558-1565.
(30) www.huntsman.com, accessed Nov 27, 2008.
(31) www.asbury.com, accessed February 7, 2009.
(32) www.vorbeck.com, accessed February 7, 2009.
(33) Brunauer, S.; Emmett, P. H.; Teller, E. *J. Am. Chem. Soc.* **1938**, *60*, 309-19.
(34) Kim, H.; Macosko, C. W. *Macromolecules* **2008**, *41*, 3317-3327.
(35) Cooper, S. L.; Seymour, R. W.; Estes, G. M. *Macromolecules* **1970**, *3*, 579-83.
(36) Senich, G. A.; MacKnight, W. J. *Macromolecules* **1980**, *13*, 106-10.
(37) Pye, D. G.; Hoehn, H. H.; Panar, M. *J. Appl. Polym. Sci.* **1976**, *20*, 1921-31.
(38) Jeong, H.-K.; Krych, W.; Ramanan, H.; Nair, S.; Marand, E.; Tsapatsis, M. *Chem. Mater.* **2004**, *16*, 3838-3845.
(39) Yang, W. P.; Macosko, C. W.; Wellinghoff, S. T. *Polymer* **1986**, *27*, 1235-40.
(40) Fractal dimension d_f of crumpled sheets can be 2.5 (good solvents) ~ 3.0 (poor solvents). This gives the radius of gyration ~ $(R^2 \cdot h)^{1/df}$ of 15 ~ 90 for good solvents and 10 ~ 40 nm for poor solvents assuming FGS diameter R = 25-200 nm and thickness ~ 1.8 nm (thickness of FGS).
(41) Wen, X.; Garland, C. W.; Hwa, T.; Kardar, M.; Kokufuta, E.; Li, Y.; Orkisz, M.; Tanaka, T. *Nature* **1992**, *355*, 426-8.
(42) Seymour, R. W.; Allegrezza, A. E.; Cooper, S. L. *Macromolecules* **1973**, *6*, 896-901.
(43) Seymour, R. W.; Cooper, S. L. *Macromolecules* **1973**, *6*, 48-53.
(44) Miller, J. A.; Lin, S. B.; Hwang, K. K. S.; Wu, K. S.; Gibson, P. E.; Cooper, S. L. *Macromolecules* **1985**, *18*, 32-44.
(45) Hirata, M.; Gotou, T.; Horiuchi, S.; Fujiwara, M.; Ohba, M. *Carbon* **2004**, *42*, 2929-2937.

(46) Wang, D. H.; Arlen, M. J.; Baek, J.-B.; Vaia, R. A.; Tan, L.-S. *Macromolecules* **2007**, *40*, 6100-6111.
(47) Eda, G.; Fanchini, G.; Chhowalla, M. *Nat. Nanotechnol.* **2008**, *3*, 270-274.
(48) Stankovich, S.; Dikin, D. A.; Dommett, G. H. B.; Kohlhaas, K. M.; Zimney, E. J.; Stach, E. A.; Piner, R. D.; Nguyen, S. T.; Ruoff, R. S. *Nature* **2006**, *442*, 282-286.
(49) Zalan, Z.; Lazar, L.; Fueloep, F. *Curr. Org. Chem.* **2005**, *9*, 357-376.
(50) Mori, T.; Tanaka, K. *Acta Metall.* **1973**, *21*, 571-574.
(51) Sheng, N.; Boyce, M. C.; Parks, D. M.; Rutledge, G. C.; Abes, J. I.; Cohen, R. E. *Polymer* **2004**, *45*, 487-506.
(52) Kim, H.; Macosko, C. W. *Polymer* **2009**, *50*, 3797-3809.
(53) Tandon, G. P.; Weng, G. J. *Polym. Compos.* **1984**, *5*, 327-333.
(54) Eshelby, J. D. *Proc. Roy. Soc. (London)* **1957**, *241*, 376-396.
(55) Eshelby, J. D. *Proc. Roy. Soc. (London)* **1959**, *252*, 561-569.
(56) Kelly, B. T. *Physics of Graphite*; 1st ed.; Applied Science: London, 1981.
(57) Lee, C.; Wei, X.; Kysar, J. W.; Hone, J. *Science* **2008**, *321*, 385-388.
(58) Qi, H. J.; Boyce, M. C. *Mech. Mater.* **2005**, *37*, 817-839.
(59) Cho, J.; Luo, J. J.; Daniel, I. M. *Compos. Sci. Technol.* **2007**, *67*, 2399-2407.
(60) Brune, D. A.; Bicerano, J. *Polymer* **2001**, *43*, 369-387.
(61) Schaefer, D. W.; Justice, R. S. *Macromolecules* **2007**, *40*, 8501-8517.
(62) Lape, N. K.; Nuxoll, E. E.; Cussler, E. L. *J. Membr. Sci.* **2004**, *236*, 29-37.
(63) Bharadwaj, R. K. *Macromolecules* **2001**, *34*, 9189-9192.
(64) Forsyth, P. A., Jr.; Marcelja, S.; Mitchell, D. J.; Ninham, B. W. *Adv. Colloid Interface Sci.* **1978**, *9*, 37-60.

Chapter 4. Graphene/Polyester Nanocomposites: Quantification of Graphene Dispersion

4.1. Overview

In the previous chapter, morphology and properties of graphene/TPU composites resulting from different composite processing were discussed. The most important factor that determines properties of layered nanocomposites is the extent of reinforcement dispersion, which is frequently quantified by average ratio of diameter to thickness of dispersed platelets, or aspect ratio A_f. This chapter focuses on quantification of graphene dispersion. As the model polymer, rigid, semi-crystalline, engineering polyester (poly(ethylene-2,6-naphthalate), PEN) was used. Two different graphitic layers: un-exfoliated graphite and functionalized graphene sheets (FGS), that can result in substantially different states of dispersion, were incorporated into PEN by melt compounding. GO could not be used due to lack of thermal stability. Dimensional and surface characteristics of graphite and FGS are substantially different as indicated by atomic force microscopy (AFM), Raman and X-ray photoelectron spectroscopy (XPS) results in Chapter 2. Their dispersion was quantified and compared using a range of characterization techniques: electron microscopy, X-ray scattering, melt rheology and solid property measurements. Dispersion level from rheological measurements on molten samples is compared with results from electrical conductivity experiments as well as tensile modulus, thermal expansion and hydrogen permeability measurements on the solid samples. All results presented in this chapter were previously published[1] in Macromolecules in 2008.

4.2. Introduction

After incorporation into polymer, the state of dispersion of graphene must be determined adequately to evaluate the reinforcement efficiency. Among various methods used for characterizing dispersion of layered nanocomposites, electronic microscopy and

X-ray diffraction have been most widely used.[2,3] Imaging with transmission electron microscopy (TEM) provides real space morphological information.[3-5] However, TEM only visualizes a small area. On the other hand, X-ray scattering yields structural information averaged over a larger sample volume. One of the drawbacks with X-ray scattering is that it is often difficult to interpret results based on reciprocal space to find out the structure and shape of the scattering particles. Moreover, some minor morphological information can be missed (e.g. small amount of intercalated structure surrounded by exfoliated morphology in the case of polymer layered nanocomposites) since scattering intensity depends on the concentration of the scattering entity.

Although indirect, solid state composite properties can be used to estimate reinforcement efficiency. These measurements are also very valuable to assess the practical performance of these composites. Composite theories for stiffness, thermal expansion and gas barrier properties have been proposed,[6-9] and fitting experimentally measured properties with these models has provided a quantitative measure for layered composite dispersion.[10-13] However, aspect ratio data from composite theories will only be a rough estimate for dispersion since theories are based on simplified assumptions such as perfect adhesion between two phases and unidirectional alignment of disks, which are seldom realized in practice.[10] Additionally, composite modeling also requires accurate material parameters of the matrix and the reinforcement for quantitative analysis.

A polymer melt filled with nano-inclusions has distinctive rheological behavior: development of a yield stress and a frequency independent modulus.[14-16] One can extract quantitative measures for the dispersion such as an average aspect ratio of additives from the concentration where the rigid platelets form a network having non-zero rigidity.[16-18] The threshold for this rigidity percolation can also be compared with the onset of connectivity percolation, which is easily determined from electrical conductivity measurements on nanocomposites with conducting fillers.[19,20] If there are strong colloidal interaction between platelets in the polymer matrix then they will form fractal aggregates of reinforcing flocs.[18] With this idea, a fractal dimension of the gelled network can be

inferred from how the elastic modulus and limits of linear viscoelasticity scale with the filler concentration.[21]

Dispersion of unexfoliated graphite and FGS into polymer was explored with melt blending. The matrix polymer, PEN is a high performance engineering thermoplastic which is used for many practical applications, especially in a film form for producing magnetic data storage devices.[22] The polymer substrates used for magnetic tapes must be mechanically robust and dimensionally stable upon temperature or humidity changes to enable high density data storage. Reinforcement with nano-size inclusions will lead to better dimensional stability. We first attempted to use organically modified montmorillonite (Cloisite 20A and 30B, Southern Clay Products) as reinforcements for PEN. However, the resulting nanocomposites had high brittleness, even lower melt viscosity than neat polymer and nearly no increase in tensile modulus. The high processing temperature, 300 °C, most likely caused thermal degradation of alkylammonium modifiers of clays. Loss of the modifiers may have resulted in poor dispersion and degradation of PEN. We then turned to graphite which can be exfoliated without surfactants. Furthermore, its stiffness exceeds that of other inorganic nano particles and its in-plane coefficient of thermal expansion is negative near room temperature.[23,24] As well as these advantages, gas permeabilities of PEN are expected to drop significantly after incorporation of graphite due to its high aspect ratio and impermeability.[25] The ability of graphite to make PEN electrically conductive is also a potential advantage for recording tapes.

4.3. Experimental

4.3.1. Material Characterization

Matrix polymer, poly(ethylene-2,6-naphthalate) or PEN (X-10 PEN homopolymer, intrinsic viscosity: 0.79 dl/g, *ortho*-chlorophenol) was obtained from Excell LLC (Dupont Polyester) in pellet form. PEN resin was dried in an oven at 120°C for more than 24 hrs before melt blending. Flake graphite (surfaced enhanced, grade # 3775) was purchased from Asbury Carbons.[26] The provider[27] reported that nominal size

of particles is 8 μm and specific surface area is around 24 m^2/g. This value is close to the surface area 29 g/m^2 estimated from Brunauer, Emmet and Teller (BET)[28] N_2 absorption (Autosorb-1, Quantachrome Instruments). FGS, a thermally exfoliated graphite oxide with 700 - 1500 m^2/g of reported BET surface area[29] was received from Princeton University and Vorbeck Materials.[30] The density of graphite, 2.28 g/cm^3 was calculated from unit cell dimension data of perfectly crystalline graphite (hexagonal, a = 2.46 and c = 6.69 Å)[31] and the density of FGS was assumed to be equal to that of graphite. The density of amorphous PEN (1.33 g/cm^3)[32] was used rather than the density of the crystalline form (1.41 - 1.44 g/cm^3)[33,34] since all specimens used for the testing are highly amorphous (% crystal < 5%) due to the rapid quenching after melt processing. The melt density of PEN was approximated by 1.20 g/cm^3, 90% of its amorphous density. Poly(ethylene terephthalate) which has a similar molecular structure and amorphous density (1.34 g/cm^3)[35] has the melt density of 1.20 g/cm^3.[36]

Prior to blending into PEN, particle dimensions of as-received graphite particles were measured with contact-mode AFM. Graphite was deposited on a mica substrate (grade V1, Ted Pella) from tetrahydrofuran (THF) dispersion prepared at 10 μg/mL. Experimental procedures for AFM are described in detail in Chapter 2.

4.3.2. Melt Compounding

Before preparing blends, the PEN pellets were cryogenically pulverized to ~ 100 μm powders for 1 min using a Spex 6700 Freezer/Mill to prepare a more homogeneous pre-blend with graphite or FGS, and to facilitate feeding into the extruder. PEN/graphite and PEN/FGS mixtures of 4.1 - 4.3 g were prepared at various graphite (0, 1, 3, 5, 6, 7, 10, 15 and 20 wt%) and FGS loadings (0.5, 1, 1.5, 2, 3 and 4 wt%). They were fed into a recirculating, conical twin screw extruder (Microcompounder, DACA Instruments) at 280 °C with N_2 purge. Compounding was performed at a screw speed of 360 RPM for 8 min.

4.3.3. Direct Characterization of Dispersion

We used TEM and X-ray scattering to investigate the dispersion of graphite and FGS. DACA extruded graphite composites were microtomed into 60~90 nm thick slices at room temperature with a diamond knife (Reichert Ultracut) and digital images were obtained using a JEOL® 1210 electron microscope at an accelerating voltage of 120 kV. No straining was required to obtain good electron contrast between PEN and graphite.

X-ray scattering analysis was performed with a combined small and wide angle instrument (SAXSESS, Anton Paar) with CuK_α radiation. Powders of the nanocomposite samples were produced by cryo-pulverization for 30 sec and placed between Kapton tapes. A generator voltage of 40 kV and current of 50 mA was used.

4.3.4. Melt Rheology

Rheological measurements were carried out with a strain controlled rotational rheometer (ARES, TA Instruments) at 290 °C under N_2 atmosphere. 0.6 ~ 0.7 g of extruded composites were dried at 120 °C for at least 24 hrs and loaded onto a 25 mm parallel plate fixture. They were squeezed into disks ~1 mm thick by slowly lowering the upper plate. After sample loading, a dynamic time sweep was conducted at 1 rad/s using small amplitude strain until no change in storage modulus *G'* was observed (~ 1 hr). Subsequently, using a dynamic strain sweep at 1 rad/s, the critical strain, γ_{crit}, where *G'* drops to 90% of its limiting low strain value was recorded. After a waiting time of 30 min, a frequency sweep at $\gamma < \gamma_{crit}$ from 100 rad/s to 0.01 rad/s was started. Occasionally, an additional test from low (0.01 rad/s) to high (100 rad/s) frequency was carried out to check the long term melt stability. Results from two consecutive frequency sweep tests were reproducible to within 10%, indicating that PEN was stable for > 3 hr at 290 °C.

4.3.5. Property Measurements

For electrical conductivity measurements, specimens with 3 different geometries were used to investigate the influence of processing history on electrical conductivity of composites. D samples are ~ 1 mm thick disks recovered after rheology tests with long

annealing history. They were removed from the rheometer plates gently to minimize deformation of samples then remelted at 300 °C and compressed slightly to make the disk surface flat. F samples are ~ 70 μm thick films with higher degree of graphite alignments. They were formed by pressing extrudates against Teflon sheets at 280 kPa and 280 °C. They were quenched into ice water to minimize PEN crystallinity build-up after pressing and dried for at least 48 hrs at room temperature in a vacuum oven before property measurements. B samples are bar shape samples (2 cm × 3 cm × 1 mm) designed to have less graphite orientation. Extrudates were processed into powders by cryo-pulverization and these composite powders were pressed (~ 70 kPa for 10 min), then annealed (without pressure for 1 hr) in a mold at 300 °C in order to relax any preferred orientation of the graphite and FGS. After annealing, these bars were cooled in air. By differential scanning calorimetry, the D and F samples have < 5% crystallinity, while the degree of crystallinity of B samples is generally around 10%. Surfaces of all the samples were polished with fine sandpaper (Wetordry Ultrafine P600) to reduce contact resistance between the sample and the conductivity probes. Surface resistance was measured with an 11-point DC probe (PRS-801 Prostat).

For the gas permeability and stiffness testing, films (F samples) were used due to their high in-plane filler orientation and small thickness. Hydrogen permeability of composite films at 35°C was determined based on a constant volume-variable pressure method using a home-made apparatus.[37,38] Hydrogen flowing at 1 atm and 80 cc/min was fed to one side of a 4.2 cm diameter film sample and the pressure in the opposite, evacuated chamber was monitored. Permeation constants were calculated using the pressure gradient, the pressure change with time and the film thickness.[37]

Specimen for tensile modulus and thermal expansion measurements were prepared by cutting strips 4 mm wide and 30 mm long from the center of the films. They were clamped with film fixtures on a Rheometrics Solids Analyzer II. Complex moduli, E^* were measured in dynamic strain sweep mode under 10 N static force pre-tension at room temperature. Thermal expansion was measured from the change in length of the same films at constant tension (~ 0.1 MPa) while decreasing temperature from 65 to 45,

35 and 25 °C in a convection chamber with a dry N_2 purge. In order to exclude any effects from a hygroscopic expansion of PEN, samples were dehydrated at 65 °C for 2 hrs.

4.4. Results and Discussion

4.4.1. Characterization of graphite and FGS

Lateral and thickness dimensions of as-received graphite were analyzed using AFM. The thickness, *h* of graphite averaged over 62 un-aggregated particles was 37 nm. This agrees with a value of ~30 nm calculated from the BET surface area 29 g/m^2 and density of graphite, assuming disk-shaped particles (see Section 2.3.1). The AFM measured diameter of graphite ranged from 100 to 1000 nm while FGS was 50 ~ 400 nm as discussed in Chapter 2. Minimum thickness of isolated FGS measured with AFM was ~ 1.8 nm.

Raman spectroscopy and XPS (Chapter 2) were employed to characterize chemical structure of FGS. Raman spectroscopy (Figure 2-4) of FGS indicated a significant transformation of sp^2 domain to sp^3 hybridization during oxidation treatments[39] and corroborates the structural distortion and weakening of the planar geometry. Existence of oxygen functionalities on the graphene surface was also confirmed by XPS (Figure 2-3 (d)). Surface oxygen groups are expected to promote the dispersion since it will render graphene surfaces to have more polar character.

4.4.2. TEM Analysis

TEM micrographs of PEN composites as extruded containing 3 wt% of graphite and FGS are shown in Figure 4-1. The graphite platelets appear as thick flat objects in Figure 4-1 (a) and (b). Particle dimensions were determined using an imaging analysis program. Particle thickness was defined by a full width at half maximum (FWHM) of a line intensity profile across the particle. After investigating 95 particles, an arithmetic average of diameter and thickness of graphite are found to be 487 and 36 nm, respectively. Mean thickness of 36 nm suggests that there was no change in thickness

during melt compounding when compared with the mean thickness of as-received material (37 nm) estimated by AFM. This is much greater than the inter-lamellar spacing of 0.34 nm indicating each stack is composed of ~ 100 single graphene layers. Although melt compounding may break up weakly aggregated graphite flakes, the multiple layer structure suggests that the layers were not delaminated at all by thermodynamic interaction with PEN or by intensive shear mixing. This is probably due to strong van der Waals binding between the closely spaced graphene layers. Aspect ratios, A_f which is the ratio of the lateral dimension to the thickness were estimated for individual platelets and Figure 4-2 shows a relatively narrow shape distribution of graphite. Its mean value is 20.8, median 18.4 and standard deviation 14.1. Interestingly, most graphite flakes appeared to exhibit a preferred orientation implying alignment during extrusion process (Figure 4-1 (b)).

In stark contrast with PEN/graphite, in PEN/FGS composites thin FGS sheets with high aspect ratio are distributed over the entire imaging area (Figure 4-1 (c)). Statistical analysis conducted for 88 FGS particles yielded a mean diameter and thickness of 222 and 2.9 nm, respectively. Even though FGS has smaller diameter than graphite, its average aspect ratio (88.4) is greater than that of graphite (20.8) due to even smaller thickness. FGS displays a wider aspect ratio distribution than graphite as evidenced by a higher standard deviation (56.4) and an average of aspect ratio of FGS is 88.4. However, the mean aspect ratio is expected to be greater than this value since atomically thin FGS layers are likely to be invisible in TEM. Figure 4-1 (d) shows the wrinkled nature of FGS which may be explained by the transformation of carbons from planar (sp^2-hybridized) to distorted structure (sp^3-hybridized) during the oxidation and pyrolysis process. This type of conversion was also confirmed by the higher D to G intensity ratio of FGS in Raman spectroscopy and the XPS results (see Figure 2-3 (d)). There is also stacking of wrinkled sheets that resembles the so called intercalated morphology in the nanocomposite literature. Incomplete oxide intercalation and thermal exfoliation may lead to the stacking of layers.

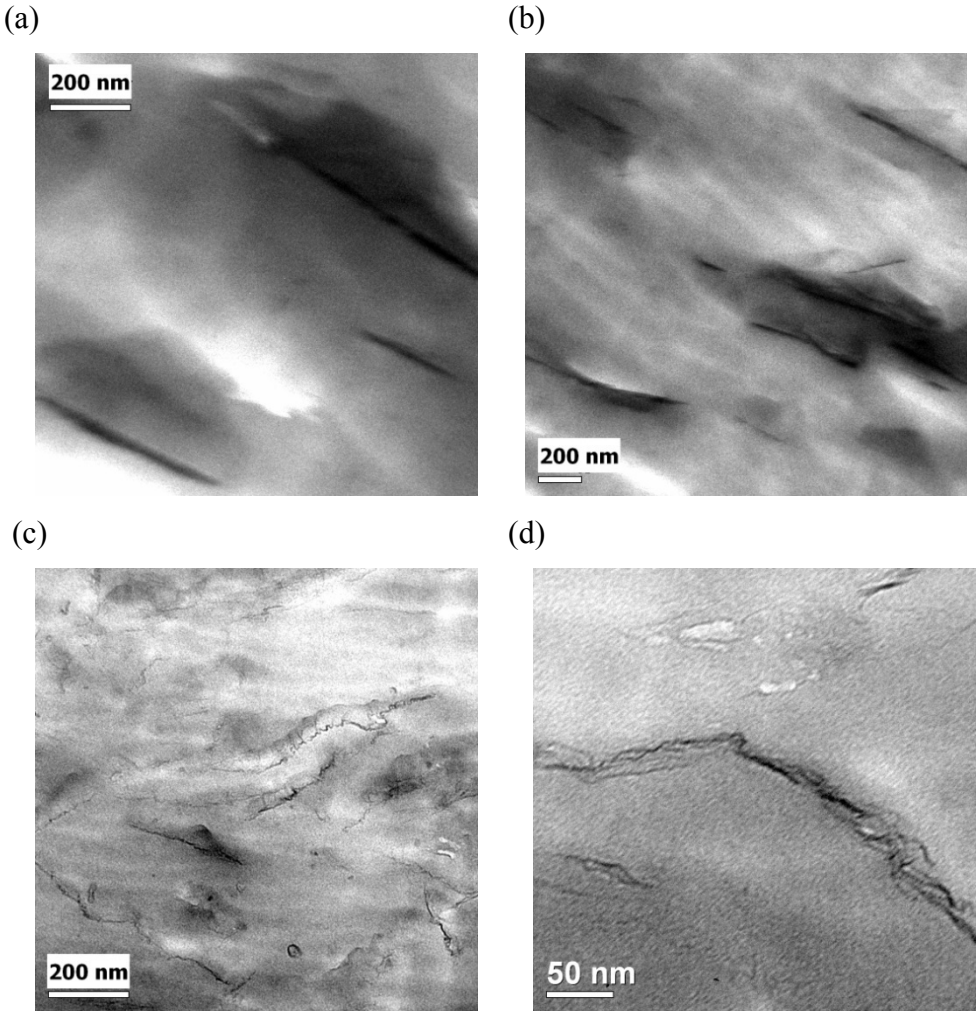

Figure 4-1. TEM micrographs of PEN with (a) and (b) 3 wt% graphite, and (c) and (d) 3 wt% FGS.

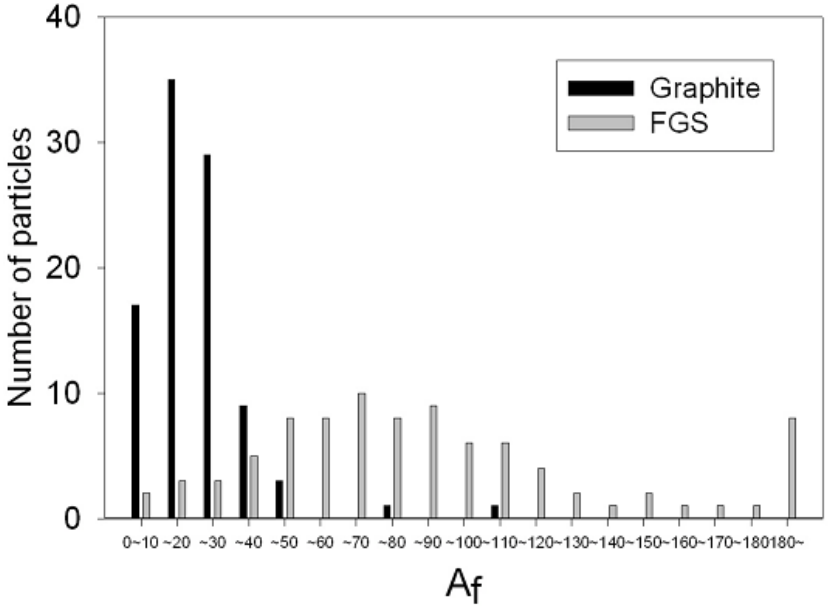

Figure 4-2. Shape distribution of graphite and FGS particles from TEM analysis.

4.4.3. X-ray Scattering

Figure 4-3 (a) presents X-ray scattering intensity profiles of pristine graphite, PEN and PEN/graphite composite (10 wt%). A sharp peak located at scattering vector q = 18.6 nm^{-1} in the scattering profile of unmixed graphite powder corresponds to the d_{002} spacing of graphite (d = 0.34 nm).[40] A peak appears at the same q in the profile of PEN/graphite composites, which implies that graphite is still ordered in layers even after melt compounding. However, for neat FGS (Figure 4-3 (b)), neither graphite nor graphite oxide (q = 8.4 ~ 9.7 nm^{-1}, d = 0.65 ~ 0.75 nm)[41] peaks are present, signifying nearly complete exfoliation during the rapid thermal treatment. Note that the broad reflection located around q ~ 4 nm^{-1} for graphite and FGS powders are scattering from window Kapton tapes. The characteristic reflections of graphite and graphite oxide is still absent after melt processing, corroborating the highly exfoliated morphology of FGS in PEN. There are no particular reflections for the stacked morphology of FGS planes observed by TEM (Figure 4-1 (d)), which suggests that stacking is rare, or that the sheets are more than 10 nm apart and thus scatter at lower angles than we can detect.

(a) (b)

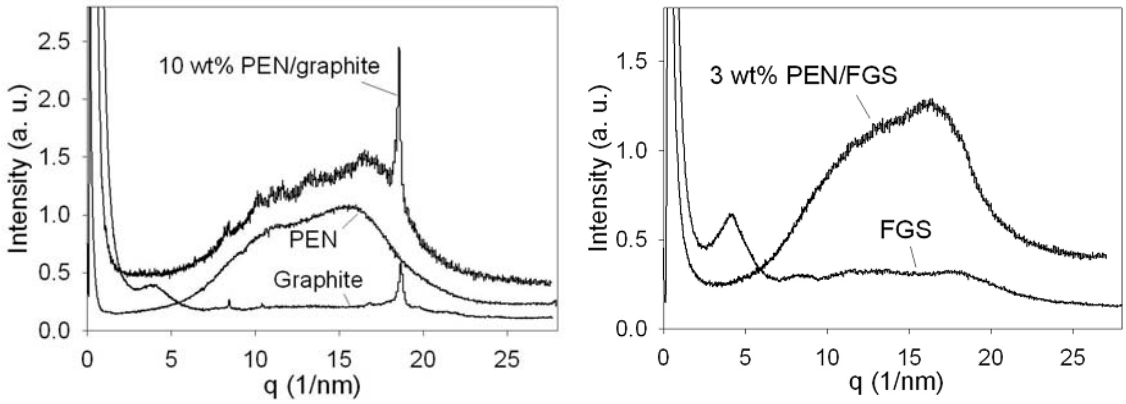

Figure 4-3. X-ray scattering intensity profiles of (a) graphite, PEN and PEN/graphite composite (10 wt%), (b) FGS and PEN/FGS composite (3 wt%). Scattering at $q \sim 4$ nm^{-1} in the profile of graphite and FGS is from Kapton tapes used for window materials.

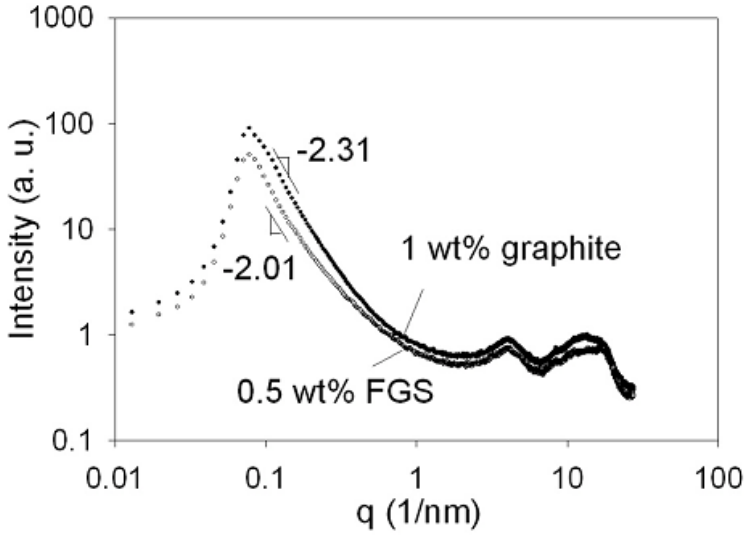

Figure 4-4. X-ray scattering profiles of 1 wt% graphite and 0.5 wt% FGS sample. Fractal dimensions of graphite and FGS were determined from the slope in the small angle range (q = 0.13 ~ 0.25 nm^{-1}). The beam block attenuated the intensity below q = 0.1 nm^{-1}. Scattering around $q \sim 4$ nm^{-1} is from Kapton tapes.

The slope of X-ray scattering intensity at small angles can give the dimension d_f of fractal aggregates.[18,42]

$$I(q) \propto \frac{1}{q^{d_f}} \tag{4.1}$$

Lower fractal dimension translates to a more open structure, thus higher level of dispersion. Figure 4-4 shows log scattering intensity vs. log q for dilute FGS and graphite composites. The fractal dimensions averaged over the lowest accessible q range, 0.13 ~ 0.25 nm^{-1} are 2.31 and 2.01, respectively. The aggregate structure at the length scale probed, ~ 10 nm, is less dense in FGS composites than in graphite composites.

4.4.4. Melt Rheology

Linear viscoelastic measurements were used to estimate fractal dimension and aspect ratio following the method developed by Vermant *et al.*[18] to study clay dispersion in polypropylene. The melt rheology results are summarized in Table 4-1 and 4-2 along with the other composite properties.

4.4.4.1. Melt Stability of PEN Composites

Figure 4-5 shows the change in the elastic modulus *G'* at 1 rad/s vs. annealing time at 290 °C. *G'* of the 2 wt% FGS composite displays about 40% growth with time and becomes constant by 2000 sec. This increase in elastic constant may be due to rebuilding via Brownian motion of a network structure which was disrupted during sample loading. However, it may also arise from molecular weight increase of PEN. It was previously reported that molecular weight of polyesters, including PEN, in the melt state grows as annealing proceeds under inert atmosphere via end group reactions.[43] Since the samples were stored at 120 °C for at least 48 hour before the testing, water content in PEN could be significantly reduced from its equilibrium value. Molecular weight will increase to the new equilibrium value by chain coupling.

Table 4-1. Properties of PEN/graphite Composites

Concentration		*Rheology*		*Surface resistance, R samples (B samples)*	*H_2 permeability*	*Tensile modulus*	*CTE*
		γ_{crit}	*G`* at 0.1 rad/s				
wt %	vol %*	%	Pa	Ohms	Barrer	GPa	$\times 10^5$ /°C
0	0	63	32.1	1.4×10^{13} (3.0×10^{12})	1.43	2.35	7.74
1	0.6	60	42.8	-	-	2.54	7.32
3	1.8	45	47.5	-	1.14	2.76	6.63
5	3.0	12	142	2.9×10^{12} (1.1×10^{12})	1.07	3.59	6.32
6	3.6	-	-	(1.4×10^{7})	-	-	-
7	4.2	0.56	4310	1.5×10^{12} (1.1×10^{7})	0.90	4.02	5.48
10	6.1	0.34	22500	5.1×10^{10}	0.76	4.52	4.60
15	9.3	0.24	84200	-	-	-	-
20	12.7	0.13	278000	(2.5×10^{5})	-	7.27	2.90

Table 4-2. Properties of PEN/FGS Composites

Concentration		*Rheology*		*Surface resistance, R samples*	*H_2 permeability*	*Tensile modulus*	*CTE*
		γ_{crit}	*G`* at 0.01 rad/s				
wt %	vol %*	%	Pa	Ohms	Barrer	GPa	$\times 10^5$ /°C
0.5	0.3	44	7.12	2.5×10^{13}	-	-	-
1.0	0.6	43	98.7	1.3×10^{9}	1.05	2.70	7.22
1.5	0.8	9.1	943	7.1×10^{7}	-	-	-
2.0	1.2	3.3	5870	1.1×10^{6}	-	-	-
3.0	1.8	1.1	33100	2.1×10^{5}	0.94	3.09	6.77
4.0	2.4	0.4	185000	2.6×10^{4}	0.61	3.69	6.71

* Note that volume fraction of graphite and FGS shown here is based on the amorphous density of PEN (1.33 g/cm^3), not its melt density (1.20 g/cm^3).

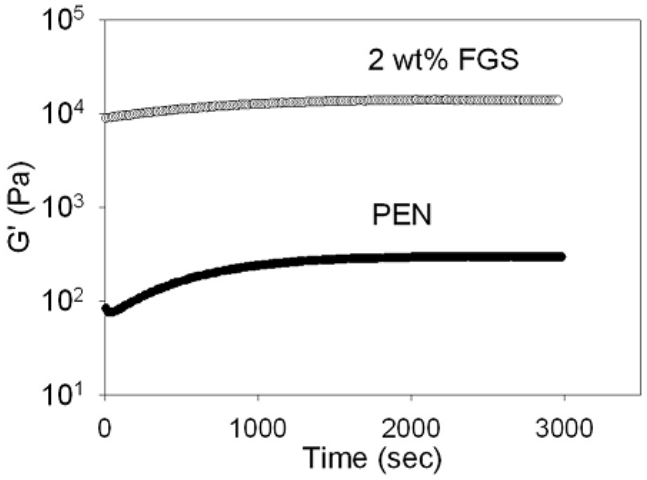

Figure 4-5. Evolution in *G'* at 1 rad/s for neat PEN and 2 wt% FGS at 290 °C with time after sample loading.

4.4.4.2. Linear Viscoelastic Response

After performing the time sweep until no significant change (change less than 2% within 10 min) in *G'* was observed, strain sweep tests at 290 °C were subsequently carried out to find the limit of linear viscoelasticity. Figure 4-6 shows that the critical strain, γ_{crit} decreases significantly with filler content. The reduction at lower volume fraction originates from individual aggregates which enhance straining in the surrounding media.[18,44] The critical strain decreases more dramatically when it reaches a critical volume fraction for both types of fillers. For the graphite/PEN system, γ_{crit} of the 7 wt% sample is 100 times smaller than that of 3 wt%, whereas such a large change is not observed from 0 to 3 wt%. (Figure 4-7) A similar drastic transition in the critical strain of FGS composites occurs near 1 wt% (0.5 vol%). Above this transition, γ_{crit} arises from the break-up of the connected network of FGS sheets reducing the elastic character of composite melts. At this higher volume fraction, critical strain tends to scale with a power of layered filler concentration.[18,21] The power law constant of this scaling is -3.08 for FGS and -1.24 for graphite (see Figure 4-7) indicating that the FGS network is much more strain sensitive.

(a)

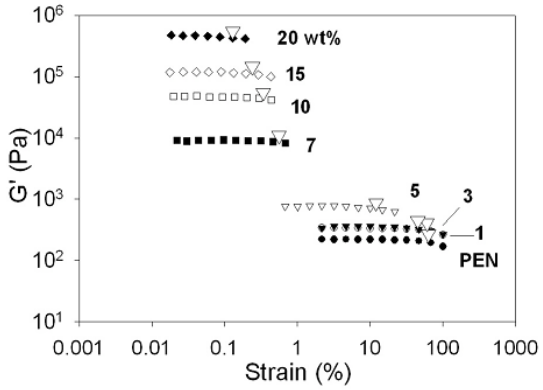

(b)

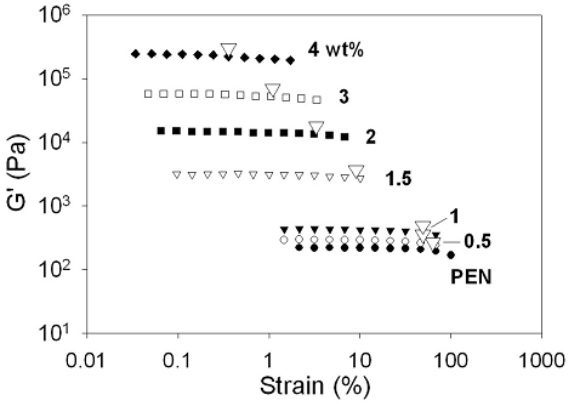

Figure 4-6. Dynamic strain sweeps of (a) graphite and (b) FGS composite melts at 290 °C. Critical strains, γ_{crit} determined by $G'/G'_0 = 0.9$ are marked with ∇.

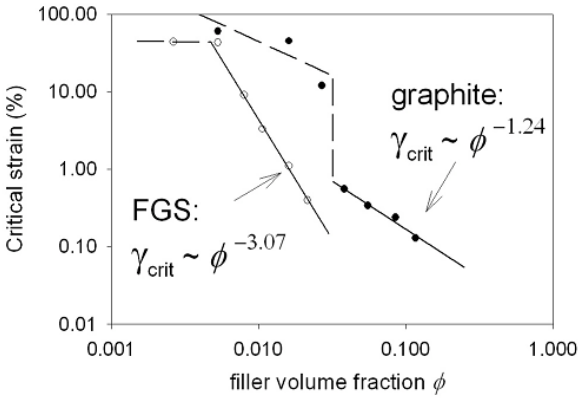

Figure 4-7. Scaling of critical strain at 1 rad/s of graphite (closed) and FGS (open symbols) composites melts.

(a)

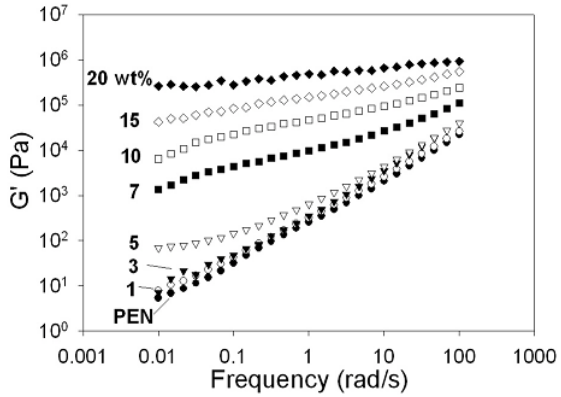

(b)

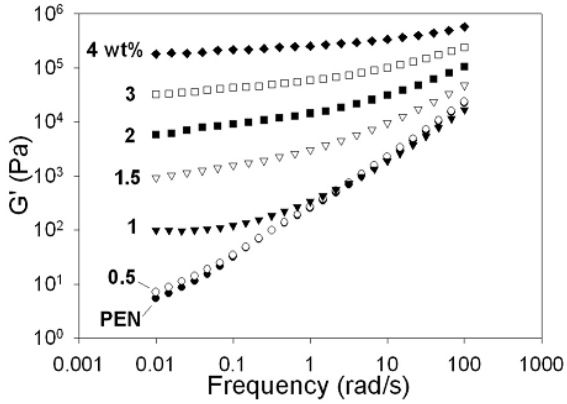

Figure 4-8. Dynamic frequency sweeps of (a) graphite and (b) FGS composite melts at 290 °C.

Dynamic frequency sweep tests were conducted at $\gamma < \gamma_{crit}$. Storage moduli of PEN and PEN composites at 290 °C are shown in Figure 4-8 as a function of frequency. For the entire range of frequency, *G'* increases with concentration of graphite and FGS. Neat PEN and composites with low graphite incorporation display terminal behavior down to lowest test frequency (~ 0.01 rad/s). At higher concentration than 5 wt% for graphite and 1 wt% for FGS, *G'* shows a plateau at low frequency, which is a characteristic response of solid-like materials.[14,15] Interestingly, the critical volume fraction where transitions from terminal to non-terminal behavior take place coincides with the volume fraction where critical strain starts to decrease more sensitively with

filler concentration. This coincidence implies that these two transitions stem from a common origin: formation of a space filling elastic network. Above this particular volume fraction, there is a significant reinforcement in elastic moduli at low frequency, and this growth in moduli with the volume fraction of the additive is more pronounced with increasing the concentration of FGS than that of graphite. An increase in *G'* to ~ 10^5 GPa at 0.01 rad/s is achieved by adding only 4 wt% of FGS, but a same increase in *G'* requires 15 ~ 20 wt% of graphite.

4.4.4.3. Analysis Based on Percolation Concepts

The elasticity of layered composite melts signifies the presence of a space filling rigid network which resists deformation. The elastic moduli of the percolated colloidal suspension can be expressed near the percolation threshold by a power law correlation on the difference between volume fraction of particles ϕ and the threshold value ϕ_{per}.[45-47]

$$G' \propto (\phi - \phi_{per})^{\nu} \tag{4.2}$$

Assuming the shear modulus of PEN dispersed with graphite and FGS follows this power law scaling, the percolation threshold ϕ_{per} and exponent ν of our system were evaluated by applying equation (4.2) to the *G'* value at ω = 0.1 rad/s for graphite and at 0.01 rad/s for FGS composites. When converting weight fraction to volume fraction, densities provided in Experimental section were used (ρ_{PEN} = 1.20 and $\rho_{graphite}$ = 2.28 g/cm^3). Least square regressions were carried out until optimum ϕ_{per} and ν were found that best fit the data. Figure 4-9 indicates that both systems exhibit power law dependence. The onsets of percolation determined by using the power law relationship are 0.024 (4.5 wt%) and 0.0027 (0.51 wt%) for graphite and FGS, respectively. For FGS, the onset of percolation of 0.27 vol% is close to the point where the critical strain starts to drop more sensitively (0.47 vol%) from Figure 4-7. The scaling exponents of graphite and FGS systems are 2.16 and 3.78. The lower volume fraction at the onset of rigidity percolation and the higher exponent of FGS confirm that FGS is much more effective in increasing viscoelasticity of PEN. Theoretically, the power law exponent for the rigidity percolation

of 3 dimensional networks is expected to be greater than 3.[47-49] Thus FGS/PEN fits rigidity percolation, but for graphite/PEN melts the exponent is smaller than 3. As shown in the frequency sweep results of graphite composites, slow relaxation takes place as frequency becomes smaller than 0.1 rad/s at higher loading (7, 10 and 15 wt%). We chose *G'* at 0.1 rad/s for the analysis. Therefore, it is possible that the elastic character of PEN/graphite networks is not truly reflected by *G'* at 0.1 rad/s. Also, graphite with a low aspect ratio may form an unstable transient network in the polymer host that does not transmit externally imposed load as efficiently as FGS.

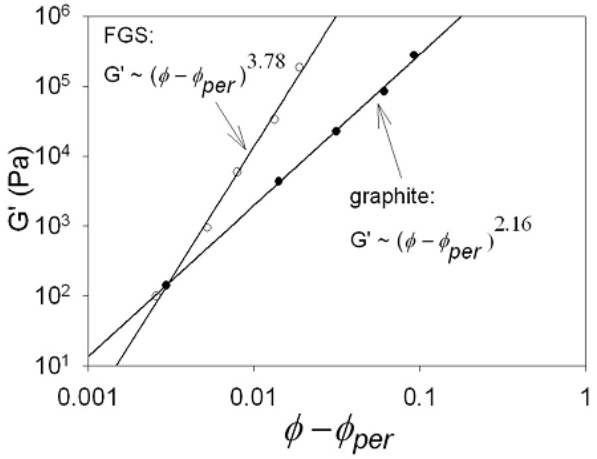

Figure 4-9. *G'* at ω = 0.1 rad/s for graphite (closed) and 0.01 rad/s for FGS (open symbols) vs. the difference between filler volume fraction and percolation volume fraction (ϕ_{perc} = 0.024 for graphite and 0.0027 for FGS).

The lower percolation threshold of FGS is strong evidence for better dispersion. Ren and coworkers showed that a relationship can be constructed between the percolation threshold and the aspect ratio, A_f of a tactoid.[17] Supposing imaginary spheres surrounding each tactoid, the expression for the ratio of particle diameter 2*r* to thickness *h* can be written as

$$A_f = \frac{2r}{h} = \frac{3\phi_{sphere}}{2\phi_{per}} \tag{4.3}$$

Percolation of interpenetrating, randomly packed spheres occurs at ϕ_{sphere} = 0.29.[50,51] Using the onsets of percolation of graphite and FGS from melt rheology (Table 4-3), equation (4.3) gives aspect ratios for graphite and FGS of 18 and 161, respectively. (see Table 4-4) Average aspect ratio of FGS determined by rheological measurements is about 9 times higher than that of graphite, which is in line with TEM and X-ray scattering results.

Table 4-3. Volumetric Percolation Threshold of Graphite and FGS Composites

	Graphite/PEN	FGS/PEN
From melt rheology	0.024	0.0027
From electrical conductivity	0.030 - 0.036	0.003 - 0.006

Table 4-4. Comparisons of Aspect Ratios of Graphite and FGS from Different Characterization Techniques

	TEM	*Melt rheology*	*Electrical conductivity*	*Hydrogen permeability*	*Tensile Stiffness*	Thermal Expansion
Graphite	21	18	~ 13	16	21	16
FGS	88	161	~ 100	55	32*	10*

* Note that these aspect ratio values were obtained using in-plane tensile modulus and CTE of graphite.

4.4.4.4. Analysis Based on Fractal Gel Concepts

Our graphite/PEN system has many similarities with a flocculated suspension: high viscosity and non-zero elastic modulus[52-55] and thus can be viewed as a colloidal gel. The scaling relationships between viscoelastic properties of colloidal gels and particle concentration proposed by Shih and coworkers[21] can be applied. Assuming the elastic network composed of graphite particles can be treated as fractal aggregates of graphite

flocs, their shear moduli, *G'*, and limits of linearity, γ_{crit}, above the gelation threshold can be scaled with the volume fraction of the flocs. When the bonds between flocs are stronger than the links within each floc,

$$G' \propto \phi^{(3+x)/(3-d_f)} \tag{4.4}$$

$$\gamma_{crit} \propto \phi^{-(1+x)/(3-d_f)} \tag{4.5}$$

where d_f is the fractal dimension of the aggregates and x is the fractal dimension of a backbone in the aggregate which is solely responsible for elasticity. In order to apply this model to our system, critical strains (Figure 4-6) and storage moduli at low frequency (Figure 4-8) above percolation threshold were chosen. As shown in Figure 4-7 and 4-9, *G'* and γ_{crit} scale with the filler volume fraction and more steeply with PEN/FGS than PEN/graphite. The *G'* scaling exponent of FGS composites is as high as 5.16, indicating the elastic network constructed with FGS is more efficient in storing elastic energy than that of graphite. The exponent of 5.16 for FGS composites is significantly higher than the scaling exponent reported for *G'* and the volume fraction of carbon nanotubes in polypropylene melts, ~ 2.8.[20] This large difference in scaling exponent implies that scaling behaviors depend on the dimensionality of reinforcing additives. Two dimensional platelets should be more advantageous in enhancing elastic modulus than one dimensional tubes.

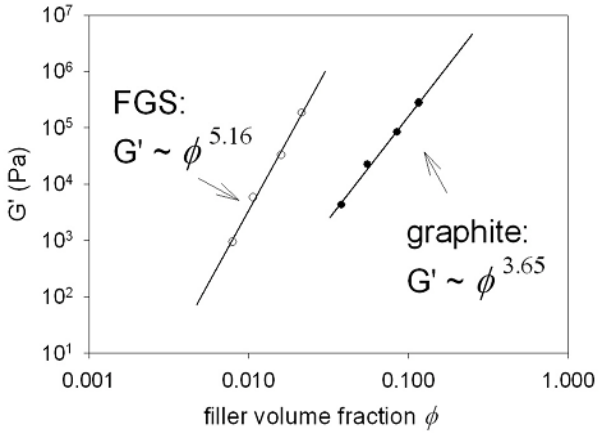

Figure 4-10. Scaling of *G'* at 0.1 rad/s for graphite (closed) and at 0.01 rad/s for FGS composites (open symbols) as a function of filler volume fraction.

Solving for d_f and x using equations (4.4) and (4.5) gives $d_f = 2.04$ for FGS, which is close to the value obtained from X-ray scattering analysis ($d_f = 2.01$). The relatively high backbone fractal dimension $x = 1.95$ suggests that most elements in a FGS floc contribute to the elasticity of the network. In other words, structural defects which are elastically inactive such as dangling ends rarely exist. For the graphite system, Shih's model gives $d_f = 2.17$. However, the backbone fractal dimension of graphite flocs x is near 0, which is not physically realistic. This may reflect instability in the graphite/PEN network, which is also indicated by the decreasing low frequency *G'* values in Figure 4-8 (a).

4.4.5. Electrical Conductivity Measurements

Graphite is very attractive for its potential to increase the electrical conductivity of insulating polymers at very low concentration. Also, the threshold concentration for electrical conduction provides another measure of graphite dispersion. The connectivity percolation from conductivity measurements is valuable since it can be used to examine the validity of rigidity percolation data from melt rheology.

Similar to the viscoelastic properties, the electrical conductivity of composites reinforced with anisotropic conducting materials is easily influenced by the deformation history. It has been noted that rheological and electrical properties of suspensions of carbon nanotubes can be altered drastically by flow.[19,20] Surface resistance of composites produced under three different processing conditions (D, F and B samples) are shown in Figure 4-11. At a certain concentration of graphitic reinforcements, resistance of PEN begins to drop precipitously. This transition indicates that graphite platelets provide connected pathways for electron transfer. The onset of electrical percolation clearly occurs at lower volume fraction for FGS, but there is an influence of the processing history in both. The thin, squeezed out, F samples exhibit a higher percolation threshold (graphite between 10 and 20 wt%, and FGS between 1.5 and 2 wt%) than the thicker, annealed disk, D samples (graphite between 5 and 7 wt%, and FGS between 0.5 and 1 wt%). The lower threshold of FGS can be explained by its higher aspect ratio. The higher

threshold for F samples is attributed to the alignment of platelets parallel to the film surface during compression molding and loss in connectivity between platelets due to these alignments. In contrast, the lower percolation threshold for D samples owes to the structure recovery during rheology testing at elevated temperature. B samples which were formed by molding, then annealing cryo-pulverized powders exhibit the lowest percolation (between 5 and 6 wt%) among graphite samples. This process may create the most disordered state of graphite orientation and help graphitic disks to maintain their contact with other platelets. Annealing under the quiescent condition for longer times could lead to an even lower percolation threshold.

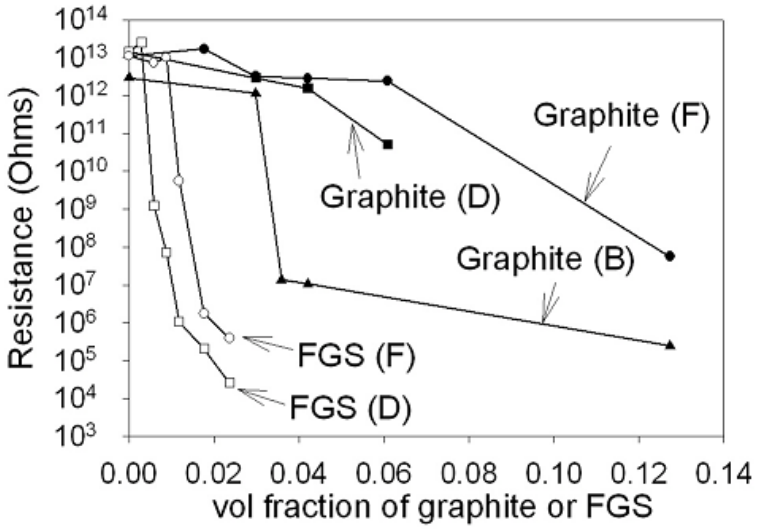

Figure 4-11. Surface resistance of graphite and FGS composites. D: ~ 1 mm thick disk shape samples after rheology tests with longer annealing history, F: ~ 70 μm thick biaxially squeezed film samples with filler orientation and B: bar shape samples (2 cm × 3 cm × 1 mm, molded from cryogenically pulverized powders and annealed 1 hr at 300 °C).

It is known that connectivity percolation takes place at a lower concentration of additives than rigidity percolation since networks that barely span the system volume may still have zero elasticity.[20,48,49,56] However, at least for our system, the threshold

volume fractions for electrical percolation are comparable to or even higher than the rigidity percolation determined by rheological measurements. (Table 4-3) For carbon nanotubes, Du and coworkers[19] showed that conductivity percolation was higher than rigidity percolation by rheology. They attribute this to polymer chains' bridging particles. In our case, the average diameter of the unperturbed PEN chains is approximately 16 nm,[57] which is greater than the distance for the electron tunneling to occur between graphite layers (~ 5 nm). Thus bridging may account for the even lower onset of rigidity percolation from melt rheology than connectivity percolation. It is also possible that small deformation of the D samples during unloading from rheometer plates and remelting caused graphite layers to be oriented again, which in turn reduces connectivity between them. Also, the contact resistance between the sample and probes can interfere with measuring conductivity of samples, especially with low graphite loading.[58]

4.4.6. Hydrogen Permeation

The high aspect ratio of graphitic additives suggests their potential use for reducing gas permeabilities of polymer films.[25,59] Gas permeability through a polymer filled with high aspect ratio, impermeable flakes can be decreased substantially via a reduced cross section for gas diffusion and a tortuous path mechanism.[60] After comparing several different models for gas permeability of membranes filled with aligned mono-dispersed impermeable disks, Picard *et al.*[13] found that the following model of Lape *et al.*[9] for flakes placed in random array describes the barrier performance of layered silicate nanocomposites most accurately:

$$\frac{P}{P_m} = \frac{1-\phi}{(1+A_f\phi/3)^2} \tag{4.6}$$

where P_m and P are permeabilities of gas molecules through unfilled and filled polymer membranes and ϕ is a volume fraction of disks. Since Lape's formula is a function of the aspect ratio, we can use it to evaluate dispersion. Hydrogen permeability at 35 °C through the 70 μm film samples (F samples) is shown in Figure 4-12 after converting filler weight fraction into volume fraction using the amorphous density of PEN (ρ_{PEN} = 1.33 and

$\rho_{graphite}$ = 2.28 g/cm^3). Both graphite and FGS reduce the hydrogen permeability of PEN. Fitting these data with Lape's model gives a higher aspect ratio for FGS (A_f = 55) than graphite (A_f = 16). The aspect ratio for FGS inferred is lower than one from TEM, A_f ~ 88, rheological measurements, A_f ~ 161 or electrical conductivity, A_f ~ 100 (Table 4-4). The barrier performance may be reduced by the defect vacancies in FGS sheets, produced by the superheating synthesis process (i.e. holes on the FGS surface).[61] Also, graphitic flakes are not perfectly aligned in the plane of the film contrary to the assumption of the composite theory.

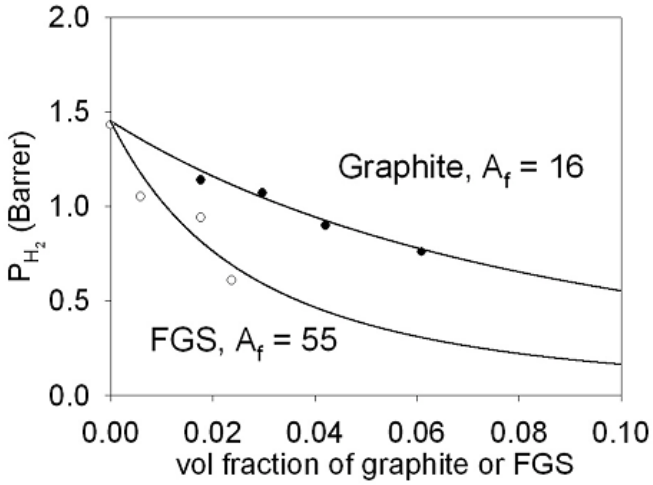

Figure 4-12. Hydrogen permeability of graphite (closed) and FGS (open symbols) composites at 35 °C. Curves represent theoretical trends based on Lape's model with A_f as an adjustable parameter.

4.4.7. Mechanical Properties

The exceptionally high stiffness and aspect ratio gives graphite potential for enhancing mechanical properties of polymers.[62] Tensile modulus and thermal expansion of PEN/graphite and PEN/FGS composites were measured and compared to composite theories. (see Table 4-1 and 2)

(a)

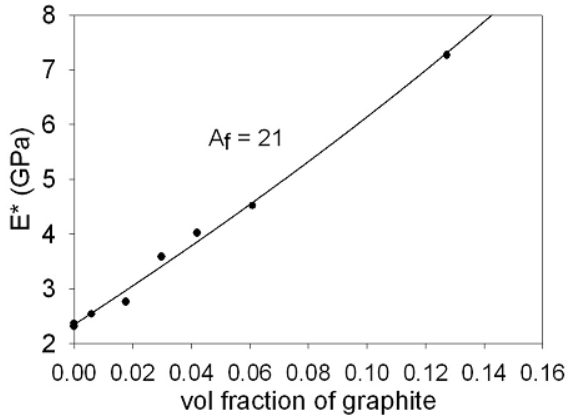

(b)

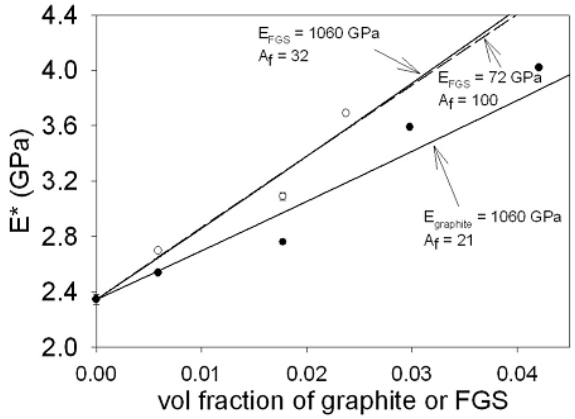

Figure 4-13. (a) Tensile moduli of graphite/PEN. (b) Moduli of graphite (closed) and FGS (open symbols) composites are compared at low filler concentration. Straight lines are predictions based on Mori-Tanaka theory. A dashed line shows how theoretical stiffness changes when in-plane tensile modulus and aspect ratio of FGS are changed to 72 GPa and 100, respectively.

4.4.7.1. Tensile Modulus

Embedding materials with high stiffness into polymers leads to an increase in material stiffness allowing for stress redistribution from a low modulus matrix to a high modulus filler phase.[63] Complex Young's moduli of composites from strain sweep tests are presented in Figure 4-13. While there were significant improvements in stiffness of

the composite from incorporating graphitic reinforcements, FGS turns out to be only slightly better than graphite in improving stiffness. For instance, the tensile modulus of 4 wt% (ϕ_{FGS} = 0.024) PEN/FGS composites is 3.7 GPa vs. 3.1 GPa for PEN containing 5 wt% graphite ($\phi_{graphite}$ = 0.030).

As mentioned in Section 3.4.7, the dispersion of layered nanocomposites can be analyzed quantitatively using micromechanical models for composite stiffness.[10,12] Mori and Tanaka showed that moduli of composites filled with unidirectionally aligned ellipsoids can be predicted when the stiffness and the Poisson's ratio of each component and the aspect ratio of reinforcement is known.[6] Tandon and Weng[7] adopted these ideas to derive analytical expressions for effective elastic moduli of composites which are transverse isotropic (see equation (3.1)). The experimentally measured Young's modulus of PEN (E_{PEN} = 2.35 GPa) and the literature modulus of graphite in the basal plane ($E_{graphite}$ = 1060 GPa)[31] were used for composite modeling based on equation (3.1). Poisson's ratios ν of PEN and graphite are 0.32 [64] and 0.006.[65] As pointed out by Cho *et al.*,[65] out of plane Poisson's ratio values of graphite determined either experimentally or theoretically vary over a wide range. However, whichever value is chosen for this analysis, there is no significant variation in predicted aspect ratio since the effect of Poisson deformation is negligible due to the small thickness of the platelets. The aspect ratio of graphite and FGS that best fit experimental results are 21 and 32, respectively.

While a higher degree of exfoliation for FGS is in agreement with results from other characterization techniques, an aspect ratio of 32 for FGS is much smaller than ones from rheology and conductivity measurements. It should be noted that for this analysis in-plane modulus of a single graphene sheet was assumed to be 1060 GPa, which may not be valid for FGS which have structural abnormalities (wrinkling and atomistic defects) that the stiffness modeling cannot account for. For the case of carbon nanotubes, the waviness of flexible additives is reported to significantly reduce the overall stiffness of their composites with polymers.[66] Also, the wrinkled structure of FGS will precipitously reduce the elastic modulus in tensile deformation since a main deformation mode under the extension will be bending of the crumpled sheets rather than stretching of or bending

between sp^2 hybridized C-C bonds. If we assume the aspect ratio of FGS evaluated from conductivity measurements is true ($A_f \sim 100$), from the Mori-Tanaka model the same extent of stiffening will be achieved when effective in-plane stiffness of FGS sheets is around 72 GPa (see Figure 4-13 (b)). Further study to determine the effective tensile stiffness of FGS will be required to obtain more accurate measures for the aspect ratio of these two dimensional thin sheets.

4.4.7.2. Thermal Expansion

Another advantage that can be expected from dispersing high aspect ratio rigid platelets with superior dimensional stability is a reduction in thermal expansion of polymeric materials.[25,67] Internal stress from a thermal expansion mismatch between two phases is transmitted across an interface minimizing the overall dimensional change of matrix material.[63] Thermal expansion coefficients are shown in Figure 4-14, and Table 4-1 and 2. The thermal expansion of PEN was suppressed by nearly the same amount, ~15%, by incorporating 3 wt% of graphite or FGS. The performance of FGS is surprisingly poor considering its high aspect ratio and the negative in-plane thermal expansion of graphite. The aspect ratio of both plate-like additives can be estimated based on a model proposed by Chow.[8,11] He used Eshelby's misfit theory[68,69] to derive theoretical predictions for coefficients of thermal expansion (CTE) of a polymer filled with aligned ellipsoids. The effective transverse CTE, α_{11} is

$$\alpha_{11} = \alpha_m + \frac{K_f}{K_m}\frac{(\beta_f - \beta_m)J_3\phi}{2I_1J_3 + J_1I_3} \tag{4.7}$$

where β_i and K_i are the volumetric thermal expansion coefficient and the bulk modulus of filler f or matrix m, respectively. I_j and J_j (j = 1 or 3) are functions of β_i, K_i, shear moduli G_i of each component, volume fraction of filler ϕ and elements of Eshelby's tensor. Exact formulas are found in Chow.[8] For PEN films, coefficients of thermal expansion in plane, $\alpha_{PEN//}$, and in thickness direction, $\alpha_{PEN\perp}$ are estimated to be 7.74×10^{-5} and 8.55×10^{-5} /°C, respectively from measurements with Rheometrics Solids Analyzer and Dynamic

Mechanical analyzer 7E (Perkin-Elmer). It is assumed that $\alpha_{//}$ and $\alpha_{\perp}$ are -1.5 × 10^{-6} /°C and 27 × 10^{-6} /°C for both graphite and FGS.[23,24] Summation of linear CTE's in three perpendicular directions ($\beta = 2\alpha_{//} + \alpha_{\perp}$ for transversely isotropic materials) gave the volumetric coefficients of thermal expansion, β of 2.4 × 10^{-4} for PEN, and 2.4 × 10^{-5} /°C for graphite and FGS. By approximating matrix and filler phase as isotropic, $G_{PEN} = E_{PEN}/2(1+\nu_{PEN}) =$ 0.89 GPa, $G_{graphite}$ = 527 GPa, $K_{PEN} = E_{PEN}/(3\text{-}6\,\nu_{PEN})$ = 2.17 GPa, and $K_{graphite}$ = 358 GPa.[63] Regression with experimental data using these material parameters suggest that the aspect ratios of graphite and FGS are 16 and 10, respectively. Theoretical modeling based on Chow's theory suggests that FGS only provides retraction in thermal expansion that is comparable with what rigid disks (E = 1060 GPa and $\alpha_{//}$ = -1.5 × 10^{-6} /°C) with aspect ratio of 10 potentially do. This low reinforcement efficiency of FGS is again probably due to the highly distorted and wavy structure of FGS which may render FGS less resistive to tensile deformation and thermal expansion than rigid graphite platelets. Moreover, it must be noted that the theory assumes perfect interfacial adhesion between the matrix and filler and unidirectional alignment of platelets.

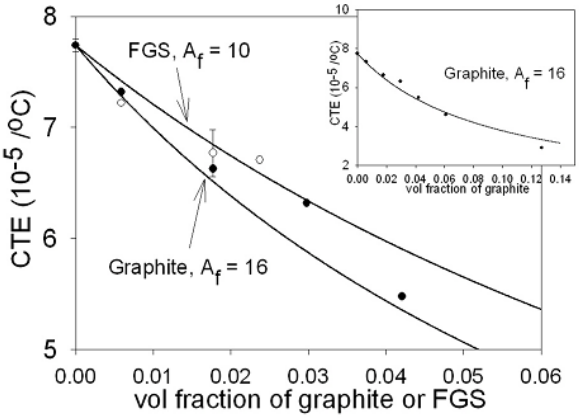

Figure 4-14. Coefficients of thermal expansion of graphite (closed) and FGS (open symbols) composites. Solid curves are model predictions based on Chow's theory with A_f as an adjustable parameter. The inset shows thermal expansion of graphite composites at higher graphite concentration.

4.5. Summary

FGS and graphite were melt blended into PEN using a small scale, twin screw extruder. Electron microscopy and X-ray scattering techniques were employed to investigate dispersion of graphite and FGS directly. Both methods demonstrated that FGS sheets form an exfoliated morphology (A_f = 88) in the PEN matrix after melt compounding, whereas graphite is incorporated as un-intercalated thick tactoids (A_f = 21). Melt rheology was also used to probe the microstructure of graphite and FGS in a PEN melt. Both graphite and FGS show linear viscoelastic behavior characterized by a reduction in critical strain and an increase in low-frequency shear modulus as the concentration of the reinforcement is increased. The extent of dispersion of both fillers was determined quantitatively from the critical percolation volume fraction. The aspect ratio of FGS (A_f = 161) from rheological measurements is substantially higher than that of graphite (A_f = 18), which agrees with TEM estimates. It is also consistent with the higher fractal dimension of graphite (d_f = 2.31) than FGS (d_f = 2.01) from X-ray scattering.

Electrical percolation data compared favorably with the threshold for rigidity percolation from rheological measurements for both fillers. A significantly lower electrical percolation threshold with FGS (ϕ_{per} ~ 0.003) compared with graphite (ϕ_{per} ~ 0.030) also confirmed better dispersion of FGS sheets. When we compare these with other systems, the onsets of rigidity and connectivity percolation for FGS are as low as those reported for carbon nanotube networks, ϕ_{per} ~ 0.003.[19,20] Gas barrier performance of composites reinforced with FGS was superior to that of graphite composites, and this was attributed to its higher aspect ratio. However, stiffness and dimensional stability gained by incorporating FGS are not as notable as the improvements of other properties. We believe that this is due to atomistic defects from oxidation and pyrolysis, and wrinkling of FGS sheets. These structural characteristics could reduce the effective tensile stiffness and thus reinforcement efficiency of FGS, in spite of its high aspect ratio. If graphite can be exfoliated and maintain its structural flatness and rigidity after the exfoliation,

mechanical and thermal properties may be enhanced. However, the wrinkled structure of FGS may be valuable in reducing reaggregation.

In summary, all the estimations for the dispersion of graphite platelets from characterization based on different physical phenomena agree quantitatively (A_f = 13 ~ 21) while aspect ratios of FGS spread over a wide range. (Table 4-4) As mentioned earlier, using the same in-plane stiffness and CTE for both graphite and FGS is problematic. Another reason for this large discrepancy among A_f values for FGS could be complexities associated with real composite morphology such as imperfect interfacial bonding, random orientation and size distribution of anisotropic fillers, that composite theories used in this study do not account for. Attempts to take these departures from ideality into account should be made to obtain more reliable measures for the dispersion of layered nanocomposites.

4.6. References

(1) Kim, H.; Macosko, C. W. *Macromolecules* **2008**, *41*, 3317-3327.

(2) Vaia, R. A.; Jandt, K. D.; Kramer, E. J.; Giannelis, E. P. *Macromolecules* **1995**, *28*, 8080-5.

(3) Lee, H.-S.; Fasulo, P. D.; Rodgers, W. R.; Paul, D. R. *Polymer* **2005**, *46*, 11673-11689.

(4) Vaia, R. A.; Jandt, K. D.; Kramer, E. J.; Giannelis, E. P. *Chem. Mater.* **1996**, *8*, 2628-2635.

(5) Dennis, H. R.; Hunter, D. L.; Chang, D.; Kim, S.; White, J. L.; Cho, J. W.; Paul, D. R. *Polymer* **2001**, *42*, 9513-9522.

(6) Mori, T.; Tanaka, K. *Acta Metall.* **1973**, *21*, 571-574.

(7) Tandon, G. P.; Weng, G. J. *Polym. Compos.* **1984**, *5*, 327-333.

(8) Chow, T. S. *J. Polym. Sci., Part B: Polym. Phys.* **1978**, *16*, 967-70.

(9) Lape, N. K.; Nuxoll, E. E.; Cussler, E. L. *J. Membr. Sci.* **2004**, *236*, 29-37.

(10) Fornes, T. D.; Paul, D. R. *Polymer* **2003**, *44*, 4993-5013.

(11) Yoon, P. J.; Fornes, T. D.; Paul, D. R. *Polymer* **2002**, *43*, 6727-6741.

(12) Sheng, N.; Boyce, M. C.; Parks, D. M.; Rutledge, G. C.; Abes, J. I.; Cohen, R. E. *Polymer* **2004**, *45*, 487-506.

(13) Picard, E.; Vermogen, A.; Gerard, J. F.; Espuche, E. *J. Membr. Sci.* **2007**, *292*, 133-144.

(14) Krishnamoorti, R.; Giannelis, E. P. *Macromolecules* **1997**, *30*, 4097-4102.

(15) Solomon, M. J.; Almusallam, A. S.; Seefeldt, K. F.; Somwangthanaroj, A.; Varadan, P. *Macromolecules* **2001**, *34*, 1864-1872.

(16) Jeon, H. S.; Rameshwaram, J. K.; Kim, G. *J. Polym. Sci., Part B: Polym. Phys.* **2004**, *42*, 1000-1009.

(17) Ren, J.; Silva, A. S.; Krishnamoorti, R. *Macromolecules* **2000**, *33*, 3739-3746.

(18) Vermant, J.; Ceccia, S.; Dolgovskij, M. K.; Maffettone, P. L.; Macosko, C. W. *J. Rheol.* **2007**, *51*, 429-450.

(19) Du, F.; Scogna, R. C.; Zhou, W.; Brand, S.; Fischer, J. E.; Winey, K. I. *Macromolecules* **2004**, *37*, 9048-9055.

(20) Kharchenko, S. B.; Douglas, J. F.; Obrzut, J.; Grulke, E. A.; Migler, K. B. *Nat. Mater.* **2004**, *3*, 564-568.

(21) Shih, W. H.; Shih, W. Y.; Kim, S. I.; Liu, J.; Aksay, I. A. *Phys. Rev. A* **1990**, *42*, 4772-9.

(22) Weick, B. L.; Bhushan, B. *IEEE Trans. Magn.* **1995**, *31*, 2937-9.

(23) Nelson, J. B.; Riley, D. P. *Proc. Phys. Soc.* **1945**, *57*, 477.

(24) Kelly, B. T. *Carbon* **1972**, *10*, 429-33.

(25) Kalaitzidou, K.; Fukushima, H.; Drzal, L. T. *Carbon* **2007**, *45*, 1446-1452.

(26) www.asbury.com, accessed Sept 15, 2007.

(27) Tamashuasky, A. V. In *National Lubricating Grease Institute 72nd Annual Meeting* San Antonio, TX, 2005.

(28) Brunauer, S.; Emmett, P. H.; Teller, E. *J. Am. Chem. Soc.* **1938**, *60*, 309-19.

(29) Schniepp, H. C.; Li, J.-L.; McAllister, M. J.; Sai, H.; Herrera-Alonso, M.; Adamson, D. H.; Prud'homme, R. K.; Car, R.; Saville, D. A.; Aksay, I. A. *J. Phys. Chem. B* **2006**, *110*, 8535-8539.

(30) www.vorbeck.com, accessed Sept 15, 2007.

(31) Kelly, B. T. *Physics of Graphite*; 1st ed.; Applied Science: London, 1981.

(32) Ouchi, I.; Aoki, H.; Shimotsuma, S.; Asai, T.; Hosoi, M. *Proc. Japan Cong. Mater. Res.* **1974**, *17*, 217-23.

(33) Mencik, Z. *Chem. Prum.* **1967**, *17*, 78-81.

(34) Buchner, S.; Wiswe, D.; Zachmann, H. G. *Polymer* **1989**, *30*, 480-8.

(35) Daubeny, R. d. P.; Bunn, C. W.; Brown, C. J. *Proc. Roy. Soc. (London)* **1954**, *A226*, 531-42.

(36) http://www.stelray.com/density_val.htm, accessed Sep 15, 2007.

(37) Pye, D. G.; Hoehn, H. H.; Panar, M. *J. Appl. Polym. Sci.* **1976**, *20*, 1921-31.

(38) Jeong, H.-K.; Krych, W.; Ramanan, H.; Nair, S.; Marand, E.; Tsapatsis, M. *Chem. Mater.* **2004**, *16*, 3838-3845.

(39) Kudin, K. N.; Ozbas, B.; Schniepp, H. C.; Prud'homme, R. K.; Aksay, I. A.; Car, R. *Nano Lett.* **2008**, *8*, 36-41.

(40) Bacon, G. E. *Acta Cryst.* **1951**, *4*, 558-61.

(41) Hontoria-Lucas, C.; Lopez-Peinado, A. J.; Lopez-Gonzalez, J. d. D.; Rojas-Cervantes, M. L.; Martin-Aranda, R. M. *Carbon* **1995**, *33*, 1585-92.

(42) Schaefer, D. W.; Justice, R. S.; Koerner, H.; Vaia, R.; Zhao, C.; Yang, M.; Vale, J. *Mater. Res. Soc. Symp. Proc.* **2005**, *840*, 57-62.

(43) Yoon, K. H.; Lee, S. C.; Park, I. H.; Lee, H. M.; Park, O. O.; Son, T. W. *Polymer* **1997**, *38*, 6079-6081.

(44) Ohl, N.; Gleissle, W. *J. Rheol.* **1993**, *37*, 381-406.

(45) Zosel, A. *Rheol. Acta* **1982**, *21*, 72-80.

(46) Wong, R. B. K.; Lelievre, J. *Rheol. Acta* **1981**, *20*, 299-307.

(47) Kanai, H.; Navarrete, R. C.; Macosko, C. W.; Scriven, L. E. *Rheol. Acta* **1992**, *31*, 333-44.

(48) Feng, S.; Sen, P. N. *Phys. Rev. Lett.* **1984**, *52*, 216-219.

(49) Thorpe, M. F. In *Physics of Disordered Materials*; Adler, D., Fritzsche, H., Ovshinsky, S., Eds.; Plenum Press: New York, 1985, p 55-61.

(50) Shante, V. K. S.; Kirkpatrick, S. *Adv. Phys.* **1971**, *20*, 325.

(51) Balberg, I. *Physical Review B* **1985**, *31*, 4053-4055.

(52) Patel, P. D.; Russel, W. B. *J. Rheol.* **1987**, *31*, 599-618.

(53) Heyes, D. M.; McKenzie, D. J.; Buscall, R. *J. Colloid Interface Sci.* **1991**, *142*, 303-16.

(54) Rueb, C. J.; Zukoski, C. F. *J. Rheol.* **1997**, *41*, 197-218.

(55) Rueb, C. J.; Zukoski, C. F. *J. Rheol.* **1998**, *42*, 1451-1476.

(56) Head, D. A.; Levine, A. J.; MacKintosh, F. C. *Phys. Rev. E* **2003**, *68*, 061907/1-061907/15.

(57) Since Mark-Houwink parameters for PEN in *o*-chlorophenol are not available, viscosity average molecular weight, M_v, of PEN is estimated to be 72 000 g/mol from the intrinsic viscosity (0.79 dl/g) using values for poly(ethylene terephthalate) in the same solvent ($k = 2.25 \times 10^{-4}$ dL/g and $a = 0.73$, Hergenrother, W. L.; Nelson, C. J. *J. Polym. Sci. Part A Polym. Chem.* **1974**, *12*, 2905). Assuming weight average molecular weight can be approximated by M_v and the polydispersity index is ~ 2 which is typical for condensation polymers gives number average molecular weight of 36 000 g/mol and average degree of polymerization of ~148. The theoretically estimated characteristic ratio ($C_r = \langle r^2 \rangle_0/(n\langle l^2 \rangle)$) of unperturbed PEN chains is 5.39 (Tonelli, A. E. *Polymer* **2001**, *43*, 637) and the length of PEN repeating unit, l, is 0.68 nm using group additivity. Thus, the average diameter of the random PEN coil (twice of radius of gyration, $2(\langle r^2 \rangle_0/6)^{0.5}$) is ~16 nm.

(58) Zimney, E. J.; Dommett, G. H. B.; Rouff, R. S.; Dikin, D. A. *Meas. Sci. Technol.* **2007**, *18*, 2067-2073.

(59) Matayabas Jr., J. C.; Turner, S. R. In *Polymer-Clay Nanocomposites*; Pinnavaia, T. J., Beall, G. W., Eds.; John Wiley & Sons: Chichester, 2000.

(60) Cussler, E. L.; Hughes, S. E.; Ward, W. J., III; Aris, R. *J. Membr. Sci.* **1988**, *38*, 161-74.

(61) Li, J.-L.; Kudin, K. N.; McAllister, M. J.; Prud'homme, R. K.; Aksay, I. A.; Car, R. *Phys. Rev. Lett.* **2006**, *96*, 176101/1-176101/4.

(62) Kalaitzidou, K.; Fukushima, H.; Drzal, L. T. *Composites: Part A* **2007**, *38*, 1675-1682.

(63) Hull, D.; Clyne, T. W. *An Introduction to Composite Materials*; 2nd ed.; Cambridge University Press: London, 1996.

(64) Ma, T.; Bhushan, B.; Murooka, H.; Kobayashi, I.; Osawa, T. *Rev. Sci. Instrum.* **2002**, *73*, 1813-1820.

(65) Cho, J.; Luo, J. J.; Daniel, I. M. *Compos. Sci. Technol.* **2007**, *67*, 2399-2407.

(66) Fisher, F. T.; Bradshaw, R. D.; Brinson, L. C. *Compos. Sci. Technol.* **2003**, *63*, 1689-1703.

(67) Yano, K.; Usuki, A.; Okada, A. *J. Polym. Sci., Part A: Polym. Chem.* **1997**, *35*, 2289-2294.

(68) Eshelby, J. D. *Proc. Roy. Soc. (London)* **1957**, *241*, 376-396.

(69) Eshelby, J. D. *Proc. Roy. Soc. (London)* **1959**, *252*, 561-569.

Chapter 5. Graphene/Polycarbonate Nanocomposite: Graphite Orientation

5.1. Overview

Previous chapters focused on determining the state of graphene dispersion from direct morphological characterization and indirect melt and solid property measurements. Graphene dispersion could be quantified using parameters such as average particle aspect ratio and cluster fractal dimension. Composite properties can be also influenced by the orientation of graphene disks inside the matrix. Even at the same volume fraction and dispersion level of reinforcements, solid or melt-state responses of composites may vary significantly depending on orientational state of particles. In this chapter, effects of flow induced graphite orientation on properties of polycarbonate (PC) are discussed. All results shown in this chapter are reproduced from an article previously published in Polymer.[1]

5.2. Introduction

Orientation of high aspect ratio particles plays an important role in composite properties. In-plane alignment of graphite ellipsoids are favored for improving mechanical and barrier properties in selected directions. Composite stiffness will be highest in a direction along which layers are oriented, whereas gas permeation will be lowest perpendicular to the orientation.[2,3] Property improvements that require rigidity and connectivity percolation of filler networks generally benefit from the random orientation.[4,5] Shear orientation of carbon nanotubes (CNT) or clay/polymer hybrid melts can change their viscoelastic behavior from solid to liquid-like.[4,6] Electrical conduction of anisotropic particle networks decreases as their orientation becomes more anisotropic.[5,7-9] Orientation eliminates contacts between neighboring particles destroying the continuous network needed to resist deformation or transfer charge carriers.

For the matrix material for studying orientation effects of graphene inside, PC was used. PC is one of the most important commodity polymers due to good mechanical and thermal properties, impact resistance and optical transparency. Its amorphous nature allows us to circumvent complexities of interpreting property changes associated with crystallization versus graphite addition. Its high melt stability prevents thermal degradation during prolonged rheological measurements. Pötschke and coworkers reported that electrical conductivity and melt viscoelasticity of PC could be modified significantly with small incorporation of carbon nanotubes (1 ~ 2 wt%).[10,11] Similar benefits are also expected from graphitic nano-platelets. We chose two graphite reinforcements that can lead to different states of dispersion: functionalized graphene sheets (FGS) and un-exfoliated flake graphite. After blending PC with graphite and FGS using melt compounding, orientation of graphite plates in samples was controlled via different types of post-processing: long-term annealing, compression and injection molding. Dispersion and orientation of graphite nano-fillers were characterized with electron microscopy and X-ray scattering. Their effects on melt viscoelasticity and electrical conductivity are also presented as well as tensile and bending moduli, thermal expansion and gas permeability.

5.3. Experimental

5.3.1. Materials

The matrix material used in this study was Calibre 201-22 PC resin from Dow Chemical. 201-22 is an injection molding grade[12] with a melt flow index of 22 g/10 min at 300 °C and its solid density is 1.2 g/cm^3. Polystyrene-calibrated number (M_n) and weight (M_w) averaged molecular weight of Calibre 202-22 are 27.1 and 50.4 kg/mol respectively, as determined by size exclusion chromatography (SEC) in chloroform. Pellets were dried in an oven at 90 °C at least for 24 hrs before melt processing. As additive particles, flake graphite (surface enhanced, grade # 3775) from Asbury Carbons,[13] which was also used for poly(ethylene-2,6-naphthalate) study (Chapter 4), was used. As reported in Chapter 4, specific surface area of the flake graphite is 29 m^2/g,

which is close to 24 m^2/g provided by the supplier and higher than that of typical natural graphite.[14] FGS provided by Vorbeck materials[15] was also used. Its BET surface area, ~ 800 m^2/g is substantially greater than that of graphite and within the range of 700 - 1500 m^2/g, an estimate by Schniepp and coworkers.[16]

Melt density of PC, ~ 1.1 g/cm^3 was calculated based on Bohlen and Kirchheim's volumetric expansion coefficient data.[17] Density of graphite, 2.28 g/cm^3 was estimated from unit cell dimensions of perfectly crystalline graphite:[18] FGS is assumed to have the same density. As discussed in Chapter 2, FGS is in a nearly fully exfoliated state with structural distortions (e.g. buckling) from oxidation and superheating.

5.3.2. Processing

Graphite and FGS were incorporated into PC by melt blending, using a DACA microcompounder, a small scale, conical, twin screw extruder with a recirculation channel.[19] PC blends containing 0, 1, 3, 5, 6, 7, 8.5, 10 and 12 wt% of graphite and 0.25, 0.5, 0.75, 1.0, 1.25, 1.5, 2.0, 2.5 and 3.0 wt% of FGS were prepared with the DACA extruder at 250 °C for 8 min under N_2 purge. Screw speed was 200 RPM. Due to the limited amount of FGS available to us, large scale twin screw compounding was carried out only with graphite. 200 ~ 250 g of PC pellets were physically mixed with 0, 1, 5 and 10 wt% of graphite by shaking them together in a plastic container. Graphite was added in ~ 1% excess by weight than calculated amount to compensate for losses in the feed hopper. They were loaded onto the hopper of a 16 mm co-rotating PRISM TSE 16TC twin screw extruder. Screws were configured with three kneading blocks and one back-mixing block separated by forward conveying zones.[20] Temperature was maintained at 250 °C in the mixing zones and the exit die, and 230 °C in the feeding zone. Screw speed was kept around 110 RPM in order not to exceed 75 ~ 90% of maximum allowed torque level (20 N·m). Extrudates were cooled in a water bath and dried by hot air before pelletized. SEC confirmed matrix molecular weights changed less than 2% during melt processing.

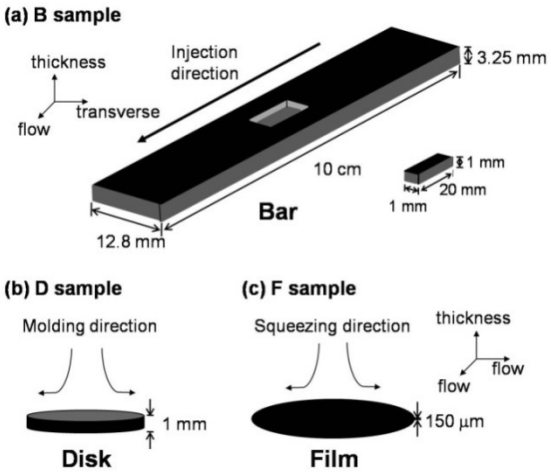

Figure 5-1. Sample geometries and definitions for 3 orthogonal directions for (a) B, (b) D and (c) F samples.

After melt processing, extruded materials were stored at 90 °C to prevent moisture inclusion. They were then molded into three different geometries (see Figure 5-1) in order to study the influence of processing on graphite orientation and composite properties. Sample geometries were 150 ~ 200 μm thick films (F samples), rectangular bars (10 cm × 3.25 mm × 12.8 mm, B samples) and 1 mm thick, 25 mm diameter disks (D samples). F samples were formed by placing DACA extrudates between Teflon coated aluminum foil in a hydraulic hot press at 260 °C and applying pressure (100 kPa) for 2 min. B samples were produced by ram injection molding (Morgan Press, Morgan Industries). 100 grams of twin screw extruded pellets were fed into the injection molder. The barrel, nozzle and mold temperature were set to 265, 275 and 135 °C, respectively. For samples with higher graphite concentration, higher processing temperature was required (for instance, 280, 290 and 145 °C for 10 wt% graphite samples) to facilitate mold filling. D samples were compression molded from DACA extrudates using disk-shaped molds and the hot press. After melting at 260 ~ 270 °C, they were pressed under 50 kPa pressure in the 1 mm thick molds for 2 min. D samples were annealed at 265 °C for 30 min. In order to reduce effects from orientation of graphite and FGS during compression molding, some disks were annealed longer at 230 ~ 250 °C for 24 ~ 48 hrs

under N_2 atmosphere using the environmental chamber of the rotational rheometer (ARES, TA Instruments).

5.3.3. Direct Characterization of Dispersion and Orientation

Dispersion of graphitic additives in PC matrix was characterized with transmission electron microscopy (TEM). PC composites containing 6 wt% graphite and 3 wt% FGS as DACA extruded were microtomed (Reichert Ultracut) at room temperature into 70 ~ 90 nm thick slices with a diamond knife and placed onto 400-mesh Cu grids. Micrographs were collected using a JEOL 1210 electron microscope at the accelerating voltage of 120 kV.

Wide angle X-ray scattering was conducted with a microdiffractometer (Bruker-AXS) and CuKα radiation (45 kV and 40 mA). 1 mm × 1 mm × 20 mm bar-shaped specimens (B and D samples) and 1 mm wide, 20 mm long films (F samples) were cut from the composite samples, and mounted in a 1/4 circle Eulerian sample holder. Due to the spatial variations of graphite orientation in the B samples, 1 mm thick bars were obtained from a fixed location, an outer skin at the center of the largest face (10 cm × 12.8 mm) as illustrated in Figure 5-1 (a). X-rays were directed in 3 different directions (flow, transverse and thickness) for B samples to probe graphite orientation. For F and D samples, only flow and thickness directions were used due to their transverse isotropy. All azimuthal scans in Figure 5-4 and 5-5 are shown after background subtraction using scattered intensity from neat PC samples with the same geometry.

5.3.4. Melt Rheology

Viscoelastic properties of the composite melts were studied with the ARES rheometer. 0.6 ~ 0.7 g of DACA extrudates were dried at 90 °C and placed on 25 mm parallel plates at 230 °C. After about 5 min heating, the upper plate was slowly lowered at 0.002 mm/s until the plates were ~ 1 mm apart. A "dynamic strain sweep" at frequency ω of 1 rad/s was used to find the critical strain γ_{crit} for linear viscoelasticity; γ_{crit} was the strain at which G' drops to 90% of its limiting low strain value. Then, "dynamic time

sweep" was run for 10,000 ~ 12,000 s at 0.1 rad/s to monitor changes in dynamic storage modulus *G'* and loss modulus *G''* versus time. Test strain was set at less than 10% of the critical strain before annealing to avoid shear induced orientation of graphite layers. After the time sweep, γ_{crit} after annealing was evaluated using a second strain sweep. A time sweep at 0.1 rad/s for 10,000 ~ 12,000 s followed to monitor the recovery of the graphite network disrupted by the large amplitude straining. Finally, a dynamic frequency sweep was conducted from 100 rad/s to 0.01 rad/s at $\gamma < \gamma_{crit}$. Occasionally, the length of the time sweep was doubled (t = 20,000 ~ 24,000 s) or extended to even longer to examine the effect of prolonged annealing on the structural evolution of the graphite networks. Results were reproduced in tests repeated with varying the gap between parallel plates, which confirms ~ 1 mm gap was large enough to ensure the sample uniformity. Note that the longest dimensions of particles (graphite : 10 ~ 1,000 nm and FGS : 50 ~ 400 nm) are significantly smaller than 1 mm.

5.3.5. Property Measurements

Surface resistance was measured using an 11-probe DC resistance meter (Prostat-801). Sample surfaces were polished ~ 10 μm deep with fine sandpaper (P600 grade) to reduce contact resistance. Resistance was obtained from 3 ~ 4 different areas near the center of as-squeezed F samples and annealed D samples and their geometric average values are reported. For B samples, the probe was placed at the center of the 10 cm × 12.8 mm plane, the same location where X-ray scattering specimens were obtained. Measurements were made on both unpolished and polished sides of B samples to find effects of polishing on the conductivity measurements.

Dynamic tensile and bending moduli of composite samples were measured with a Rheometrics Solids Analyzer II (RSA II). For tests in tensile mode, F samples were used due to their small sample thickness and high in-plane particle orientation. 5 mm wide and 30 mm long strips were cut from the films and clamped between film fixtures of the RSA II. Dynamic strain sweep tests at 1 rad/s were started from 0.002% strain under a static pretension of ~ 10 N to prevent sample buckling. For three point bending tests, we

used the injection molded bars (B samples). They were placed on two outer points which are 4.8 cm apart and deformed by the third central point from the opposite side. Dynamic strain sweeps from 0.002% were conducted under a static bending force of 20 N. For thermal expansion measurements, dimensional changes of F samples were traced while sequentially changing temperature from 65 to 50, 35 and 25 °C in the N_2 convection chamber of RSA II. Prior to the measurements, specimens were dried at 65 °C with N_2 dry purge for 3.5 hrs to exclude effects from hygroscopic expansion.

N_2 and He permeation coefficients through the film (F) samples were determined at 35 °C based on a constant volume-variable pressure method using a home-built gas permeation apparatus.[21,22] N_2 or He was introduced in one side of a 42 mm diameter composite disk at 1 atm; the opposite side was evacuated overnight. Permeability was calculated from the pressure change over time in the downstream compartment, pressure difference across the membrane (1 atm), and the sample thickness and area.

5.4. Results and Discussion

5.4.1. TEM Analysis

Figure 5-2 shows TEM micrographs of 6 wt% graphite/PC, and 3 wt% FGS/PC composites. In Figure 5-2 (a) and (b), only one or two graphite platelets (~ 40 nm thick) oriented perpendicular to the sample surface are visible over the entire imaging area (2 μm × 2 μm). During melt blending, there was no noticeable change in particle thickness from the average thickness of unmixed particles estimated from the BET surface area assuming disk-like particles (~ 30 nm) or from the thickness measured by AFM analysis (~ 37 nm, see Section 4.4.1). This indicates only breaking up of weakly aggregated graphite platelets took place during melt compounding. The multiple layer structure of graphite becomes more evident from the face-on view of a graphite particle in Figure 5-2 (c). The image is very dark indicating many graphene layers. In contrast, in the micrographs of FGS/PC, such dark images are never observed. Also, much thinner FGS layers (1 ~ 4 nm thick) are more evenly distributed despite their lower concentration (Figure 5-2 (d)). Considering the average thickness of fully exfoliated FGS layers, ~ 1.8

nm measured by Schniepp *et al.*, [16] or ~ 1.1 nm estimated from the BET surface area ~ 800 m^2/g of as-received FGS particles (Chapter 2), this range of thickness corresponds to a single or a few stacked sheets. Lateral dimensions of FGS appearing on micrographs are within the range of AFM estimates, 50 ~ 400 nm. It is noteworthy that edges of FGS sheets in Figure 5-2 (d) are aligned in one direction, which signifies a flow induced orientation during extrusion process. Higher magnification imaging reveals wrinkling of FGS layers (Figure 5-2 (f)). As suggested by Raman spectroscopy and XPS results in Chapter 2, planar graphene carbons (sp^2-hybridized) were transformed into out of plane ones (sp^3-hybridized) by surface oxygen functionalities (C-O and C-O-C), resulting in buckling of the sheets.

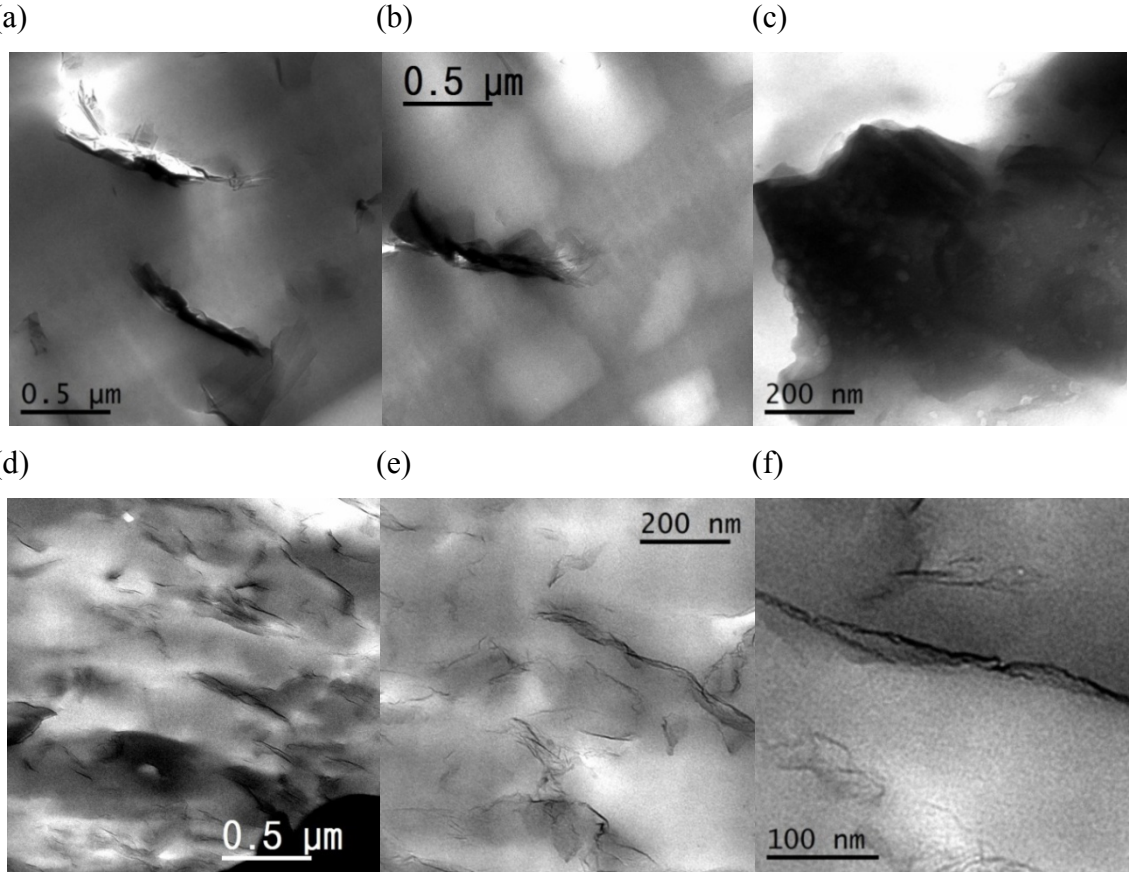

Figure 5-2. TEM micrographs of PC composites microtomed from microcompounder extrudates. 6 wt% graphite: (a) and (b) particles oriented edge on, and (c) particles face on. 3 wt% FGS: (d), (e) and (f).

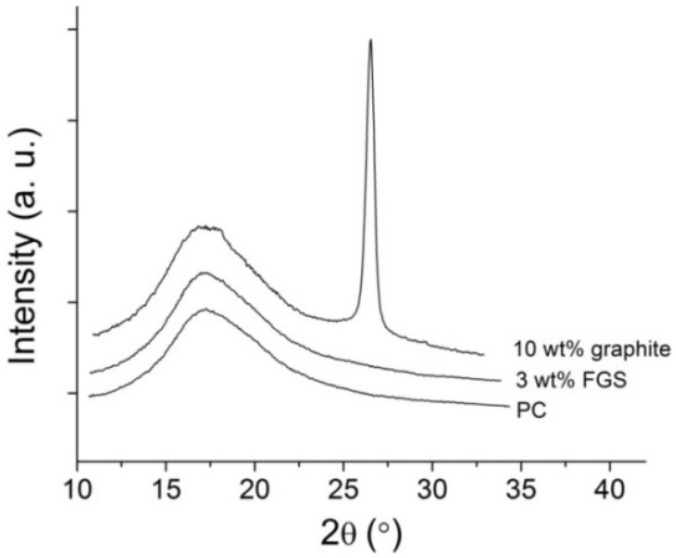

Figure 5-3. Scattering intensity profile of neat PC and 3 wt% FGS/PC as DACA extruded, and 10 wt% graphite/PC B sample from X-ray incident in transverse direction. Curves are offset vertically for clarity.

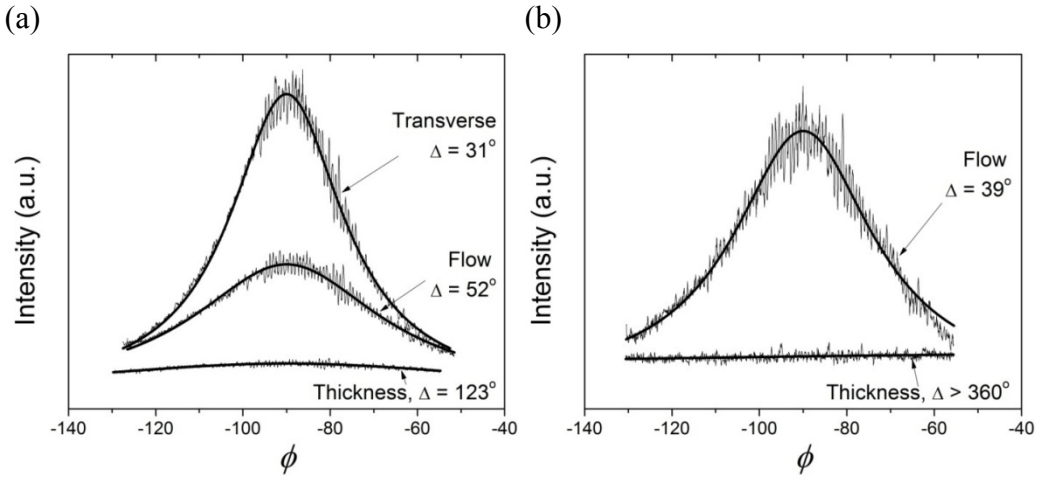

Figure 5-4. Azimuthal X-ray scattering scans (scattered curves) at 2θ = 26.4° ± 0.4 of (a) skin parts of 10 wt% graphite B samples and (b) 7 wt% graphite F samples with X-ray directions in flow, transverse and thickness direction. Fits (smooth curves) with the Lorentzian distribution function (equation (5.1)) are also shown.

5.4.2. X-ray Scattering

Dispersion and orientation of graphite in PC composites were analyzed from 2-dimensional X-ray scattering. When the intensity is integrated as a function of scattering angle 2θ, a sharp reflection is present at 2θ = 26.4° for graphite composites which corresponds to the interlayer spacing of un-intercalated graphite (d = 0.34 nm) while this peak is absent for FGS composites and neat PC (Figure 5-3). This corroborates the TEM results: after melt dispersion in PC, graphite remains highly layered while FGS is highly exfoliated. Regardless of their previous processing history, every graphite sample exhibited this reflection in its X-ray scattering pattern. There was also a variation in intensity depending on the azimuthal angle ϕ in the 2-D scattering profile along the semicircle of 2θ = 26.4°. Azimuthal scans integrated over 2θ = 26.0 – 26.8° of 10 wt% graphite B sample are shown in Figure 5-4 (a). In the scans of the flow and the transverse directions, scattering from graphite interlayer is strong and intensity is concentrated at ϕ = -90 °, indicating graphite platelets near the sample skin adopt in-plane orientation parallel to the surface (co-planar with transverse and flow direction). For D and F samples, X-ray was only directed along only 2 axes since these samples are transversely isotropic. Similar to the injection molded B samples, intensity is concentrated at ϕ = -90 ° from the X-ray scan in flow direction, implying graphite alignment parallel to the sample surface (Figure 5-4 (b) and Figure 5-5). Extent of alignment of anisotropic particles can be quantified by fitting scattering intensity distribution $I(\phi)$ with the Lorentzian function[4,8,23]

$$I(\phi) = \frac{1}{\pi} \frac{\Delta / 2}{(\phi - \phi_0)^2 + (\Delta / 2)^2} \tag{5.1}$$

where ϕ_0 and Δ are the center and a full width at half maximum (FWHM) of the distribution, respectively. As shown in Figure 5-4, FWHM, Δ of azimuthal scans in flow or transverse direction are all smaller than 90°. Shear and extensional flow of PC/graphite melt during injection and compression molding is expected to orient the platelets.

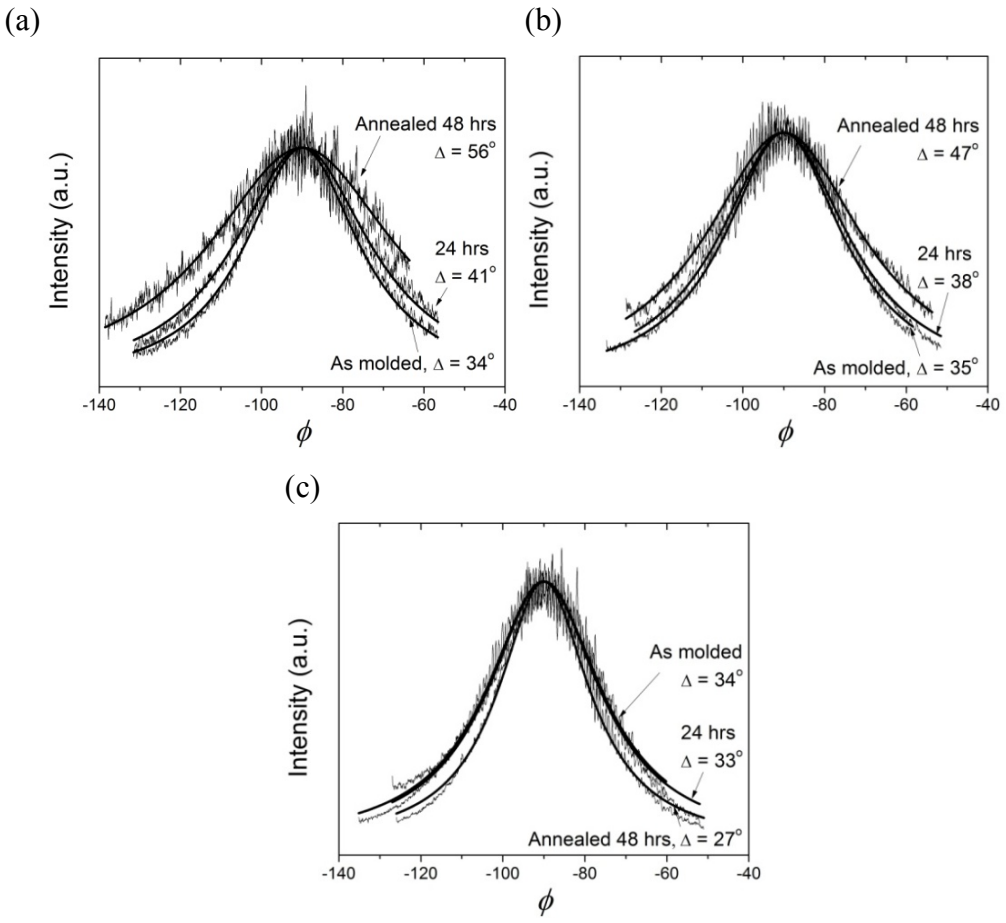

Figure 5-5. Azimuthal X-ray scattering scans (scattered curves) at 2θ = 26.4° ± 0.4 in the flow direction and Lorentzian fits (smooth curves) using equation (5.1) for (a) 3 wt%, (b) 7 wt% and (c) 12 wt% graphite/PC D samples with varying annealing time: 0, 24 and 48 hrs. For clarity, scattering intensities were scaled to give the same peak heights.

X-ray scattering experiments were also performed on as-molded and annealed graphite D samples with varying annealing times. Figure 5-5 shows the azimuthal scattering intensity profiles at $2\theta = 26.4°$, with X-ray along the flow direction, of 3, 7 and 12 wt% graphite/PC disks annealed at 230 °C for 0, 24 and 48 hrs. The as-molded samples all exhibit intensity maxima around $\phi = -90°$ indicating an anisotropic orientation of graphite. Spread in scattering intensity could be also quantified as the FWHM evaluated using equation (5.1). Quantified intensity spreads for as-molded disks are all

around $\Delta = 33 \sim 35°$ regardless of graphite concentration. In the case of 3 wt% graphite samples, this intensity concentration diminishes as annealing proceeds presumably due to particle disorientation. FWHM is relatively small before annealing, $\Delta = 34°$ and grows to $\Delta = 41°$ and 56° for samples annealed for 24 and 48 hrs, respectively. However, even after 48 hrs annealing, graphite orientation was not relaxed to the completely isotropic state indicating very slow disorientation processes. Although slower, the 7 wt% sample also displays a similar spread in scattering intensity over time: FWHM increases from 35° (as-molded) to 38° (24 hrs annealing) and 47° (48 hrs). However, the intensity scan of the 12 wt% sample barely changed with annealing. The FWHM turned out to be even smaller (33° and 27° for 24 and 48 hrs samples) than the un-annealed one (34°). This lack of disorientation processes in the 12 wt% sample can be explained by steric hindrance imposed by neighboring particles. Anisotropic inclusions such as rod-like or disk-like hard particles are known to form an ordered phase as the degree of anisotropy and volume fraction of particles increase.[24,25] Orientational freedom of these high aspect ratio platelets can be limited due to the volume excluded by particles in proximity. This is similar to the transition of discotic liquid crystals into the nematic phase. If, in fact, the 12 wt% graphite is in a nematic phase, an isotropic distribution will not be achieved even after prolonged annealing.

5.4.3. Melt Rheology

Linear viscoelastic properties of graphite/PC and FGS/PC composite melts were studied with shear rheometry. Figure 5-6 shows dynamic time sweeps of (a) graphite and (b) FGS composites. A time sweep for neat PC suggests a long-term thermal stability of PC melts. *G'* and *G''* of PC changed less than 5% over 30,000 s. Matrix M_n (~ 27.3) and M_w (~ 50.5 kg/mol) measured after the time sweeps were identical with those of as-received and as-extruded Calibre 201-22. However, graphite or FGS composites behaved differently depending on the amount of the reinforcement added. *G'* of PC containing 1 and 3 wt% of graphite remained nearly unchanged over 8,000 to 11,000 s (Figure 5-6 (a)). When graphite concentration was greater than 3 wt%, *G'* rose steadily over time. At

longer time scale (t > 7,500 s), logarithm of elastic modulus of 5, 7, 10 and 12 wt% samples grows almost linearly with logarithm of time, implying a power-law scaling ($G' \propto t^{\beta}$). The power-law exponent β evaluated at t = 7,500 – 10,000 s was highest for the 7 wt% sample. A similar trend was observed for FGS samples (Figure 5-6 (b)): *G'* of the sample with intermediate FGS concentration, 1.5 wt% increased faster than that of 1.0 and 2.5 wt% as suggested by the highest exponent determined at t = 15,000 – 20,000 s. It should be also noted that *G'* increase of 1.0, 1.5 and 2.5 wt% FGS samples is slower than that of 5, 7 and 10 wt% graphite samples.

(a)

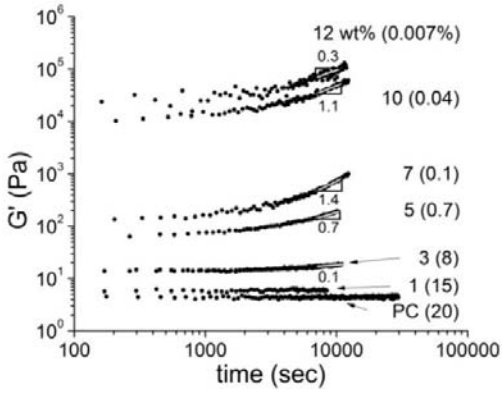

(b)

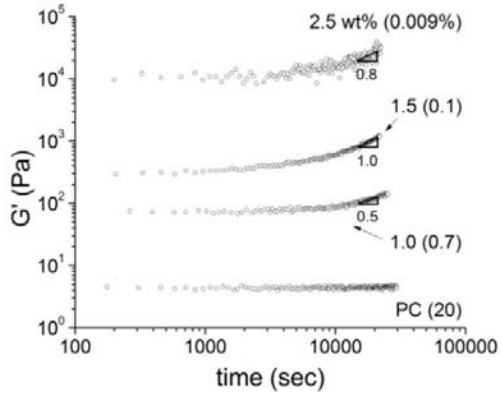

Figure 5-6. Dynamic time sweeps at 0.1 rad/s of (a) graphite/PC and (b) FGS/PC composites at 230 °C. Scaling exponents shown were evaluated at t = 7,500 - 10,000 s for graphite/PC and t = 15,000 – 20,000 s for FGS/PC composites. Values in parenthesis refer % test shear strains.

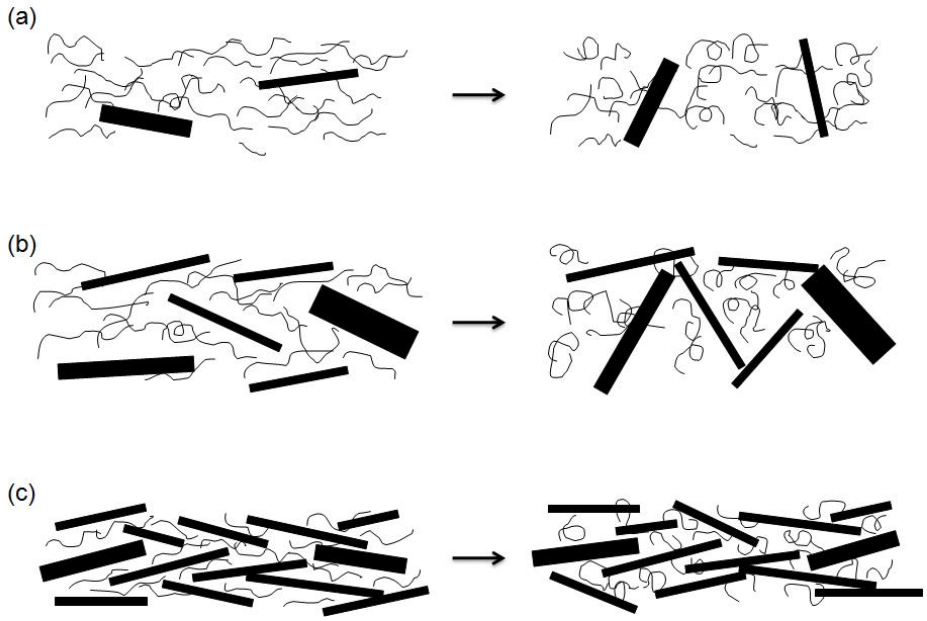

Figure 5-7. Disorientation mechanisms for graphite at (a) dilute, (b) semi-dilute and (c) concentrated regime.

This *G'* increase with annealing time can be explained by the increased effective volume of rotating disks[26] and the restoration of an elastic network[27] which was disturbed by the squeezing flow during sample loading. X-ray diffraction (Figure 5-5) showed that particles start to disorient after the cessation of the flow and that disorientation of particles depends on particle concentration.[28] As illustrated in Figure 5-7 (a), even complete randomization of particles at very dilute concentration will not result in particle contact since their spheres of rotation will not intersect. This can explain the weak or no increase in *G'* for PC melts with low graphite or FGS concentration: the number density of particles is not high enough to form a percolated network. When the particle concentration becomes greater (Figure 5-7 (b)), platelets can interact after the rotary relaxation via direct contacts or bridging by polymer chains, and build a sample spanning filler network, which gives rise to the elastic response to small amplitude shearing. However, in the concentrated regime, isotropic orientation cannot be achieved due to excluded volume interactions between particles. This is illustrated by the fact that

platelets in 12 wt% graphite samples remained correlated even after 48 hrs annealing (Figure 5-5 (c) and 5-7 (c)). Due to this confinement, *G'* rise of the 12 wt% sample is significantly slower than that of 5 and 7 wt%.

(a)

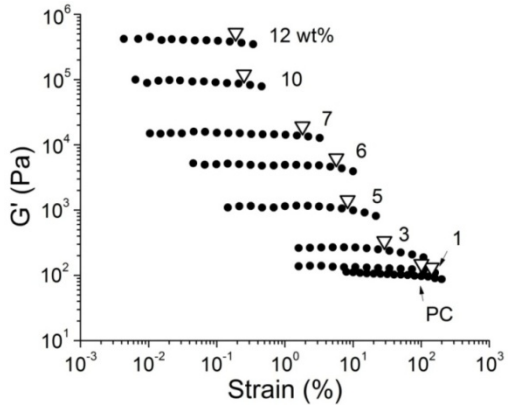

(b)

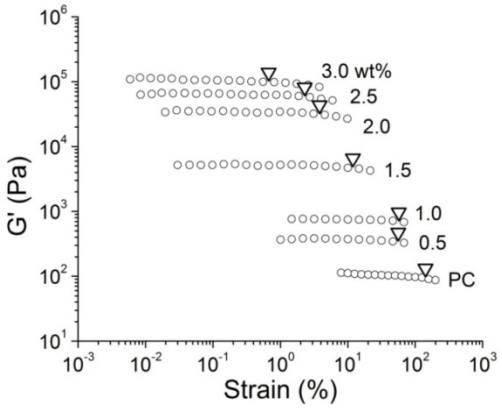

Figure 5-8. Dynamic strain sweeps at 1 rad/s of (a) graphite and (b) FGS/PC composites at 230 °C. Critical strains by the 90% rule are marked with ∇.

After this structure recovery by long-term annealing, dynamic strain sweeps were carried out. Figure 5-8 summarizes results from strain sweeps at 1 rad/s of (a) graphite and (b) FGS composites. This behavior is similar to flocculated gels.[29-31] Both graphite and FGS composites exhibit enhanced melt elasticity with increasing filler loading. They yield at large deformation, as characterized by a decline in *G'* with increased strain from

the critical strain values. Critical strain γ_{crit} decreases at higher amount of graphite or FGS, which indicates formation of more fragile filler networks. The decrease in yield strain becomes more pronounced from a certain volume fraction of inclusions: between 3 and 5 wt% for graphite and between 1.0 and 1.5 wt% for FGS. These volume fractions coincide with the onset concentrations where the marked increase in *G'* during the time sweep starts to be monitored, implying they stem from a common origin: percolation of graphite network.

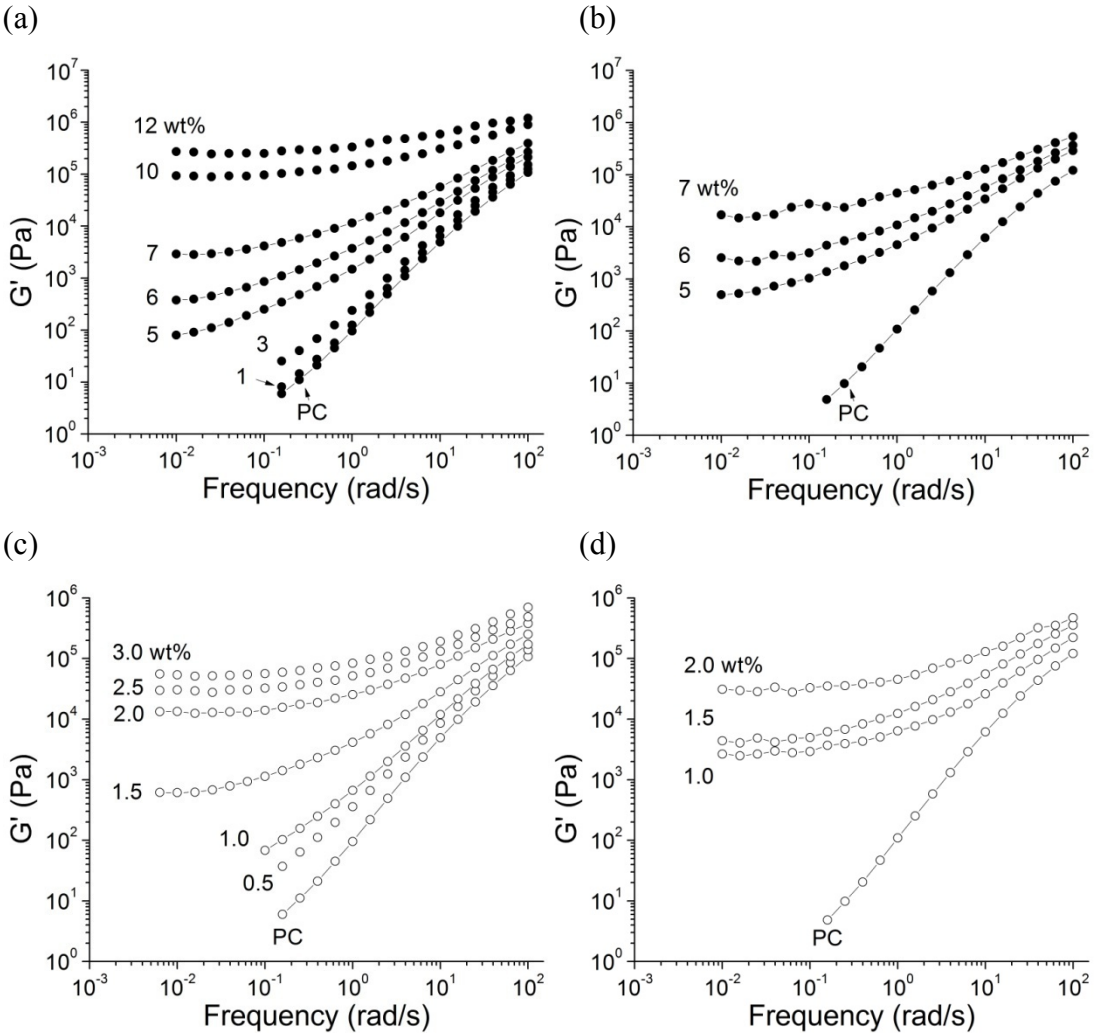

Figure 5-9. Dynamic frequency sweeps of graphite/PC melts after annealing for (a) 10,000 and (b) 20,000 s, and FGS/PC melts after annealing for (c) 10,000 and (d) 20,000 s at 230 °C.

Dynamic frequency sweeps of PC composites after another annealing period of 10,000 ~ 12,000 s are shown in Figure 5-9 (a) and (c). *G'* at low frequency becomes independent of the test frequency above a critical concentration, which is a typical solid-like response of layered nanocomposite melts[6,32-35] and indicates formation of a network of filler-filler contacts. The transition from terminal to non-terminal behavior occurs between 3 and 5 wt% for graphite and between 1.0 and 1.5 wt% for FGS. These critical volume fractions agree with the onset of rigidity percolation found with time and strain sweeps (Figure 5-6 and 5-8). From the percolation threshold ϕ_{per}, the particle average aspect ratio, A_f which is a ratio of diameter to thickness can be estimated assuming mono-dispersed disk-shaped particulates.[33,34,36] Using equation (4.3) with $\phi_{sphere} = 0.29$,[37] $\phi_{per, graphite} = 0.020$ (4 wt%) and $\phi_{per, FGS} = 0.006$ (1.25 wt%) gives $A_f \sim 22$ for graphite and ~ 72 for FGS. When converting the weight fraction to the volume fraction, densities of melt PC and graphite provided in Experimental Section were used. The higher aspect ratio of FGS agrees with the TEM results.

After loading and before each strain sweep and frequency sweep test, graphite and FGS were allowed to disorient for at least 10,000 s. However, Figure 5-6 indicates that network growth is incomplete as *G'* of PC composites continuously rises. Rheological measurements were repeated after extended annealing ($t \sim 20{,}000$ s) for samples near or above the rigidity percolation: 5, 6 and 7 wt% graphite and 1.0, 1.5 and 2.0 wt% FGS composites (Figure 5-9 (b) and (d)). *G'* is higher for all samples, especially at low frequency, implying the elasticity kept growing during the additional 10,000 s of annealing. The rheological behavior of 1.0 wt% FGS sample was altered most dramatically from terminal (Figure 5-9 (c)) to frequency-independent (Figure 5-9 (d)). It suggests the FGS network can expand to the entire sample volume even at 1.0 wt%. Percolation volume fraction of 1.0 wt% corresponds to the average A_f of 90 according to equation (4.3). A_f values for graphite and FGS from melt rheology are compared with ones from other composite property measurements in Table 5-1.

Table 5-1. Percolation Volume Fraction and Aspect Ratio of Graphite and FGS

Sample	Electrical conductivity		Melt rheology		Tensile modulus	Thermal expansion	N_2 permeation
	ϕ_{per}	A_f	ϕ_{per}	A_f	A_f	A_f	A_f
Graphite, D[a]	0.027 - 0.033	15	0.015 - 0.025	20	-	-	-
Graphite, F	0.047 - 0.055	9	-	-	19	19	11
FGS, D[a]	0.005 - 0.007	73	~ 0.005	90	-	-	-
FGS, F	0.008 - 0.011	46	-	-	21[b]	30[b]	51

[a] Note that the electrical percolation is from solid D samples annealed for 48 hrs and the rheological percolation is from frequency sweeps of melt samples following time sweeps for 20,000 s (Figure 5-9 (b) and (d)).

[b] Note that these aspect ratio values were obtained using in-plane tensile modulus and CTE of graphite.

Viscoelastic properties of polymer melts filled with anisotropic nano-particles can be greatly affected by flow.[4,6,9] Large strain shear or extensional flow may induce orientation of particles, and consequently a decrease in viscosity, storage and loss moduli of the suspension. A sequence of rheological tests on 0.5 wt% FGS/PC melts demonstrates dramatic changes in rheological responses depending on preceding flow history (Figure 5-10). A time sweep test was first conducted on 0.5 wt% FGS/PC. *G'* rose steadily over 40,000 s (1-DTS) and eventually appeared to level off in the semi-logarithmic (log *G'* – linear time) plot. A frequency sweep (2-DFS) following 1-DTS indicated the presence of elastic FGS networks as evidenced by *G'* independent of frequency for $\omega < 0.1$ rad/s. A significant drop in elasticity at large amplitude strain (> 1%) destroyed the fragile filler network (3-DSS). A series of strain sweeps (4, 5 and 6-DSS) up to higher strain was used to completely orient the FGS layers. Orientation of FGS was confirmed with a frequency sweep (7-DFS) which showed the terminal response down to 0.2 rad/s. Then, the sample was annealed for another 40,000 s (8-DTS in Figure 5-10 (a)). 8-DTS and 9-DFS show re-formation of a viscoelastic solid.

Rheological measurements demonstrate that these layered nanocomposite melts can undergo reversible changes between liquid-like and solid-like state influenced by the previous history, e.g. large amplitude deformation and long-term annealing.

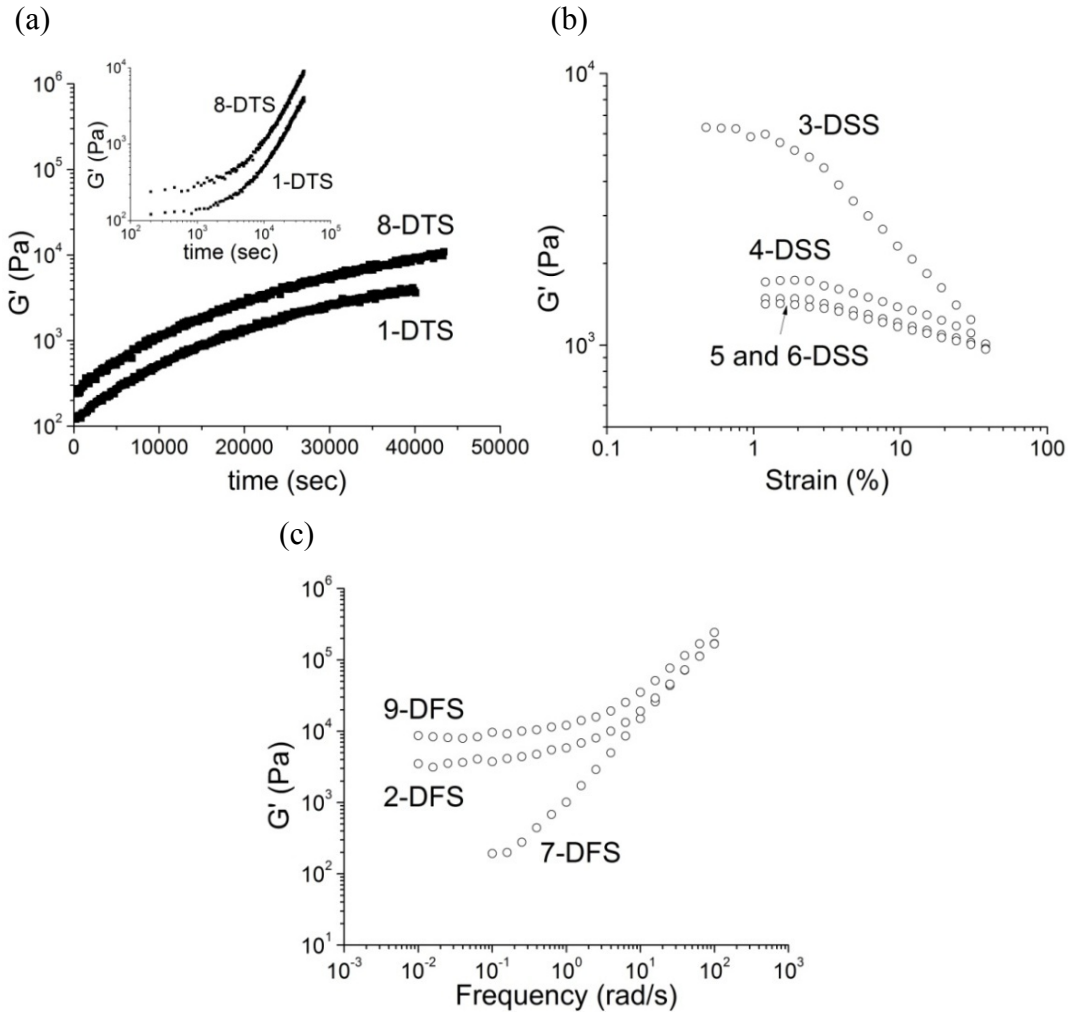

Figure 5-10. In the sequence 1 to 9, a single sample of 0.5 wt% FGS/PC was subjected to (a) dynamic time sweeps at 0.1 rad/s, (b) strain sweeps at 1 rad/s and (c) frequency sweeps at 230 °C. (a) The inset shows time sweep results in a double-logarithmic plot.

5.4.4. Mechanisms for Particle Disorientation

Randomization of nano-scale hard disks can be governed by either Brownian motions of particles,[28] or other non-Brownian interactions.[32,38-40] Rotary diffusivity D_r of a circular Brownian disk with a diameter d in a medium with a viscosity η at temperature T is[28,39]

$$D_r = \frac{3kT}{4\eta d^3} \tag{5.2}$$

Assuming a rigid disk with average diameter, 200 nm,[34] its rotary diffusion coefficient in PC at 230 °C (η_0^* = 4,000 Pa·s) is 1.6 × 10^{-4} s^{-1}. The rotational relaxation time $1/D_r$ = 60,000 s is on the order of the experimental time for FGS network formation (40,000 ~ 50,000 s) in the semi-dilute condition (0.5 wt%, Figure 5-10 (a)). In the case of layered silicate/polymer composites, particle reorganization takes place much faster via particle-particle[32] or particle-matrix[38,40] interactions than expected by Brownian dynamics. Ren and coworkers[39] reported that growth in *G'* of layered silicates in polystyrene melts displays a logarithmic scaling on time ($G' \propto t^{\beta}$) under low amplitude oscillatory shearing, which is similar to the aging kinetics of soft colloidal glasses after quenching below the glass transition.[41] They also found that the particle randomization lacked Brownian characters (i.e. dependence on temperature and matrix viscosity). In fact, modulus of PC composite melts also follows this scaling at t > 10,000 s signifying its analogy to aging colloidal glasses (Figure 5-6 and 10 (a) inset). Moreover, although particle disorientation was not detected from X-ray scattering for the 12 wt% graphite/PC melt, *G'* rose steadily implying the elasticity gain cannot simply be correlated with rotary relaxation of disks. Abou and coworkers[42] found that in aqueous suspensions of Laponite, an average relaxation time required for the escape of particles from "cages" formed by their neighbors via Brownian motions increases exponentially with the aging time. Likewise, as the system ages, the "cage diffusion" of graphitic particles will become more difficult, thus raising the viscoelasticity of the suspension.

5.4.5. Electrical Conductivity

The DC surface resistance of FGS/PC and graphite/PC composites with three different geometries (D, F and B samples) is tabulated in Table 5-2 and 3. Figure 5-11 shows how different types of graphite additives and processing influence the surface resistance of PC. While both graphite and FGS improve the electrical conductivity of PC implying electric percolation within the matrix, the resistance of FGS composites begins to decrease at much lower concentration.

Table 5-2. Solid Properties of PC/graphite Composites

Concentration		Surface resistance			Gas permeability		Modulus		CTE
					He	N_2	Tensile	Bending	
		F	D[a]	B	F		F	B	F
wt %	vol %	Ohms			Barrer		GPa	GPa	$\times 10^5$ /°C
0	0	1.3×10^{13}	8.8×10^{13}	5.5×10^{13}	12.5	0.36	2.08	2.58	7.89
1	0.5	2.8×10^{13}	5.1×10^{13}	4.3×10^{13}	-	-	2.16	2.76	7.56
3	1.6	-	7.7×10^{13}	-	10.6	0.32	2.45	-	6.70
5	2.7	-	3.7×10^{13}	3.4×10^{13}	9.32	0.31	2.50	3.21	6.28
6	3.3	-	1.4×10^{12}	-	-	-	-	-	-
7	3.8	3.5×10^{13}	1.7×10^{9}	-	8.61	0.26	2.96	-	5.43
8.5	4.7	7.8×10^{12}	1.9×10^{7}	-	8.02	0.26	3.36	-	5.85
10	5.5	7.3×10^{11}	3.3×10^{6}	7.6×10^{7}	7.29	0.21	3.69	4.23	4.57
12	6.7	1.5×10^{10}	3.4×10^{5}	-	6.82	0.23	4.16	-	4.89
15	8.5	1.6×10^{7}	7.8×10^{4}	-	-	-	5.17	-	3.53

[a] Annealed for 48 hrs.

Table 5-3. Solid Properties of PC/FGS Composites

Concentration		Surface resistance		Gas permeability		Tensile modulus	CTE
				He	N_2		
		F	D[a]	F		F	F
wt %	vol %	Ohms		Barrer		GPa	$\times 10^5$ /°C
0	0	1.3×10^{13}	8.8×10^{13}	12.5	0.36	2.08	7.89
0.25	0.13	-	1.8×10^{13}	-	-	-	-
0.50	0.26	7.2×10^{12}	2.4×10^{13}	11.5	0.33	2.15	7.17
0.75	0.40	-	1.9×10^{13}	-	-	-	-
1.00	0.53	9.8×10^{12}	2.4×10^{13}	-	-	2.22	7.07
1.25	0.66	-	3.3×10^{8}	-	-	-	-
1.50	0.80	7.3×10^{12}	1.6×10^{6}	10.2	0.30	2.27	7.11
2.00	1.06	1.1×10^{8}	8.0×10^{5}	9.7	-	2.51	6.64
2.50	1.33	6.4×10^{6}	6.6×10^{5}	8.9	0.24	2.51	6.73
3.00	1.60	2.8×10^{6}	2.0×10^{5}	8.8	0.20	-	-

[a] Annealed for 48 hrs.

As well as the state of dispersion, orientation of nano-fillers is also important for determining electrical conduction of composites.[8] We can see this by comparing electrical percolation and graphite orientation quantified with X-ray scattering of D and F samples. Threshold volume fraction ϕ_{per} of graphite and FGS for electric percolation was determined as the concentration of composites where their resistance decreases to 10% of the resistance of neat PC. These are summarized in Table 5-1 along with rheological percolation. The corresponding A_f values calculated using equation (4.3) are also shown. For both graphite and FGS composites, ϕ_{per} of F samples is substantially greater than that of D samples implying that flow during compression molding aligns the disk-like particles, losing connectivity between them. Percolation thresholds and A_f of D samples from conductivity and rheological measurements are in good agreement. As azimuthal X-

ray scattering scans suggest (Figure 5-4 and 5-5), graphite orientation in the annealed D samples is less pronounced than that in F samples. Therefore, electrical percolation of D samples better describes the level of dispersion since equation (4.3) assumes a perfectly random orientation of disks.

Note that resistance of the 10 wt% graphite B sample measured on the unpolished surface is significantly higher than for the polished surface (see the inset in Figure 5-11). A thin skin layer of PC formed during injection molding probably interfered with the conductivity measurements; removing ~ 10 μm thick skin exposed graphite particles to the surface.

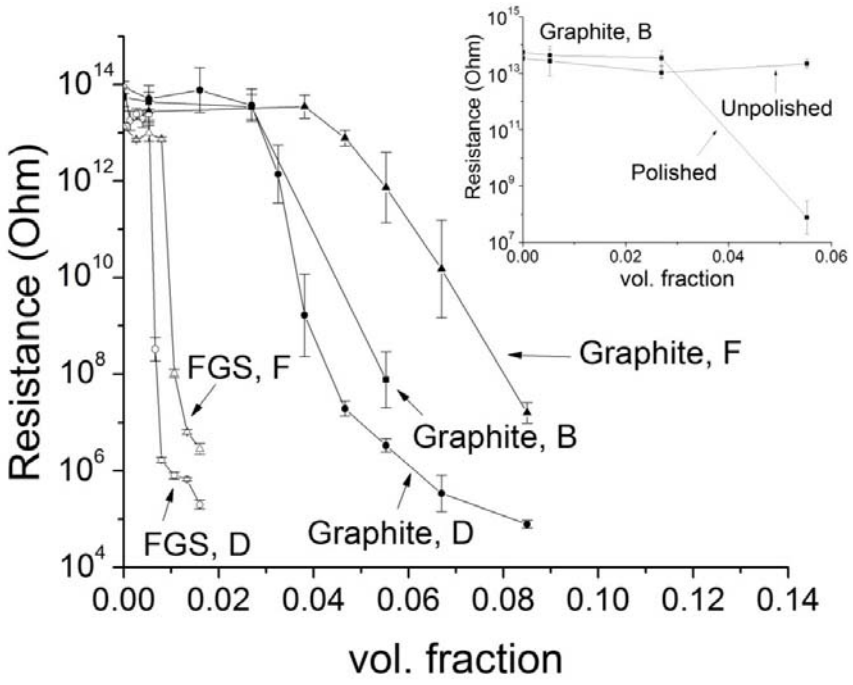

Figure 5-11. Surface resistance of graphite and FGS/PC composites. D: denoted by circles. ~ 1 mm thick disks annealed for 48 hrs at 240 °C. F: triangles. ~ 150 μm thick films from compression molding at 260 °C. B: rectangles. 10 cm × 3.25 mm × 12.8 mm injection molded bars. The inset compares resistance values measured on the polished surface and the unpolished surface of graphite B samples.

5.4.6. Mechanical Properties

Another benefit from graphite dispersion is that it can improve stiffness and dimensional stability of polymers substantially by small incorporation of nano-platelets with high aspect ratio and excellent in-plane mechanical properties.[34,43-46] Stiffness and thermal expansion of graphite/PC and FGS/PC composites were measured from dynamic mechanical analysis with RSA II and presented with other solid composite properties in Table 5-2 and 5-3.

(a)

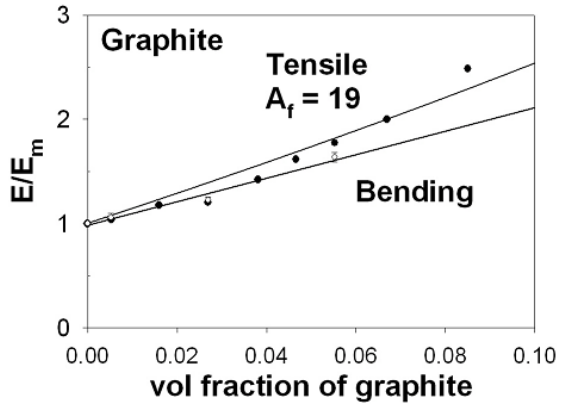

(b)

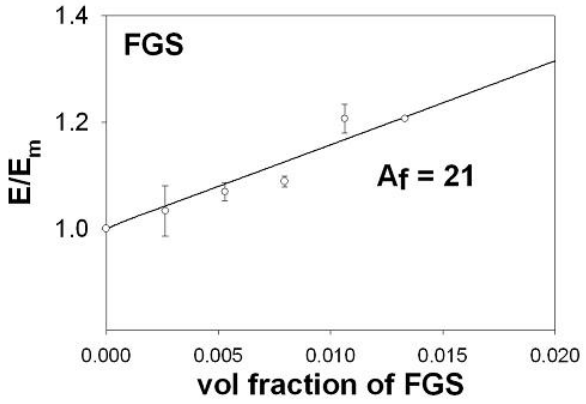

Figure 5-12. (a) Tensile (denoted by closed circles) and bending (open circles with error bars) modulus of graphite/PC composites normalized by stiffness of neat PC. A trend for tensile modulus based on the Mori-Tanaka theory and a linear fit of bending modulus data are also shown. (b) Tensile modulus of FGS/PC composites with a fit based on the Mori-Tanaka model as A_f an adjustable parameter.

5.4.6.1. Tensile and Blending Modulus

Figure 5-12 shows dynamic tensile and 3-point bending moduli of graphite composites and tensile moduli of FGS composites normalized by modulus of neat PC. Addition of either graphite or FGS increases the stiffness of PC. Young's modulus of 15 wt% graphite composites is ~ 150% higher than modulus of neat polymer (2.1 GPa). There is also a notable increase in bending stiffness of PC. Bending modulus of PC (2.6 GPa) was improved by ~ 60% by incorporating 10 wt% of graphite, which is a slightly less enhancement than that in tensile modulus (~ 80%) that same amount of graphite can offer. However, despite its higher aspect ratio, modulus gains by FGS are not significantly higher than ones by graphite. E of 2 wt% FGS composites (2.51 GPa) is slightly higher than that of 3 wt% graphite composites (2.45 GPa). Substantially greater modulus increase (~ 80%) by only 1 wt% of FGS was reported for poly(methyl methacrylate) (PMMA, E = 2.1 GPa) by Ramanathan and coworkers.[47] However, their composites were produced via solvent processing which generally leads to better dispersion than melt compounding. Also, the pendant carbonyl groups on PMMA are expected to have stronger interactions with polar oxygens on FGS surface.

Stiffness of composites reinforced with ellipsoidal inclusions can be predicted by a micromechanical model proposed by Mori and Tanaka[48] and Tandon and Weng[49] which were introduced in Chapter 3 and 4. Assuming graphite and FGS particles incorporated in PC can be approximated by ellipsoids, their average aspect ratio was estimated from equation (3.1) with matrix (E_{PC} = 2.1 GPa) and in-plane filler modulus ($E_{graphite}$ = 1060 GPa)[18,50], matrix (ν_{PC} = 0.37)[51] and filler Poisson's ratio ($\nu_{graphite}$ = 0.006).[52] The aspect ratio of graphite is 19, which is close to A_f from melt rheology and electrical conductivity measurements (Table 5-1). Although Poisson's ratio of graphite are reported in a wide range ($\nu_{graphite}$ = -0.171 – 4.958),[52] the result was not changed appreciably (A_f = 19 – 20) by using different reported $\nu_{graphite}$ due to small thickness of graphite. Note that the trend for bending stiffness of graphite composites shown in Figure 5-12 (a) is a linear fit, not based on the Mori-Tanaka theory. The average A_f of FGS from composite modeling is 21 which is far smaller than ones inferred via other characterization routes.

In Chapter 4, we reported this same low stiffening performance of FGS for poly(ethylene-2,6-naphthalate) and explained it by differences between graphite and FGS structure.[34] In Figure 5-2 (f), FGS appears to have an accordion-like structure composed of irregularly wrinkled sheets. FGS is formed by oxidation and superheating of graphite which may result in significant structural distortions such as sheet crumpling and atomistic vacancies.[53] Stiffening performance of graphene layers could be reduced by these processes since their main deformation mode under in-plane tensile stress will be straightening of wrinkled sheets rather than stretching of, or bending between C-C bonds, which accounts for the extremely high stiffness of planar graphene. Moreover, the high diameter to thickness ratio of FGS will render it more flexible than graphite. Graphene thin films, often called 2-dimensional macromolecules[54] can be frozen into a curved structure within the polymer matrix, which further reduces their effective stiffening efficiency. Schniepp *et al.* also found that folding of the sheets can be aided by pre-existing defect lines on FGS.[55] It should be also noted that Tandon and Weng assumed uni-directional alignments of mono-dispersed ellipsoids with perfect matrix adhesion, which is hardly realized in practice. Figure 5-4 (b) suggests that graphite orientation even in compression molded F samples is far from perfect in-plane orientation ($\Delta = 0°$). Deviation from the complete planar orientation can reduce composite modulus substantially.[56] Modulus estimation for PC composites containing 10 wt% ($\phi = 0.055$) of graphite platelets ($A_f = 20$) based on equation 13 in reference 56 and the Mori-Tanaka's theory suggests that tensile stiffness can vary from 3.26 for 3-dimensional random alignment to 3.84 Pa for unidirectional orientation.

5.4.6.2. Thermal Expansion

Coefficients of thermal expansion (CTE) of PC composites evaluated from dynamic temperature sweeps are shown in Figure 5-13. Substantial decrease in thermal expansion of PC is evident for both composites. This can be compared to Chow's micromechanical theory[57] which predicts transverse linear CTE of composites containing uni-directionally aligned mono-dispersed ellipsoidal dispersions (equation 4.7). For the

calculation of material parameters for CTE modeling such as volumetric thermal expansion coefficient and the bulk modulus of each phase, refer to Section 4.4.7.2. Assuming PC is isotropic, β_{PC} was estimated from experimentally measured linear CTE ($\alpha_{PC//} = \alpha_{PC\perp} = 7.9 \times 10^{-5}$ /°C). For graphite and FGS, $\alpha_{//} = -1.5 \times 10^{-6}$ and $\alpha_{\perp} = 27 \times 10^{-6}$ /°C.[58,59] Fitting the experimental data with Chow's model gives an average A_f of FGS (30), slightly higher than that of graphite (A_f = 19). While graphite shows a good agreement in A_f estimated from other techniques (Table 5-1), FGS turns out to be only marginally better than graphite in reducing thermal expansion of PC considering its high A_f. Again, we believe that the structural distortion and higher flexibility of FGS increase its effective thermal expansion.

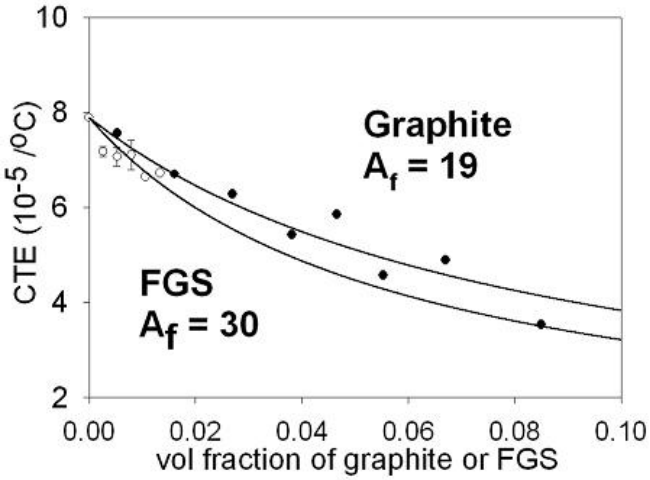

Figure 5-13. Coefficients of thermal expansion of graphite (closed) and FGS (open symbols) composites. Solid curves represent model predictions based on Chow's theory.

5.4.7. Gas Barrier Properties

Permeation rate of gas molecules diffusing through membranes can be decreased by embedding high aspect ratio, impermeable particles that provide tortuous paths and reduce the cross sectional area available for permeation.[60] Graphite can be a good candidate for these types of reinforcements due to its high aspect ratio.[34,44,61] N_2 and He permeation through PC films (F samples) reinforced with graphite and FGS were

evaluated at 35 ˚C (Figure 5-14). Permeability of neat PC is in close agreement with reported values (P_{He} = 13.6, P_{N2} = 0.29 Barrers at 35 ˚C).[62] While both additives are capable of suppressing N_2 and He permeation, the permeability of FGS composites is significantly smaller than that of graphite composites.

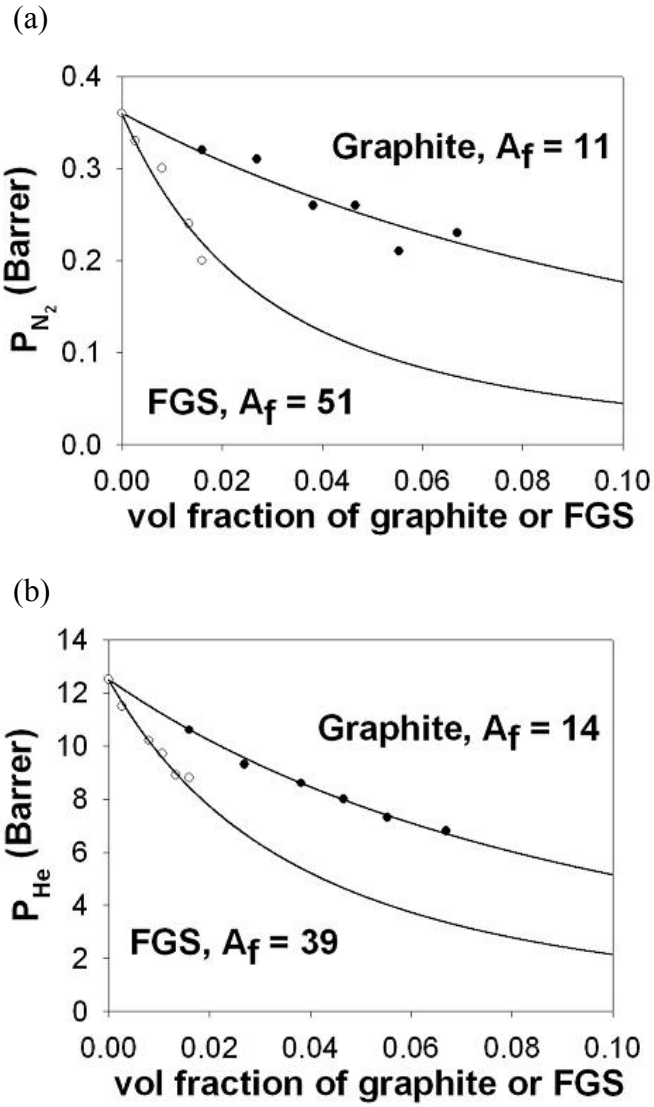

Figure 5-14. (a) N_2 and (b) He permeation constants of graphite and FGS/PC composites at 35 ˚C. Curves are predictions based on the model of Lape and coworkers.

Composite modeling based on Lape *et al.*[63] can be also performed to quantitatively estimate A_f from gas permeation data of composites.[34,64] Equation (4.6) predicts that graphite decreases gas permeation as much as impermeable flakes with A_f = 11 ~ 14, while for FGS A_f = 51 for N_2 permeation and 39 for He. Better dispersion for FGS is in line with observation from the other methods. However, the values of A_f for FGS (39 ~ 51) are lower than the values from melt rheology and electrical conductivity measurements (Table 5-1). Equation (4.6) assumes that embedded disks have perfect planar alignment. From the X-ray scattering results (Figure 5-4 (b)), some misalignment of graphite can be inferred, which potentially reduces the barrier efficiency of the composites.[3] For instance, the relative permeability (P/P_m) of PC filled with 3 wt% (ϕ = 0.016) graphene layers (A_f = 90) can vary between 0.57 (perfect planar alignment) and 0.79 (random orientation) based on equation 4 in reference 3. Interestingly, FGS appears to be slightly better for blocking diffusion of N_2 than He as the higher A_f from N_2 diffusion measurements suggests. On the FGS surfaces, there can be atomistic perforations that CO_2 evolution left during pyrolysis treatments, which more likely allow penetration of smaller molecules such as He than larger ones: the kinetic diameter of N_2 is 3.64 Å versus 2.89 Å for He.[65] Furthermore, increased free volume near the graphene-PC interface may selectively expedite transmission of smaller permeants.[66]

5.5. Summary

Graphite and thermally exfoliated graphite oxide (FGS) were blended into PC via melt extrusion. Electron microscopy and X-ray diffraction revealed un-intercalated morphology of graphite, while FGS appears to be highly exfoliated throughout the entire matrix. From 2-dimensional X-ray diffraction, flow induced orientation of graphite in compression or injection molded samples was also confirmed. While graphite orientation in dilute conditions can be relaxed toward an isotropic state by thermal annealing, particles at high concentration remain aligned even after prolonged annealing due to geometric restrictions.

Melt rheology was employed to investigate viscoelastic properties of the PC composites. After annealing for 10,000 s, both graphite and FGS in PC exhibit solid-like responses above rigidity percolation, which is between 3 and 5 wt% for graphite and 1.0 and 1.5 wt% for FGS. However, with extended annealing, even 0.5 wt% FGS composites become viscoelastic solids. Percolation concentration of 0.5 wt% is considerably lower than that of melt-mixed expanded graphite (~ 4 wt%)[35] or multi-walled carbon nanotubes (1 ~ 2 wt%)[10,11] in the same polymer. The 0.5 wt% FGS sample also shows interesting reversibility between liquid-like and solid-like behavior, affected by previous processing: long-term annealing and large amplitude shearing.

Surface resistance of PC composites starts to drop precipitously above connectivity percolation concentrations (6 wt% for graphite and 1.25 wt% for FGS) which are in agreement with the rigidity percolation from melt rheology. At the same filler concentration, electrical conductivity of squeezed films or injection molded samples is noticeably lower than annealed disks, which is attributed to alignment of graphitic platelets.

Both graphite and FGS lead to improved PC stiffness and dimensional stability. However, the increase in modulus and the decrease in CTE from FGS dispersion are not as significant as expected from the high aspect ratio found via percolation. Sheet wrinkling and atomistic defects on the surface after oxidation and pyrolysis treatments may account for its low performance in mechanical properties. N_2 and He permeability could be reduced by incorporation of graphite and FGS. Interestingly, FGS turns out to be more effective barrier against diffusing molecules with a larger kinetic diameter implying its potential for materials for gas separation.

We found a dramatic variation in composite properties which is influenced by both dispersion and orientation of graphitic reinforcements. In order to achieve highest property enhancements, morphology of polymer/graphite composites must be controlled properly. Even though higher aspect ratio of additives is favorable for most applications, high flexibility of thin sheets may reduce their stiffening performance. In applications that require good melt viscoelasticity and electrical conductivity, isotropic filler

orientation is desired. However, most conventional manufacturing processes such as injection molding and extrusion will orient graphite particles, which may improve stiffness and barrier properties in specific directions but also reduce electrical conductivity gains.

5.6. References

(1) Kim, H.; Macosko, C. W. *Polymer* **2009**, *50*, 3797-3809.

(2) Hull, D.; Clyne, T. W. *An Introduction to Composite Materials*; 2nd ed.; Cambridge University Press: London, 1996.

(3) Bharadwaj, R. K. *Macromolecules* **2001**, *34*, 9189-9192.

(4) Du, F.; Scogna, R. C.; Zhou, W.; Brand, S.; Fischer, J. E.; Winey, K. I. *Macromolecules* **2004**, *37*, 9048-9055.

(5) Celzard, A.; McRae, E.; Deleuze, C.; Dufort, M.; Furdin, G.; Mareche, J. F. *Phys. Rev. B: Condens. Matter* **1996**, *53*, 6209-14.

(6) Krishnamoorti, R.; Giannelis, E. P. *Macromolecules* **1997**, *30*, 4097-4102.

(7) Balberg, I.; Binenbaum, N. *Physical Review B* **1983**, *28*, 3799-3812.

(8) Du, F.; Fischer, J. E.; Winey, K. I. *Phys. Rev. B: Condens. Matter Mater. Phys.* **2005**, *72*, 121404/1-121404/4.

(9) Kharchenko, S. B.; Douglas, J. F.; Obrzut, J.; Grulke, E. A.; Migler, K. B. *Nat. Mater.* **2004**, *3*, 564-568.

(10) Potschke, P.; Fornes, T. D.; Paul, D. R. *Polymer* **2002**, *43*, 3247-3255.

(11) Potschke, P.; Dudkin, S. M.; Alig, I. *Polymer* **2003**, *44*, 5023-5030.

(12) http://automotive.dow.com/materials/products/calibre/201.htm, accessed January 10, 2008.

(13) www.asbury.com, accessed January 10, 2008.

(14) Tamashuasky, A. V. In *National Lubricating Grease Institute 72nd Annual Meeting* San Antonio, TX, 2005.

(15) www.vorbeck.com, accessed January 10, 2008.

(16) Schniepp, H. C.; Li, J.-L.; McAllister, M. J.; Sai, H.; Herrera-Alonso, M.; Adamson, D. H.; Prud'homme, R. K.; Car, R.; Saville, D. A.; Aksay, I. A. *J. Phys. Chem. B* **2006**, *110*, 8535-8539.

(17) Bohlen, J.; Kirchheim, R. *Macromolecules* **2001**, *34*, 4210-4215.

(18) Kelly, B. T. *Physics of Graphite*; 1st ed.; Applied Science: London, 1981.

(19) Maric, M.; Macosko, C. W. *Polym. Eng. Sci.* **2001**, *41*, 118-130.

(20) Spitael, P.; Macosko, C. W. *Polym. Eng. Sci.* **2004**, *44*, 2090-2100.

(21) Pye, D. G.; Hoehn, H. H.; Panar, M. *J. Appl. Polym. Sci.* **1976**, *20*, 1921-31.

(22) Jeong, H.-K.; Krych, W.; Ramanan, H.; Nair, S.; Marand, E.; Tsapatsis, M. *Chem. Mater.* **2004**, *16*, 3838-3845.

(23) Haggenmueller, R.; Gommans, H. H.; Rinzler, A. G.; Fischer, J. E.; Winey, K. I. *Chem. Phys. Lett.* **2000**, *330*, 219-225.

(24) Forsyth, P. A., Jr.; Marcelja, S.; Mitchell, D. J.; Ninham, B. W. *Adv. Colloid Interface Sci.* **1978**, *9*, 37-60.

(25) Davis, V. A.; Ericson, L. M.; Parra-Vasquez, A. N. G.; Fan, H.; Wang, Y.; Prieto, V.; Longoria, J. A.; Ramesh, S.; Saini, R. K.; Kittrell, C.; Billups, W. E.; Adams, W. W.; Hauge, R. H.; Smalley, R. E.; Pasquali, M. *Macromolecules* **2004**, *37*, 154-160.

(26) Bonn, D.; Kellay, H.; Tanaka, H.; Wegdam, G.; Meunier, J. *Langmuir* **1999**, *15*, 7534-7536.

(27) Alig, I.; Skipa, T.; Lellinger, D.; Poetschke, P. *Polymer* **2008**, *49*, 3524-3532.

(28) Larson, R. G. *The Structure and Rheology of Complex Fluids*; Oxford Press: New York, 1999.

(29) Mewis, J.; Spaull, A. J. B. *Adv. Colloid Interface Sci.* **1976**, *6*, 173-200.

(30) Patel, P. D.; Russel, W. B. *J. Rheol.* **1987**, *31*, 599-618.

(31) Rueb, C. J.; Zukoski, C. F. *J. Rheol.* **1997**, *41*, 197-218.

(32) Solomon, M. J.; Almusallam, A. S.; Seefeldt, K. F.; Somwangthanaroj, A.; Varadan, P. *Macromolecules* **2001**, *34*, 1864-1872.

(33) Vermant, J.; Ceccia, S.; Dolgovskij, M. K.; Maffettone, P. L.; Macosko, C. W. *J. Rheol.* **2007**, *51*, 429-450.

(34) Kim, H.; Macosko, C. W. *Macromolecules* **2008**, *41*, 3317-3327.

(35) Abdel-Goad, M.; Poetschke, P.; Zhou, D.; Mark, J. E.; Heinrich, G. *J. Macromol. Sci., Part A: Pure Appl. Chem.* **2007**, *44*, 591-598.

(36) Ren, J.; Silva, A. S.; Krishnamoorti, R. *Macromolecules* **2000**, *33*, 3739-3746.

(37) Shante, V. K. S.; Kirkpatrick, S. *Adv. Phys.* **1971**, *20*, 325.

(38) Schmidt, G.; Nakatani, A. I.; Butler, P. D.; Karim, A.; Han, C. C. *Macromolecules* **2000**, *33*, 7219-7222.

(39) Ren, J.; Casanueva, B. F.; Mitchell, C. A.; Krishnamoorti, R. *Macromolecules* **2003**, *36*, 4188-4194.

(40) Lele, A.; Mackley, M.; Galgali, G.; Ramesh, C. *J. Rheol.* **2002**, *46*, 1091-1110.

(41) Bonn, D.; Tanase, S.; Abou, B.; Tanaka, H.; Meunier, J. *Phys. Rev. Lett.* **2002**, *89*, 015701/1-015701/4.

(42) Abou, B.; Bonn, D.; Meunier, J. *Phys. Rev. E* **2001**, *64*, 021510/1-021510/6.

(43) Kalaitzidou, K.; Fukushima, H.; Drzal, L. T. *Composites: Part A* **2007**, *38*, 1675-1682.

(44) Kalaitzidou, K.; Fukushima, H.; Drzal, L. T. *Carbon* **2007**, *45*, 1446-1452.

(45) Drzal, L. T.; Fukushima, H. *Polym. Prepr. (Am. Chem. Soc., Div. Polym. Chem.)* **2001**, *42*, 42-43.

(46) Fukushima, H.; Drzal, L. T. *Ann Tech Conf- Soc Plast Eng* **2003**, 2230-2234.

(47) Ramanathan, T.; Abdala, A. A.; Stankovich, S.; Dikin, D. A.; Herrera-Alonso, M.; Piner, R. D.; Adamson, D. H.; Schniepp, H. C.; Chen, X.; Ruoff, R. S.; Nguyen, S. T.; Aksay, I. A.; Prud'Homme, R. K.; Brinson, L. C. *Nat. Nanotechnol.* **2008**, *3*, 327-331.

(48) Mori, T.; Tanaka, K. *Acta Metall.* **1973**, *21*, 571-574.

(49) Tandon, G. P.; Weng, G. J. *Polym. Compos.* **1984**, *5*, 327-333.

(50) Lee, C.; Wei, X.; Kysar, J. W.; Hone, J. *Science* **2008**, *321*, 385-388.

(51) Gilmour, I. W.; Trainor, A.; Haward, R. N. *J. Appl. Polym. Sci.* **1979**, *23*, 3129-38.

(52) Cho, J.; Luo, J. J.; Daniel, I. M. *Compos. Sci. Technol.* **2007**, *67*, 2399-2407.

(53) Li, J.-L.; Kudin, K. N.; McAllister, M. J.; Prud'homme, R. K.; Aksay, I. A.; Car, R. *Phys. Rev. Lett.* **2006**, *96*, 176101/1-176101/4.

(54) Wen, X.; Garland, C. W.; Hwa, T.; Kardar, M.; Kokufuta, E.; Li, Y.; Orkisz, M.; Tanaka, T. *Nature* **1992**, *355*, 426-8.

(55) Schniepp, H. C.; Kudin, K. N.; Li, J.-L.; Prud'homme, R. K.; Car, R.; Saville, D. A.; Aksay, I. A. *ACS Nano* **2008**, *2*, 2577-2584.

(56) Fornes, T. D.; Paul, D. R. *Polymer* **2003**, *44*, 4993-5013.

(57) Chow, T. S. *J. Polym. Sci., Part B: Polym. Phys.* **1978**, *16*, 967-70.

(58) Nelson, J. B.; Riley, D. P. *Proc. Phys. Soc.* **1945**, *57*, 477.

(59) Kelly, B. T. *Carbon* **1972**, *10*, 429-33.

(60) Cussler, E. L.; Hughes, S. E.; Ward, W. J., III; Aris, R. *J. Membr. Sci.* **1988**, *38*, 161-74.

(61) Prud'homme, R. K.; O'Neil, C. D.; Ozbas, B.; Aksay, I. A.; Register, R. A.; Adamson, D. H. WO 2008130431, **2007**

(62) Pixton, M. R.; Paul, D. R. In *Polymeric Gas Separation Membranes*; Paul, D. R., Yampol'skii, Y. P., Eds.; CRC Press: Boca Raton, 1994, p 83-153.

(63) Lape, N. K.; Nuxoll, E. E.; Cussler, E. L. *J. Membr. Sci.* **2004**, *236*, 29-37.

(64) Picard, E.; Vermogen, A.; Gerard, J. F.; Espuche, E. *J. Membr. Sci.* **2007**, *292*, 133-144.

(65) Cussler, E. L. *Diffusion: Mass Transfer in Fluid Systems*; 2nd ed.; Cambridge University Press: Cambridge, 1997.

(66) Osman, M. A.; Mittal, V.; Morbidelli, M.; Suter, U. W. *Macromolecules* **2003**, *36*, 9851-9858.

Chapter 6. Graphene/Polystyrene Nanocomposites: In-line Rheological and Dielectric Spectroscopy

6.1. Introduction

Viscoelastic and electrical properties of polymer melts can be altered significantly via internal percolation of rigid and conductive nano-fillers. For anisotropic particles, property changes from the percolation highly depend on their orientation. As illustrated in the previous chapter, flow alignment of graphitic platelets can substantially reduce the melt-state elasticity and electrical conductivity of polycarbonate composites. Properties affected by the flow can be recovered via prolonged annealing. Rotary relaxation of aligned particles during annealing may improve the connectivity and rigidity of the sample-spanning networks. However, the mechanisms for the disk disorientation and the network restoration in viscoelastic media have not been understood well. Ren and coworkers[1] reported that disorientation of layered silicates in polystyrene (PS) melts lacks characters expected from Brownian motions of particles (e.g. strong dependence on matrix viscosity, temperature and particle size). The elasticity increase upon annealing is rather analogous to the physical aging of colloidal glasses such as aqueous Laponite suspensions.[2] Physical aging of the filled systems after shear rejuvenation[2,3] can find its similarity from colloidal glasses that age toward lower energy states after quenching below the glass transition temperature. In order to explain this resemblance with the glassy systems, Abou *et al.*[2] introduced the classical mode-coupling theory:[4] translational diffusion of particles is strongly coupled with the mobility of the nearest neighbors. Escape of particles trapped inside "cages" by particles in proximity will become increasingly sluggish. This increase in particle relaxation time will lead to viscoelasticity growth as the system ages.

In this chapter, the aging kinetics of PS melts containing high aspect ratio graphene sheets is discussed. Melt compounded PS/functionalized graphene sheets (FGS) composites were subjected to long-term thermal curing after shear-induced particle

orientation. After deformation, micro-structural evolution of stress-resisting and charge-conducting FGS clusters in PS is studied with melt-state rheological and dielectric measurements. Conditions for physical annealing such as temperature, matrix molecular weight, shear amplitude and frequency are varied to examine their effects on the aging response.

6.2. Experimental

6.2.1. Materials

Three relatively mono-dispersed PS (M_w/M_n ~ 1.05) with different molecular weights were used as the matrix material. PS 17k was synthesized by living anionic polymerization at University of Minnesota. PS 59k was provided by Dr. Steve Hahn of Dow Chemical and 161k was purchased from Pressure Chemical. Their number (M_n) and weight (M_w) molecular weights, and M_w/M_n were determined with size exclusion chromatography (Waters 717 Plus HPLC Autosampler) with PS standards (EasiCal PS-2, Polymer Laboratories) at room temperature using tetrahydrofuran. Values are summarized with their zero-shear viscosity measured at 180 °C in Table 6-1. As described in preceding chapters in more detail, FGS provided from Vorbeck Materials was used as the viscoelasticity and conductivity modifier for PS. Un-exfoliated flake graphite (surface enhanced, grade # 3775) obtained from Asbury Carbons was also used. Specific surface area of FGS (~ 800 m^2/g) is substantially greater than that of flake graphite (29 m^2/g). Average thickness of exfoliated FGS sheets estimated by atomic force microscopy is only 1.8 nm, while its diameter ranges 50 ~ 400 nm suggesting high aspect ratio of platelets.

Table 6-1. Molecular Weights, Viscosity and Mixing Temperature of PS Samples

Sample	17k	59k	161k
M_w (kg/mol)	17.2	59.4	161
M_n (kg/mol)	16.1	56.2	154
M_w/M_n	1.06	1.06	1.04
η_0 at 180 °C (Pa·s)	38	1100	27000
T_{mix} (°C where $\eta \sim 750$ Pa· s)	155	180	225

For the melt compounding of FGS or graphite into PS, a conical, co-rotating twin screw extruder (DACA Microcompounder) was used. ~ 4 g of FGS/PS mixtures vacuum dehydrated for 24 hrs at 70 °C were fed into the compounder and mixed at 155 (PS17k), 180 (59k) and 225 °C (161k) for 8 min as summarized in Table 6-1. In order to have comparable stress level during mixing for the different molecular weight PS matrices, matrix shear viscosity was matched by choosing different mixing temperatures.[5] As shown in Figure 6-3, complex viscosity η^* at angular frequency ω = 100 rad/s (shear rate, $\dot{\gamma} \sim 100$ /s assuming the Cox-Merz relationship[6] holds) at chosen temperatures is ~ 750 Pa·s for all PS samples. Mixing screw speed was set at 170 RPM for the shear rate of ~ 100 s^{-1} in the DACA mixer.[7]

6.2.2. Characterization

Dispersion of FGS in PS nanocomposites was characterized with transmission electron microscopy (TEM). As-extruded 3.0 wt% FGS/PS 59k was microtomed into ~ 90 nm thick slices with a diamond knife at room temperature using Reichert Ultracut. They were transferred onto 400-mech Cu grids. Micrographs were obtained using JEOL 1210 electron microscope at an accelerating voltage of 120 kV.

Rheological characterization of as-received PS and FGS/PS melt-blends was performed with a strain-controlled rotational rheometer (TA Instruments, ARES).

Vacuum dried (70-80 °C) as-received PS samples were loaded onto 25-mm parallel plates either as molded disks (59k and 161k) or as powders (17k). After sample melting at test temperature ranging 130-240 °C, dynamic storage (G') and loss (G") moduli were measured in dynamic frequency sweeps (frequency, ω = 0.1-100 rad/s) applying strain γ less than 80% using auto-strain adjustments. Dynamic time, strain and frequency sweeps of FGS composites shown in Figure 6-5 and 6-15 were obtained using a 25-mm cone-and-plate geometry. As-extruded composites were loaded onto the heated plate after drying at 80 °C in a vacuum oven. Dynamic time sweep tests were employed both for large-amplitude oscillatory shearing (LAOS) at γ > 120% for FGS orientation and for physical aging of the samples under quiescent thermal annealing at γ < 0.5% for ~ 80,000 s. For typical time sweep tests, reduced frequency $a_T\omega$ was kept at 0.2 rad/s at different temperature using frequency shift factors a_T used for the time-temperature superposition (TTS) of G' and G" of neat PS (Figure 6-2). LAOS lasted longer than 10 min until no change in G' and G" was observed. Following prolonged annealing or LAOS, strain sweeps were conducted at 1 rad/s in order to estimate the onset strain γ_{crit} of non-linear viscoelasticity. γ_{crit} was determined from the strain where G' decreases to 90% of linear viscoelastic values. Dynamic frequency sweeps were performed at $\gamma < \gamma_{crit}$ in the ω range of 0.01-100 rad/s.

6.2.3. In-line Rheological and Dielectric Measurements

Viscoelastic and dielectric spectra of melt-state PS and composites could be obtained simultaneously by shearing samples between 25-mm parallel disk electrodes (ARES dielectric option,[8] see Figure 6-1). Agilent 4980A LCR bridge was used for both applying AC voltage to the sample and measuring current. Dry extrudates were gently compressed between the electrodes until they were ~ 1 mm apart. Then, LAOS (γ > 120%) was applied to the sample until elastic moduli, real ε' and imaginary parts ε" of dielectric permittivity ceased declining (~ 10 min). After LAOS, strain magnitude was

reduced and annealing for ~ 80,000 s began in time sweeps, monitoring temporal changes in viscoelastic and dielectric properties.

(a)

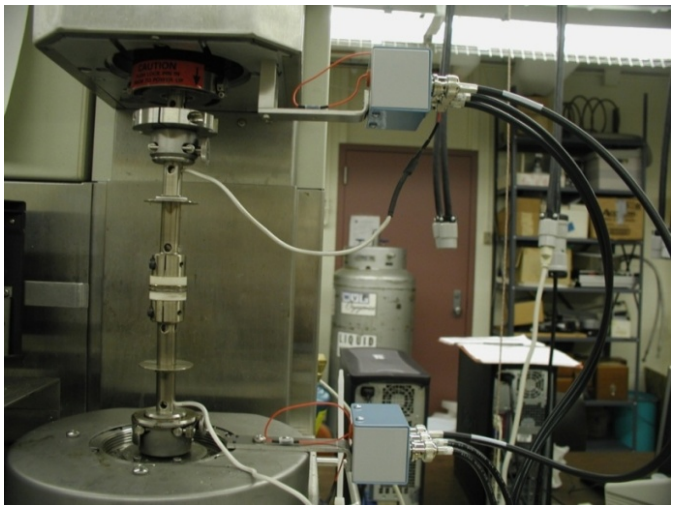

(b)

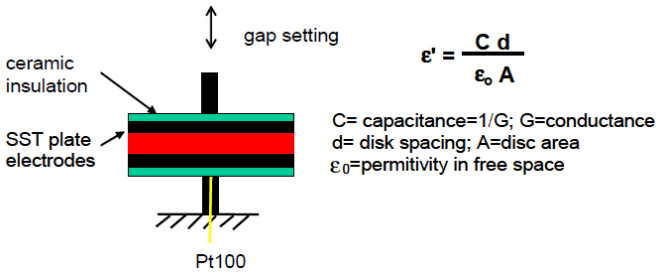

Figure 6-1. (a) ARES 25-mm parallel plate electrodes used for in-line rheological and dielectric measurements. (b) Schematic describing the parallel plate geometry adopted from reference 8.

Sample capacitance C and dissipation factor D (together leading to complex capacitance C^*) were monitored at root-mean-square potential of 1 V at different AC frequency ν (= $\omega_d/2\pi$, ω_d : angular AC frequency in rad/s) in the range of 20-2×10^6 Hz. Complex permittivity $\varepsilon^*(\omega_d)$ could be calculated using[9]

$$\varepsilon^*(\omega_d) = \varepsilon'(\omega_d) - i\varepsilon''(\omega_d) = \frac{C^*(\omega_d)}{C_0} = \frac{C^*(\omega_d)d}{\varepsilon_o A} \tag{6.1}$$

where, A, d, C_0 and ε_0 are the area of, distance between electrodes sandwiching the specimen, capacitance of vacuum given A and d, and vacuum permittivity (8.854×10^{-12} F/m), respectively. From the measured dielectric functions, complex electrical conductivity σ^* can be also computed using[9]

$$\sigma^*(\omega_d) = \sigma'(\omega_d) + i\sigma''(\omega_d) = i\omega_d\varepsilon_0\varepsilon^* = \omega_d\varepsilon_0\varepsilon'' + i\omega_d\varepsilon_0\varepsilon' \quad (6.2)$$

where σ' and σ" are the real and imaginary part of complex electrical conductivity. Dielectric functions were averaged over 2 AC cycles ("medium" averaging time). Temperature (matrix viscosity), test strain and frequency were altered to investigate their effects on aging of the composite melts.

6.3. Results and Discussion

6.3.1. Rheological Characterization of Matrix

Master curves of G' and G" were obtained at the reference temperature T_0 of 140, 165 and 200 °C for PS 17k, 59k and 161k, respectively via TTS using frequency shift factor a_T. At these reference temperatures, zero-shear η^* is ~ 5,000 Pa·s regardless of the matrix molecular weight (see Figure 6-3). Figure 6-2 (a), (c) and (e) show that all G' and G" curves of each PS sample can be shifted onto a single master curve via horizontal shifts. Frequency-dependence of G' and G" ($G' \sim \omega^{1.8\sim2.0}$ and $G'' \sim \omega^1$) reveals the Newtonian relaxation of PS melts at ω < 10 rad/s. G' and G" of PS 161k and 59k becomes equal at 24 and 36 rad/s, respectively. This implies their longest relaxation time λ_N, the inverse of the cross-over frequency, are close at chosen reference temperatures: λ_N = ~ 0.04 for 161k and ~ 0.03 s for 59k. Note that G' and G" of 17k do not intersect since it is not entangled: the entanglement molecular weight of PS is 18 kg/mol.[10] Frequency shift factors a_T used for TTS were plotted in Figure 6-2 (b), (d) and (f) with respect to temperature. Temperature T dependence of a_T could be fitted with the Williams-Landel-Ferry (WLF) equation,[11]

$$\log(a_T) = -\frac{C_1(T - T_o)}{C_2 + (T - T_o)} \quad (6.3)$$

where C_1 and C_2 are empirical adjustable parameters. C_1 and C_2 from the curve regression above T_0 are listed in Figure 6-2 (b), (d) and (f). Extrapolation of the WLF trends also predicts a_T below T_0 well.

Complex viscosities η^* (= $(G'^2+G''^2)^{0.5}/\omega$) of as-received PS were measured at different temperatures and shown in Figure 6-3 (a), (c) and (e) as a function of ω. Regardless of matrix molecular weight, all display a Newtonian viscosity at lower frequency and a shear thinning behavior at higher frequency. The shear thinning response sets in at higher frequency as the temperature increases and matrix molecular weight decreases, which can facilitate polymer chain relaxation. Master curves (Figure 6-2 (b), (d) and (f)) for complex viscosity were obtained at T_0 of 140, 165 and 200 °C for PS 17k, 59k and 161k respectively using a_T values from TTS. The magnitude of power-law exponent a ($G' \sim \omega^a$) estimated from the shear thinning regime ($a_T\omega$ = 50–500 rad/s) is greater for higher matrix molecular weight, suggestive of more pronounced viscosity reduction.

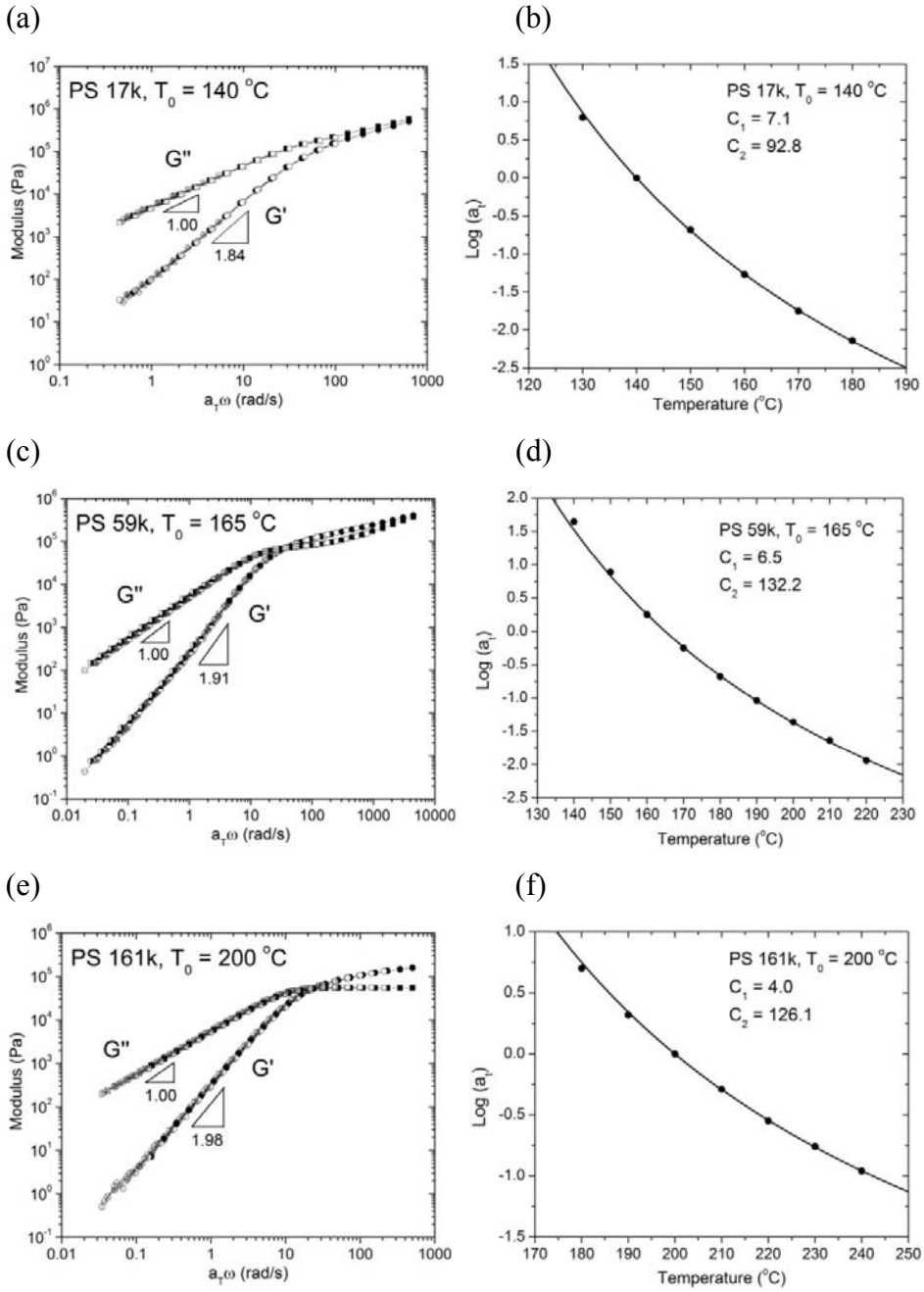

Figure 6-2. Time-temperature superposed *G*' and *G*" master curves and frequency shift factors a_T used for different temperatures of (a), (b) PS 17k, (c), (d) 59k and (e), (f) 161k to the reference temperature T_0 of 140, 165 and 200 °C, respectively. (a), (c) and (e) Terminal slopes of *G*' or *G*'' versus ω and (b), (d) and (f) curve fits of a_T versus temperature based on the WLF equation are also shown.

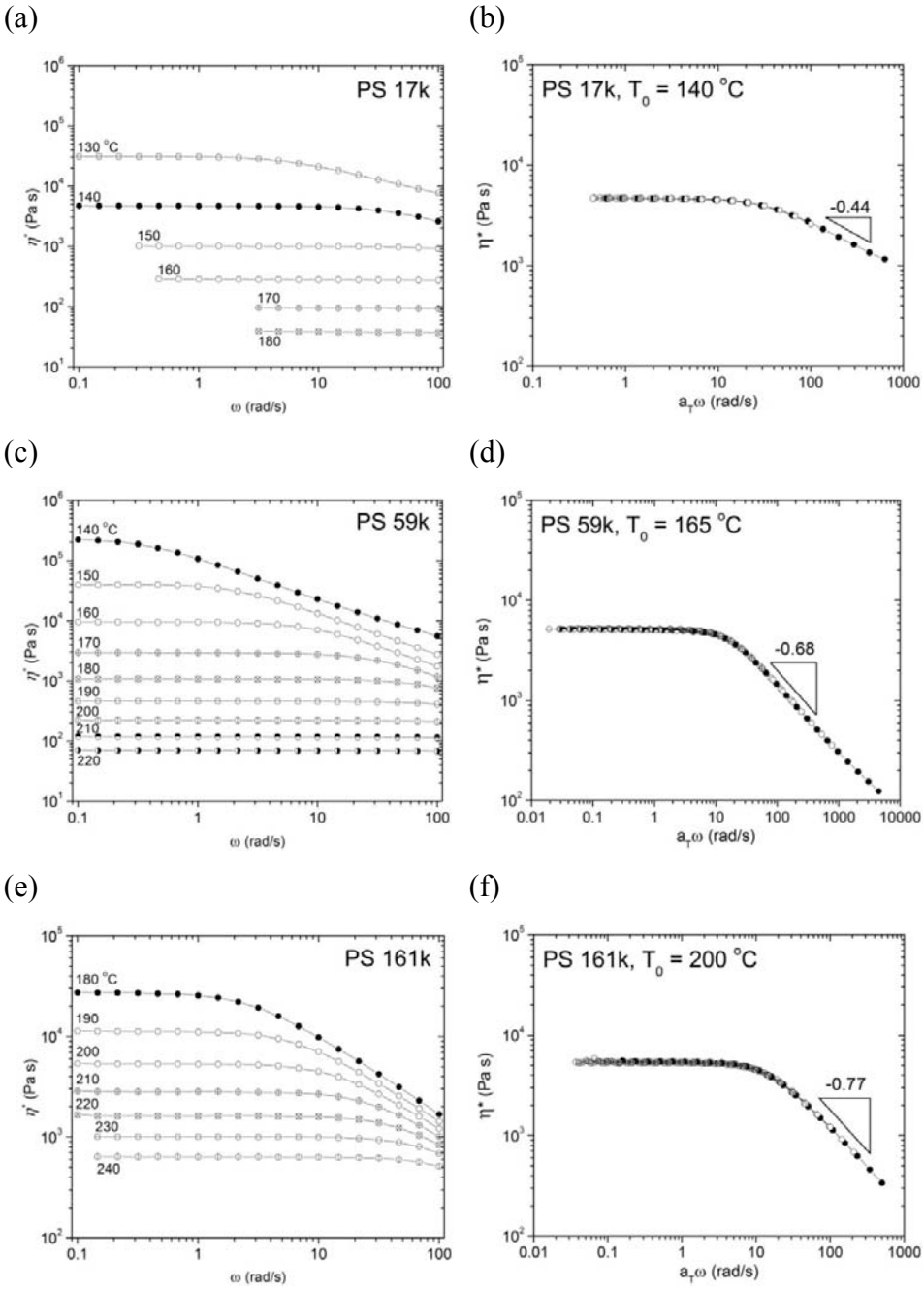

Figure 6-3. Complex viscosity as a function of angular frequency at different temperatures and time-temperature superposed viscosity of (a), (b) PS 17k (T_0 = 140 °C), (c), (d) 59k (165 °C), (e) and (f) 161k (200 °C). (b), (d) and (f) Power law exponents for shear thinning evaluated at $a_T\omega$ = 50-500 rad/s are also shown.

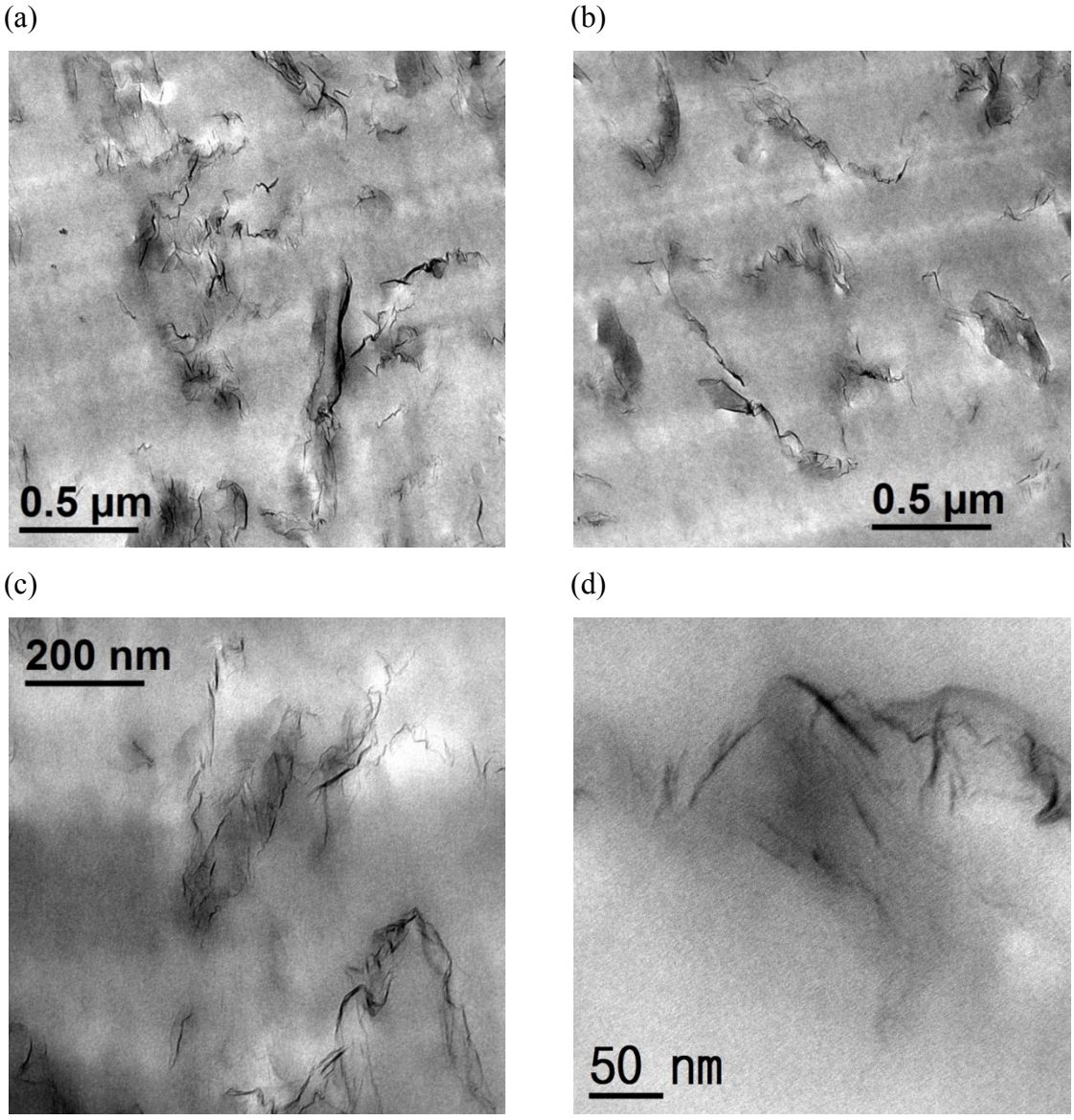

Figure 6-4. TEM micrographs of as-extruded 3 wt% FGS/PS 59k composites.

6.3.2. TEM

TEM images of 3 wt% FGS/PS 59k are shown in Figure 6-4. Spatial distribution of melt blended FGS is nearly homogeneous in Figure 6-4 (a) and (b). Particle diameter ranges from tens to hundreds of nm, which is comparable with the estimates from atomic force microscopy, 50-400 nm (Section 2.3.1). Flexibility of thin carbon sheets can be inferred from the highly crumpled structure. Thickness dimension of isolated sheets is

only 1 ~ 5 nm (Figure 6-4 (c) and (d)). However, some layers are closely spaced with one another signifying incomplete layer separation. This real-space morphological characterization reveals that dispersed FGS cannot simply be approximated as completely isolated rigid disks.

6.3.3. Rheology and Electrical Conductivity of PS Composites

Dynamic frequency and strain sweeps of melt-processed pure PS 59k and 0.5, 1.0, 2.0 and 3.0 wt% FGS composites are compared in Figure 6-5. "As-sheared" samples (Figure 6-5 (a)) were subjected to LAOS at γ > 120% before measurements. Incorporation of FGS increases *G*' of PS significantly. Most dramatic increase in *G*' at low frequency (ω ~ 0.1 rad/s) takes place between 2 and 3 wt%, which signifies rigidity percolation. Unlike neat PS which displays terminal relaxation down to the lowest frequency, *G*' of composites becomes increasingly frequency-independent in their frequency sweeps as higher amount of FGS is incorporated. This signature of viscoelastic solids[12-14] is more clearly observed from the "as-annealed" samples. As-annealed (Figure 6-5 (b)) denotes samples annealed for ~ 80,000 s at 200 °C using small-strain time sweeps prior to the frequency sweep tests. As a consequence of annealing, composites all exhibit higher elastic modulus than as-sheared samples over the entire frequency range. This *G*' enhancement is most pronounced at small frequency, which is an indication for transition from liquid-like to solid-like responses through 80,000 s' annealing. Note that *G*" changes less sensitively by FGS addition for both as-sheared and as-annealed samples as summarized in Figure B-1 in Appendix B.

Dynamic strain sweeps at 200 °C of as-sheared and as-annealed samples are shown in Figure 6-5 (c) and (d). Linear viscoelastic moduli could be improved via particle dispersion and prolonged annealing. *G*' starts to decline at higher strain implying the onset of the non-linear viscoelastic responses. The limiting strains γ_{crit} for linear viscoelasticity determined by the "90% rule" are also listed in Figure 6-5 (c) and (d). FGS addition progressively reduces γ_{crit} of the composites: network-like structures can be distorted at smaller deformation at higher FGS volume fraction.[12-15] For most samples,

γ_{crit} measured in as-annealed state are significantly smaller than that in as-sheared state suggesting increased fragility of filling networks and *G*' diminishes more steeply at $\gamma > \gamma_{crit}$. *G*" decrease at $\gamma > \gamma_{crit}$ (Appendix B) is less pronounced implying the network disruption is better reflected by *G*' changes. However, for the highly concentrated 3 wt% samples, the yield stain is greater in as-sheared state. This will be discussed later in this chapter.

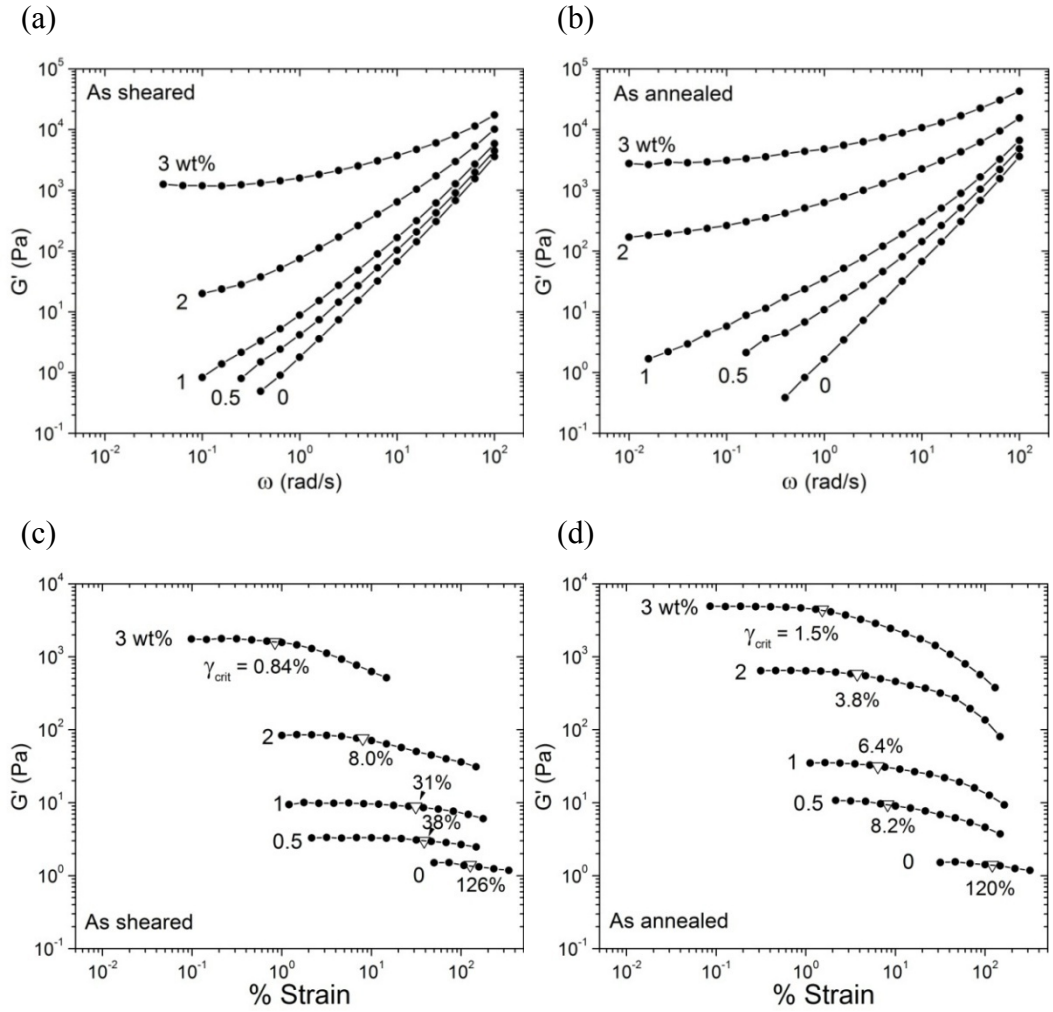

Figure 6-5. Dynamic frequency sweeps of (a) as-sheared and (b) as-annealed PS 59k/FGS composite at 200 °C and dynamic strain sweeps at 1 rad/s of (c) as-sheared and (d) as-annealed composites at 200 °C. Critical strains determined by the 90% rule are marked with ∇.

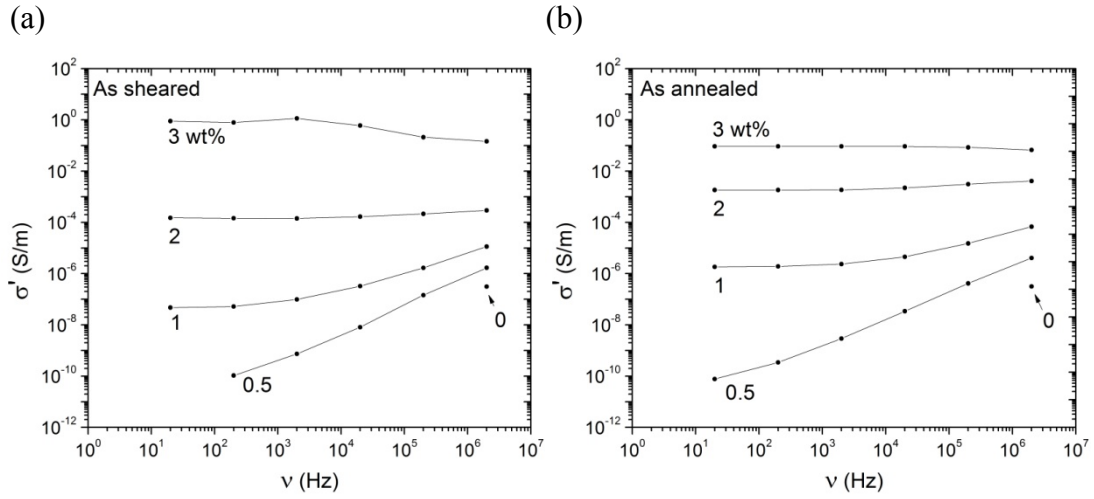

Figure 6-6. σ' of PS 59k/FGS previously (a) deformed by LAOS at $\gamma > 120\%$ and (b) annealed for ~ 80,000 s at 200 °C.

Real parts σ' of electrical conductivity of as-sheared and as-annealed FGS/PS 59k were measured at 200 °C at different ν using the ARES dielectric option (Figure 6-6 (a) and (b)). Note that σ' of neat PS 59k could not be measured reliably at $\nu < 2 \times 10^6$ Hz due to limited measurement accuracy for the sample capacitance range of the LCR meter.[16] AC conductivity of PS can be enhanced after FGS dispersion via formation of percolated pathways of carbon sheets for electron conduction. Constant σ' at lower ν at higher FGS incorporation is indicative of DC conductivity. Electrical percolation of the as-annealed samples between 0.5 and 1.0 wt% can be inferred from the largest change in low-frequency σ' and appearance of the DC plateau. Slightly higher FGS loading (1.0 ~ 2.0 wt%) was required for the rheological percolation. Higher threshold for rigidity percolation than connectivity percolation was also reported for polypropylene/multi-walled carbon-nanotube (MWCNT) polymer composites.[17] 1 wt% increase in FGS concentration improves DC conductivity ~ 10^4 times, but G' at low ω only 10 ~ 100 times. Note the contrast in conductivity between FGS (~ 10^3 S/m)[18] and PS (10^{-13} ~ 10^{-7} S/m at ν = 20-20^6 Hz)[19] is considerably greater than the shear modulus contrast: ~ 10 GPa for FGS[20] versus 20 Pa for PS (Figure 6-7 (a)). Except 3 wt% FGS samples,

annealing provided additional conductivity gains. Connectivity between conductive carbon sheets could be improved by particle disorientation.

6.3.4. In-line Rheological and Dielectric Spectroscopy

Temporal changes of FGS structure in PS during annealing could be examined via on-line viscoelastic and electrical property measurements. Figure 6-7 shows dynamic time sweep results for G', G'' and σ' of neat PS 59k and 59k containing 1 wt% FGS through annealing at 200 °C after LAOS. 10% and 0.5% strain was applied to PS and 1 wt% FGS composites, respectively which are much smaller than their critical strains evaluated from the strain sweeps (Figure 6-5 (d)). Rheological frequency of 4.58 rad/s was employed, which corresponds to reduced frequency $a_T\omega$ of 0.2 rad/s for the reference temperature, T_0 = 165 °C. σ' was estimated from the imaginary part ε'' of measured dielectric permittivity via equation (6.2). Due to low sample capacitance of PS 59k at lower ν, ε'' thus σ' was monitored only at the highest available frequency, 2×10^6 Hz. As shown in Figure 6-7 (a) and (b), properties of PS remained nearly unchanged over 70,000 s suggesting long-term thermal stability of the matrix.

Unlike neat PS, 1 wt% composites displayed steady increase in shear moduli and dielectric constants (Figure 6-7 (c)). This implies structural evolution of the composite system into new metastable states, possibly with lower energy. Loss of filler-filler contacts caused by LAOS followed by slow restoration via particle disorientation may account for these aging responses.[1,14,21] Remarkably, viscoelastic and dielectric functions changed continuously for more than ~ 24 hrs, never reaching steady states. A linear increase in the double-logarithmic scale (Figure 6-7 (d)) is suggestive of that property gains became slower proportionally to the age of the system. Analogous logarithmic scaling between viscoelasticity and the sample age ($G' \sim t^{\beta}$) was also reported for aqueous suspensions of Laponite clay[2] and polymer melts containing layered silicates.[1] Bonn and coworkers[2,22] found both viscosity and diffusive relaxation time determined by dynamic light scattering of jammed Laponite particles in water increase exponentially

with aging time. This reflects collective diffusion processes of the particles. Due to the structural arrest, escape from surrounding particles will become increasingly sluggish.

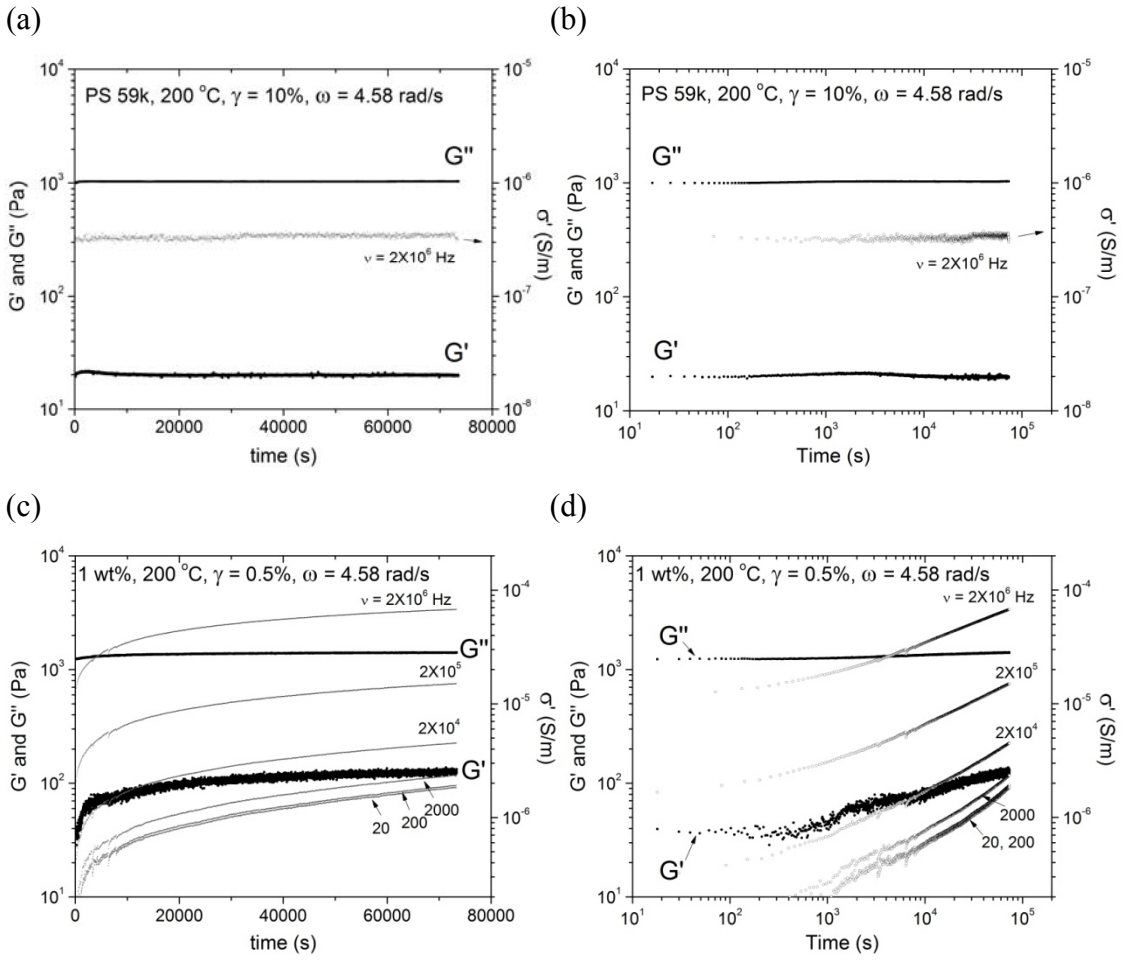

Figure 6-7. *G*', *G*" and σ' changes during dynamic time sweeps at 200 °C and $a_T\omega = 0.2$ rad/s ($\omega = 4.58$ rad/s) of (a) melt extruded PS 59k ($\gamma = 10\%$) and (c) PS 59k containing 1 wt% FGS ($\gamma = 0.5\%$). Same plots are reproduced in the double logarithmic scale for (b) PS 59k and (d) 1 wt% FGS/PS59k.

6.3.4.1. Annealing Temperature

Aging responses of 1 wt% FGS/PS 59k at different annealing temperatures (165, 180 and 200 °C) are shown in Figure 6-8. For the time sweeps ($\gamma = 5\%$) at different

temperature, reduced frequencies $a_T\omega$ were kept at 0.2 rad/s using a_T values determined from TTS (Figure 6-2 (d), T_0 = 165 °C). Steady G' and σ' increases during the time sweeps are evident for all temperatures. Raising the annealing temperature facilitated growth in G' and σ' presumably due to reduced medium viscosity expediting particle disorientation process.[1]

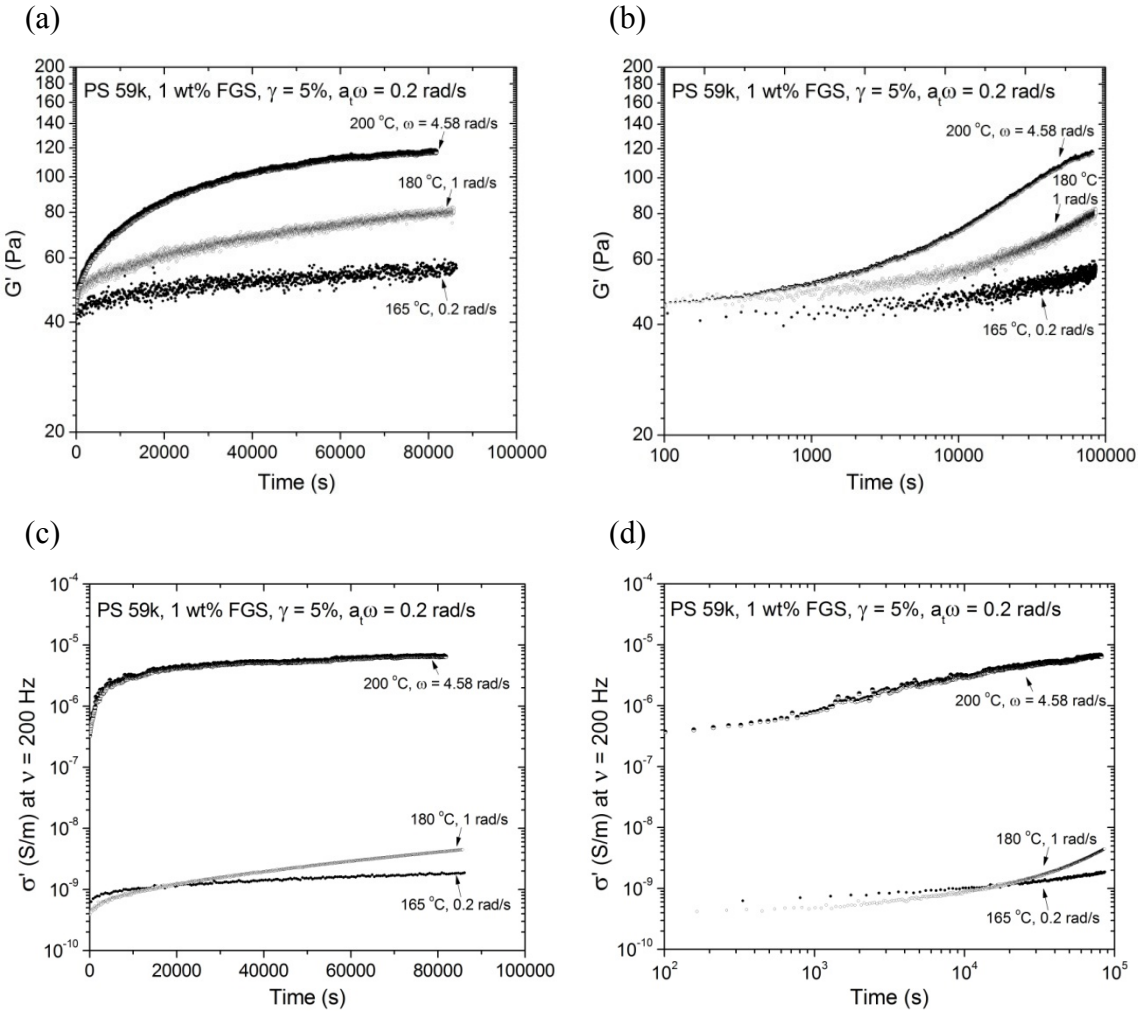

Figure 6-8. (a), (b) G' and, (c), (d) σ' at ν = 200 Hz of 1 wt% FGS/PS 59k measured during time sweeps (γ = 5% and $a_T\omega$ = 0.2 rad/s) at 165, 180 and 200 °C.

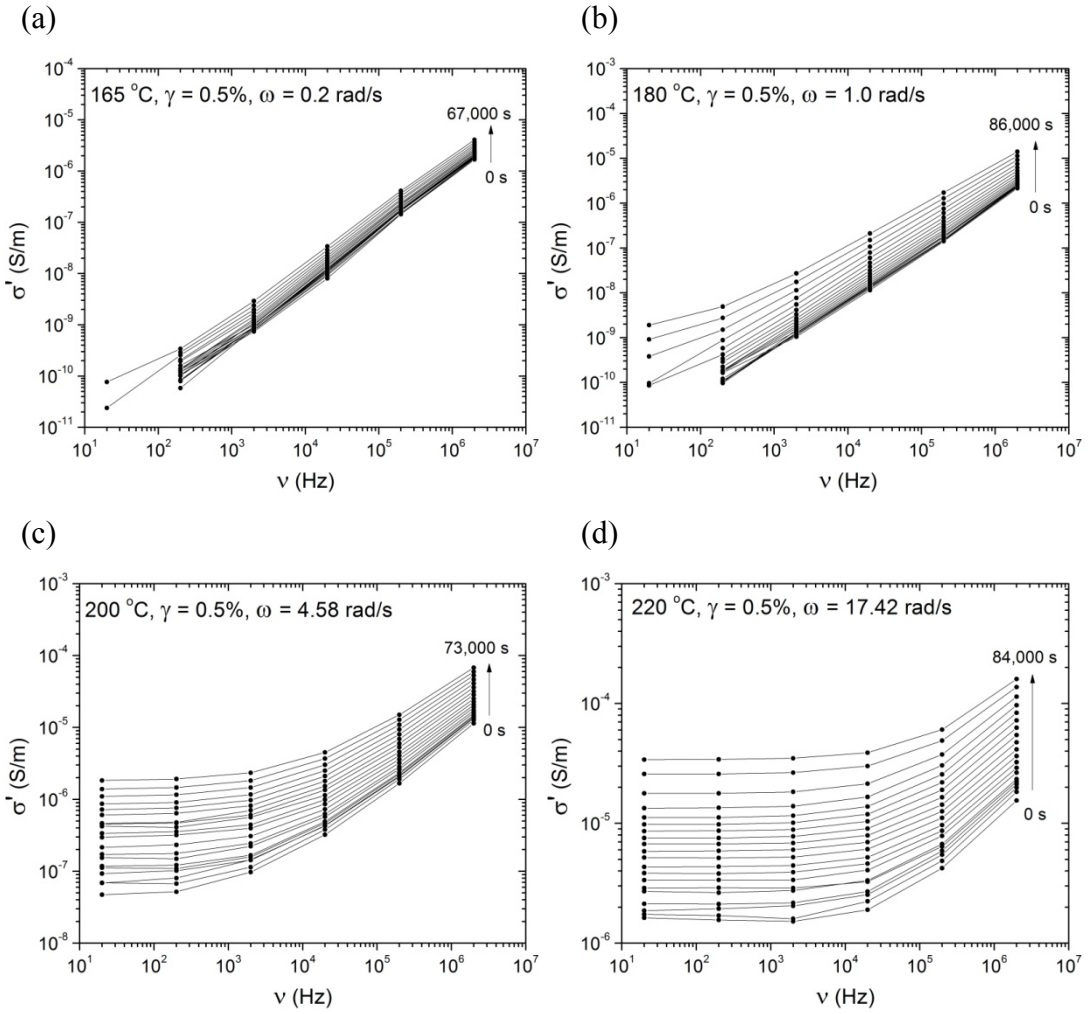

Figure 6-9. σ' of 1 wt% FGS/PS 59k measured during time sweeps (γ = 0.5% and $a_T\omega$ = 0.2 rad/s) at (a) 165, (b) 180, (c) 200 and (d) 220 °C.

AC conductivity spectra of 1 wt% FGS/PS 59k annealed through times sweeps (γ = 0.5% and $a_T\omega$ = 0.2 rad/s) at different temperatures are presented in Figure 6-9. Regardless of annealing temperature, the conductivity increase is universal for the entire ν range implying increased connectivity in FGS networks.[21,23] Especially conductivity enhancement at lower frequency is most pronounced. σ' at ν = 20 Hz increased nearly 100 times for ~ 24 hrs at 200 and 220 °C. At higher temperature, electrical conductivity becomes more frequency-independent (DC conductivity) and the cross-over between the

DC plateau and the power-law response occurs at higher frequency. According to the charge carrier diffusion model,[23-26] the average time τ_ξ for the charge carriers to travel a percolated cluster of a correlation length ξ is inversely proportional to this cross-over frequency ω_c:

$$\omega_c \propto \frac{1}{\tau_\xi} \propto \left|\phi - \phi_{perc}\right|^{\zeta d_f} \tag{6.4}$$

where ζ and d_f are the critical exponents[27] associated with the cluster size and fractal dimension of the percolating cluster, respectively. When ω_d (= $2\pi\nu$) < ω_c, charge carriers can travel different clusters within one AC cycle, giving rise to the DC conductivity response. The frequency-dependence of σ' at ω_d > ω_c originates from anomalous diffusion of the charge carriers that can explore only a part of fractal-like clusters in one period.[25,26] ω_c also reflects the distance of the particle composition ϕ from the percolation threshold ϕ_{perc}. Higher ω_c at higher annealing temperature implies increased effective particle volume via faster disorientation of disks. Note that analogous conductivity recovery following cessation of shear was also observed for MWCNT in polymer melts.[21,23] However, conductivity rise of MWCNT takes place more rapidly (e.g. several orders of decades increase less than 1 hr), which may imply different recovery mechanisms between graphene and MWCNT networks. The re-formation of entangled MWCNT networks after shear can be accelerated via elastic restoring forces.[28] In contrast, disorientation of disk-like particles originated purely from thermal diffusion of particles.

6.3.4.2. Particle Concentration

Disorientation kinetics of PS 59k with different FGS concentration is compared in Figure 6-10. Measurements were conducted during time sweeps (γ = 5% and $a_T\omega$ = 0.2 rad/s) over ~ 80,000 s at 200 °C. Aging experiments reveal that initial G' and σ' growth is fastest at intermediate concentration (~ 2 wt%). In dilute conditions where spheres of rotation for disks barely intersect, percolation will require significant rotation of aligned

particles, which may slow down increases in properties that benefit from percolation. In the concentrated regime, a relatively larger fraction of particles may remain percolated even after the extensive shear deformation. Therefore, property recovery as a consequence of particle disorientation will be less significant.

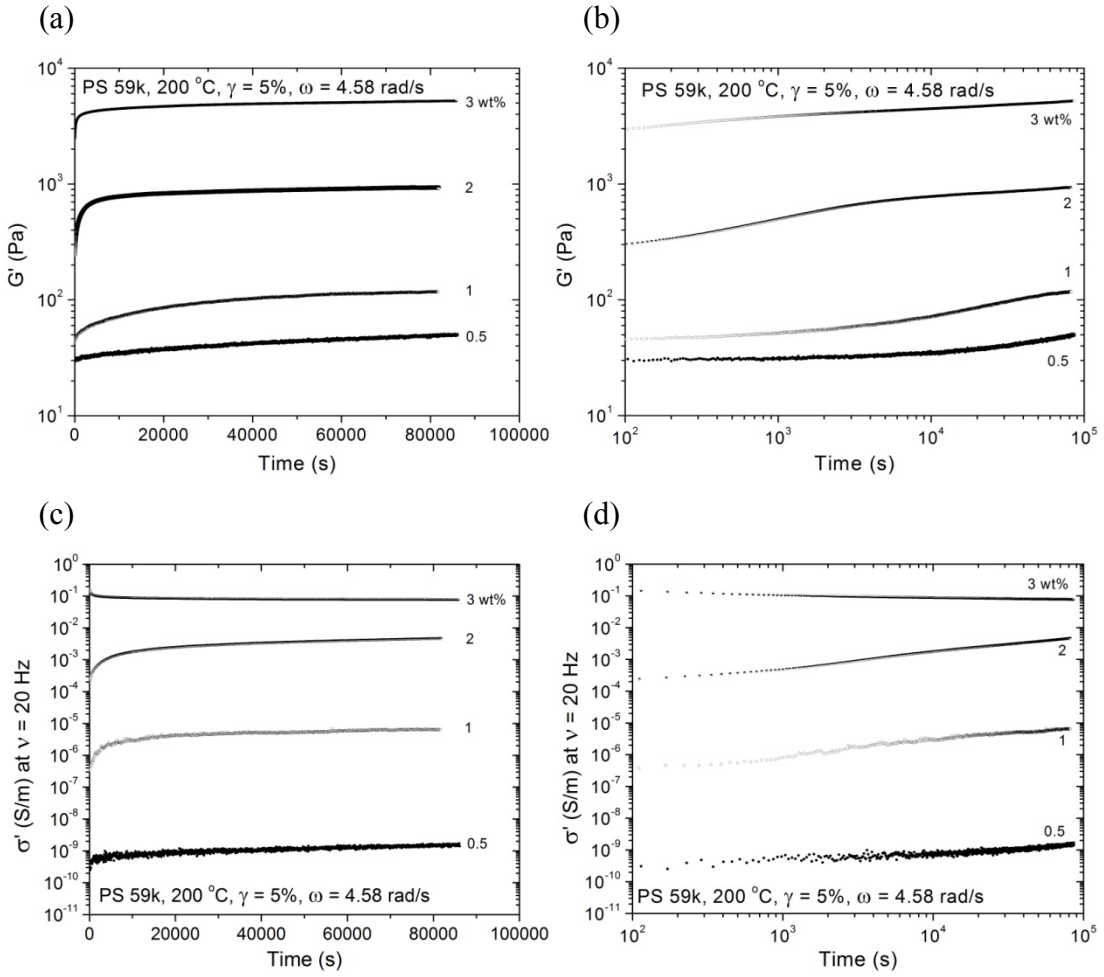

Figure 6-10. (a), (b) G' and (c), (d) σ' at ν = 20 Hz changes during time sweeps at γ = 5% and $a_T\omega$ = 0.2 rad/s of PS 59k containing 0.5, 1.0, 2.0 and 3.0 wt% FGS at 200 °C.

Interestingly, 3 wt% sample shows a steady decline in σ' over time signifying diminished connectivity. Critical strain of as-annealed 3 wt% FGS is higher than that of as-sheared one unlike samples with lower FGS concentration (compare Figure 6-5 (c) and

(d)). These results may imply that prolonged annealing rather induces parallel arrangement of highly concentrated platelets[14,29] in nematic transition, and loss in contacts between particles.

Most significant rise at 200 °C in AC electrical conductivity (Figure 6-11) upon annealing (time sweeps at $a_T\omega$ = 0.2 rad/s and γ = 0.5%) was also found from the intermediate FGS concentration (1.0 wt%). 3 wt% FGS sample was an exception: annealing decreases σ' for entire ν. Note that the DC plateau expands toward higher ν at higher particle concentration suggesting increased distance from ϕ_{perc}.

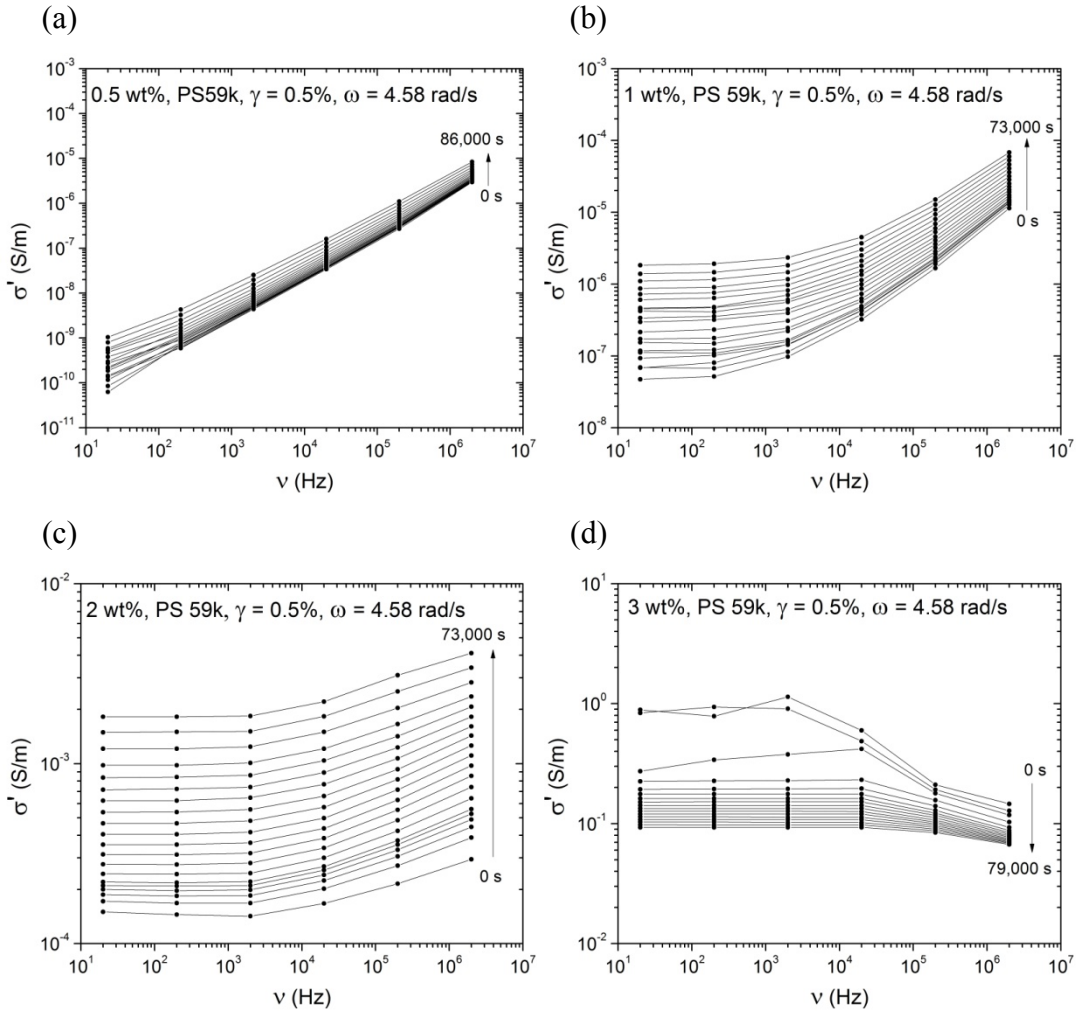

Figure 6-11. σ' measured during time sweeps (γ = 0.5% and $a_T\omega$ = 0.2 rad/s) for ~ 80,000 s of (a) 0.5, (b) 1.0, (c) 2.0 and (d) 3.0 wt% FGS/PS 59k at 200 °C.

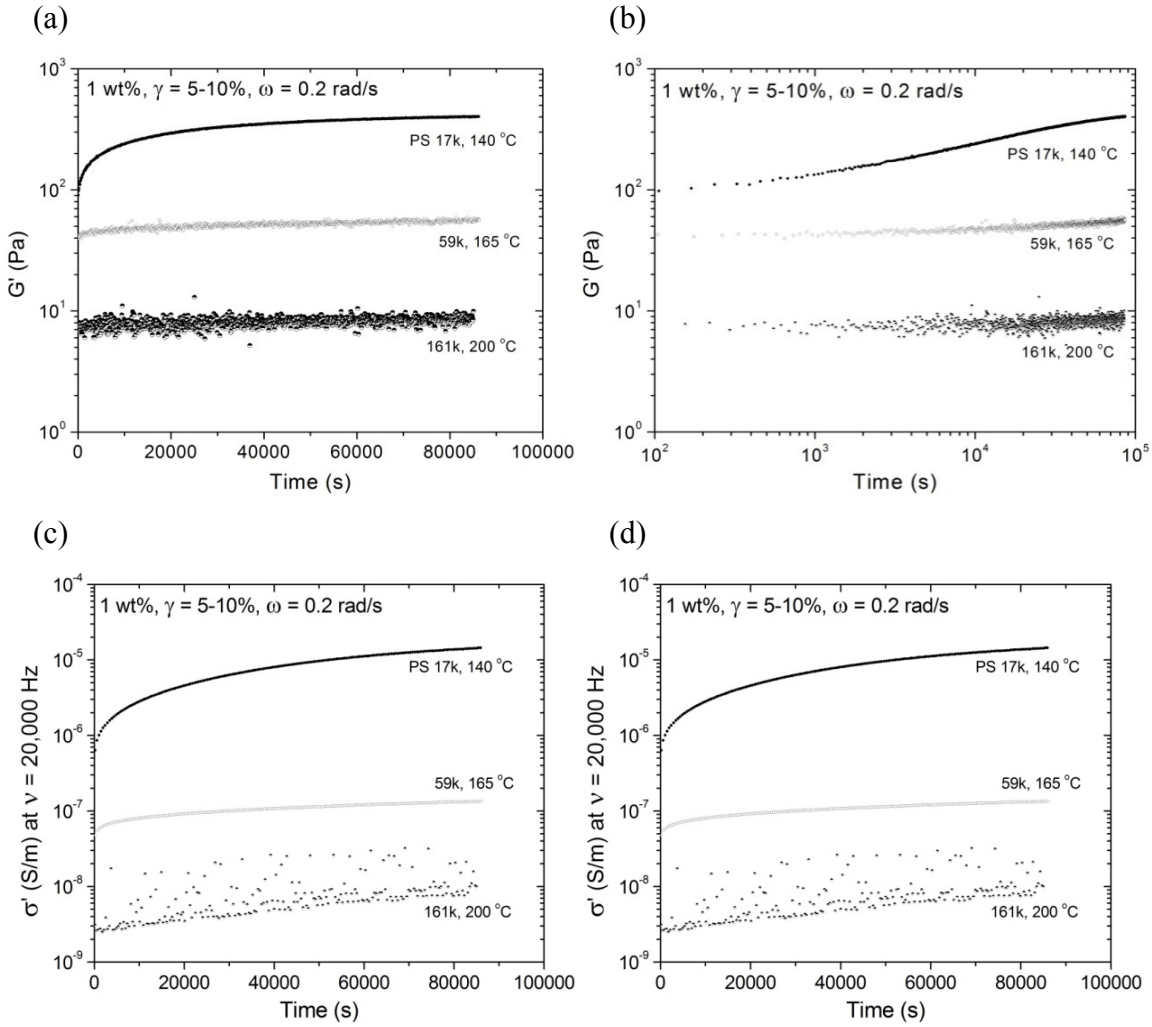

Figure 6-12. (a), (b) G' and (c), (d) σ' at 20,000 Hz changes of PS 17k at 140 °C, 59k at 165 °C and 161k at 200 °C containing 1 wt% of FGS during dynamic time sweeps at γ = 5-10% and $a_T\omega$ = 0.2 rad/s.

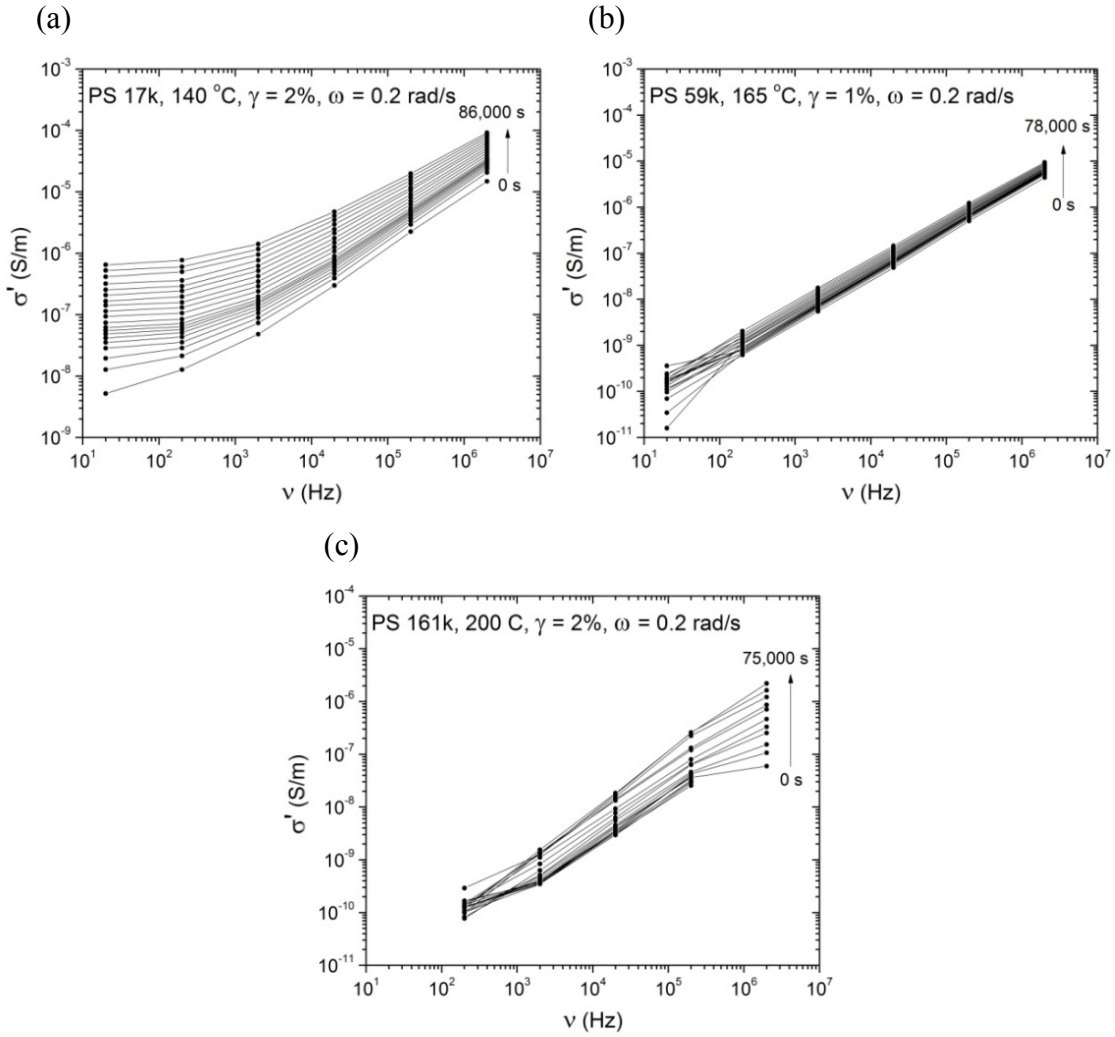

Figure 6-13. σ' of (a) PS 17k at 140 °C, (b) PS 59k at 165 °C and (c) PS 161k at 200 °C containing 1 wt% FGS measured during dynamic time sweeps for ~ 80,000 s at γ = 1-2% and $a_T\omega$ = 0.2 rad/s.

6.3.4.3. Matrix Molecular Weight

Effects of matrix molecular weight on physical aging of melt-state FGS/PS were also studied (Figure 6-12). In-line rheological and dielectric measurements were carried out on PS 17k, 59k and 161k containing 1 wt% FGS. The reference temperature T_0 for TTS (Figure 6-2) was selected as the test temperature for each PS where the complex viscosity at $a_T\omega$ = 0.2 rad/s is ~ 5,000 Pa·s for all PS. Despite the same matrix viscosity,

their aging behaviors at 200 °C are starkly different. FGS in PS 17k exhibited the most dramatic viscoelastic and dielectric variations over ~ 80,000 s. However, properties of 59k and 161k barely changed through annealing. These results indicate that aging kinetics of PS/FGS melts is not merely determined by the matrix viscosity, but chain relaxation dynamics[30] may also play a role. There will be no or less significant chain entanglement in PS 17k due to molecular weight close to the entanglement molecular of PS (18 kg/mol).[10] Also, at fixed matrix viscosity, the most dramatic transformation in σ' spectrum was found from PS 17k especially at low ν as presented in Figure 6-13. In contrast, the power-law response of conductivity of 1 wt% FGS in PS 59k and 161k remained unchanged for entire annealing period of ~ 80,000 s.

6.3.4.4. Shear Strain, Frequency and Particle Shape

Aging of 0.5 wt% FGS/PS 17k at 140 °C was monitored varying strain and frequency of oscillatory deformation. G' grew at nearly similar rate at 2 and 10% strain as shown in Figure 6-14 (a) and (b). Except reduced starting G' value (Figure 6-14 (a)) and delayed increase (Figure 6-14 (b)), the logarithmic scaling ($G' \sim t^{\beta}$) at longer aging time at 50% strain is essentially identical with those at 2 and 10% strain. From dynamic strain sweeps using the cone-and-plate geometry (Figure 6-15 (a)), critical strain γ_{crit} for the same sample was identified at 140 °C: 5.9% after prolonged annealing and 27.9% after LAOS. Reduction in γ_{crit} after aging agrees with the previous observation (Figure 6-5 (c) and (d)). Since 2% strain is smaller than γ_{crit} of the annealed sample, deformation of FGS networks during time sweeps can be minimized. 10% stain which is smaller than γ_{crit} of highly oriented samples, but greater than that of the as-annealed sample may result in slight re-orientation of FGS. However, strain greater than γ_{crit} after LAOS (27.9%) could not curb the elasticity sufficiently over time: the sample aged even at 50% strain. While the cone-and-plate geometry was also used for the time sweep at γ = 50% to apply high deformation uniformly throughout the sample, the aging response was not altered significantly (Figure 6-15 (b)). Only γ as high as 150% could restrain the G' growth

completely. Extrapolations of strain sweeps of 0.5 wt% FGS/PS 17k following annealing and LAOS intersect at γ = 86.7%. Possibly, applied deformation has to be greater than this value for complete suppression of aging. Surprisingly, σ' at ν = 20 Hz grows much faster at γ = 50% than 2 and 10% strain, which implies that the conductivity increase is facilitated by larger deformation that can possibly break up and reorganize filler networks during annealing.

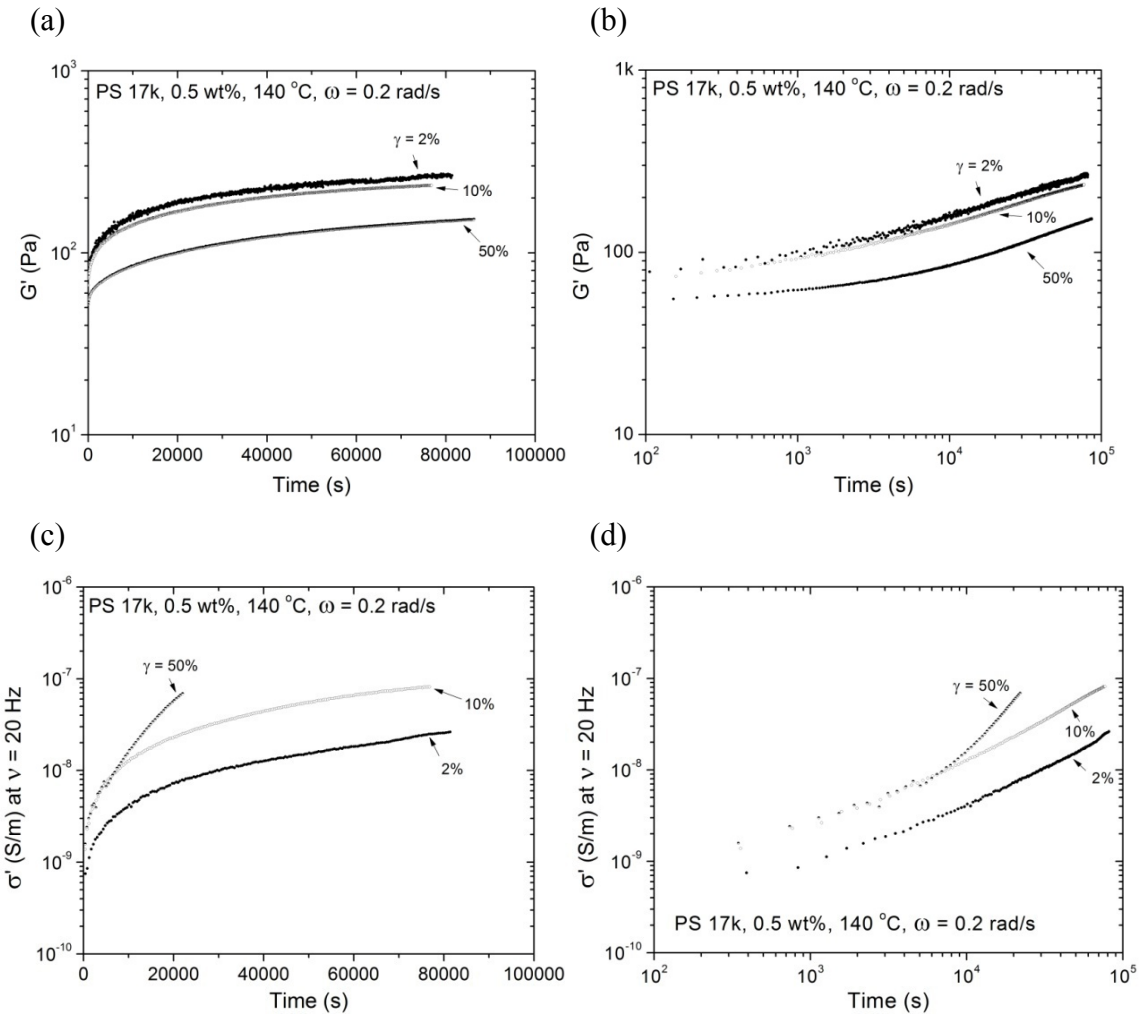

Figure 6-14. (a), (b) G' and (c), (d) σ' at 20 Hz of PS 17k with 0.5 wt% FGS at 140 °C during dynamic time sweeps at $a_T\omega$ = 0.2 rad/s using 2, 10 and 50% strain.

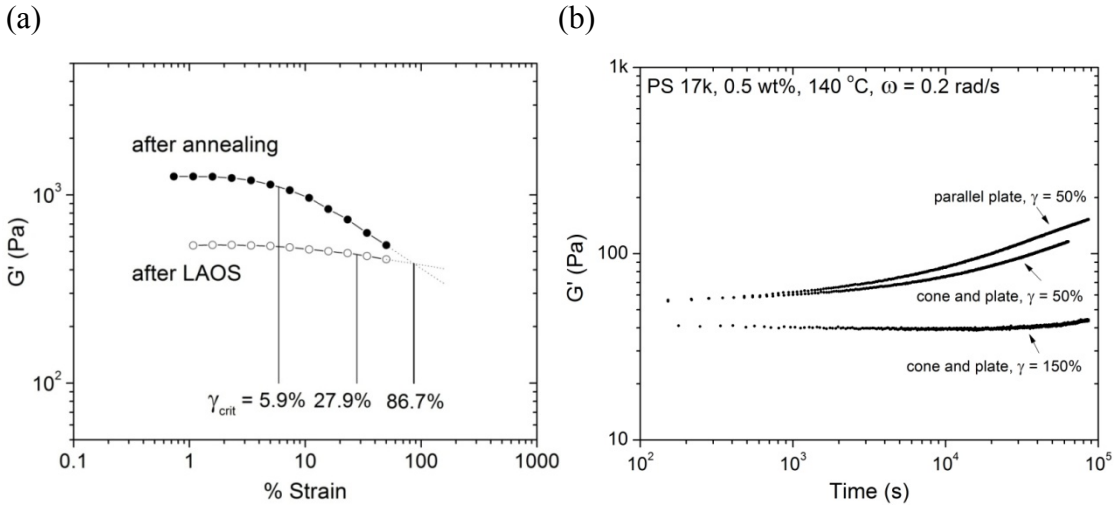

Figure 6-15. (a) Dynamic strain sweeps of 0.5 wt%/PS 17k composites at 140 °C conducted following LAOS using 120% strain and annealing at 140 °C for ~ 80,000 s. (b) Dynamic time sweeps of 0.5 wt% FGS/PS 17k at 140 °C using parallel plate and cone-and-plate geometry.

We also investigated effects of frequency of sinusoidal shear deformation for time sweeps and type of graphitic additives on property increase of composite melts. Influence of deformation frequency is minimal as indicated by nearly parallel G' and σ' growth between $a_T\omega = 0.2$ ($\omega = 17.42$) versus 0.053 rad/s (4.58 rad/s) (Figure 6-16). G' changes of graphite and FGS in PS 59k at 200 °C were compared in Figure 6-17 (a) and (b). Particle concentration of 5 wt% for graphite and 1 wt% for FGS were chosen for similar G' magnitude. No significant differences in viscoelasticity increase were detected by use of graphite versus FGS. Aspect ratio of graphite is smaller but it has higher bending stiffness while FGS is dispersed as highly flexible thin layers (see Figure 4-1 in Chapter 4). However, in Figure 6-17 (d), FGS shows a steady logarithmic increase in σ' over time while σ' growth becomes much faster at $t > 30{,}000$ sec for graphite.

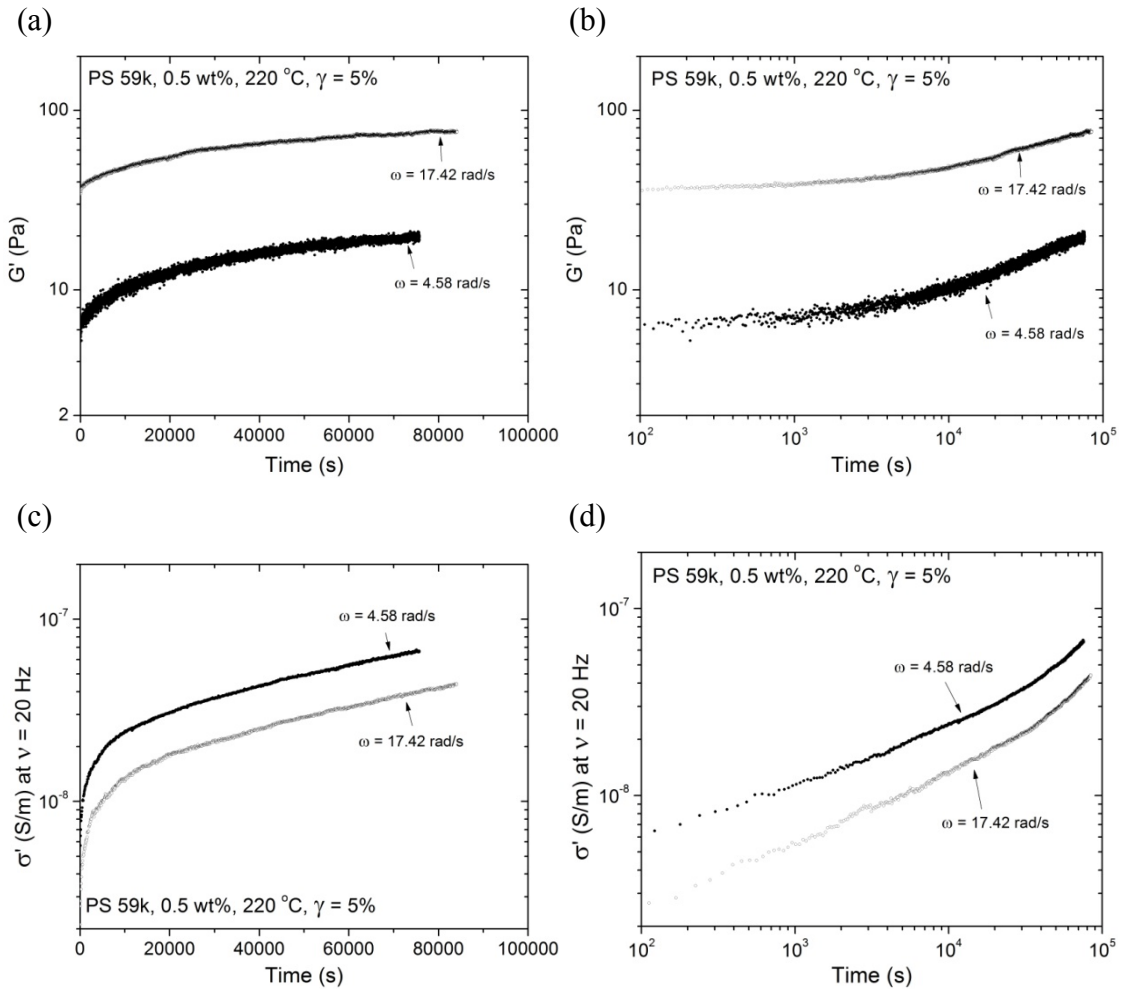

Figure 6-16. (a), (b) *G*' and (c), (d) σ" at ν = 20 Hz of 0.5 wt% FGS/PS 59k at 220 °C measured during dynamic time sweeps at γ = 5% and $a_T\omega$ = 0.053 (ω = 4.58) and 0.2 rad/s (17.42 rad/s).

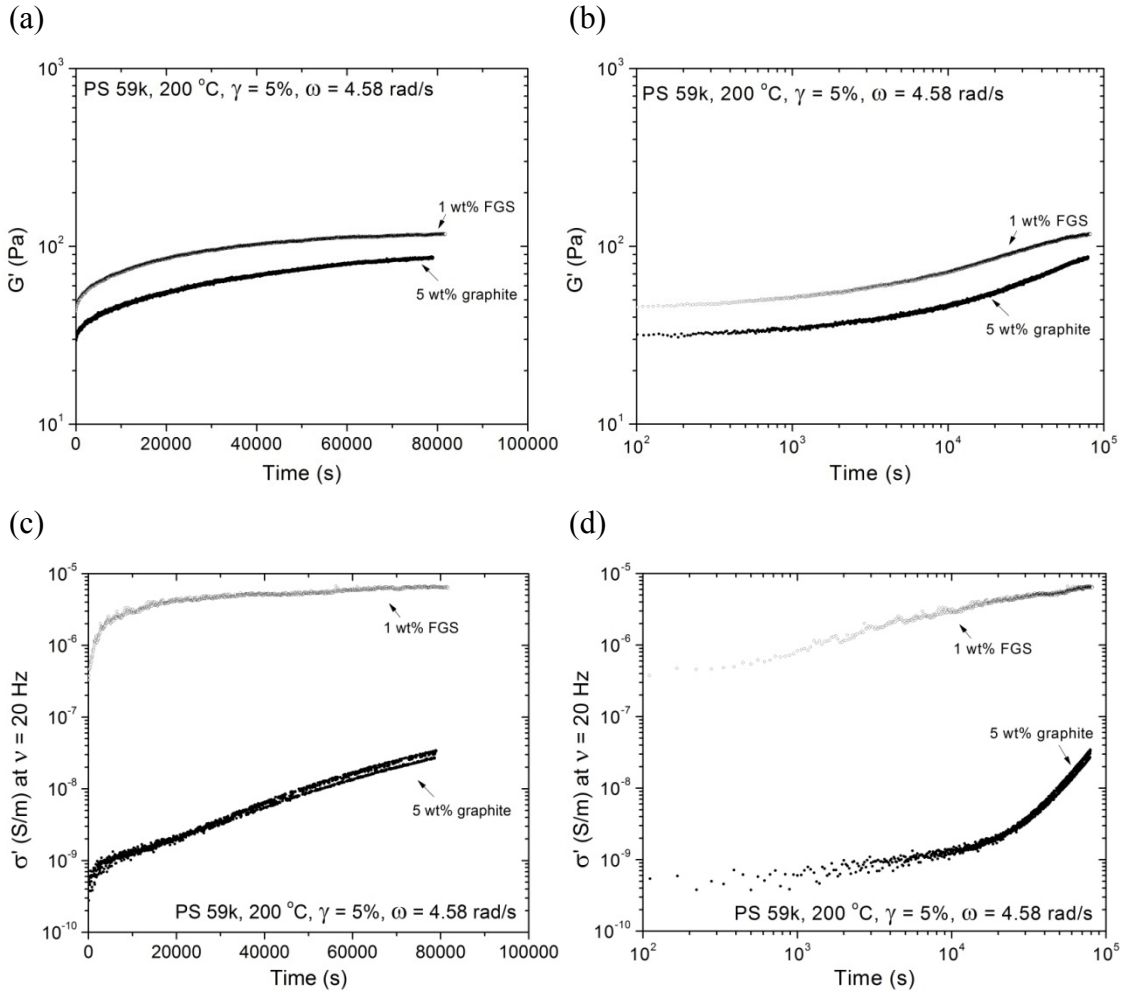

Figure 6-17. (a), (b) G' and (c), (d) σ' at $\nu = 20$ Hz of PS 59k containing 1 wt% FGS and 5 wt% graphite at 200 °C measured during dynamic time sweeps at $\gamma = 5\%$ and $a_T\omega = 0.2$ rad/s.

6.4. Summary

Dynamics for elasticity and electrical conductivity recovery of melt-state PS/FGS after cessation of large-amplitude shear was studied with in-line rheological and dielectric spectroscopy. After prolonged thermal annealing, composites gained enhanced viscoelasticity and electrical conductivity as a consequence of particle percolation. Aging also reduced the yield strain for FGS networks. Temporal growth in material elasticity resembles that of aging colloidal glasses below glass transition temperature: logarithmic

scaling with annealing time. Shear modulus and electrical conductivity increased faster at higher temperature and intermediate particle concentration. However, even at the same matrix viscosity, more rapid property restoration was observed from lower matrix molecular weight indicating particle disorientation is coupled with relaxation dynamics of matrix polymer. Application of deformation greater than critical strain during physical aging retarded G' increase, but also facilitated ε'' growth. Any particular correlations between frequency of oscillatory deformation and the aging response of composites were not found. The temperature dependence is indicative of that rotary relaxation is governed by thermal diffusion of particles. However, real aging process will be more intricate, affected by relaxation characteristics of polymer chains and excluded volume interaction of neighboring particles.

6.5. References

(1) Ren, J.; Casanueva, B. F.; Mitchell, C. A.; Krishnamoorti, R. *Macromolecules* **2003**, *36*, 4188-4194.

(2) Abou, B.; Bonn, D.; Meunier, J. *Phys. Rev. E* **2001**, *64*, 021510/1-021510/6.

(3) Trappe, V.; Prasad, V.; Cipelletti, L.; Segre, P. H.; Weitz, D. A. *Nature* **2001**, *411*, 772-775.

(4) Pusey, P. N.; Van Megen, W. *Phys. Rev. Lett.* **1987**, *59*, 2083-6.

(5) Dolgovskij, M. K. Ph. D. Thesis, University of Minnesota, 2006.

(6) Cox, W. P.; Merz, E. H. *J. Polym. Sci.* **1958**, *28*, 619-22.

(7) Maric, M.; Macosko, C. W. *Polym. Eng. Sci.* **2001**, *41*, 118-130.

(8) Dielectric Option for ARES, http://www.tainstruments.com/library_download.aspx?file=APN005_V1_DETA.pdf, Accessed August 15, 2009.

(9) Kremer, F.; Schonhals, A. In *Broadband Dielectric Spectroscopy*; Kremer, F., Schonhals, A., Eds.; Springer: Berlin, 2003.

(10) Fetters, L. J.; Lohse, D. J.; Milner, S. T.; Graessley, W. W. *Macromolecules* **1999**, *32*, 6847-6851.

(11) Williams, M. L.; Landel, R. F.; Ferry, J. D. *J. Am. Chem. Soc.* **1955**, *77*, 3701-7.

(12) Vermant, J.; Ceccia, S.; Dolgovskij, M. K.; Maffettone, P. L.; Macosko, C. W. *J. Rheol.* **2007**, *51*, 429-450.

(13) Kim, H.; Macosko, C. W. *Macromolecules* **2008**, *41*, 3317-3327.

(14) Kim, H.; Macosko, C. W. *Polymer* **2009**, *50*, 3797-3809.

(15) Shih, W. H.; Shih, W. Y.; Kim, S. I.; Liu, J.; Aksay, I. A. *Phys. Rev. A* **1990**, *42*, 4772-9.

(16) Agilent E4980A Precision LCR Meter Data Sheet, http://cp.literature.agilent.com/litweb/pdf/5989-4435EN.pdf, Accessed July 11, 2009.

(17) Kharchenko, S. B.; Douglas, J. F.; Obrzut, J.; Grulke, E. A.; Migler, K. B. *Nat. Mater.* **2004**, *3*, 564-568.

(18) Schniepp, H. C.; Li, J.-L.; McAllister, M. J.; Sai, H.; Herrera-Alonso, M.; Adamson, D. H.; Prud'homme, R. K.; Car, R.; Saville, D. A.; Aksay, I. A. *J. Phys. Chem. B* **2006**, *110*, 8535-8539.

(19) AC conductivity at $\nu = 2\times10^6$ Hz of PS at 200 °C is ~ 10^{-7} S/m (Figure 6-6). Assuming ε'' is nearly constant in the range of $\nu = 20\text{-}2\times10^6$ Hz, conductivity of PS can be estimated to be 10^{-13} ~ 10^{-7} S/m from equation (6.2).

(20) Lee, C.; Wei, X.; Kysar, J. W.; Hone, J. *Science* **2008**, *321*, 385-388.

(21) Alig, I.; Skipa, T.; Lellinger, D.; Poetschke, P. *Polymer* **2008**, *49*, 3524-3532.

(22) Bonn, D.; Tanase, S.; Abou, B.; Tanaka, H.; Meunier, J. *Phys. Rev. Lett.* **2002**, *89*, 015701/1-015701/4.

(23) Alig, I.; Lellinger, D.; Dudkin, S. M.; Poetschke, P. *Polymer* **2007**, *48*, 1020-1029.

(24) Scher, H.; Lax, M. *Phys. Rev. B* **1973**, *7*, 4491-502.

(25) Gefen, Y.; Aharony, A.; Alexander, S. *Phys. Rev. Lett.* **1983**, *50*, 77-80.

(26) Potschke, P.; Dudkin, S. M.; Alig, I. *Polymer* **2003**, *44*, 5023-5030.

(27) Stauffer, D.; Aharony, A. *Introduction to Percolation Theory*; Taylor & Francis: London, 1994.

(28) Lin-Gibson, S.; Pathak, J. A.; Grulke, E. A.; Wang, H.; Hobbie, E. K. *Phys. Rev. Lett.* **2004**, *92*, 048302/1-048302/4.

(29) Forsyth, P. A., Jr.; Marcelja, S.; Mitchell, D. J.; Ninham, B. W. *Adv. Colloid Interface Sci.* **1978**, *9*, 37-60.

(30) Du, F.; Scogna, R. C.; Zhou, W.; Brand, S.; Fischer, J. E.; Winey, K. I. *Macromolecules* **2004**, *37*, 9048-9055.

Chapter 7. Summary and Future Suggestions

7.1. Summary of Main Results

This thesis addressed processing, morphology and properties of graphene/polymer nanocomposites. Superior mechanical,[1] electrical[2] and thermal properties and potential high aspect ratio make graphene a versatile polymer reinforcement. Exfoliated carbon sheets can be obtained by instantaneously heating graphite oxide (GO) up to 1050 °C in an inert atmosphere.[3] Resulting functionalized graphene sheets (FGS) are as electrically conductive as natural graphite and can be processed into polymers via any routes including melt extrusion. However, atomistic defect formation and size reduction during thermal exfoliation can limit their reinforcement efficiency. GO can be modified with organic functional groups via liquid-phase reaction,[4] which enables fabrication of exfoliated nanocomposites using solvent blending. While large diameter of GO can be preserved and surface functionalization may lead to mechanically tough composites, isocyanate treated GO (iGO) cannot be processed at elevated temperature and additional chemical reduction steps are necessary for recovery of high electrical conductivity. Other physical and chemical characteristics of these reinforcements derived from GO are summarized in Chapter 2.

These exfoliated carbon sheets can be embedded into matrix polymers using melt and solvent processing, and *in-situ* polymerization. Although not as economically and environmentally viable as melt processing, blending with a polyurethane elastomer in solvents resulted in better dispersion of graphene as characterized by electron microscopy. Improved graphene dispersion from solvent mixing could be also inferred from higher electrical conductivity, mechanical and gas barrier properties of the composites. Electrical percolation could be achieved less than 0.5 wt% of FGS. 3 wt% iGO increased tensile modulus of the polyurethane up to 10 times and reduced nitrogen permeation by 90%. It is notable that property gains for *in-situ* polymerized composites were not as pronounced even though blending was conducted in solvents. Adding functionalized graphene might influence polymerization and physical properties of the

matrix. These processing-dispersion-property relationships of polyurethane/graphene composites are discussed in Chapter 3.

In Chapter 4, graphene dispersion characterized with a number of techniques is compared. Dispersion of FGS in poly(ethylene-2,6-naphthalate) (PEN) could be quantified in real space using imaging with transmission electron microscopy, and in reciprocal space using X-ray scattering. The results were comparable with dispersion extracted from percolation analyses: rigidity percolation from melt rheology and connectivity percolation from electrical conductivity. Solid properties such as hydrogen permeation, tensile modulus and thermal expansion were also measured. Fitting experimental data with composite theories provided average aspect ratios (A_f) of dispersed graphene. However, A_f evaluated from composite mechanical properties shows large discrepancy from those quantified from other techniques. This difference may originate from the non-ideal structure and morphology of dispersed FGS.

Another important factor that determines properties of layered nanocomposites is orientation of anisotropic fillers. Injection, compression molding and thermal annealing altered orientational state of graphite layers in polycarbonate (PC) substantially. Layer alignment quantified with X-ray scattering was greater for injection and compression molded samples indicating flow-induced orientation. Melt viscoelasticity and electrical conductivity of highly oriented samples were lower than those of annealed samples. Orientation-property relationships of graphene/PC composites are covered in Chapter 5 as well as solid composite properties.

In Chapter 5, electrical conductivity measured ex-situ on solid samples was reported. Chapter 6 presents viscoelastic and electrical properties of polystyrene (PS)/FGS composites monitored in-situ in melt state. PS composites exhibited variation in rheological and dielectric functions depending on previous processing history. Restoration of elasticity and electrical conduction following large-amplitude shearing was monitored. The aging response was affected significantly by annealing temperature, particle concentration, matrix molecular weight and strain magnitude, while frequency of oscillatory deformation and particle shape have minimal influence.

7.2. Suggestions for Future Research

This thesis listed benefits of graphene-based polymer nanocomposites. Electrical, mechanical and gas barrier properties of elastomers and engineering plastics can be substantially enhanced by adding even less than 3 wt% graphene. However, for practical applications, a number of issues in material design and processing have to be resolved. Two exfoliated carbon sheets used in this thesis work are derived from GO. Although oxidation is essential for thermal exfoliation and surface functionalization, it introduces substantial structural defects in flat graphene structure. As we discovered from the PEN and PC studies, oxidation-induced sheet weakening and particle size reduction could be detrimental especially when reinforcing glassy polymers. There have been several reports claiming splitting graphene without chemical functionalization.[5,6] While intercalation with surfactants[6] could be used for non-destructive exfoliation of graphite, it is restricted to lab-scale due to low yield, and difficult removal or recycle of surfactants may impose another challenge. Even thermal expansion of GO for FGS, an approach regarded as most suitable for large-scale graphene production[7] has its own limitation. Volume expansion of FGS is very sensitive to experimental conditions such as moisture content[3] and extent of oxidation. Design of large-scale or continuous processes and quality control of produced graphene should be pre-requisites for practical interest.

This thesis covered a variety of polymeric matrices: polyurethane, PEN and PC. Well exfoliated morphology of FGS in these polymers could be obtained due to their relatively high polarity. However, dispersion of graphene into other non-polar polymers has not been explored yet. Polyolefins such as polyethylene and polypropylene can be good candidates to study because they are produced and used in two largest tonnage.[8,9] Reinforcing polyolefins with layered silicates has not been successful without dispersion aids due to their low miscibility.[10] A preliminary study which is summarized in Appendix C indicated that FGS is also poorly dispersed into linear low density polyethylene via melt compounding and resulting tensile stiffness increase was not as pronounced. Strategies to maximize dispersion of graphene into the polymers with low chemical compatibility should be developed. One possible solution is modification of polyolefins

with polar functional groups. Functionalization of polyolefins has proven to improve miscibility and adhesion with polar polymers.[11]

Controlling spatial distribution of graphene inside the matrix is as important as achieving good dispersion. By controlling dispersed morphology appropriately, higher property gains can be achieved with less additives. It was shown that viscoelasticity and electrical conductivity of PC and PS can be reduced drastically by orientation of graphene layers. Since particle alignment by shear or extensional flow is inevitable in polymer processing in practice such as extrusion, injection and blow molding, methods to restore random filler orientation after processing have to be found for maximized electrical conductivity increase. Although subjecting oriented composites to prolonged thermal annealing may help, it is not economically practical, and not a feasible option for polymers that are prone to thermal degradation. In case of anisotropic conductive fillers such as carbon nanotubes (CNT), applying an electric voltage could align the rods to the direction of the electric field.[12,13] Moreover, forming co-continuous morphology of polymer blends of filler-rich and filler-less phase is known to reduce threshold for electrical percolation (double percolation).[14]

New application areas will open up for graphene nanocomposites with exceptional electrical, thermal and mechanical properties. CNT has proven to enhance polymers' shape-memory properties.[15] For this application, the reinforcing particles have to promote strain-induced crystallization of polymers for shape fixity after deformation, and be highly conductive for selective melting of polymer crystallites by applied heat or electricity for shape recovery. Since graphene can meet all these requirements, understanding shape-memory effects of polymers containing graphene will be beneficial. Also, electrical conduction through elastomers containing graphene may change drastically through elongation. This orientation-induced conductivity variation implies using graphene composites as sensors actuated by material deformation. Another possible application is using graphitic reinforcements to improve thermal conduction of polymers. Measuring thermal conductivity of graphene composite has been difficult since most commonly used thermal conductivity measurement set-ups (ASTM C 518) require large

volume of specimens.[16] More efficient ways for measuring thermal properties of thin graphene containing films need to be sought. Another practical use of conductive composites is electro-magnetic interference (EMI) deflection.[17] Testing graphene nanocomposites for EMI shielding performance may be explored in the future.

7.3. References

(1) Lee, C.; Wei, X.; Kysar, J. W.; Hone, J. *Science* **2008**, *321*, 385-388.

(2) Novoselov, K. S.; Geim, A. K.; Morozov, S. V.; Jiang, D.; Zhang, Y.; Dubonos, S. V.; Grigorieva, I. V.; Firsov, A. A. *Science* **2004**, *306*, 666-669.

(3) Schniepp, H. C.; Li, J.-L.; McAllister, M. J.; Sai, H.; Herrera-Alonso, M.; Adamson, D. H.; Prud'homme, R. K.; Car, R.; Saville, D. A.; Aksay, I. A. *J. Phys. Chem. B* **2006**, *110*, 8535-8539.

(4) Stankovich, S.; Piner, R. D.; Nguyen, S. T.; Ruoff, R. S. *Carbon* **2006**, *44*, 3342-3347.

(5) Hernandez, Y.; Nicolosi, V.; Lotya, M.; Blighe, F. M.; Sun, Z.; De, S.; McGovern, I. T.; Holland, B.; Byrne, M.; Gun'Ko, Y. K.; Boland, J. J.; Niraj, P.; Duesberg, G.; Krishnamurthy, S.; Goodhue, R.; Hutchison, J.; Scardaci, V.; Ferrari, A. C.; Coleman, J. N. *Nat. Nanotechnol.* **2008**, *3*, 563-568.

(6) Lotya, M.; Hernandez, Y.; King, P. J.; Smith, R. J.; Nicolosi, V.; Karlsson, L. S.; Blighe, F. M.; De, S.; Wang, Z.; McGovern, I. T.; Duesberg, G. S.; Coleman, J. N. *J. Am. Chem. Soc.* **2009**, *131*, 3611-3620.

(7) Jacoby, M. *Chem. Eng. News* **2009**, *87*, 14-20.

(8) Kaplan, W. A. *Modern Plastics Encyclopedia '98/ With Buyers' Guide*; McGraw-Hill/ Modern Plastics: New York, 1998; Vol. A-15.

(9) Reisch, M. S. *Chem. Eng. News* **1997**, *75*, 14.

(10) Kawasumi, M.; Hasegawa, N.; Kato, M.; Usuki, A.; Okada, A. *Macromolecules* **1997**, *30*, 6333-6338.

(11) Lu, Q.-W.; Macosko, C. W. *Polymer* **2004**, *45*, 1981-1991.

(12) Krupke, R.; Hennrich, F.; Weber, H. B.; Beckmann, D.; Hampe, O.; Malik, S.; Kappes, M. M.; von Loehneysen, H. *Appl. Phys. A: Mater. Sci. Process.* **2003**, *76*, 397-400.

(13) Mrozek, R. A.; Taton, T. A. *Chem. Mater.* **2005**, *17*, 3384-3388.

(14) Sumita, M.; Sakata, K.; Hayakawa, Y.; Asai, S.; Miyasaka, K.; Tanemura, M. *Colloid Polym. Sci.* **1992**, *270*, 134-9.

(15) Koerner, H.; Price, G.; Pearce, N. A.; Alexander, M.; Vaia, R. A. *Nat. Mater.* **2004**, *3*, 115-120.

(16) Harikrishnan, G.; Macosko, C. W.; Choi, J. H.; Bischof, J. C.; Singh, S. N. *J. Cell. Plast.* **2008**, *44*, 481-491.

(17) Al-Saleh, M. H.; Sundararaj, U. *Macromol. Mater. Eng.* **2008**, *293*, 789.

Chapter 8. Bibliography

1. Abdel-Goad, M.; Poetschke, P.; Zhou, D.; Mark, J. E.; Heinrich, G. *J. Macromol. Sci., Part A: Pure Appl. Chem.* **2007**, *44*, 591-598.
2. Abou, B.; Bonn, D.; Meunier, J. *Phys. Rev. E* **2001**, *64*, 021510/1-021510/6.
3. Ajayan, P. M.; Stephan, O.; Colliex, C.; Trauth, D. *Science* **1994**, *265*, 1212-1214.
4. Alexandre, M.; Dubois, P. *Mater. Sci. Eng., R* **2000**, *R28*, 1-63.
5. Alig, I.; Lellinger, D.; Dudkin, S. M.; Poetschke, P. *Polymer* **2007**, *48*, 1020-1029.
6. Alig, I.; Skipa, T.; Lellinger, D.; Poetschke, P. *Polymer* **2008**, *49*, 3524-3532.
7. Al-Jishi, R.; Dresselhaus, G. *Phys. Rev. B* **1982**, *26*, 4514-22.
8. Al-Saleh, M. H.; Sundararaj, U. *Macromol. Mater. Eng.* **2008**, *293*, 789.
9. Bacon, G. E. *Acta Cryst.* **1951**, *4*, 558-61.
10. Balberg, I. *Physical Review B* **1985**, *31*, 4053-4055.
11. Balberg, I.; Binenbaum, N. *Physical Review B* **1983**, *28*, 3799-3812.
12. Behabtu, N.; Green, M. J.; Pasquali, M. *Nanotoday* **2008**, *3*, 24-34.
13. Bharadwaj, R. K. *Macromolecules* **2001**, *34*, 9189-9192.
14. Bohlen, J.; Kirchheim, R. *Macromolecules* **2001**, *34*, 4210-4215.
15. Bonn, D.; Kellay, H.; Tanaka, H.; Wegdam, G.; Meunier, J. *Langmuir* **1999**, *15*, 7534-7536.
16. Bonn, D.; Tanase, S.; Abou, B.; Tanaka, H.; Meunier, J. *Phys. Rev. Lett.* **2002**, *89*, 015701/1-015701/4.
17. Brodie, B. C. *Philos. Trans. R. Soc. London* **1859**, *149*, 249-259.
18. Brunauer, S.; Emmett, P. H.; Teller, E. *J. Am. Chem. Soc.* **1938**, *60*, 309-19.
19. Brune, D. A.; Bicerano, J. *Polymer* **2001**, *43*, 369-387.
20. Bryning, M. B.; Islam, M. F.; Kikkawa, J. M.; Yodh, A. G. *Adv. Mater.* **2005**, *17*, 1186-1191.
21. Buchner, S.; Wiswe, D.; Zachmann, H. G. *Polymer* **1989**, *30*, 480-8.
22. Carr, K. E. *Carbon* **1970**, *8*, 155-66.
23. Celzard, A.; McRae, E.; Deleuze, C.; Dufort, M.; Furdin, G.; Mareche, J. F. *Phys. Rev. B: Condens. Matter* **1996**, *53*, 6209-14.
24. Chavarria, F.; Paul, D. R. *Polymer* **2006**, *47*, 7760-7773.
25. Chen, G.; Wu, D.; Weng, W.; Wu, C. *Carbon* **2003**, *41*, 619-621.
26. Cho, J. W.; Paul, D. R. *Polymer* **2000**, *42*, 1083-1094.
27. Cho, J.; Luo, J. J.; Daniel, I. M. *Compos. Sci. Technol.* **2007**, *67*, 2399-2407.
28. Choi, E. S.; Brooks, J. S.; Eaton, D. L.; Al-Haik, M. S.; Hussaini, M. Y.; Garmestani, H.; Li, D.; Dahmen, K. J. *J. Appl. Phys.* **2003**, *94*, 6034-6039.
29. Chow, T. S. *J. Polym. Sci., Part B: Polym. Phys.* **1978**, *16*, 967-70.
30. Chung, D. D. L. *J. Mater. Sci.* **1987**, *22*, 4190-4198.
31. Cooper, S. L.; Seymour, R. W.; Estes, G. M. *Macromolecules* **1970**, *3*, 579-83.
32. Cox, W. P.; Merz, E. H. *J. Polym. Sci.* **1958**, *28*, 619-22.

33. Cussler, E. L. *Diffusion: Mass Transfer in Fluid Systems*; 2nd ed.; Cambridge University Press: Cambridge, 1997.
34. Cussler, E. L.; Hughes, S. E.; Ward, W. J., III; Aris, R. *J. Membr. Sci.* **1988**, *38*, 161-74.
35. Daubeny, R. d. P.; Bunn, C. W.; Brown, C. J. *Proc. Roy. Soc. (London)* **1954**, *A226*, 531-42.
36. Davis, V. A.; Ericson, L. M.; Parra-Vasquez, A. N. G.; Fan, H.; Wang, Y.; Prieto, V.; Longoria, J. A.; Ramesh, S.; Saini, R. K.; Kittrell, C.; Billups, W. E.; Adams, W. W.; Hauge, R. H.; Smalley, R. E.; Pasquali, M. *Macromolecules* **2004**, *37*, 154-160.
37. Dennis, H. R.; Hunter, D. L.; Chang, D.; Kim, S.; White, J. L.; Cho, J. W.; Paul, D. R. *Polymer* **2001**, *42*, 9513-9522.
38. Dolgovskij, M. K. Ph. D. Thesis, University of Minnesota, 2006.
39. Dresselhaus, M. S.; Dresselhaus, G.; Jorio, A.; Souza Filho, A. G.; Saito, R. *Carbon* **2002**, *40*, 2043-2061.
40. Drzal, L. T.; Fukushima, H. *Polym. Prepr. (Am. Chem. Soc., Div. Polym. Chem.)* **2001**, *42*, 42-43.
41. Du, F.; Fischer, J. E.; Winey, K. I. *Phys. Rev. B: Condens. Matter Mater. Phys.* **2005**, *72*, 121404/1-121404/4.
42. Du, F.; Scogna, R. C.; Zhou, W.; Brand, S.; Fischer, J. E.; Winey, K. I. *Macromolecules* **2004**, *37*, 9048-9055.
43. Eda, G.; Fanchini, G.; Chhowalla, M. *Nat. Nanotechnol.* **2008**, *3*, 270-274.
44. Emtsev, K. V.; Bostwick, A.; Horn, K.; Jobst, J.; Kellogg, G. L.; Ley, L.; McChesney, J. L.; Ohta, T.; Reshanov, S. A.; Roehrl, J.; Rotenberg, E.; Schmid, A. K.; Waldmann, D.; Weber, H. B.; Seyller, T. *Nat. Mater.* **2009**, *8*, 203-207.
45. Eshelby, J. D. *Proc. Roy. Soc. (London)* **1957**, *241*, 376-396.
46. Feng, S.; Sen, P. N. *Phys. Rev. Lett.* **1984**, *52*, 216-219.
47. Fetters, L. J.; Lohse, D. J.; Milner, S. T.; Graessley, W. W. *Macromolecules* **1999**, *32*, 6847-6851.
48. Finnigan, B.; Martin, D.; Halley, P.; Truss, R.; Campbell, K. *Polymer* **2004**, *45*, 2249-2260.
49. Fisher, F. T.; Bradshaw, R. D.; Brinson, L. C. *Compos. Sci. Technol.* **2003**, *63*, 1689-1703.
50. Fornes, T. D.; Paul, D. R. *Polymer* **2003**, *44*, 4993-5013.
51. Fornes, T. D.; Yoon, P. J.; Paul, D. R. *Polymer* **2003**, *44*, 7545-7556.
52. Forsyth, P. A., Jr.; Marcelja, S.; Mitchell, D. J.; Ninham, B. W. *Adv. Colloid Interface Sci.* **1978**, *9*, 37-60.
53. Fukushima, H. PhD Thesis, Michigan State University, 2003.
54. Fukushima, H.; Drzal, L. T. *Ann Tech Conf- Soc Plast Eng* **2003**, 2230-2234.
55. Gefen, Y.; Aharony, A.; Alexander, S. *Phys. Rev. Lett.* **1983**, *50*, 77-80.

56. Gilman, J. W.; Jackson, C. L.; Morgan, A. B.; Harris, R., Jr.; Manias, E.; Giannelis, E. P.; Wuthenow, M.; Hilton, D.; Phillips, S. H. *Chem. Mater.* **2000**, *12*, 1866-1873.
57. Gilmour, I. W.; Trainor, A.; Haward, R. N. *J. Appl. Polym. Sci.* **1979**, *23*, 3129-38.
58. Haggenmueller, R.; Gommans, H. H.; Rinzler, A. G.; Fischer, J. E.; Winey, K. I. *Chem. Phys. Lett.* **2000**, *330*, 219-225.
59. Harikrishnan, G.; Macosko, C. W.; Choi, J. H.; Bischof, J. C.; Singh, S. N. *J. Cell. Plast.* **2008**, *44*, 481-491.
60. Head, D. A.; Levine, A. J.; MacKintosh, F. C. *Phys. Rev. E* **2003**, *68*, 061907/1-061907/15.
61. Hennig, G. R. *Prog. Inorg. Chem.* **1959**, *1*, 125-205.
62. Hernandez, Y.; Nicolosi, V.; Lotya, M.; Blighe, F. M.; Sun, Z.; De, S.; McGovern, I. T.; Holland, B.; Byrne, M.; Gun'Ko, Y. K.; Boland, J. J.; Niraj, P.; Duesberg, G.; Krishnamurthy, S.; Goodhue, R.; Hutchison, J.; Scardaci, V.; Ferrari, A. C.; Coleman, J. N. *Nat. Nanotechnol.* **2008**, *3*, 563-568.
63. Herrera-Alonso, M.; Abdala, A. A.; McAllister, M. J.; Aksay, I. A.; Prud'homme, R. K. *Langmuir* **2007**, *23*, 10644-10649.
64. Heyes, D. M.; McKenzie, D. J.; Buscall, R. *J. Colloid Interface Sci.* **1991**, *142*, 303-16.
65. Hirata, M.; Gotou, T.; Horiuchi, S.; Fujiwara, M.; Ohba, M. *Carbon* **2004**, *42*, 2929-2937.
66. Hontoria-Lucas, C.; Lopez-Peinado, A. J.; Lopez-Gonzalez, J. d. D.; Rojas-Cervantes, M. L.; Martin-Aranda, R. M. *Carbon* **1995**, *33*, 1585-92.
67. Hull, D.; Clyne, T. W. *An Introduction to Composite Materials*; 2nd ed.; Cambridge University Press: London, 1996.
68. Hummers, W. S., Jr.; Offeman, R. E. *J. Am. Chem. Soc.* **1958**, *80*, 1339.
69. Jacoby, M. *Chem. Eng. News* **2009**, *87*, 14-20.
70. Jeon, H. S.; Rameshwaram, J. K.; Kim, G. *J. Polym. Sci., Part B: Polym. Phys.* **2004**, *42*, 1000-1009.
71. Jeong, H.-K.; Krych, W.; Ramanan, H.; Nair, S.; Marand, E.; Tsapatsis, M. *Chem. Mater.* **2004**, *16*, 3838-3845.
72. Jeong, H.-K.; Lee, Y. P.; Lahaye, R. J. W. E.; Park, M.-H.; An, K. H.; Kim, I. J.; Yang, C.-W.; Park, C. Y.; Ruoff, R. S.; Lee, Y. H. *J. Am. Chem. Soc.* **2008**, *130*, 1362-1366.
73. Kalaitzidou, K.; Fukushima, H.; Drzal, L. T. *Carbon* **2007**, *45*, 1446-1452.
74. Kalaitzidou, K.; Fukushima, H.; Drzal, L. T. *Compos. Sci. Technol.* **2007**, *67*, 2045-2051.
75. Kalaitzidou, K.; Fukushima, H.; Drzal, L. T. *Composites: Part A* **2007**, *38*, 1675-1682.
76. Kanai, H.; Navarrete, R. C.; Macosko, C. W.; Scriven, L. E. *Rheol. Acta* **1992**, *31*, 333-44.
77. Kaplan, W. A. *Modern Plastics Encyclopedia '98/ With Buyers' Guide*;

McGraw-Hill/ Modern Plastics: New York, 1998; Vol. A-15.
78. Kawasumi, M.; Hasegawa, N.; Kato, M.; Usuki, A.; Okada, A. *Macromolecules* **1997**, *30*, 6333-6338.
79. Kelly, B. T. *Carbon* **1972**, *10*, 429-33.
80. Kelly, B. T. *Physics of Graphite*; 1st ed.; Applied Science: London, 1981.
81. Kharchenko, S. B.; Douglas, J. F.; Obrzut, J.; Grulke, E. A.; Migler, K. B. *Nat. Mater.* **2004**, *3*, 564-568.
82. Kim, H.; Macosko, C. W. *Ann Tech Conf- Soc Plast Eng* **2009**, 122-125.
83. Kim, H.; Macosko, C. W. *Macromolecules* **2008**, *41*, 3317-3327.
84. Kim, H.; Macosko, C. W. *Polymer* **2009**, *50*, 3797-3809.
85. Kim, K. S.; Zhao, Y.; Jang, H.; Lee, S. Y.; Kim, J. M.; Kim, K. S.; Ahn, J.-H.; Kim, P.; Choi, J.-Y.; Hong, B. H. *Nature* **2009**, *457*, 706-710.
86. Koerner, H.; Price, G.; Pearce, N. A.; Alexander, M.; Vaia, R. A. *Nat. Mater.* **2004**, *3*, 115-120.
87. Kojima, Y.; Usuki, A.; Kawasumi, M.; Okada, A.; Fukushima, Y.; Kurauchi, T.; Kamigaito, O. *J. Mater. Res.* **1993**, *8*, 1185-9.
88. Kovtyukhova, N. I.; Ollivier, P. J.; Martin, B. R.; Mallouk, T. E.; Chizhik, S. A.; Buzaneva, E. V.; Gorchinskiy, A. D. *Chem. Mater.* **1999**, *11*, 771-778.
89. Kremer, F.; Schonhals, A. In *Broadband Dielectric Spectroscopy*; Kremer, F., Schonhals, A., Eds.; Springer: Berlin, 2003.
90. Krishnamoorti, R.; Giannelis, E. P. *Macromolecules* **1997**, *30*, 4097-4102.
91. Krupke, R.; Hennrich, F.; Weber, H. B.; Beckmann, D.; Hampe, O.; Malik, S.; Kappes, M. M.; von Loehneysen, H. *Appl. Phys. A: Mater. Sci. Process.* **2003**, *76*, 397-400.
92. Kudin, K. N.; Ozbas, B.; Schniepp, H. C.; Prud'homme, R. K.; Aksay, I. A.; Car, R. *Nano Lett.* **2008**, *8*, 36-41.
93. Lamda, N. M. K.; Woodhouse, K. A.; Cooper, S. L. *Polyurethanes in biomedical applications*; CRC Press: Boca Raton, FL, 1998.
94. Lape, N. K.; Nuxoll, E. E.; Cussler, E. L. *J. Membr. Sci.* **2004**, *236*, 29-37.
95. Larson, R. G. *The Structure and Rheology of Complex Fluids*; Oxford Press: New York, 1999.
96. Lee, C.; Wei, X.; Kysar, J. W.; Hone, J. *Science* **2008**, *321*, 385-388.
97. Lee, H.-S.; Fasulo, P. D.; Rodgers, W. R.; Paul, D. R. *Polymer* **2005**, *46*, 11673-11689.
98. Lele, A.; Mackley, M.; Galgali, G.; Ramesh, C. *J. Rheol.* **2002**, *46*, 1091-1110.
99. Li, J.-L.; Kudin, K. N.; McAllister, M. J.; Prud'homme, R. K.; Aksay, I. A.; Car, R. *Phys. Rev. Lett.* **2006**, *96*, 176101/1-176101/4.
100. Liff, S. M.; Kumar, N.; McKinley, G. H. *Nat. Mater.* **2007**, *6*, 76-83.
101. Lin-Gibson, S.; Pathak, J. A.; Grulke, E. A.; Wang, H.; Hobbie, E. K. *Phys. Rev. Lett.* **2004**, *92*, 048302/1-048302/4.

102. Lotya, M.; Hernandez, Y.; King, P. J.; Smith, R. J.; Nicolosi, V.; Karlsson, L. S.; Blighe, F. M.; De, S.; Wang, Z.; McGovern, I. T.; Duesberg, G. S.; Coleman, J. N. *J. Am. Chem. Soc.* **2009**, *131*, 3611-3620.
103. Lu, Q.-W.; Macosko, C. W. *Polymer* **2004**, *45*, 1981-1991.
104. Ma, T.; Bhushan, B.; Murooka, H.; Kobayashi, I.; Osawa, T. *Rev. Sci. Instrum.* **2002**, *73*, 1813-1820.
105. Maric, M.; Macosko, C. W. *Polym. Eng. Sci.* **2001**, *41*, 118-130.
106. Matayabas Jr., J. C.; Turner, S. R. In *Polymer-Clay Nanocomposites*; Pinnavaia, T. J., Beall, G. W., Eds.; John Wiley & Sons: Chichester, 2000.
107. Matsuo, Y.; Tabata, T.; Fukunaga, T.; Fukutsuka, T.; Sugie, Y. *Carbon* **2005**, *43*, 2875-2882.
108. McAllister, M. J.; Li, J.-L.; Adamson, D. H.; Schniepp, H. C.; Abdala, A. A.; Liu, J.; Herrera-Alonso, M.; Milius, D. L.; Car, R.; Prud'homme, R. K.; Aksay, I. A. *Chem. Mater.* **2007**, *19*, 4396-4404.
109. Mencik, Z. *Chem. Prum.* **1967**, *17*, 78-81.
110. Messersmith, P. B.; Giannelis, E. P. *J. Polym. Sci., Part A: Polym. Chem.* **1995**, *33*, 1047-57.
111. Mewis, J.; Spaull, A. J. B. *Adv. Colloid Interface Sci.* **1976**, *6*, 173-200.
112. Miller, J. A.; Lin, S. B.; Hwang, K. K. S.; Wu, K. S.; Gibson, P. E.; Cooper, S. L. *Macromolecules* **1985**, *18*, 32-44.
113. Moniruzzaman, M.; Winey, K. I. *Macromolecules* **2006**, *39*, 5194-5205.
114. Mori, T.; Tanaka, K. *Acta Metall.* **1973**, *21*, 571-574.
115. Mrozek, R. A.; Taton, T. A. *Chem. Mater.* **2005**, *17*, 3384-3388.
116. Nelson, J. B.; Riley, D. P. *Proc. Phys. Soc.* **1945**, *57*, 477.
117. Novoselov, K. S.; Geim, A. K.; Morozov, S. V.; Jiang, D.; Zhang, Y.; Dubonos, S. V.; Grigorieva, I. V.; Firsov, A. A. *Science* **2004**, *306*, 666-669.
118. Ohl, N.; Gleissle, W. *J. Rheol.* **1993**, *37*, 381-406.
119. Osman, M. A.; Mittal, V.; Morbidelli, M.; Suter, U. W. *Macromolecules* **2003**, *36*, 9851-9858.
120. Ouchi, I.; Aoki, H.; Shimotsuma, S.; Asai, T.; Hosoi, M. *Proc. Japan Cong. Mater. Res.* **1974**, *17*, 217-23.
121. Pan, Y.-X.; Yu, Z.-Z.; Ou, Y.-C.; Hu, G.-H. *J. Polym. Sci., Part B: Polym. Phys.* **2000**, *38*, 1626-1633.
122. Patel, P. D.; Russel, W. B. *J. Rheol.* **1987**, *31*, 599-618.
123. Pattanayak, A.; Jana, S. C. *Polymer* **2005**, *46*, 3275-3288.
124. Picard, E.; Vermogen, A.; Gerard, J. F.; Espuche, E. *J. Membr. Sci.* **2007**, *292*, 133-144.
125. Pixton, M. R.; Paul, D. R. In *Polymeric Gas Separation Membranes*; Paul, D. R., Yampol'skii, Y. P., Eds.; CRC Press: Boca Raton, 1994, p 83-153.
126. Poetschke, P.; Bhattacharyya, A. R.; Janke, A.; Goering, H. *Compos. Interfaces* **2003**, *10*, 389-404.

127. Potschke, P.; Dudkin, S. M.; Alig, I. *Polymer* **2003**, *44*, 5023-5030.
128. Potschke, P.; Fornes, T. D.; Paul, D. R. *Polymer* **2002**, *43*, 3247-3255.
129. Prud'homme, R. K.; O'Neil, C. D.; Ozbas, B.; Aksay, I. A.; Register, R. A.; Adamson, D. H. WO 2008130431, **2007**
130. Pusey, P. N.; Van Megen, W. *Phys. Rev. Lett.* **1987**, *59*, 2083-6.
131. Pye, D. G.; Hoehn, H. H.; Panar, M. *J. Appl. Polym. Sci.* **1976**, *20*, 1921-31.
132. Qi, H. J.; Boyce, M. C. *Mech. Mater.* **2005**, *37*, 817-839.
133. Ramanathan, T.; Abdala, A. A.; Stankovich, S.; Dikin, D. A.; Herrera-Alonso, M.; Piner, R. D.; Adamson, D. H.; Schniepp, H. C.; Chen, X.; Ruoff, R. S.; Nguyen, S. T.; Aksay, I. A.; Prud'Homme, R. K.; Brinson, L. C. *Nat. Nanotechnol.* **2008**, *3*, 327-331.
134. Reisch, M. S. *Chem. Eng. News* **1997**, *75*, 14.
135. Ren, J.; Casanueva, B. F.; Mitchell, C. A.; Krishnamoorti, R. *Macromolecules* **2003**, *36*, 4188-4194.
136. Ren, J.; Silva, A. S.; Krishnamoorti, R. *Macromolecules* **2000**, *33*, 3739-3746.
137. Rueb, C. J.; Zukoski, C. F. *J. Rheol.* **1997**, *41*, 197-218.
138. Schaefer, D. W.; Justice, R. S. *Macromolecules* **2007**, *40*, 8501-8517.
139. Schaefer, D. W.; Justice, R. S.; Koerner, H.; Vaia, R.; Zhao, C.; Yang, M.; Vale, J. *Mater. Res. Soc. Symp. Proc.* **2005**, *840*, 57-62.
140. Scher, H.; Lax, M. *Phys. Rev. B* **1973**, *7*, 4491-502.
141. Schmidt, G.; Nakatani, A. I.; Butler, P. D.; Karim, A.; Han, C. C. *Macromolecules* **2000**, *33*, 7219-7222.
142. Schniepp, H. C.; Kudin, K. N.; Li, J.-L.; Prud'homme, R. K.; Car, R.; Saville, D. A.; Aksay, I. A. *ACS Nano* **2008**, *2*, 2577-2584.
143. Schniepp, H. C.; Li, J.-L.; McAllister, M. J.; Sai, H.; Herrera-Alonso, M.; Adamson, D. H.; Prud'homme, R. K.; Car, R.; Saville, D. A.; Aksay, I. A. *J. Phys. Chem. B* **2006**, *110*, 8535-8539.
144. Senich, G. A.; MacKnight, W. J. *Macromolecules* **1980**, *13*, 106-10.
145. Seymour, R. W.; Allegrezza, A. E.; Cooper, S. L. *Macromolecules* **1973**, *6*, 896-901.
146. Seymour, R. W.; Cooper, S. L. *Macromolecules* **1973**, *6*, 48-53.
147. Shante, V. K. S.; Kirkpatrick, S. *Adv. Phys.* **1971**, *20*, 325.
148. Shen, J.-W.; Chen, X.-M.; Huang, W.-Y. *J. Appl. Polym. Sci.* **2003**, *88*, 1864-1869.
149. Sheng, N.; Boyce, M. C.; Parks, D. M.; Rutledge, G. C.; Abes, J. I.; Cohen, R. E. *Polymer* **2004**, *45*, 487-506.
150. Shih, W. H.; Shih, W. Y.; Kim, S. I.; Liu, J.; Aksay, I. A. *Phys. Rev. A* **1990**, *42*, 4772-9.
151. Smith, A. W.; Rasor, N. S. *Phys. Rev.* **1956**, *104*, 885-91.
152. Solomon, M. J.; Almusallam, A. S.; Seefeldt, K. F.; Somwangthanaroj, A.; Varadan, P. *Macromolecules* **2001**, *34*, 1864-1872.

153. Spitael, P.; Macosko, C. W. *Polym. Eng. Sci.* **2004**, *44*, 2090-2100.
154. Stankovich, S.; Dikin, D. A.; Dommett, G. H. B.; Kohlhaas, K. M.; Zimney, E. J.; Stach, E. A.; Piner, R. D.; Nguyen, S. T.; Ruoff, R. S. *Nature* **2006**, *442*, 282-286.
155. Stankovich, S.; Dikin, D. A.; Piner, R. D.; Kohlhaas, K. A.; Kleinhammes, A.; Jia, Y.; Wu, Y.; Nguyen, S. T.; Ruoff, R. S. *Carbon* **2007**, *45*, 1558-1565.
156. Stankovich, S.; Piner, R. D.; Nguyen, S. T.; Ruoff, R. S. *Carbon* **2006**, *44*, 3342-3347.
157. Staudenmaier, L. *Ber. Dtsch. Chem. Ges.* **1898**, *31*, 1481.
158. Stauffer, D.; Aharony, A. *Introduction to Percolation Theory*; Taylor & Francis: London, 1994.
159. Sumita, M.; Sakata, K.; Hayakawa, Y.; Asai, S.; Miyasaka, K.; Tanemura, M. *Colloid Polym. Sci.* **1992**, *270*, 134-9.
160. Sun, Y.-P.; Fu, K.; Lin, Y.; Huang, W. *Acc. Chem. Res.* **2002**, *35*, 1096-1104.
161. Szabo, T.; Berkesi, O.; Dekany, I. *Carbon* **2005**, *43*, 3186-3189.
162. Tamashuasky, A. V. In *National Lubricating Grease Institute 72nd Annual Meeting* San Antonio, TX, 2005.
163. Tandon, G. P.; Weng, G. J. *Polym. Compos.* **1984**, *5*, 327-333.
164. Thorpe, M. F. In *Physics of Disordered Materials*; Adler, D., Fritzsche, H., Ovshinsky, S., Eds.; Plenum Press: New York, 1985, p 55-61.
165. Tien, Y. I.; Wei, K. H. *Macromolecules* **2001**, *34*, 9045-9052.
166. Titelman, G. I.; Gelman, V.; Bron, S.; Khalfin, R. L.; Cohen, Y.; Bianco-Peled, H. *Carbon* **2005**, *43*, 641-649.
167. Trappe, V.; Prasad, V.; Cipelletti, L.; Segre, P. H.; Weitz, D. A. *Nature* **2001**, *411*, 772-775.
168. Tuinstra, F.; Koenig, J. L. *J. Chem. Phys.* **1970**, *53*, 1126-30.
169. Usuki, A.; Kawasumi, M.; Kojima, Y.; Okada, A.; Kurauchi, T.; Kamigaito, O. *J. Mater. Res.* **1993**, *8*, 1174-8.
170. Usuki, A.; Kojima, Y.; Kawasumi, M.; Okada, A.; Fukushima, Y.; Kurauchi, T.; Kamigaito, O. *J. Mater. Res.* **1993**, *8*, 1179-84.
171. Vaia, R. A.; Giannelis, E. P. *Macromolecules* **1997**, *30*, 7990-7999.
172. Vaia, R. A.; Jandt, K. D.; Kramer, E. J.; Giannelis, E. P. *Chem. Mater.* **1996**, *8*, 2628-2635.
173. van Olphen, H. *Clay Colloid Chemistry*; 2nd ed.; John Wiley & Sons: New York, 1977.
174. Vermant, J.; Ceccia, S.; Dolgovskij, M. K.; Maffettone, P. L.; Macosko, C. W. *J. Rheol.* **2007**, *51*, 429-450.
175. Viculis, L. M.; Mack, J. J.; Kaner, R. B. *Science* **2003**, *299*, 1361.
176. Viculis, L. M.; Mack, J. J.; Mayer, O. M.; Hahn, H. T.; Kaner, R. B. *J. Mater. Chem.* **2005**, *15*, 974-978.
177. Wang, D. H.; Arlen, M. J.; Baek, J.-B.; Vaia, R. A.; Tan, L.-S. *Macromolecules* **2007**, *40*, 6100-6111.

178. Weick, B. L.; Bhushan, B. *IEEE Trans. Magn.* **1995**, *31*, 2937-9.
179. Wen, X.; Garland, C. W.; Hwa, T.; Kardar, M.; Kokufuta, E.; Li, Y.; Orkisz, M.; Tanaka, T. *Nature* **1992**, *355*, 426-8.
180. Widya, T.; Macosko, C. *J. Macromol. Sci., Part B: Phys.* **2005**, *44*, 897-908.
181. Williams, M. L.; Landel, R. F.; Ferry, J. D. *J. Am. Chem. Soc.* **1955**, *77*, 3701-7.
182. Wong, R. B. K.; Lelievre, J. *Rheol. Acta* **1981**, *20*, 299-307.
183. Woods, G. *The ICI polyurethanes book*; Wiley: New York, 1990.
184. Xia, H.; Song, M. *J. Mater. Chem.* **2006**, *16*, 1843-1851.
185. Yang, D.; Velamakanni, A.; Bozoklu, G.; Park, S.; Stoller, M.; Piner, R. D.; Stankovich, S.; Jung, I.; Field, D. A.; Ventrice, C. A., Jr.; Ruoff, R. S. *Carbon* **2009**, *47*, 145-152.
186. Yang, W. P.; Macosko, C. W.; Wellinghoff, S. T. *Polymer* **1986**, *27*, 1235-40.
187. Yano, K.; Usuki, A.; Okada, A. *J. Polym. Sci., Part A: Polym. Chem.* **1997**, *35*, 2289-2294.
188. Yano, K.; Usuki, A.; Okada, A.; Kurauchi, T.; Kamigaito, O. *J. Polym. Sci., Part A: Polym. Chem.* **1993**, *31*, 2493-8.
189. Yoon, K. H.; Lee, S. C.; Park, I. H.; Lee, H. M.; Park, O. O.; Son, T. W. *Polymer* **1997**, *38*, 6079-6081.
190. Yoon, P. J.; Fornes, T. D.; Paul, D. R. *Polymer* **2002**, *43*, 6727-6741.
191. Zalan, Z.; Lazar, L.; Fueloep, F. *Curr. Org. Chem.* **2005**, *9*, 357-376.
192. Zheng, W.; Wong, S.-C.; Sue, H.-J. *Polymer* **2002**, *43*, 6767-6773.
193. Zhu, J.; Kim, J.; Peng, H.; Margrave, J. L.; Khabashesku, V. N.; Barrera, E. V. *Nano Lett.* **2003**, *3*, 1107-1113.
194. Zimney, E. J.; Dommett, G. H. B.; Rouff, R. S.; Dikin, D. A. *Meas. Sci. Technol.* **2007**, *18*, 2067-2073.
195. Zosel, A. *Rheol. Acta* **1982**, *21*, 72-80.
196. Zou, J.-F.; Yu, Z.-Z.; Pan, Y.-X.; Fang, X.-P.; Ou, Y.-C. *J. Polym. Sci., Part B: Polym. Phys.* **2002**, *40*, 954-963.

Appendix A. Solid Properties of TPU Composites

Table A-1. DC Surface Resistance of TPU Composites

Sample		Concentration (wt%)		Surface resistance (Ohms)
		wt%	vol%	
TPU/graphite	Melt blend, bar	0	0	6.3×10^{10}
		3	1.6	7.4×10^{9}
		5	2.7	1.1×10^{10}
		10	5.6	5.1×10^{9}
		15	8.6	3.1×10^{6}
		20	11.7	2.5×10^{4}
	Melt blend, film	0	0	8.6×10^{10}
		1	0.5	2.3×10^{10}
		3	1.6	3.2×10^{10}
		5	2.7	4.9×10^{10}
		10	5.6	3.0×10^{9}
		15	8.6	8.6×10^{6}
		20	11.7	1.2×10^{6}
TPU/FGS	Melt blend, bar	1.0	0.5	1.7×10^{9}
		1.5	0.8	2.8×10^{7}
		2.0	1.1	5.2×10^{5}
		3.0	1.6	4.0×10^{2}
	Melt blend, film	0.5	0.3	4.8×10^{10}
		1.0	0.5	5.4×10^{8}
		1.5	0.8	2.3×10^{7}
		2.0	1.1	1.7×10^{6}
		3.0	1.6	4.5×10^{5}
		4.0	2.2	5.0×10^{2}
	Solvent blend	0	0	4.6×10^{10}
		0.5	0.3	2.1×10^{7}
		1.0	0.5	5.8×10^{4}
		3.0	1.6	1.6×10^{2}
	In-situ polymerized	0	0	5.3×10^{10}
		0.5	0.2	3.7×10^{10}
		0.9	0.5	8.2×10^{5}
		2.7	1.4	7.4×10^{2}

Table A-2. Mechanical Properties of TPU Composites

Sample		wt%	Modulus (MPa)	% Strain at break	Tensile Stress (MPa)	Toughness (MPa)
Melt blend	Graphite	0	6.1	1660	17.5	157
		3	6.4	1460	15.5	154
		5	8.7	1810	16.2	198
		10	8.8	1090	13.8	113
		15	22.5	590	13.9	66.4
		20	-	410	14.3	47.7
	FGS	0.5	9.1	1940	18.9	220
		1.0	11.5	1400	17.5	163
		1.5	14.5	1130	13.9	113
		2.0	15.7	830	12.4	83.3
		3.0	20.8	400	11.4	36.3
		4.0	-	380	14.4	43.5
Solvent blend	FGS	0	6.6	1030	22.2	94.6
		0.5	13.3	1540	15.8	125
		1.0	15.5	920	14.4	69.9
		3.0	53.2	830	9.64	45.5
	Ph-iGO	0.5	12.1	1270	21.8	128
		1.0	18.7	1210	15.0	96.6
		3.0	69.1	1160	13.4	82.2
	AcPh-iGO	0.5	10.5	960	13.0	64.9
		1.0	19.6	1190	13.2	81.7
		3.0	38.1	790	9.51	54.4
In-situ polymerized	FGS	0	7.2	1260	14.4	103
		0.5	7.0	1090	35.6	167
		0.9	11.7	980	33.1	113
		2.7	23.1	850	17.8	105
	GO	0.5	7.2	1250	44.9	199
		0.9	9.8	1230	19.9	134
		2.8	28.7	1570	13.8	158

Table A-3. N_2 and He Permeability of TPU Composites

Sample		wt%	N_2 permeation	He permeation
			Barrers	
Melt blend	Graphite	0	0.92	6.3
		1	0.83	-
		3	0.88	-
		5	0.72	-
		10	0.58	-
		15	0.47	-
		20	0.29	-
	FGS	0.5	0.66	6.0
		1.0	0.64	5.4
		1.5	0.57	5.0
		2.0	0.50	4.2
		3.0	0.44	3.8
		4.0	0.40	3.2
Solvent blend	FGS	0	0.81	5.9
		0.5	0.41	3.1
		1.0	0.26	2.4
		3.0	0.15	1.7
	Ph-iGO	0.5	0.41	4.1
		1.0	0.28	4.2
		3.0	0.01	1.5
	AcPh-iGO	0.5	0.38	4.2
		1.0	0.21	4.0
		3.0	0.05	2.3
In-situ polymerized	FGS	0	0.63	5.2
		0.5	0.41	4.6
		2.7	0.18	2.5
	GO	0.5	0.43	3.8
		0.9	0.33	2.8
		2.8	0.24	3.3

Appendix B. Rheological Properties of Polystyrene/Functionalized Graphene Sheets Composites

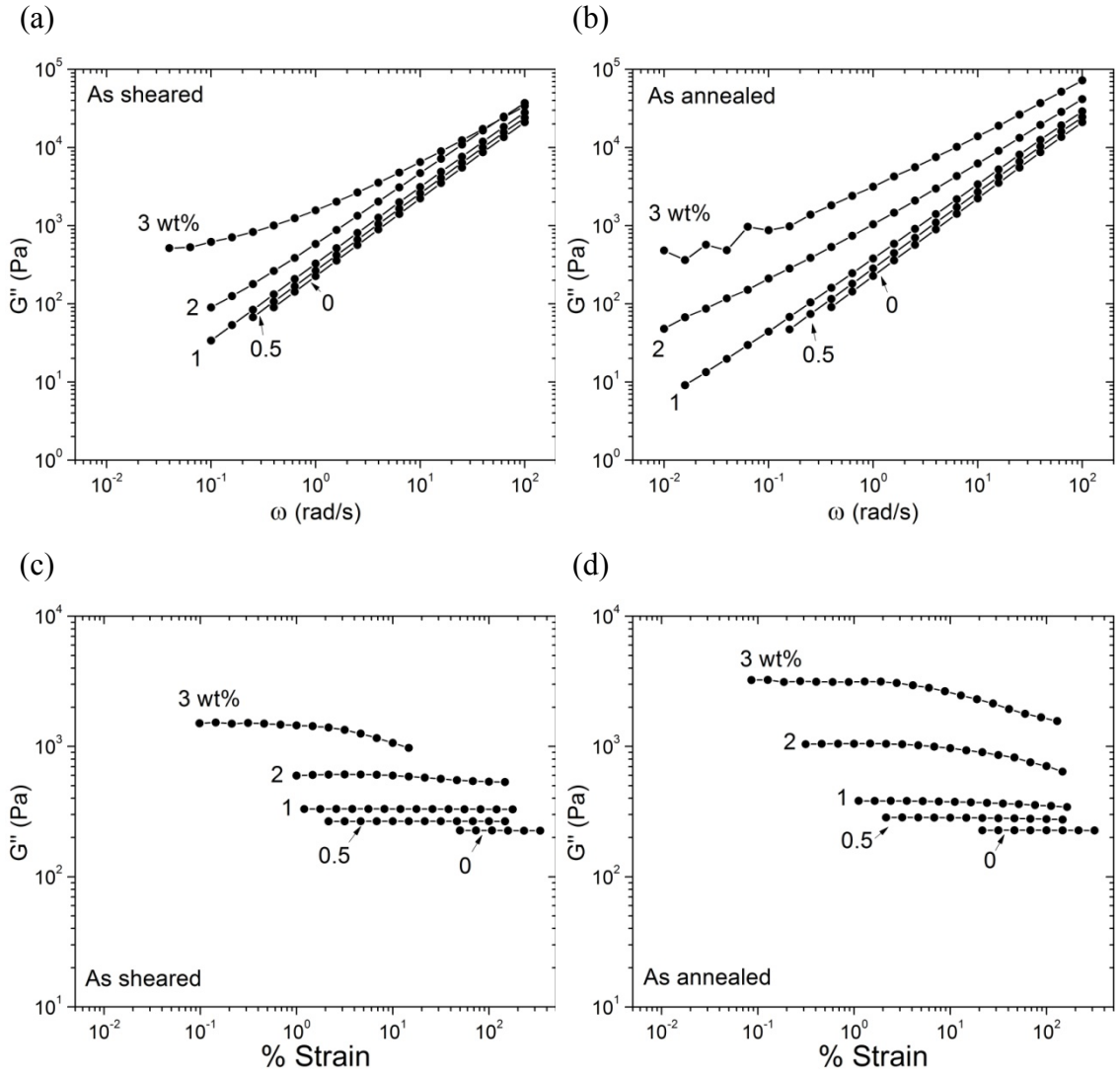

Figure B-1. *G*" from dynamic frequency sweeps of (a) as-sheared and (b) as-annealed PS 59k/FGS composites at 200 °C and from dynamic strain sweeps at 1 rad/s of (c) as-sheared and (d) as-annealed composites at 200 °C.

Appendix C. Functionalized Graphene Sheets Reinforced Polyethylene Composites

Polyethylene (PE) is one of the most important commodity polymers being produced and processed nearly 60 million tons/yr.[1] Good weatherability, and flexibility and elasticity that can be tuned by molecular architecture and crystallinity make PE attractive materials in a broad range of applications from houseware to automotive and construction. Properties of PE can be improved via reinforcements with high aspect ratio, rigid graphene sheets. In this part of thesis, preliminary results of melt processing and characterization of linear low density PE reinforced with functionalized graphene sheets (FGS) are covered.

For the matrix PE, Dow affinity EG-8200 was chosen. EG-8200 is a low-density PE derived from saturation of ethylene-octene copolymers (weight average molecular weight = 82 kg/mol, melt flow index: 5 g/10 min at 190 °C).[2] Same PE, but grafted with maleic anhydride (MA) functional groups (EG-8200-MA) was also provided from Dow chemical. FGS was obtained from two different sources: Petroleum Institute (PI) in United Arab Emirates, and Vorbeck Materials. They were synthesized in same procedures: oxidation of graphite using Staudenmaier's approach,[3] followed by rapid pyrolysis in an oven preheated at ~ 1050 °C.[4] They will be denoted as FGS-PI and FGS-Vorbeck respectively for the remainder of this section. Some FGS-PI was dispersed, compressed in water, and collected after water evaporation for densification. Higher bulk density of resulting FGS (see Figure C-1) facilitated feeding into the melt extruders. Also note substantially different apparent densities of as-synthesized FGS from PI and Vorbeck. This implies volume expansion of GO via superheating may vary from sample to sample, highly sensitively to the experiment conditions. Densified FGS-PI was compounded with EG-8200 and EG-8200-MA using DACA microcompounder, a vertical, 4-gram scale, conical, twin-screw extruder with a recirculation channel. All blends were prepared by mixing for 8 min at 180 °C at a screw speed of 200 RPM.

DACA extrudates were processed into ~ 0.1 mm thick films using hot pressing at 180 °C for further testing.

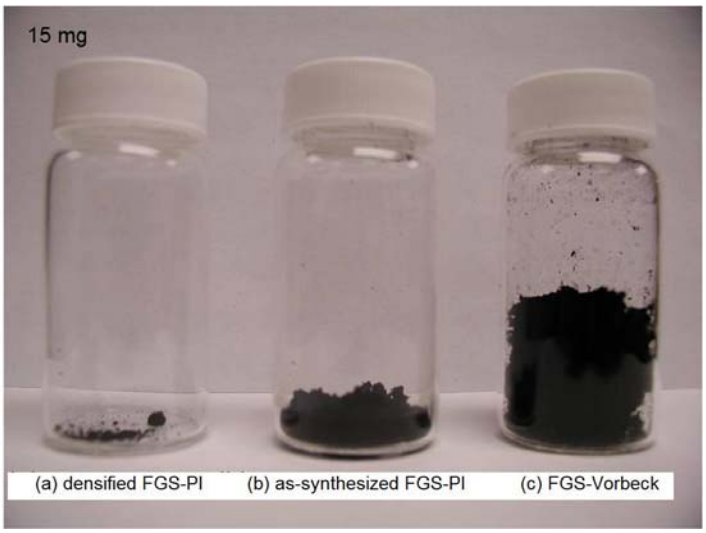

Figure C-1. Volume of ~ 15 mg of (a) as-densified FGS-PI, (b) as-synthesized FGS-PI and (c) as-synthesized FGS-Vorbeck.

Extent of FGS exfoliation was examined using powder X-ray diffraction. Wide-angle X-ray diffractograms of as-received FGS were obtained using SIEMENS D5005 in the 2θ range of 5 – 40 ° at the scan rate of 0.02 °/s. Unlike graphite which exhibit a sharp reflection at $2\theta = 26.4$ °, all FGS do not show any prominent X-ray diffraction in $2\theta = 5$ – 40 ° in Figure C-2, which signifies nearly complete layer exfoliation. A weak reflection centered at $2\theta = 23 \sim 25°$ of as-densified FGS-PI may stem from a small fraction of restacked graphene or "turbostratic" graphite formed during densification process.[5]

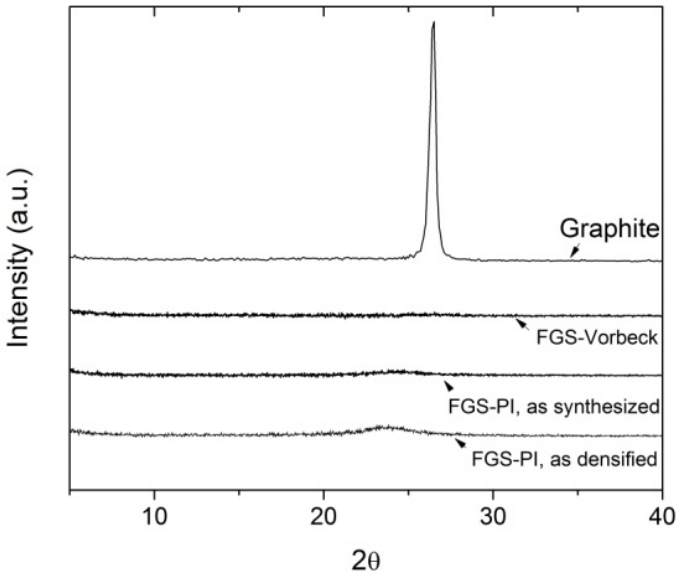

Figure C-2. Wide-angle X-ray diffraction of (from top to bottom) graphite, FGS-Vorbeck, as-synthesized and as-densified FGS-PI.

Transmission electron micrographs (TEM) of as-extruded FGS/PE composites were obtained with JEOL 1210 electron microscope. Composites were sectioned into ~ 90 nm thick slices at ~ -100 °C with a diamond knife using Reichert Ultracut. In the TEM of PE containing melt blended 1 wt% densified FGS-PI (Figure C-3 (a) and (b)), layers are spaced closely with one another. While spatial distribution of FGS-Vorbeck in PE is more homogeneous (Figure C-3 (c)), sheets imaged in higher magnification are still layered (Figure C-3 (d)) and interfacial fracture between PE and FGS is also observed.

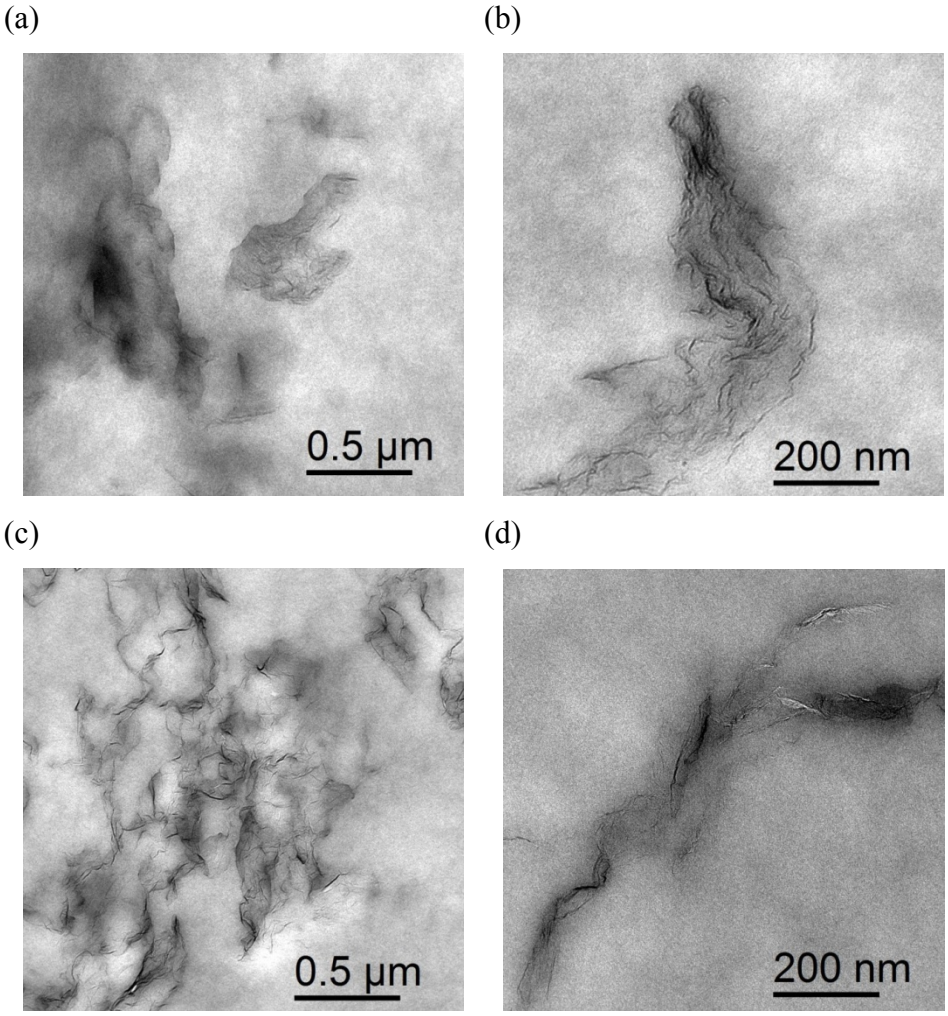

Figure C-3. TEM images of melt blended EG-8200 containing 1 wt% (a), (b) densified FGS-PI, (c) and (d) FGS-Vorbeck.

Linear viscoelastic measurements of FGS/PE composites at 200 °C were conducted with a strain-controlled, rotational rheometer (ARES, TA Instruments). After loading onto 25-mm parallel plates, samples were allowed to age for ~ 24 hrs to erase any effects from graphene orientation. Steady increase in G' monitored during annealing (dynamic time sweeps at angular frequency ω of 0.1 rad/s) (Figure C-4 (a)), which is more pronounced at higher FGS concentration, implies FGS starts to disorient and interact with one another. After this structural recovery, dynamic strain sweeps were

performed at 1 rad/s to determine the onset strain γ_{crit} for the non-linear viscoelastic response (Figure C-5 (a)). As particle concentration is increased, elasticity of PE melts is enhanced and *G*' started to decline at smaller γ_{crit}. Dynamic frequency sweeps at $\gamma < \gamma_{crit}$ (Figure C-5 (b)) indicates FGS addition increases *G*' at entire ω probed. Most drastic increase in *G*' is observed between 2 and 3 wt% of FGS. The transition from terminal to frequency independence behavior is suggestive of internal rigidity percolation of FGS. According to equation (4.3), percolation threshold of 2 ~ 3 wt% translates into an average particle aspect ratio A_f of 40 ~ 50. Comparing with particle A_f of FGS dispersed in other polymers evaluated in Chapter 3, 4 and 5, this value is considerably smaller and suggests relatively poor dispersion in PE. Note the abnormal aging response of pure EG-8200-MA, gradual *G*' growth over 24 hrs through annealing at 200 °C, as shown in Figure C-4 (b). This thermal instability of functionalized PE, possibly caused by cross-linking of chains by MA groups or residual peroxides catalyst, did not allow using melt rheology to investigate FGS dispersion.

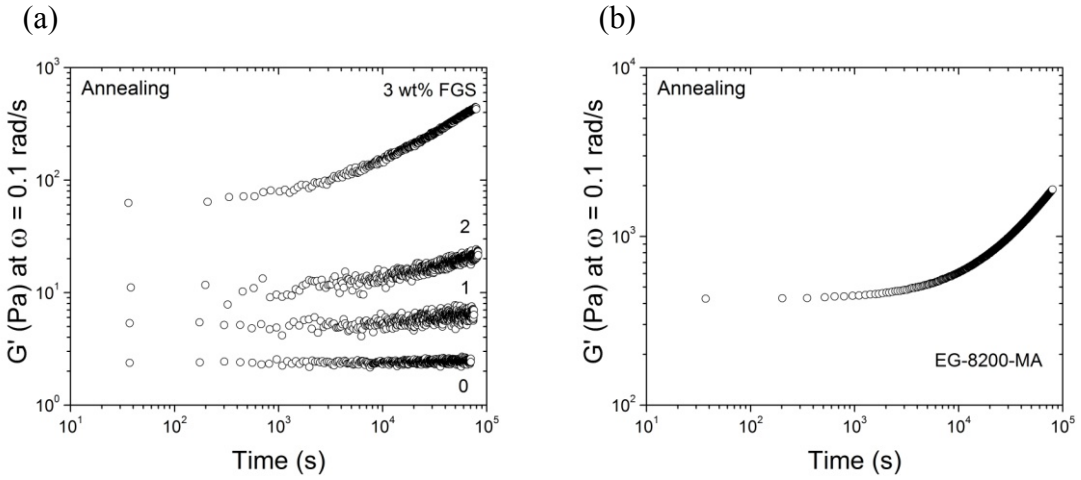

Figure C-4. *G*' change at ω = 0.1 rad/s during annealing at 200 °C of melt blended (a) EG-8200 and FGS composites and (b) EG-8200-MA.

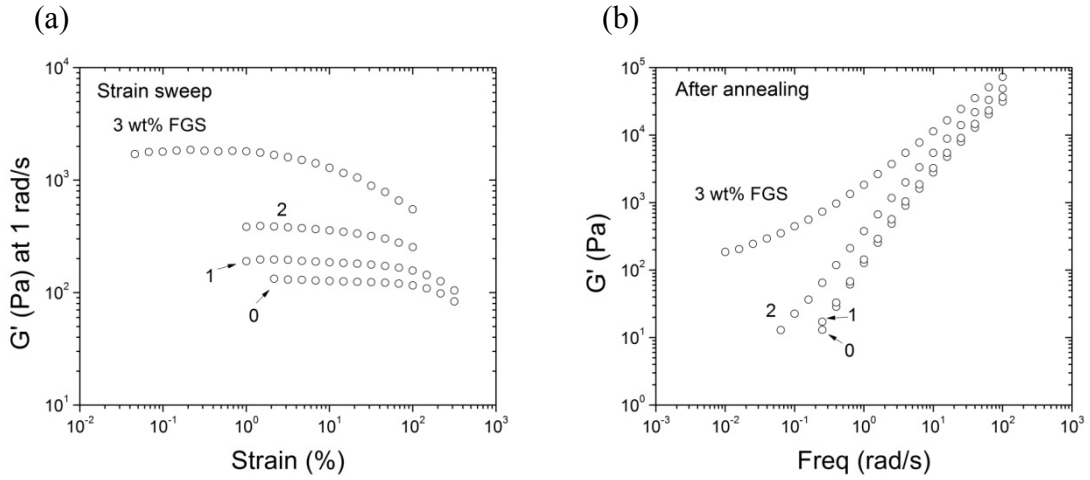

Figure C-5. (a) Dynamic strain sweeps at $\omega = 1$ rad/s and (b) frequency sweeps at $\gamma < \gamma_{crit}$ at 200 °C of EG-8200 and FGS composites.

Mechanical properties of EG-8200 dispersed with densified FGS-PI were evaluated with Rheometrics Solids Analyzer II (RSA II) and TA Instruments Minimat. Table C-1 and C-2 summarize tensile moduli measured by stretching ~ 4 mm wide films at the rate of 0.005 /s (RSA II), and ultimate mechanical properties (e.g. tensile strength, strain at break and toughness) obtained from extending the films at 0.024 /s using Minimat. Representative tensile responses of FGS/PE composites are shown in Figure C-6. 3 wt% densified FGS-PI led to ~ 100% increase in tensile moduli of EG-8200. This is a relatively small increase, considering modulus of thermoplastic polyurethane with similar tensile stiffness could be enhanced 3-10 fold by same FGS incorporation (see Figure 3-8). Using FGS-Vorbeck did not change the modulus gain appreciably. Moduli of EG-8200 and EG-8200-MA containing 1 wt% FGS are not notably different implying no significant influence of MA functionalization. However, distinctive behaviors were observed from ultimate tensile testing of EG-8200 and EG-8200-MA. While FGS slightly reduced the strain at break and tensile strength of EG-8200, FGS composites fractured at substantially higher elongation than neat polymers for MA-functionalized PE. As a consequence, toughness (e.g. the area under the stress versus strain curves) of EG-8200-

MA could be nearly doubled by 1 wt% FGS. Strong interaction between MA groups and oxygen functionalities on FGS may enhance the interfacial adhesion.

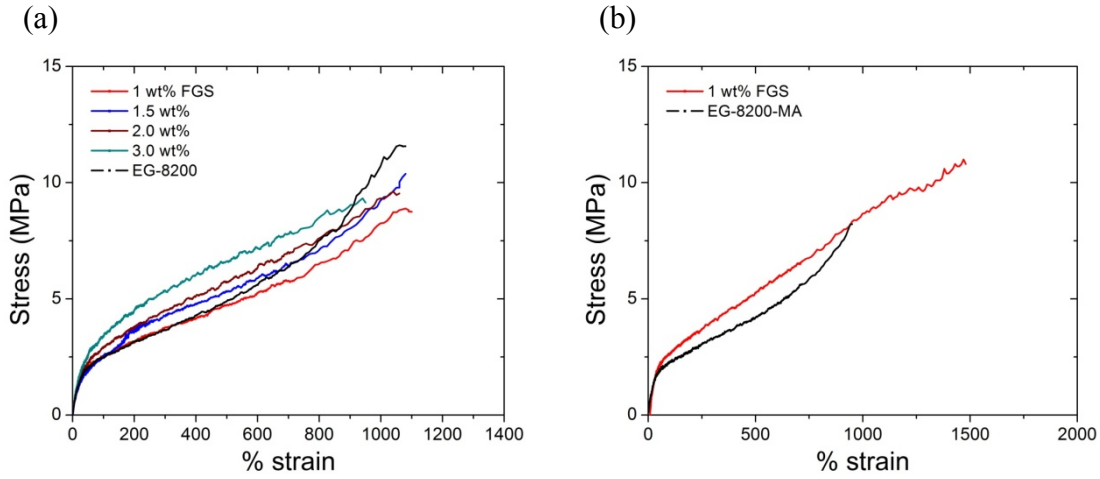

Figure C-6. Stress versus strain responses of melt blended densified FGS-PI/ (a) EG-8200 and (b) EG-8200-MA composites.

Table C-1. Mechanical Properties of FGS/EG-8200 Composites

	EG-8200	1 wt%	1.5 wt%	2 wt%	3 wt%
Modulus (Mpa)	6.4	8.4	9.6 ± 0.2	10.1 ± 0.2	11.3 ± 0.9
% Strain at break	1090 ± 40	1030 ± 60	1070 ± 50	1040 ± 50	1000 ± 40
Tensile Strength (MPa)	11.4 ± 1.7	8.3 ± 0.4	9.5 ± 0.7	9.2 ± 0.7	8.9 ± 0.8
Toughness (MPa)	60.3 ± 7.5	50.7 ± 4.3	60.4 ± 3.8	60.1 ± 4.0	63.7 ± 6.6

Table C-2. Tensile Properties of FGS/EG-8200-MA Composites

	EG-8200-MA	1 wt%
Modulus (Mpa)	6.7	8.4
% Strain at break	1000 ± 90	1430 ± 370
Tensile Strength (MPa)	7.6 ± 0.5	10.0 ± 1.3
Toughness (MPa)	43.7 ± 5.3	86.5 ± 21.6

Helium permeability of PE composites filled with FGS was determined at 35 °C based on the constant volume, variable pressure method[6] using a home-built apparatus (Table C-3).[7] Surprisingly, permeation of EG-8200 was increased by FGS dispersion regardless of the type of FGS used. Bright fringes appearing dominantly between FGS and matrix and within stacked FGS in Figure C-7 substantiate interfacial fracture due to weak adhesion and thus increased free volume available for He diffusion.

Table C-3. He Permeability of PE/FGS Composites at 35 °C

Sample	He Permeation in Barrer
EG-8200	19.0
1 wt% as-densified FGS-PI / EG-8200	22.7
1 wt% FGS-Vorbeck / EG-8200	20.7
1 wt% as-densified FGS-PI / EG-8200-MA	20.2

(a) (b)

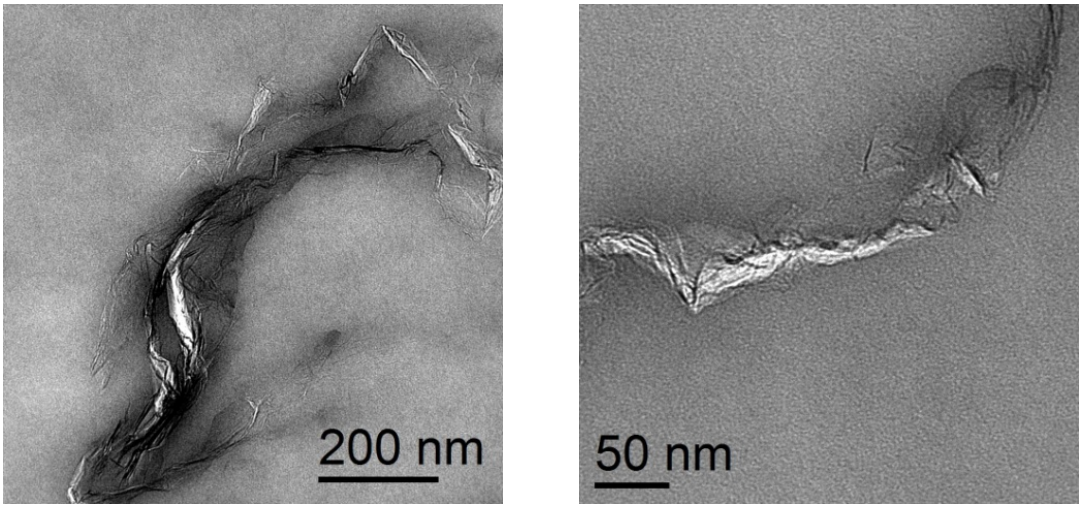

Figure C-7. TEM of 1 wt% FGS-Vorbeck/EG-8200 melt blend in higher magnification.

References

(1) Kaplan, W. A. *Modern Plastics Encyclopedia '98/ With Buyers' Guide*; McGraw-Hill/ Modern Plastics: New York, 1998; Vol. A-15.

(2) Production Selection Guide, Engage Polyolefin Elastomers, http://www.dow.com/elastomers/products/engage.htm, Accessed July 30, 2009.

(3) Staudenmaier, L. *Ber. Dtsch. Chem. Ges.* **1898**, *31*, 1481.

(4) Schniepp, H. C.; Li, J.-L.; McAllister, M. J.; Sai, H.; Herrera-Alonso, M.; Adamson, D. H.; Prud'homme, R. K.; Car, R.; Saville, D. A.; Aksay, I. A. *J. Phys. Chem. B* **2006**, *110*, 8535-8539.

(5) Herrera-Alonso, M.; Abdala, A. A.; McAllister, M. J.; Aksay, I. A.; Prud'homme, R. K. *Langmuir* **2007**, *23*, 10644-10649.

(6) Pye, D. G.; Hoehn, H. H.; Panar, M. *J. Appl. Polym. Sci.* **1976**, *20*, 1921-31.

(7) Jeong, H.-K.; Krych, W.; Ramanan, H.; Nair, S.; Marand, E.; Tsapatsis, M. *Chem. Mater.* **2004**, *16*, 3838-3845.